



Polish Maritime Research

Special Issue S1 (91) 2016
Vol. 23

ADDRESS OF PUBLISHER
& EDITOR'S OFFICE:

GDAŃSK UNIVERSITY
OF TECHNOLOGY

Faculty of Ocean Engineering
& Ship Technology
G. Narutowicza 11/12
80-233 Gdańsk, POLAND

tel.: +48 58 347 13 66
fax: +48 58 341 13 66

Marine Processes Studies and Marine Engineering

CONTENS

EDITORIAL STAFF:

Jacek Rudnicki
| Editor in Chief
Rafał Szłapczyński
| Associate Editor
Jerzy Świryczuk
| Associate Editor
Przemysław Wierzchowski
| Associate Editor
Aleksander Kniat
| Editor for international
relations

Price:
single issue: 25 zł

Prices for abroad
single issue:
- in Europe EURO 15
- overseas USD 20

WEB:
pg.edu.pl/pmr

e-mail : pmr@post.pl

ISSN 1233-2585

- | | |
|----|--|
| 4 | Qiang Zhang, Haijian Wang, Tong Guo
<i>FATIGUE DAMAGE OF V-LOCK CHAIN RING UNDER RANDOM LOAD</i> |
| 10 | Fali Huo, Deqing Yang, Yinzhi Zhao
<i>VIBRATION REDUCTION DESIGN WITH HYBRID STRUCTURES AND TOPOLOGY OPTIMIZATION</i> |
| 20 | Yue Chen, Lingyu Yang, Yi Xie, Song Yu
<i>THE RESEARCH ON CHARACTERISTIC PARAMETERS AND RESISTANCE CHART OF OPERATION AND MAINTENANCE TRIMARAN IN THE SEA</i> |
| 25 | W.C. ZHANG, H.X. Liu, X.W. ZHANG, L. ZHANG
<i>SEMI-ANALYTICAL SOLUTION OF OPTIMIZATION ON MOON-POOL SHAPED WEC</i> |
| 32 | Wenlai Xu, Ju Yang, Jing Wang, Yue Jian, Min Tang
<i>ANALYSIS OF THE START-UP OF NATURAL BIO-FILM COLONIZATION OF CONSTRUCTED RAPID INFILTRATION SYSTEM</i> |
| 36 | Bo LU
<i>SPATIAL ECONOMICS MODEL PREDICTING TRANSPORT VOLUME</i> |
| 44 | XIAO Qian-lu, LI Chun-hui, FU Xiao-yan, WANG Mei-ju
<i>EXTENDED ELLIPTIC MILD SLOPE EQUATION INCORPORATING THE NONLINEAR SHOALING EFFECT</i> |
| 52 | SUN Ning, ZHANG Ying-chao, ZHANG Wei-guo, CHENG En-lu, LIU Yun-ping
<i>HEATING CONTROL OF HEATED TWIN RADIOSONDE HUMIDITY SENSOR BASED ON DMC</i> |
| 59 | Yongming He, Yuan Wang, Yingwu Chen, Lining Xing
<i>AUTO MISSION PLANNING SYSTEM DESIGN FOR IMAGING SATELLITES AND ITS APPLICATIONS IN ENVIRONMENTAL FIELD</i> |

ADDRESS OF PUBLISHER
& EDITOR'S OFFICE:

GDAŃSK UNIVERSITY
OF TECHNOLOGY

Faculty of Ocean Engineering
& Ship Technology
G. Narutowicza 11/12
80-233 Gdańsk, POLAND

tel.: +48 58 347 13 66

fax: +48 58 341 13 66

- 71 **Wanchao Zhang, Hengxu Liu, Xuwei Zhang,
Liang Zhang, Muhammad Aqeel Ashraf,**
*OPTIMAL CONFIGURATIONS OF WAVE ENERGY CONVERTER ARRAYS WITH
A FLOATING BODY*
- 78 **SU Yil, Wang Fa-yin, AN Xiao-li**
*COUPLING MECHANISM AND COUPLING DEGREE MEASUREMENT MODEL
OF SHIPBUILDING INDUSTRY CLUSTER*
- 86 **Jianguo Jin, Zhazhou Wang, Lihua Cao**
*NUMERICAL ANALYSIS ON THE INFLUENCE OF THE TWISTED BLADE ON
THE AERODYNAMIC PERFORMANCE OF TURBINE*
- 91 **JinHuang, WunianYang, Li Peng, Muhammad Aqeel Ashraf,**
*MODEL OF ECO-WATER DRIVING FORCE AFFECTING THE EVOLVEMENT
OF RUNOFF IN THE UPPER MINJIANG RIVER BASIN*
- 97 **BO LU**
*MODELLING AND SIMULATION METHODOLOGY FOR DYNAMIC RESOURCES
ASSIGNMENT SYSTEM IN CONTAINER TERMINAL*
- 104 **Li Chunhui, Fu Xiaoyan, Li Ruijie, Dai Lu, Chen Peng**
VERTICAL DISTRIBUTION OF NEARSHORE FLOW VELOCITY
- 109 **Jie Zhao, Yumei Wang, Gaojie Yun, Muhammad Aqeel Ashraf**
*GROUND LIQUEFACTION AND DEFORMATION ANALYSIS OF BREAKWATER
STRUCTURES UNDER EARTHQUAKES*
- 115 **Xiao Wenwen, Zhao Bingxin, Wang Lili**
*MARINE INDUSTRIAL CLUSTER STRUCTURE AND ITS COUPLING
RELATIONSHIP WITH URBAN DEVELOPMENT: A CASE OF SHANDONG
PROVINCE*
- 123 **Wei Zhang, Yanjun Liu**
*SIMULATION AND EXPERIMENTAL STUDY IN THE PROCESS OF WAVE
ENERGY CONVERSION*
- 131 **Baiwei Lei, Bing Wu, Yatong Zhao, Muhammad Aqeel Ashraf**
*NUMERICAL SIMULATION AND EXPERIMENTAL STUDY ON FORMATION OF
HIGH CONCENTRATION OF H₂ GENERATED BY GAS EXPLOSION*
- 138 **Weifeng LI, Wenyao MA**
*SIMULATION ON VESSEL INTELLIGENT COLLISION AVOIDANCE BASED ON
ARTIFICIAL FISH SWARM ALGORITHM*
- 144 **SHEN YANG**
*AN ANTI-COLLISION METHOD OF SLIP BARREL FOR AUTOMATIC SHIP
LOADING IN BULK TERMINAL*
- 152 **Shen Yifan, Zhao Ning, Mi Weijian**
GROUP-BAY STOWAGE PLANNING PROBLEM FOR CONTAINER SHIP
- 160 **Xia Mengjue, Zhao Ning, Mi Weijian**
*STORAGE ALLOCATION IN AUTOMATED CONTAINER TERMINALS: THE
UPPER LEVEL*
- 175 **Kai CUI, Weikang LIN**
*MUCK PROBLEMS IN SUBWAY SHIELD TUNNELING IN SANDY COBBLE
STRATUM*
- 180 **WEI Jin, SHEN Wenbin, LI Hui, Liu Ziwei**
*NONLINEAR DRIFT OF THE SPRING GRAVIMETER CAUSED BY AIR PRESSURE
FROM THE KUNMING GS15 GRAVIMETERS*
- 187 **Hai AN, Hang YIN, Fukai HE**
*ANALYSIS AND APPLICATION OF MECHANICAL SYSTEM RELIABILITY
MODEL BASED ON COPULA FUNCTION*

Editorial

POLISH MARITIME RESEARCH is a scientific journal of worldwide circulation. The journal appears as a quarterly four times a year. The first issue of it was published in September 1994. Its main aim is to present original, innovative scientific ideas and Research & Development achievements in the field of :

Engineering, Computing & Technology, Mechanical Engineering,

which could find applications in the broad domain of maritime economy. Hence there are published papers which concern methods of the designing, manufacturing and operating processes of such technical objects and devices as : ships, port equipment, ocean engineering units, underwater vehicles and equipment as well as harbour facilities, with accounting for marine environment protection.

The Editors of POLISH MARITIME RESEARCH make also efforts to present problems dealing with education of engineers and scientific and teaching personnel. As a rule, the basic papers are supplemented by information on conferences , important scientific events as well as cooperation in carrying out international scientific research projects.

Scientific Board

Chairman : Prof. JERZY GIRTLEK - Gdańsk University of Technology, Poland

Vice-chairman : Prof. MIROSLAW L. WYSZYŃSKI - University of Birmingham, United Kingdom

Dr POUL ANDERSEN
Technical University of Denmark
Denmark

Dr MEHMET ATLAR
University of Newcastle United
Kingdom

Prof. GÖRAN BARK
Chalmers University of Technology
Sweden

Prof. SERGEY BARSUKOV
Army Institute of Odessa Ukraine

Prof. MUSTAFA BAYHAN
Süleyman Demirel University
Turkey

Prof. VINCENZO CRUPI
University of Messina, Italy

Prof. MAREK DZIDA
Gdańsk University of Technology
Poland

Prof. ODD M. FALTINSEN
Norwegian University of Science
and Technology
Norway

Prof. PATRICK V. FARRELL
University of Wisconsin Madison,
WI
USA

Prof. WOLFGANG FRICKE
Technical University Hamburg-
Harburg Germany

Prof. HASSAN GHASSEMI
Amirkabir University of Technology
Iran

Prof. STANISŁAW GUCMA
Maritime University of Szczecin
Poland

Prof. ANTONI ISKRA
Poznań University of Technology
Poland

Prof. JAN KICIŃSKI
Institute of Fluid-Flow Machinery
of PASci
Poland

Prof. ZBIGNIEW KORCZEWSKI
Gdańsk University of Technology
Poland

Prof. JANUSZ KOZAK
Gdańsk University of Technology
Poland

Prof. JAN KULCZYK
Wrocław University of Technology
Poland

Prof. NICOS LADOMMATOS
University College London United
Kingdom

Prof. JÓZEF LISOWSKI
Gdynia Maritime University Poland

Prof. JERZY MATUSIAK
Helsinki University of Technology
Finland

Prof. EUGEN NEGRUS
University of Bucharest Romania

Prof. YASUHIKO OHTA
Nagoya Institute of Technology
Japan

Dr YOSHIO SATO
National Traffic Safety and
Environment Laboratory
Japan

Prof. KLAUS SCHIER
University of Applied Sciences
Germany

Prof. FREDERICK STERN
University of Iowa, IA, USA

Prof. ILCEV DIMOV STOJCE
Durban University of Technology
South Africa

Prof. JÓZEF SZALA
Bydgoszcz University
of Technology and Agriculture
Poland

Prof. WITALIJ SZCZAGIN
State Technical University of
Kaliningrad, Russia

Prof. BORIS TIKHOMIROV
State Marine University of St.
Petersburg, Russia

Prof. DRACOS VASSALOS
University of Glasgow and
Strathclyde United Kingdom

FATIGUE DAMAGE OF V-LOCK CHAIN RING UNDER RANDOM LOAD

Qiang Zhang ^{a,b},
Haijian Wang ^b,
Tong Guo ^b,

^{a)}The State Key Laboratory of Mechanical Transmissions, Chongqing University, China

^{b)}College of Mechanical Engineering, Liaoning Technical University, Postal 123000, China

ABSTRACT

To study the influence of the random load on the V-lock chain ring for mining, the numerical simulation technology is used. The dynamic tension is obtained by using the dynamic model of the plough. The life and damage nephograms are obtained by using ANSYS Workbench. The analysis results show that the short fatigue life region of the V-lock chain ring for mining is mainly concentrated on the transition region between the medial straight edge and arc, and the fatigue damage of the link chain on the side of the motion direction of the plow head is larger than that on the other side. This link chain has strong anti-fatigue performance.

Keywords: V-lock chain ring for mining; dynamic model; fatigue damage; random load; finite element; sensitivity analysis

INTRODUCTION

The link chain is the independent component which is used for connecting the chain. The link chain is very widely used in many special equipments of the coal mine and equipments with haulage chain, such as the scraper conveyor, transfer machine, plough, cast stone scraper conveyor and fishing mechanical. It is also widely used on port transport business. Due to the special working condition, the link chain often generates the fracture phenomenon. Once the link chain is ruptured, the whole equipment will be in paralysis conditions which will seriously affect the normal production. The chain rupture accident will cause not only the serious economic loss but also the fatal accident caused by finding the fractured chain at the side of the coal wall.

Therefore, the quality performance level of the link chain is one of the main indexes for evaluating the whole aircraft reliability and machine life. Although the reliability of the chain has attracted broad attention of domestic and foreign scholars, little study has been carried on for the V-lock chain ring for mining.

This paper wants to research the fatigue damage of the V-lock chain ring for mining used in plough. The dynamic model of the plough is established to obtain the dynamic tensile force which is used as the random load. Time of the crack initiation of the link chain is calculated by using the finite elemental method. The sensitivity of the V-lock chain ring for mining is analyzed. The results of this research can provide some theoretical basis for the further study of the V-lock chain ring for mining.

DYNAMIC MODELING OF PLOUGH

$$F_u = \mu mg \quad (4)$$

BASIC HYPOTHESES

To establish the dynamic model of the plough, the following hypotheses are made. 1) The mass and friction resistance of the plow chain are ignored because the mass of the plow head is generally several tons. 2) The vertical one-dimension dynamic mode of the plough is established by neglecting the influence of the transverse vibration of the chain. 3) The polygon effect of the sprocket isn't considered.

MATHEMATICAL MODELING OF PLOUGH

The plow system is composed of the plow head, plow chain, transmission, electric control system, hydraulic system and so on. The plough usually adopts the two-terminal motor drive. The work principle of the plough is that the plow head with the plane iron moves along the guide of the middle trough on the scraper conveyor under the traction of the plow chain, and the coal is loaded into the conveyor under the action of the pyriform incline of the plow head when the plane iron cuts the coal wall. The plough does the reciprocating motion along the working face under the haulage of the plow chain. As the plow chain runs in the closed sliding framework, the opportunity of the transverse vibration of the plow chain is very little, while the longitudinal vibration is relatively obvious. The vibration has an unfavorable influence on the operation of the plough. The variation of the tensile force will affect the service life of the plow chain. The plow chain is considered as the viscoelastic body according to the structure and actual operation situation of the plough. To make things easy to study, the dynamic model of the plough is simplified. The dynamic model of the plough is shown in Figure 1.

$$m\ddot{x} = F_2 - F_1 - F_u - F_b(t) \quad (1)$$

Where m is the mass of the plow head, \ddot{x} is the acceleration of the plow head, F_1 is the tensile force of the chain between the plow head and driving device II, F_2 is the tensile force of the chain between the plow head and driving device I, F_u is the friction resistance of the plow head and $F_b(t)$ is the planning resistance of the plow head.

Where x is the displacement of the plow head, \dot{x} is the velocity of the plow head, ω is the angular velocity of the drive sprocket, R is the pitch radius of the sprocket, t is the time, k_1 and c_1 are respectively the stiffness and damping of the chain between the plow head and driving device II, k_2 and c_2 are respectively the stiffness and damping of the chain between the plow head and driving device I and F_{vr} is the surplus preload.

$$F_1 = \begin{cases} k_1(x - \omega Rt) + F_{vr} + c_1(\dot{x} - \omega R) & (k_1(x - \omega Rt) + F_{vr} + c_1(\dot{x} - \omega R)) > 0 \\ 0 & (k_1(x - \omega Rt) + F_{vr} + c_1(\dot{x} - \omega R)) \leq 0 \end{cases} \quad (2)$$

$$F_2 = \begin{cases} k_2(\omega Rt - x) + F_{vr} + c_2(\omega R - \dot{x}) & (k_2(\omega Rt - x) + F_{vr} + c_2(\omega R - \dot{x})) > 0 \\ 0 & (k_2(\omega Rt - x) + F_{vr} + c_2(\omega R - \dot{x})) \leq 0 \end{cases} \quad (3)$$

Where μ is the friction coefficient between the plow head and sliding framework, is the acceleration of gravity.

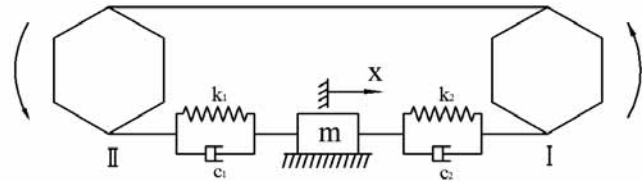


Fig.1 Dynamic model of plough

Due to the complex condition of the coal wall, the load of the plane iron caused by the coal wall is random. Many studies prove that the load of a single plane iron has the random nature. The study of the distribution functions of the cutting force and feeding distance force of the plane iron shows that the original Γ distribution will change into the normal distribution when cutting the coal seam. The imbalance of the load distribution can be evaluated by the value of the variation coefficient. Therefore, the planning resistance of the plow head $F_b(t)$ is the normal distribution stationary random process.

The surplus preload of the plow chain is

$$F_{vr} = F_v - \frac{3}{4}(F_b(t) + F_u) + (F_b(t) + F_u) \frac{x}{2L} \quad (5)$$

Where L is the face length (namely the distance between the centers of the two drive sprocket) and F_v is the pre-tightening force.

SIMULATION MODELING AND ANALYSIS OF PLOUGH

SIMULATION MODELING OF PLOUGH

The mathematical model of the plough established in above paragraphs is the nonlinear random kinetic equation which is timevarying, and the description of nonlinear factors is very complex. As it is difficult to obtain the accurate or approximate analytical solution by using the present solving methods, the numerical method is used to analyze the dynamic response of the plough further.

MATLAB/SIMULINK is used for establishing the simulation model. To get the time history of the tensile force of the plow chain, the kinetic equation of the single degree plough is solved under the random load caused by the coal wall. The simulation model of the plough is shown in Figure 2.

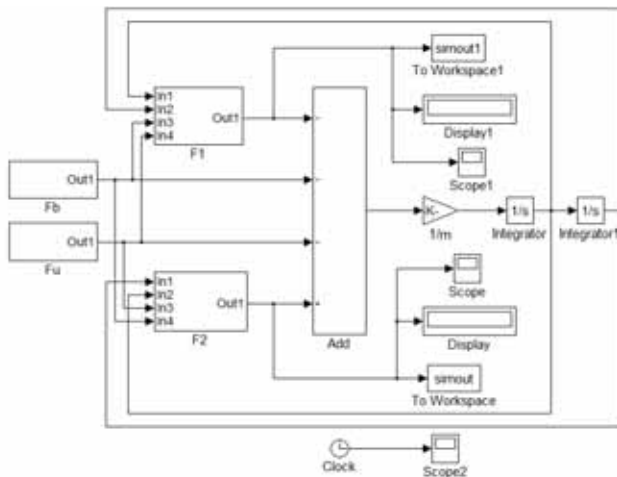


Fig.2 Simulation model of the plough

DETERMINATION OF SIMULATION PARAMETERS

The parameters of the plough of some coal mine are used as the basic simulation parameters, giving the example for calculating the fatigue life of the plow chain. The plow chain specification is $\phi 30 \times 108$ mm; the mass of the plow head is 3.4×10^3 kg; the pitch radius $R = 0.243$ m; the angular velocity of the drive sprocket $\omega = 6.17$ rad/s; the friction coefficient between the plow head and sliding framework $\mu = 0.3$; the stiffness $c_1 = c_2 = 500$ Ns/m; the damping $k_1 = k_2 = 6.95 \times 10^7$ N/m; the face length $L = 200$ m; the initial displacement $x_0 = 0$ m, and the initial velocity $\dot{x} = 1.5$ m/s. The planning resistance average is 50 KN, and the variation coefficient is 0.7. The pretightening force is 50 KN. Let the simulation time be 120 s.

ANALYSIS OF TENSILE FORCE

The time history of the plow chain tension obtained by numerical simulation is shown in Figure 3. Figure 3 shows that the tensile force of the chain is a dynamically changing process, and the tensile force at the initial time is the maximum which shows that the impact load will act on the chain when starting the chain. The waveform in Figure 3(a) is similar to the one in Figure 3(b), but their load amplitude level is different.

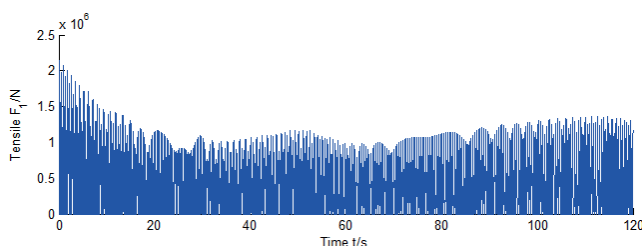


Fig.3(a) Tensile force F_1

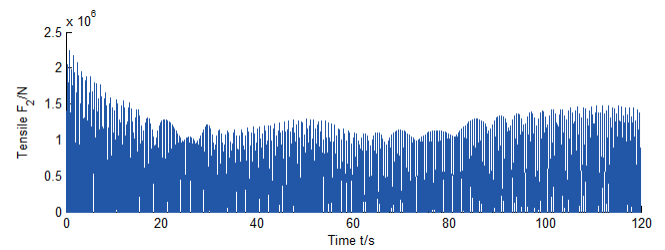


Fig.3(b) tensile force F_2

FATIGUE ANALYSIS OF V-LOCK CHAIN RING FOR MINING

ESTABLISHMENT OF FINITE ELEMENT MODEL

The research object is the $\phi 30 \times 108$ mm V-lock chain ring for mining used in the plough. This link chain is composed of the semi ring and elastic pin. The transmission system of the link chain is a complicated structure, so it is very difficult to establish the complete dynamic model. The essence of the simulation modeling is to establish a similarity relation to the actual working condition. To establish the model conveniently, the link chain system is simplified on the basis of the actual working condition. The simplified model of the link chain system which is composed of two semi forging rings and a complete link chain is shown in Figure 4(a). Under the mesh order in ANSYS Workbench software, the automatic mesh generation is performed in the simplified link chain system. The finite element model is shown in Figure 4(b). The element size is 4 mm. The node number is 197924, and element number is 56840. The material of the link chain is 23 Mn-Cr-Ni-Mo. The material parameters are as follows: Young's modulus is 210GPa, and Poisson's ratio is 0.3.

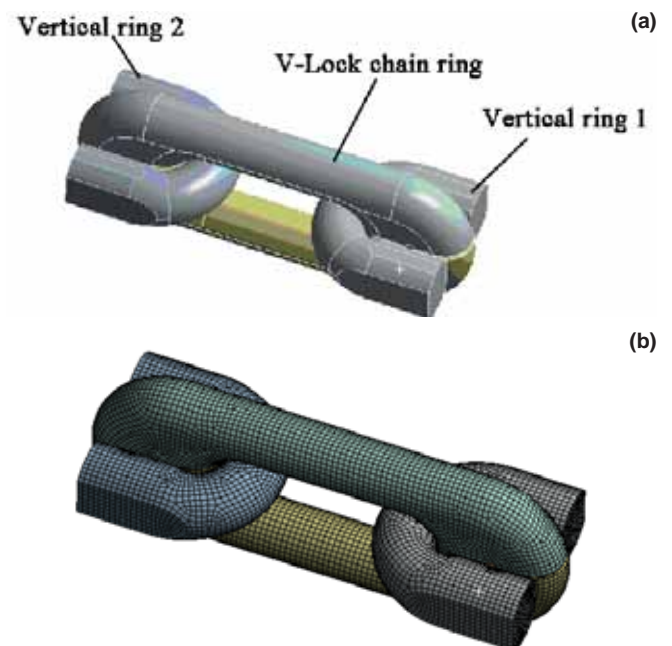


Fig.4 (a) Simplified model of link chain system and (b) Finite element model of link chain system.

FINITE ELEMENT ANALYSIS OF LINK CHAIN

The static analysis result exported from ANSYS Workbench is imported into ncode DesignLife which is the advanced fatigue analysis module of ANSYS. The tensile force is used as the random disturbing load. Goodman theory is used to correct the damage calculation for the mean stress. The fatigue life and damage cloud pictures of the V-lock chain ring for mining obtained in ncode DesignLife are shown in Figure 5 and Figure 6.

Figure 5(a) shows that the minimum fatigue life of the V-lock chain ring is 1441 cycles which are caused by neglecting the fillet, but this isn't the real life of the link chain. For the convenience of the finite element analysis, fillets of the V-lock chain ring for mining are neglected which causes the stress concentration. Therefore, the minimum fatigue life should be 44180 cycles in fact. Figure 5(b) shows that the real minimum fatigue life is 26110 cycles. 1 cycle is equal to 120s, so the minimum fatigue life of the link chain under the tensile force F_1 and F_2 are respectively 61.4 days and 36.3 days. The fatigue life under the tensile force F_2 is shorter than that under the tensile force F_1 through comparing Figure 5(a) and Figure 5(b) which shows that the tensile force F_2 causes greater damage, namely the fatigue damage of the link chain on the side of the motion direction of the plow head is larger than that on the other side. The short fatigue life region of the V-lock chain ring for mining is mainly concentrated in the transition region between the medial straight edge and arc which is the same as the welding ring and forging ring. This region will be the crack source, so the fracture failure is easier to produce in this region.

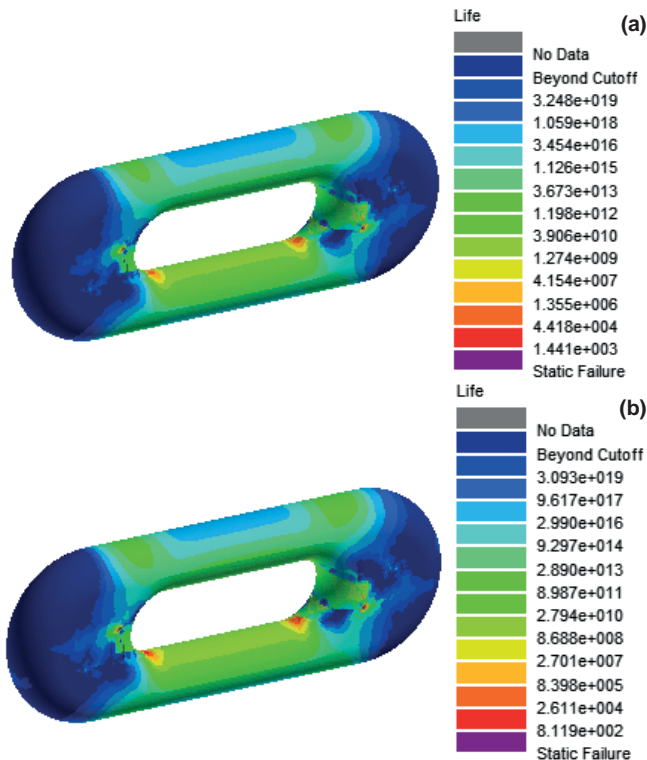


Fig.5 (a) Life of V-lock chain ring for mining under tensile force and (b) life of V-lock chain ring for mining under tensile force

The damage is the ratio of the design life and probable life. The maximum damage region is equivalent to the minimum fatigue life region. Figure 6 shows that the damage values under different tensile forces are less than 1, namely the design life is less than the probable life which shows that the V-lock chain ring for mining meets the design requirements.

The minimum fatigue life of the V-lock chain ring for mining calculated by the finite element method actually represents cracks have appeared on the link chain at this moment. But this can't express the link chain has lost the work ability. The process from the crack initiation to the complete failure of the V-lock chain ring for mining needs some time.

According to the data provided by manufacturers and coal enterprises, we can know that the average service life of the V-lock chain ring for mining used in the plough is 3.5 months.

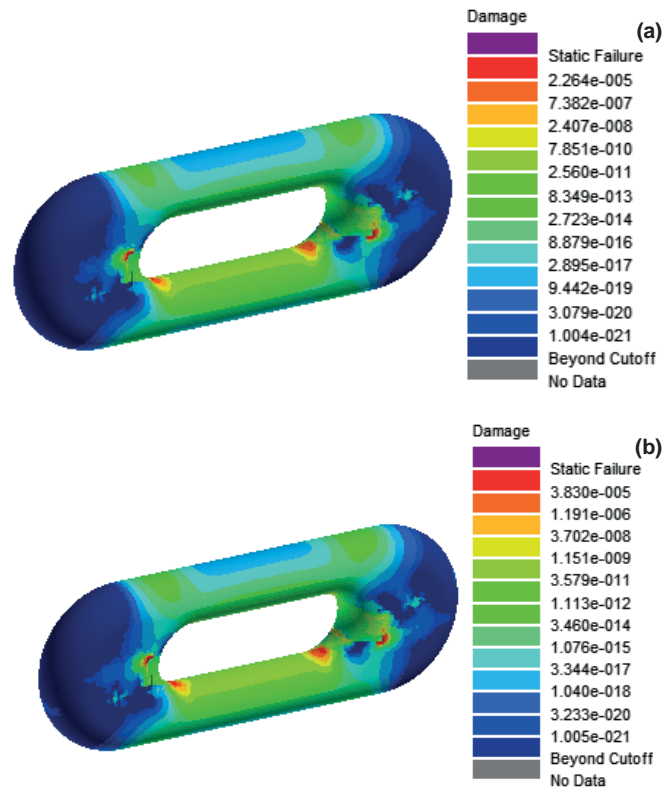


Fig.6(a) Damage of V-lock chain ring for mining under tensile force and (b) damage of V-lock chain ring for mining under tensile force

SENSITIVITY ANALYSIS OF V-LOCK CHAIN RING FOR MINING

OVERLOAD SENSITIVITY ANALYSIS OF LINK CHAIN

To study the overload sensitivity of the V-lock chain ring for mining, the scale factor of the load is used as the varying parameter. The overload working conditions are simulated by a change of the value of the scale factor. The curve of data points of the minimum fatigue life is plotted by using MATLAB. The overload sensitivity curve of the V-lock chain ring for mining is shown in Figure 7(a). Figure 7(a) shows that the minimum life decreases with the increase of the scale factor. The minimum life decreases soon in the scale factor range from 0.6 to 0.9. In

the scale factor range from 0.9 to 1.5, the minimum life changes slowly which shows that the V-lock chain ring for mining is insensitive to the overload, namely the link chain has strong anti-fatigue performance.

RESIDUAL STRESS SENSITIVITY ANALYSIS OF LINK CHAIN

The V-lock chain ring for mining will produce the residual stress in the manufacturing process. The residual stress sensitivity curve of the link chain is shown in Figure 7(b). From Figure 7(b), it can be seen that the minimum life decreases with the increase of the residual stress, and the general trend of the curve is linear. The influence of the residual stress isn't very significant.

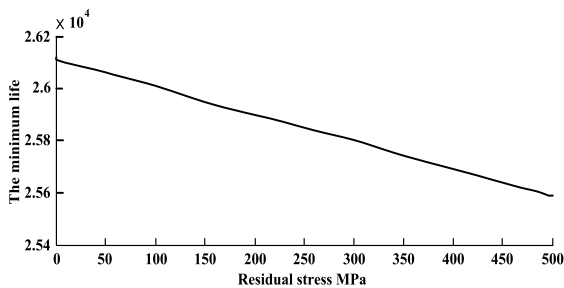
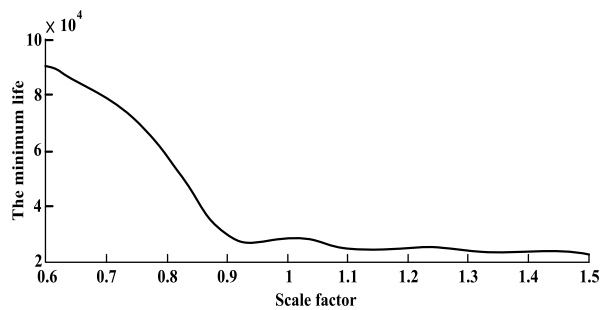


Fig.7(a) Overload sensitivity of link chain and
(b) residual stress sensitivity of link chain

SURFACE ROUGHNESS SENSITIVITY OF LINK CHAIN

The surface quality has a significant influence on the fatigue life in the high cycle fatigue, but the influence is little in the low cycle fatigue. This is because the relatively high load is the dominant factor of the whole fatigue process in the low cycle fatigue. The minimum life increases exponentially with the increase of the surface roughness factor, as shown in Figure 8. The V-lock chain ring for mining is sensitive to surface roughness. Therefore, improving the surface processing quality is a main way to prolong the service life of the link chain.

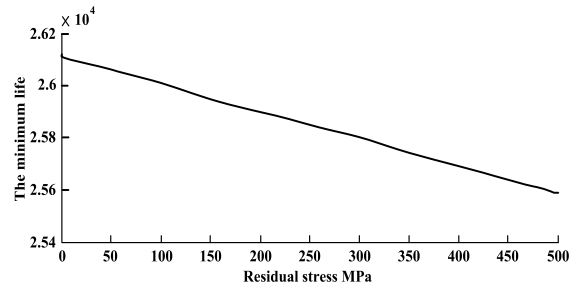


Fig.8 Surface roughness sensitivity of link chain

CONCLUSION

- 1) The tensile force of the chain transmission system is a dynamic changing process in the plough. The bilateral tensile force of the plow head is different. The tensile force on the motion direction side can cause the larger damage.
- 2) The short fatigue life region of the V-lock chain ring for mining is mainly concentrated in the transition region between the medial straight edge and arc.
- 3) Improving the surface processing quality can significantly prolong the service life of the V-lock chain ring for mining.
- 4) The V-lock chain ring for mining has strong anti-fatigue performance.
- 5) The analysis results in this paper can provide the theoretical basis for prolonging service life and the selection of the optimum maintenance period of the V-lock chain ring for mining.

ACKNOWLEDGEMENT

This work was partially supported by the National Natural Science Foundation of China (Grant No. 5150041043) and Key Laboratory of structural analysis for industrial equipment(GZ1402) and Foundation of the State Key Laboratory of Mechanical Transmissions (SKLMT-KFKT-201515).

REFERENCES

1. Zhang, Q.; Fu, Y, F.; Hu, N., (2013). Study of dynamic characteristic of mining V-lock chain ring under impact load caused by stuck chain. Journal of Hefei University of Technology (Natural Science), 36, 401-404.
2. Shih-Chuan, (2000). Fracture analysis of inter facial crack by global-local finite element. International Journal of Fracture, 2, 177-193.

3. Zhang, Q.; Fu, Y, F.; (2012). Critical damage of high strength ring chain under temperature/ mechanical loads. *Materials Review*, 26, 163-170.
4. Mao, J.;Cao, Y, L.; Jiang, G, Q., (2000). Analyzing the strength and optimizing the structure of the link chain. *Machine Design and Research*, 21, 65-68.
5. Zhang, Y, B.;Guo, W.;Gao, Y, P., (2011). Application and development of chain connector. *Coal Mine Machinery*, 32, 3-5.
6. Zhang, Q.; Fu, Y, F.; (2013). Reliability-based robust design for kinematic accuracy of the plow plane chain mesh with arbitrary distribution parameters base on NSGA-II algorithm. *Journal of China Coal Society*, 38, 505-511.
7. Ren, C, Y.;Zhao, C., (2010). Structure Analysis based on flat type connector units of scraper conveyor. *Journal of Machine Design*, 27, 74-76.
8. Zhang, Q.; Li, S., (2012). Topological optimization of pick structure based on LS-DYNA. *Disaster Advances*, 5(4), 187-193.
9. Yang, S, C.; Wang, G, Q.;Zhang, Y, B., (2012). Finite element analysis and design for connecting ring of scraper conveyor. *Coal Mine Machinery*, 33, 105-107.
10. Zhang, Q.; Fu, Y, F.; Hu, N., (2014). Dynamic simulation of scraper chain system reliability and selection of optimum maintenance period. *Machine Design & Research*, 30(2), 148-153.
11. Kang, X, M.; Li, G, Q., (2009). Single-degree of freedom dynamic model of coal plough and its simulation. *Journal of Vibration and Shock*, 28, 191-195.
12. Zhang, Q.; Wang H, J.; Fu, Y, F.; Gong, J., (2015). Mechanical property and fatigue life prediction of sprocket in scraper conveyor. *Journal of Mechanical Strength*, 37(2), 328-336.
13. Li, X, H.; Liu, X.;Jiao, L., (2010). Dynamic simulation of sliding coal plow under different working conditions. *Journal of China Coal Society*, 35, 1202-1206.
14. Kang, X, M.; Li, G, Q., (2010). Prediction of fatigue life of coal plow chain under stochastic dynamic load. *Journal of China Coal Society*, 35, 503-508.
15. Ramaswamy S.N.; Nampoothiri N.V.N.; Sckar T., (2013). Mitigation of accidental disasters in fire-works industries –construction management approach. *Disaster Advances*, 6, 41-50.
16. Wei, G., (2013). Numerical analysis of DOT shield 45° crossing the masonry structure buildings. *Disaster Advances*, 6, 20-25.
17. Zhang, Q.; Fu, Y, F., Nie, G, Q., (2013). Study of mechanical properties of V-lock chain ring under dynamic load. *Journal of machine design*, 30, 13-16.
18. Wu W.F.; Ni C.C., (2004). Probabilistic models of fatigue crack propagation and their experimental verification. *Probabilistic Engineering Mechanics*, 19, 247-257.
19. Zhang, Q.; Xu, M, J., (2014). Study on fatigue life of plow bit under different planning parameters. *Strength of Materials*, 46(2), 262-269.

CONTACT WITH AUTHOR

Qiang Zhang

Email:lgdix042@126.com
Tel.: +0086 0418-3350517;
Fax: +0086 0418-3350517

Haijian Wang

Email:qingseyuji2010@163.com

Tong Guo

Email:45381111@qq.com

VIBRATION REDUCTION DESIGN WITH HYBRID STRUCTURES AND TOPOLOGY OPTIMIZATION

Fali Huo¹

Deqing Yang²

Yinzi Zhao¹

¹ School of Naval Architecture & Ocean Engineering, Jiangsu University of Science and Technology, Zhenjiang, Jiangsu, 212003, China

² School of Naval Architecture, Ocean and Civil Engineering, Shanghai Jiao Tong University, Shanghai, 200030, China

ABSTRACT

The hybrid structures show excellent performance on vibration reduction for ship, aircraft and spacecraft designs. Meanwhile, the topology optimization is widely used for structure vibration reduction and weight control. The design of hybrid structures considering simultaneous materials selection and topology optimization are big challenges in theoretical study and engineering applications. In this paper, according to the proposed laminate component method (LCM) and solid isotropic microstructure with penalty (SIMP) method, the mathematical formulations are presented for concurrent materials selection and topology optimizations of hybrid structures. Thickness distributions of the plies in laminate components are defined as materials selection design variables by LCM method. Relative densities of elements in the components are defined as topology design variables by SIMP method. Design examples of hybrid 3-bar truss structures and hybrid floating raft with vibration reduction requirements verified the effectiveness of the presented optimization models.

Keywords: hybrid structure; vibration reduction; materials selection; topology optimization

INTRODUCTION

The vibration reduction plays important role in ship, aircraft and spacecraft designs. Hybrid structure is widely used to reduce vibration and control weight in ship, aircraft and spacecraft design for mechanical behavior, the inelastic damping behavior, and strength of hybrid structure, presently. Meanwhile, the topology optimization is the better method for vibration reduction and weight control.

In present study focus on optimal design methods for hybrid structure considering vibration reduction. Yang (2012) proposed a laminate component method (LCM) on modeling of hybrid structure for materials selection (type and size) design. By introducing the concept of laminate component, materials selection optimization design of hybrid structure is formulated as a size or topology optimization problem with all materials

for selection within one structural analysis model. In study of structure design methods, mechanical behavior, the inelastic damping behavior, and strength of metal-hybrid structures are investigated (Hidde 1992, Asundi 1997, Kawai 1998, Botelho 2006). Blasques (2012) presents a novel framework for simultaneous optimization design of topology and laminate properties of laminated composite beam cross sections. The majority of the hull structures are manufactured by metal materials which can decrease the costs; and some important components are fabricated by composites materials which can decrease structure weight and vibration levels (Barsoum 2003, Cao 2007). The design of metal-composite hybrid structure involves simultaneous determinations on materials selection, topology, geometry, and components dimensions.

In addition, structural dynamic performance like vibration levels and eigenfrequency must be taken into account for the purpose of vibration and noise reduction. Rahul (2006) dealt with optimization of hybrid fiber reinforced plastic laminated plates subjected to impact loading, Finite element method (FEM) and genetic algorithm (GA) have been used to obtain optimum laminate in terms of minimizing the cost, weight of graphite/epoxy-aramid/epoxy hybrid laminates while maximizing the strength.

The topology optimization for vibration reduction and weight control has been widely investigated. Sigmund (1999) suggested topology optimization procedure as a tool for smart materials design and discussed two applications in composite structures. Kravanja (2005) studied the simultaneous topology and size optimization of mechanical structures by the Mixed Integer Nonlinear Programming (MINLP) approach, and general multilevel MINLP formulations for mechanical superstructure were presented. Sun (2011) dealt with topology optimization of composite structure using Bi-directional Evolutional Structural Optimization (BESO) method. Stress concentration in composite structure can be reduced by BESO method and geometry of structure is easy to fabricate by techniques currently available. Coelho (2011) developed a computational procedure for two-scale topology optimization problem using parallel computing techniques, the material properties were designed in micro and macro scale respectively. Lee (2012) proposed an approach for topology optimization of structures under design-dependent pressure loading. Cherkaev (2012) introduced a new type of optimal isotropic structure for multi-material composites. Rakshit (2008) explored simultaneous geometry design and material selection for statically determinate trusses with continuous optimization model, and the available materials for selection were put in a database with design index along with the corresponding best geometry.

However, investigations of vibration reduction and weight control design on simultaneous by hybrid structure and topology optimization design are very scarce. One challenge in this problem is the establishment of a unified structural analysis and optimization model for different settings of

materials selection and components topology distributions during solving iterations. The other challenge is the definitions of materials selection design variables and topology design variables in one optimization model, these design variables are all discrete variables in nature. In this paper, by applying the proposed laminate component method (Yang, 2012) and SIMP method, the mentioned challenges are attempted. The mathematical formulations for concurrent materials selection and topology optimization of hybrid structure are proposed with respect to vibration reduction constraints. Typical metal-composite hybrid structures optimization examples are performed to demonstrate the effectiveness of the proposed models.

LAMINATE COMPONENT METHOD FOR HYBRID STRUCTURE OPTIMIZATION

Laminate component method (LCM) was firstly applied in materials selection (type and size) optimization design of hybrid structure (Yang 2012). Based on LCM method, materials selection optimization design can be formulated as a continuous optimization problem to avoid the conventional discrete optimization model depending on materials database and materials design index method. The laminate component method consists of three main steps.

- 1) First, replace the design components in hybrid structure with laminated composite components that each ply fabricated by different materials for selection.
- 2) Second, discretize and construct finite element model of the hybrid structure.
- 3) Finally, define thickness of each ply or materials topology distribution of each ply in laminated composite design components as materials selection design variables, establish optimization model with vibration reduction constraints and complete optimization.

An engineering design example of hybrid floating raft with LCM method is shown in Fig.1. The laminate component method firstly assumes each design component (No.1 to No.7)

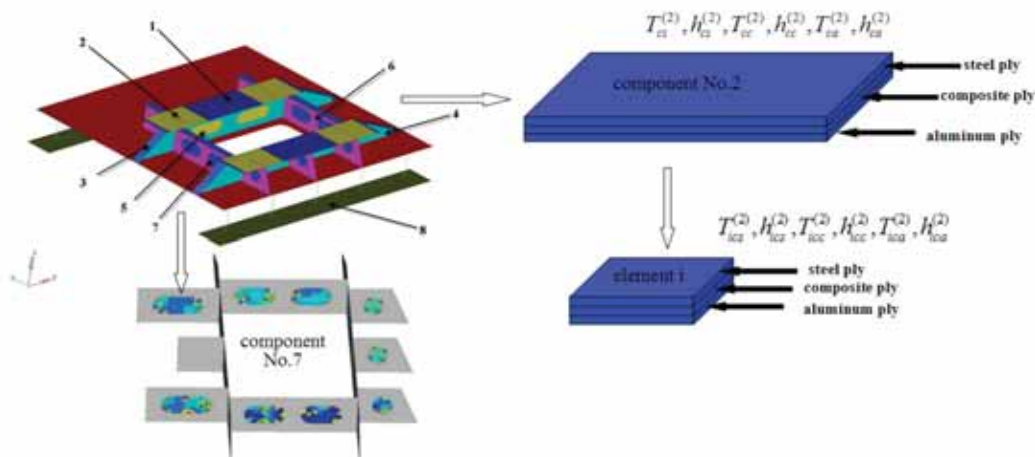


Fig. 1 Design domains and laminate components in continuum hybrid structure

is made of laminate plate with available materials for selection as each ply – steel ply, composite materials ply and aluminum ply (as shown in component No.2 in Fig.1), then finite element model of hybrid structure is constructed. Finally thickness of each ply is defined as materials selection design variables, optimization model is established and solved. Though there are four materials selection optimization models according to LCM method, in which materials elastic modulus, thickness of ply, and materials topology distribution are defined as design variables respectively, the use of thickness as materials selection design variables is the reasonable choice when topology optimization design is also required. Model II can avoid the discreteness and complexity of the structural analysis model due to the variation of materials elastic modulus and materials topology distribution. As a continuum structure, hybrid floating raft is composed by web plates, rib plates, flange plates and panels. These plates (design components) are easily replaced by laminated composite plates with LCM method.

SIMP METHOD FOR STRUCTURAL TOPOLOGY OPTIMIZATION

Many topology optimization methods like homogenization method (Bendsøe 1989, 2003), density method, evolutionary structural optimization method (Xie 1997) and ICM method (Sui 1998) have been investigated and applied in engineering. SIMP method is a widely used simple topology optimization approach (Zhou 1991) combined the finite element method and density method. A topology optimization problem based on SIMP where the objective is to minimize compliance can be written as

$$\begin{aligned} \text{Min}_{\mathbf{X}} \quad & C(\mathbf{X}) = \mathbf{U}^T \mathbf{K} \mathbf{U} = \sum_{e=1}^N (x_e)^p \mathbf{u}_e^T \mathbf{k}_e \mathbf{u}_e \\ \text{s.t.} \quad & \frac{V(\mathbf{X})}{V_0} \leq f \\ & \mathbf{K} \mathbf{U} = \mathbf{F} \\ & 0 < x_{\min} \leq x_e \leq 1 \end{aligned} \quad (1)$$

where \mathbf{U} and \mathbf{F} are the global displacement and force vectors, respectively, \mathbf{K} is the global stiffness matrix, \mathbf{u}_e and \mathbf{k}_e are the element displacement vector and stiffness matrix, respectively, $\mathbf{X} = [x_1, x_2, \dots, x_e, \dots, x_N]^T$ is the vector of design variables of relative densities of elements, x_{\min} is a vector of minimum relative densities (non-zero to avoid singularity), N is the number of elements used to discretize the design domain, p is the penalization power (typically $p=3$), $V(\mathbf{X})$ and V_0 is the material volume and design domain volume, respectively and f is the prescribed volume fraction.

In this paper, SIMP method is used to define the topological design variables of elements in each laminate component or components without materials selection design requirement. For the elements with materials selection design requirement, each element consists of multiple material plies according to laminate component method, and x_e is the topological value of the eth laminate element. x_e has no

connection with materials selection design, and it only decides the existence of the element. For the elements without materials selection design requirement in components, each element consists of isotropic material, x_e denotes the existence of the element.

HYBRID STRUCTURE DESIGN FOR VIBRATION REDUCTION BY MATERIALS SELECTION AND TOPOLOGY OPTIMIZATION ON SIMULTANEOUS

THE MATHEMATICAL MODEL OF HYBRID STRUCTURE DESIGN

By applying LCM method to deal with materials selection, and applying SIMP method to define the component topology in hybrid structure, the concurrent optimization model for materials selection and topology design is formulated as Eq.2. The weight of hybrid structure is considered as the objective function with acceleration vibration level differences, stresses and displacements on designated points and elements as constraints.

$$\begin{aligned} \text{Find} \quad & \mathbf{T}_s = [t_{1s}, t_{2s}, \dots, t_{ms}, t_{m+1s}, \dots, t_{ns}]^T \\ & \mathbf{T}_c = [t_{1c}, t_{2c}, \dots, t_{ic}, \dots, t_{mc}]^T \\ & \tilde{\mathbf{X}}_i = [\mathbf{X}_1, \mathbf{X}_2, \dots, \mathbf{X}_i, \dots, \mathbf{X}_n]^T \\ \text{Min} \quad & \text{Weight} = \sum_{i=1}^m \sum_{t=1}^{T_{ir}} (t_{ic} \cdot \rho_c + t_{is} \cdot \rho_s) \cdot se_{it} \cdot x_{it} + \sum_{i=1}^m \sum_{t=T_{ir}+1}^{T_i} (t_{ic} \cdot \rho_c + t_{is} \cdot \rho_s) \cdot se_{it} + \\ & \sum_{i=m+1}^n \sum_{t=1}^{T_{ir}} t_{is} \cdot \rho_s \cdot se_{it} \cdot x_{it} + \sum_{i=m+1}^n \sum_{t=T_{ir}+1}^{T_i} t_{is} \cdot \rho_s \cdot se_{it} \\ \text{s.t.} \quad & \sigma_e^L \leq \sigma_{ek}[\mathbf{T}_s, \mathbf{T}_c, \tilde{\mathbf{X}}_i] \leq \sigma_e^U \\ & \delta_{pk}[\mathbf{T}_s, \mathbf{T}_c, \tilde{\mathbf{X}}_i] \leq \bar{\delta}_p \\ & a_{ij}^{\max} \leq a_A^U \\ & a_{Bj}^{\max} \leq a_B^U \\ & 10^{L_e/20} - \varepsilon \leq a_{ij}^{\max} / a_{Bj}^{\max} \leq 10^{L_e/20} + \varepsilon \\ & f^L \leq j \leq f^U \\ & t_{ic} = sca \cdot t_{is} \\ & t_{is}^L \leq t_{is} \leq t_{is}^U \\ & \mathbf{X}_i = [x_{i1}, x_{i2}, \dots, x_{it}, \dots, x_{iT_{ir}}]^T \\ & 0 < x_{\min} \leq x_{it} \leq 1 \\ & i = 1, 2, \dots, n; \quad e = 1, 2, \dots, E; \quad k = 1, 2, \dots, K; \\ & p = 1, 2, \dots, P; \quad t = 1, 2, \dots, T_{iT} \end{aligned} \quad (2)$$

The meanings of design variables and constraints are listed in Nomenclature. $n \geq m$ means some components no materials type selection design requirements.

Based on the proposed model, a single unified structural analysis and optimization model is implemented during

the optimization procedure. The variation of topology and materials types during optimization iteration can be accounted in a single structural analysis model by changing thickness and relative density of each element. Then the analysis results from this single structural model are used in the single proposed optimization model as Eq.2. Optimization model and structural analysis model are unified in one model.

$$T_{ip} = T_{is} + T_{ic}$$

$$T_{is} = [1 + f(t_{is})] / 2 \cdot t_{is} + t_{s \min}$$

$$T_{ic} = [1 - f(t_{is})] / 2 \cdot t_{is} \cdot sca + t_{c \min}$$

$$f(t_{is}) = \text{sgn}[\sin(1000 \cdot t_{is} \cdot \pi)]$$

T_{is} is the equivalent thickness of steel layer in the i th component after transformation, and the T_{ic} is the equivalent thickness of composite material layer in the i th component after transformation. sgn is the sign function. The values of $f(t_{is})$. k is a non-negative integer. $t_{s \min}$ and $t_{c \min}$ are minimal thickness for steel layer and composite material layer respectively to avoid element stiffness matrix singularity. The numbers of design variables for topology, size and material selection optimization and the element numbers in FEM model in the presented concurrent optimization are large, therefore a long computation time will cost to get

$$\begin{aligned} \text{Find} \quad & \mathbf{T}_s = [t_{1s}, t_{2s}, \dots, t_{ms}, t_{m+1s}, \dots, t_{ns}]^T \\ & \mathbf{T}_c = [t_{1c}, t_{2c}, \dots, t_{ic}, \dots, t_{mc}]^T \\ & \tilde{\mathbf{X}}_i = [\mathbf{X}_1, \mathbf{X}_2, \dots, \mathbf{X}_i, \dots, \mathbf{X}_m]^T \\ \text{Min} \quad & \text{Weight} = \sum_{i=1}^m \sum_{t=1}^{T_i} (T_{ic} \cdot \rho_c + T_{is} \cdot \rho_s) \cdot se_{it} \cdot x_{it} + \sum_{i=1}^m \sum_{t=T_i+1}^{T_i} (T_{ic} \cdot \rho_c + T_{is} \cdot \rho_s) \cdot se_{it} + \\ & \sum_{i=m+1}^n \sum_{t=1}^{T_i} t_{is} \cdot \rho_s \cdot se_{it} \cdot x_{it} + \sum_{i=m+1}^n \sum_{t=T_i+1}^{T_i} t_{is} \cdot \rho_s \cdot se_{it} \\ \text{s.t.} \quad & \sigma_c^L \leq \sigma_{ek}[\mathbf{T}_s, \mathbf{T}_c, \tilde{\mathbf{X}}_i] \leq \sigma_c^U \\ & \delta_{pk}[\mathbf{T}_s, \mathbf{T}_c, \tilde{\mathbf{X}}_i] \leq \delta_p \\ & a_{Aj}^{\max} \leq a_A^U \\ & a_{Bj}^{\max} \leq a_B^U \\ & 10^{L/20} - \varepsilon \leq a_{Aj}^{\max} / a_{Bj}^{\max} \leq 10^{L/20} + \varepsilon \\ & f^L \leq j \leq f^U \\ & t_{ic} = sca \cdot t_{is} \\ & t_{is}^L \leq t_{is} \leq t_{is}^U \\ & \mathbf{X}_i = [x_{i1}, x_{i2}, \dots, x_{it}, \dots, x_{iT_i}]^T \\ & 0 < x_{\min} \leq x_{it} \leq 1 \\ & T_{ip} = T_{is} + T_{ic} \\ & T_{is} = [1 + f(t_{is})] / 2 \cdot t_{is} + t_{s \min} \\ & T_{ic} = [1 - f(t_{is})] / 2 \cdot t_{is} \cdot sca + t_{c \min} \\ & f(t_{is}) = \text{sgn}[\sin(1000 \cdot t_{is} \cdot \pi)] \\ & i = 1, 2, \dots, m; \quad e = 1, 2, \dots, E; \quad k = 1, 2, \dots, K; \\ & t = 1, 2, \dots, T_{ip}; \quad p = 1, 2, \dots, P \end{aligned}$$

(3)

one optimization result(in this example, more than twenty hours for an optimal results). For the larger structure with more design variables and elements, advanced computer or workstation, and more effective optimization algorithm should be considered.

The mathematical formulations after transformation are presented in Eqn.3.

The meanings of design variables are same as Eqn.2.

ILLUSTRATING METHOD BY EXAMPLE

STEEL-COMPOSITE MATERIAL HYBRID 3-BAR TRUSS STRUCTURE DESIGN

The method of materials selection and topology optimization on simultaneous through combining the LCM method and SIMC method for Hybrid structure design is illustrated by a 3-bar truss structure as an example. Fig.2 shows the dimensions and connection of 3-bar truss. Available materials for selection are steel and fiber reinforced composite. Thickness of steel_plate is 15mm; girder is made of 100x50x10 steel L-bar. The materials parameters for selection are steel and composite material in Table 1. Boundary conditions, reference points and loading conditions are shown in Fig. 3. There is a 454kg concentrated mass at point A. A 100N vertical force acts on point A in Z direction with frequency range 1-100Hz. The modal damping loss factor for structural frequency response is 2%. Constraints for optimization design are: (1) AVLD>5dB at point A, B and E. (2) Allowable displacement at point C is 1mm. (3) Maximum acceleration amplitude for the reference points is 0.5g.

Table 1 Materials parameters

steel	Young's modulus	210 GPa
	Poisson's ratio	0.3
	density	7850kg/m ³
fiber reinforced composite	Young's modulus	E ₁₁ =27285.7MPa
		E ₂₂ =26142.8MPa
	shear modulus	G ₁₂ =9242.9MPa
		G ₂₃ =9242.9MPa
		G ₁₃ =9242.9MPa
	Poisson's ratio	0.14
	damping coefficient	η ₁₁ =0.0729
		η ₂₂ =0.0715
		η ₁₂ =η ₂₃ =η ₁₃ =0.1068
density	1600kg/m ³	
ply angles	[90°/0°] _s	

Table 2 Design variables and objective value

Bar No.	Initial thickness of steel ply (mm)	Initial thickness of composite laminate (mm)	Optimal thickness of steel ply (mm)	Optimal thickness of composite laminate (mm)	Optimal topology density
Comp_1	20	0.03	0.005	46.632	0.435
Comp_2	20	0.03	0.005	46.632	0.385
Comp_3	20	0.03	19.1	0.03	0.062
Objective function	Initial weight (kg)	60.5	Optimal result (kg)	33.7	—

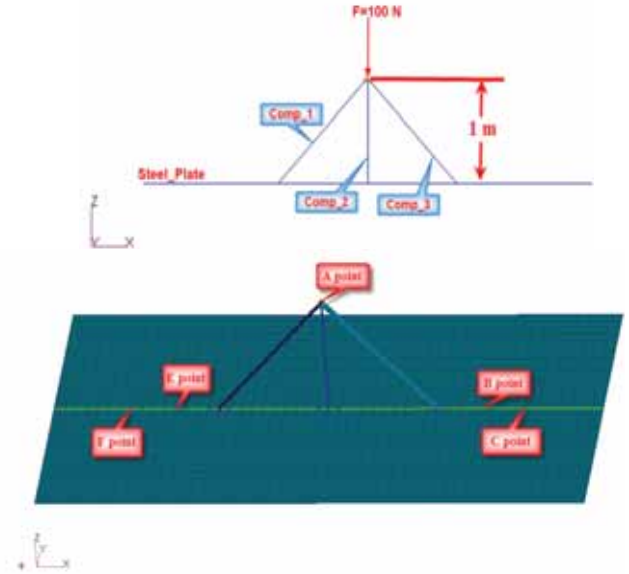


Fig.3 Boundary and loading conditions

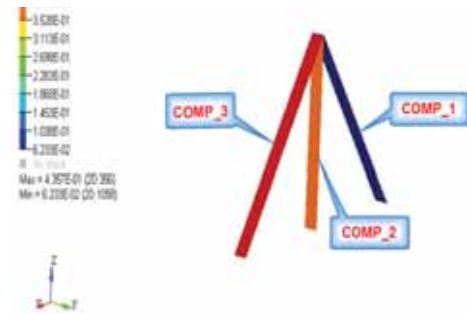


Fig.4 Topological densities of bars

Optimization results are shown in Table 2. It shows that the weight of truss decreased from 60.5kg to 33.7kg. Fig. 4 shows topological densities of bars after optimization. Since density value for bar Comp_3 is less than 0.062, it is deleted in final structural design shown in Fig.5. In final optimal topology of structure, two bars are kept, in which bar Comp_1 and bar Comp_2 are made of composite materials.

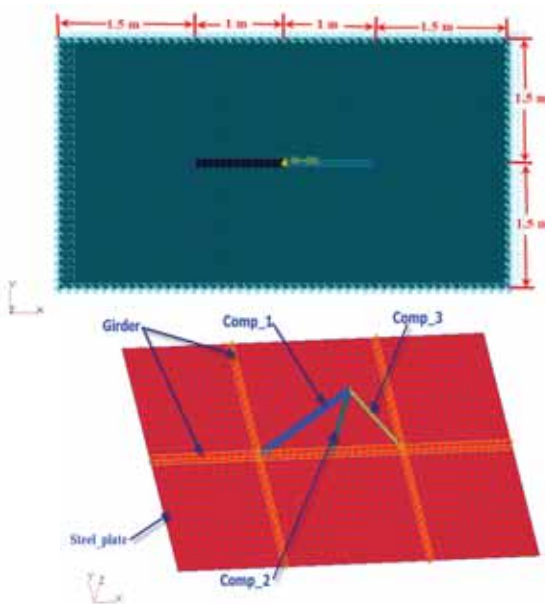


Fig.2 Dimensions of 3-bar truss

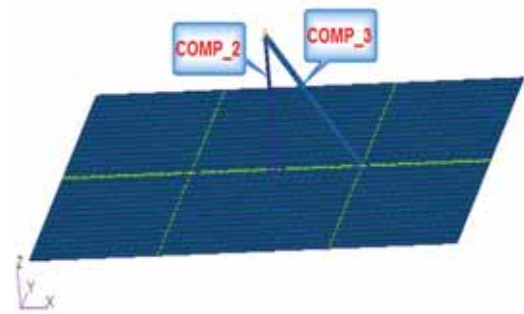


Fig.5 Final topology of 3-bar truss

STEEL-COMPOSITE MATERIAL HYBRID FLOATING RAFT DESIGN

A typical engineering floating raft is used for illustrating the feasibility of above method. The structure of the floating raft (Yang 2012) is shown in Fig.1 and Fig.6; definitions of each component are listed in Table 4.

Table 3 Parameters of the floating raft

flexible pipes and concentrated mass	80 kg
compressor	294 kg
refrigeration pump	65 kg
dimensions of the floating raft	900mm/800mm/210mm
vibration isolator	BE-60

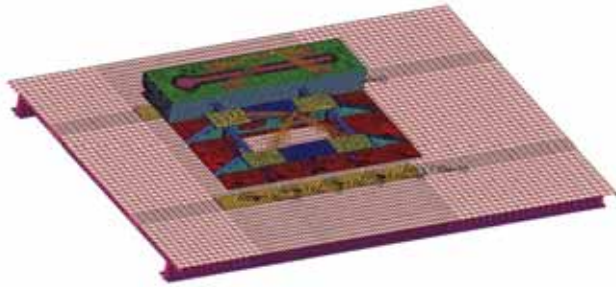


Fig.6 Finite element model of the floating raft

The Model of hybrid floating raft

The presented floating raft is a small scale model of special testing vessel in order to test the effect of vibration reduction optimization design. The joints between different components are assumed ideal. Parameters of the floating raft are shown in Table 3; the available materials for selection are steel and composite material in Table 1. Xiong (1996), and Xing (2005) investigated evaluation methods on vibration reduction of floating raft by finite element method and power flow method. Yu (2007) proposed a topology optimization model for the floating raft. The investigation results showed the effectiveness of finite element method and vibration level difference.

Fig.6 shows the finite element model of the floating raft mounted on the bottom deck of ship. The effect of vibration reduction is evaluated by AVL D at the referenced points shown in Fig.7, A_j and C_j ($j=1,2,\dots,5$) are top referenced points for isolators, B_j and D_j ($j=1,2,\dots,5$) are bottom referenced points for isolators. The unit forces act on the center of compressor and refrigeration pump at vertical direction from 1 Hz to 1000Hz.

The design requirements: 1) Determine the material types for components No.1 to No.7, and the thickness of each component; 2) Topology optimization design for component No.5 and No.7; 3) Vibration reduction requirements: AVL D at the referenced points $> 20\text{dB}$ among 1 Hz and 1000 Hz; 4) Maximum accelerations at the referenced points: $a_{(Am)_j}^{\max} \leq 80\text{mm/s}^2$; $a_{(Cm)_p}^{\max} \leq 80\text{mm/s}^2$; 5) Maximum vertical displacement less than $1/300$ of the floating raft's length, which is equal to 6.7 mm; 6) Stress constraints: $\sigma_e \leq 100\text{MPa}$, this can be satisfied by defining the maximum acceleration limits.

The upper and the lower bounds on thickness design variables are 20mm and 4mm except component No.8. The

upper and the lower bounds on thickness for the component No.8 are 60mm and 6mm. The lower bound for thickness is to avoid structural buckling and yielding. According to the design requirements, the thickness of composite laminates components should be 2.5 times of the replaced steel plates ($SCA=2.5$).

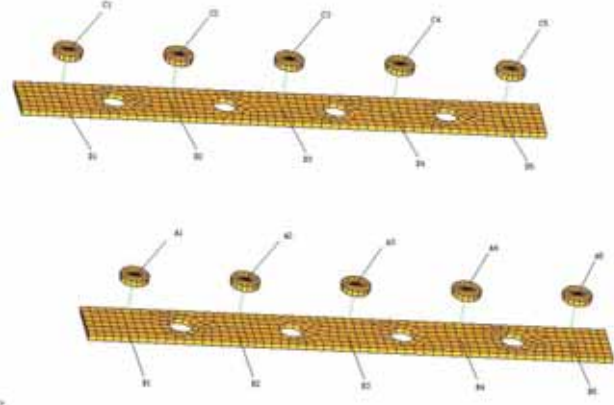


Fig.7 Locations of the reference points

Materials selection and topology optimization results on simultaneous

The results for the concurrent optimization of materials selection (type and size) and topology optimization are listed in Table 4 and Table 5 compared with Xie's results (2011) in which materials selection optimization are implemented considering vibration reduction constraints. Table 4 shows the comparisons of the objective function and the components thickness. Table 5 shows the comparison on the AVL D. Fig.8 and Fig.9 show the results of element density after topology optimization. Fig.10 and Fig.11 are the re-designed structure according to the topology optimization results. Fig.12 presents the iterative history of the objective function. It can be seen the structure weight reduces from 46.426kg to 25.940kg. Each constraint is satisfied and AVL D at some reference points are increased when materials of the web plates become composites. In the final hybrid structure, five components are made of composite materials which are quite different from the initial steel structure design.

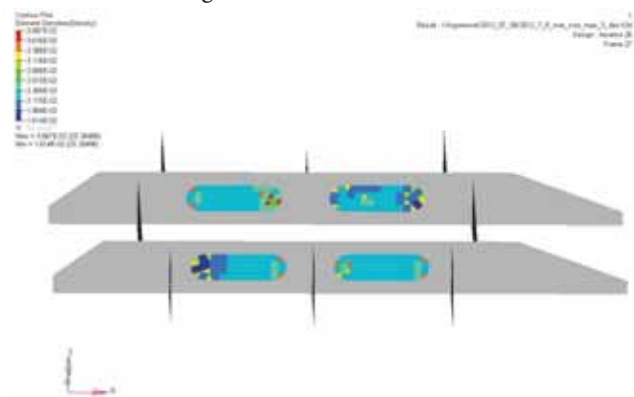


Fig.8 Topology optimization result for hlb-hole component

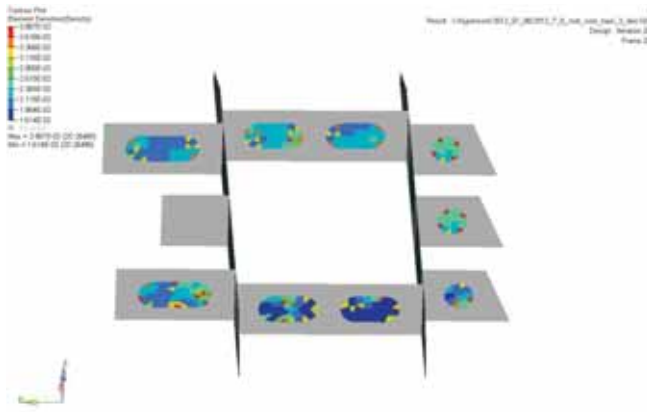


Fig.9 Topology optimization result for zlb-hole component

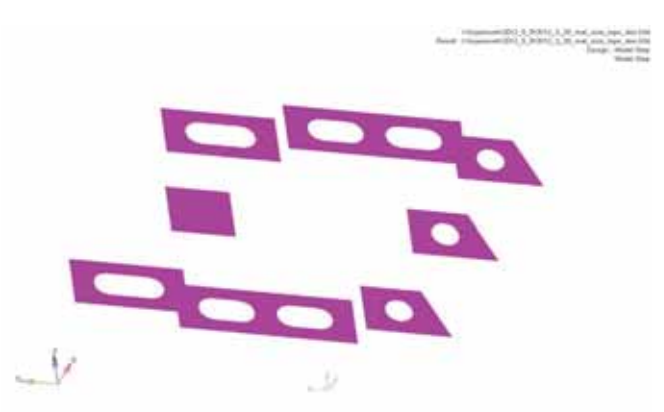


Fig.11 Re-design for zlb component

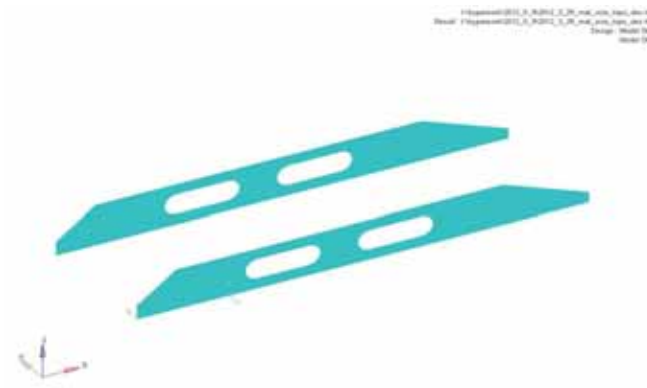


Fig.10 Re-design for hlb component

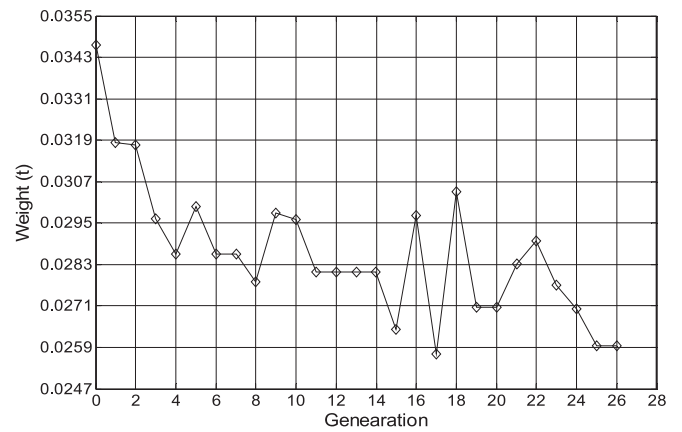


Fig.12 The iterative history of objective function

Table 5 values of AVLD and acceleration on referenced points

Reference point No.		a_{A1}^{max} (mm/s ²)	a_{B1}^{max} (mm/s ²)	AVLD (dB)	a_{G1}^{max} (mm/s ²)	a_{D1}^{max} (mm/s ²)	AVLD (dB)
1	Initial value	73.00	5.45	22.54	74.19	5.51	22.58
	Optimal value (Xie 2011)	70.25	4.25	24.37	73.40	4.37	24.51
	Optimal value	67.41	4.23	24.05	71.48	4.39	24.23
2	Initial value	69.05	2.74	28.04	69.42	2.75	28.05
	Optimal value (Xie 2011)	66.48	2.64	28.01	68.89	2.68	28.21
	Optimal value	64.10	2.56	27.97	67.41	2.60	28.28
3	Initial value	64.20	5.09	22.02	64.76	5.12	22.04
	Optimal value (Xie 2011)	61.87	3.79	24.27	64.51	3.88	24.43
	Optimal value	59.78	3.86	23.80	63.46	4.00	24.01
4	Initial value	59.39	6.92	18.67	59.94	6.99	18.67
	Optimal value (Xie 2011)	57.38	4.72	21.70	59.95	4.87	21.81
	Optimal value	55.88	4.91	21.12	59.33	5.13	21.26
5	Initial value	266.48	3.41	37.86	55.19	3.44	24.10
	Optimal value (Xie 2011)	79.60	2.73	29.29	55.47	2.80	25.93
	Optimal value	50.00	2.76	25.16	55.28	2.86	25.72

Table 4 thickness of components and objective function

Component No.	Design variables (Plate)	Initial thickness of steel ply (mm)	Initial thickness of composite ply (mm)	Optimal thickness of steel ply (Xie 2011) (mm)	Optimal thickness of composite ply (Xie 2011) (mm)	Optimal thickness of steel ply (mm)	Optimal thickness of composite ply (mm)
1	mb_1	10.01	0.03	9.9803	0.0492	4.687	0.030
2	mb_2	20.01	0.03	0.0164	49.9589	0.005	12.660
3	mb_3	6.01	0.03	5.9920	0.0200	0.005	11.514
4	zlb_1	6.01	0.03	0.0050	14.9876	0.005	11.754
5	zlb_hole	6.01	0.03	---	---	4.657	0.030
6	hlb_1	6.01	0.03	0.0243	14.9393	0.005	12.006
7	hlb_hole	6.01	0.03	---	---	0.005	12.120
8	squares	16.00	---	16.3988	---	14.70	---
Objective function	---	Initial weight(kg)	46.426	Optimal weight (Xie 2011)	36.480	Optimal weight (kg)	25.940

CONCLUSIONS

The hybrid structure optimization design for materials selection (type and size) and topology considering vibration reduction has been implemented. Combining LCM and SIMP method, a concurrent materials selection and topology optimization model for hybrid metal-composite structures is established. Typical steel-composite hybrid floating raft and hybrid truss are optimized for vibration reduction by the proposed model. The contributions of the research work and observations are summarized as follows:

1. By the proposed approach, the design variables for topology and materials selection can be combined in

a unified structural finite element analysis model, in particular, combined in each element of the design domain of the hybrid structure.

2. The optimization results also verified the effectiveness of the use of composite materials in vibration reduction design. The initial all metal-made structure of 3-bar truss and floating raft become hybrid structure after optimization design with most of components made of composite materials.

ACKNOWLEDGMENT

The work described in this paper is supported in part by grants from the National Natural Science Foundation of China (Nos. 11072149). The authors are grateful for these financial supports.

REFERENCES

1. Asundi A., Choi A. (1997) "Fiber metal laminates: an advanced material for future aircraft." *Journal of Materials processing technology*. 63, 384-94.
2. Barsoum R. (2003). "The best of both worlds: hybrid ship hulls use composites and steel." *Amptiac Quart.* 7(3), 55-61.
3. Bendsøe M., Sigmund O. (2003). "Topology optimization: theory, methods, and applications." *Springer Verlag; 2nd*; ISBN 3540429921.
4. Bendsøe M. (1989). "Optimal shape design as a material distribution problem." *Struct. Optim*, 1:193-202.
5. Blasques J. P., Stolpe M. (2012). "Multi-material topology optimization of laminated composite beam cross sections." *Composite Structures*. 94, 3278-3289.
6. Botelho E.C., Campos A.N., Barros E. D. (2006). "Damping behavior of continuous fiber/metal composite materials by the free vibration method." *Composites Part B: engineering*. 37, 255-263.
7. Cao J., Grenestedt J., Maroun W. (2007). "Steel truss/composite skin hybrid ship hull. Part I: Design and analysis." *Composites Part A-Applied Science and Manufacturing*. 38(7), 1755-1762.
8. Cherkaev A. (2012). "Optimal three-material wheel assemblage of conducting and elastic composites." *International Journal of Engineering Science*. 59, 27-39.
9. Coelho P. G., Cardoso J. B ., Fernandes P. R., etc. (2011). "Parallel computing techniques applied to the simultaneous design of structure and material." *Advances in Engineering Software*. 42, 219-227.

10. Hidde J., Herakovich C. (1992). "Inelastic response of hybrid composite laminates." *Journal of Composite Materials*. 26, 2–19.
11. Kawai M., Morishita M., Tomura S. (1998). "Inelastic behavior and strength of fiber-metal hybrid composite." *International journal of Mechanical Sciences*. 40, 183-198.
12. Kravanja S., Siliha S., Kravanja Z. (2005). "The multilevel MINLP optimization approach to structural synthesis: the simultaneous topology, material, standard and rounded dimension optimization." *Advances in Engineering Software*. 36, 568–583
13. Lee E., Martins J. R. R. A. (2012). "Structural topology optimization with design-dependent pressure loads." *Computer Methods in Applied Mechanics and engineering*. 233, 40-48.
14. Pan J., Wang D. Y. (2006) "Truss topology optimization under dynamic constraints." *Vibration and Shock*. 25 (4), 8-12.
15. Rahul, G. S., Chakraborty D., Dutta A. (2006). "Multi-objective optimization of hybrid laminates subjected to transverse impact." *Composite Structures*. 73, 360–369.
16. Rakshit S., Ananthasuresh, G. K. (2008). "Simultaneous material selection and geometry design of statically determinate trusses using continuous optimization." *Structure and Multidisciplinary Optimization*. 35, 55–68.
17. Sigmund O., Torquato A. S. (1999). "Design of smart composite materials using topology optimization." *Smart Material & Structures*. 8, 365-379.
18. Sui Y. K., Yang D. Q. (1998). "A new method for structural topological optimization based on the concept of independent continuous variables and smooth model." *Acta Mechanica Sinica* (English Edition). 18(2), 179-185.
19. Sun X., Yang F., Xie J., Huang Y. M., Zuo X. (2011). "Topology Optimization of Composite Structure Using Bi-Directional Evolutionary Structural Optimization Method." *Procedia Engineering*. 14, 2980–2985.
20. Xie X. L. (2011). "Key technologies on design and analysis of deepsea ROV and hybrid structures". *Master Degree Thesis*, Shanghai. Shanghai Jiao Tong University.
21. Xie Y. M., Steven G P. (1997). "Evolutionary structural optimization." Berlin, Heidelberg, New York: Springer.
22. Xing X. L., Wang M. Q., Song D. (2005). "Study on vibration characteristic of flexible basement floating raft vibration-isolation system." *Mechanical Science and Technology*. 2005-07.
23. Xiong Y.P., Song K.J., Wang C., Han Y.C. (1996). "Power flow analysis for a new isolation system flexible floating raft." *Chinese Journal of Mechanical Engineering*. 9, 260-264.
24. Yang D. Q., Xie X. L., Chen W. (2012). "Laminate component method for hybrid structure optimal design on vibration reduction." *Ships and Offshore Structures*. 7(3), 321-332.
25. Yu L. B. (2007). "Research on Vibration Isolation Characteristics of the Floating Raft and Topology Optimization of Raft Body." Wuhan P.R.China. Huazhong University of Science and Technology.

NOMENCLATURE

AVLD: the acceleration vibration level difference,
 $AVLD = 20 \lg (a_A/a_B)$

a_A, a_B : accelerations at point A and B

T_s : vector of thickness design variables for the components made of metal/steel.

T_c : vector of thickness design variables for the components made of composite materials

\tilde{X}_i : vector of overall topology design variables defined by SIMP method

$\mathbf{X}_i = [x_{i1}, x_{i2}, \dots, x_i, \dots, x_{it}]^T$: vector of topology design variables for the i th component, x_{it} is the topology design variable of element t in component i .

m : number of the composite components in hybrid structure

n : number of the metal/steel components

T_i : total number of the finite elements in the i th component

T_{it} : total number of topology design variables in the i th component

se_{it} : area of the i th element in the i th component

ρ_s, ρ_c : density of steel and composite materials.

σ_{ek} : stress of the e th element under the k th loading case

σ_e^L, σ_e^U : lower and upper limit of element stress.

$\delta_{pk}, \bar{\delta}_p$: displacement at point p under the k th loading case, upper limit of displacement at point p .

k : loading case number.

$a_{Aj}^{\max}, a_{Bj}^{\max}$: maximum acceleration amplitude at point A and B in the frequency j Hz

a_A^U, a_B^U : upper limit of the maximum acceleration amplitude at point A and B

L_r : lower limit of AVLD.

f^U, f^L : upper and the lower bounds of frequency domain.

t_{is}^L , t_{is}^U : upper and the lower bounds of the thickness design variables for metal/steel components.

ε , sca : relax parameter and equivalent scale of thickness for metal/steel and composite material

CONTACT WITH THE AUTHOR

Yinzhi Zhao

zhaoyz1982@126.com

School of Naval Architecture & Ocean Engineering
Jiangsu University of Science and Technology
Zhenjiang, Jiangsu, 212003

CHINA

THE RESEARCH ON CHARACTERISTIC PARAMETERS AND RESISTANCE CHART OF OPERATION AND MAINTENANCE TRIMARAN IN THE SEA

Yue Chen

Lingyu Yang

Yi Xie

Song Yu

School of Naval Architecture and Ocean Engineering, Jiangsu University of Science and Technology, Zhenjiang, China

ABSTRACT

The paper determined the volume ratio of the main hull and side hull and their position characteristic parameter of operation and maintenance trimaran. Numerical simulation technology was used to do the analysis and calculation of trimarans which have different volume ratio of the main and side hull, and on this basis, the paper tried different positions of main and side hull, finally got the trimaran with optimum resistance performance and the chart of trimaran resistance estimation, so as to provide a new way in the selection of feature parameter of offshore wind farm maintenance trimaran and its resistance estimation.

Keywords: wind power maintenance; trimaran; characteristic parameter; CFD; resistance charts

INTRODUCTION

The problem of the daily maintenance of wind turbines begins to emerge with the rapid growth of offshore wind farms. Operation and maintenance ships are indispensable vehicles in offshore wind farms, their performance directly affect the maintenance of wind turbines.

Offshore wind farms mostly use small monomer or catamaran hull. Small mono-hull ship cannot meet the requirements of operation and maintenance when the wind and waves are large. Catamarans have larger deck area than mono-hull ships and their stability have also been greatly improved, but catamarans are more likely to twist shake and anxious shake. Trimarans have better seakeeping performance and are faster than mono hull ships and catamarans. And

their safety performance have also been improved to some extent, so trimarans drew more and more attention in the operation and maintenance of wind power.

At present, slender, ultra high speed trimarans are always researched for military use, and mainly in the following aspects ^[1]: (1) the determination of molded lines of main and side hull of trimarans ; (2) relative position of main hull and side hull: through theoretical and experimental research method to determine the reasonable arrangement of the side hull, and studying the impact of the side hull position, symmetry, drainage volume and the difference of angle of attack on wave making resistance; (3) the numerical resistance prediction: including the model test, theoretical calculation and numerical simulation ; (4) researches on the manipulation of trimarans. At present, it is rare to study the

effect of side hull volume displacement on the performance of high speed trimarans^[2]. In addition, the numerical simulation or experimental methods are widely used in the estimation of the resistance of trimarans, and there are some difficulties in the estimation of the resistance of the high speed trimarans. This paper try to get the high speed trimarans resistance estimation chart by exploring the resistance performance of high speed trimarans , the displacement of the main and side hull and relative position, providing certain reference and help for estimating the trimaran characteristic parameters and resistance for the design.

THE DETERMINATION OF THE CHARACTERISTIC PARAMETERS OF THE TRIMARAN

MAIN FACTORS

MAIN BODY ELEMENT

The main elements of operation and maintenance trimaran, as shown in table 1:

Tab. 1 elements of the main body

Elements	Main hull	Side hull
Waterline length (m)	20	7.5
Modeled breadth (m)	4	1.5
Water breadth (m)	3.8	1.2
Modeled depth (m)	2.5	2
Draught (m)	1.2	0.7
Block coefficient	0.41	0.41
Displacement (t)	38.7	2.6

RELATIVE POSITION RELATION OF MAIN HULL AND SIDE HULL

The relative position of the main hull is expressed by the transverse space b and the longitudinal space l , as shown in figure 1. The effect due to the difference of side hull position on the resistance and seakeeping performance is more obvious, different locations may produce great influence on the performance of trimaran^[3].

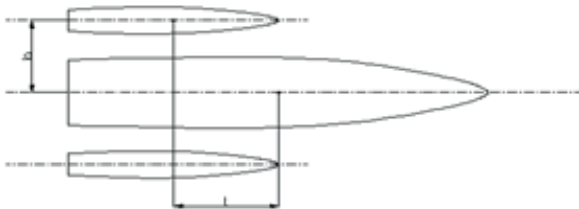


Fig. 1 the relative position of main hull and side hull

For basic ship types, the stern transom plate of side hulls are flush with the stern transom plate of main hull , transverse space b is 101.25 % of B , 4.05 m.

HULL MODEL

According to the scales, round bilges are adopt as the line shape of the cross section of the trimaran main and side hull, side hulls are symmetrically arranged on two sides of the main body, NAPA was used to design the line type of the hulls, a built model as shown in Figure 2:



Fig. 2 Trimaran model

CHARACTERISTIC PARAMETERS

Two characteristic parameters: the proportion of the displacement of the side body and the relative position of the main body, are studied in this paper.

SIDE HULL DISPLACEMENT PROPORTION OF TOTAL DRAINAGE VOLUME

For trimarans, the main hulls are all slender, the displacement of one side hull is usually blow 10% of the total displacement^{[4][5]}. Wind farm maintenance mainly includes the maintenance of personnel transport and landing or leaving wind power towers, requires fast and efficient ship. Because of the bad weather in wind farm, good stability, rapidity and good seakeeping performance are required for the ship of operation and maintenance. Thus the displacement of side hull is bigger than ultrahigh speed trimaran. The proportion of the displacement of the base ship type is 12%. Considering the needs for the research on the performance of the operation and maintenance ships, this paper determines the other three sets: 9%, 15% and 18%, respectively.

THE PARAMETER OF MAIN HULL AND SIDE HULL POSITION

(1) longitudinal position

Due to the side hull, the resistance of trimarans become complicated. The relative position of side hull and main hull makes a huge difference on the resistance of trimarans. The wave interference between main hull and side hull has a great impact on resistance of trimarans, if the side body position is appropriate, the resistance of trimarans will be greatly reduced^{[6][7]}. Thus this paper identified three different longitudinal space: the middle($l = 0$), postmedian($l = 3.175$ m) and tail ($l = 6.35$ m), to study the impact on resistance.

(2) transverse position

Similarly, side hull cannot be too close to main hull, because the cross rolling of main hull will become larger and there

will be a flow blocking effect; also cannot too big, because that will weaken the interference between side hull and main hull, it is difficult to guarantee the transverse strength and the stability of connecting bridges. This paper identifies four different transverse space b : 3.9 m, 4.05 m, 4.2 m, 4.4 m, to explore the influence of resistance.

NUMERICAL SIMULATION OF RESISTANCE

STUDY ON SIMULATION METHODS

The trimaran model can be imported into CFD FINE-Marine to do simulation calculation, however, the simulation method must be verified. This paper choose a trimaran with ship model resistance test data, the scale is shown in the table:

Tab. 2 verify the scale of trimaran

Element	Waterline length (m)	Modeled breadth (m)	Draught (m)	Displacement (kg)	Block coefficient
Main hull	1.94	0.4	0.11	33.1	0.436
Side hull	0.695	0.14	0.085	2.95	0.416

The model of the trimaran model as shown in Fig. 3:

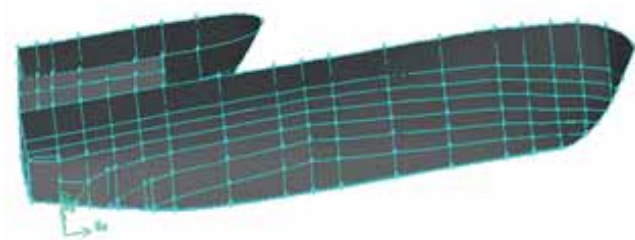


Fig.3 Calculation Model

THE COMPUTATIONAL DOMAIN AND MESH

The selection of computational domain can not only ensure the capture of flow field information, but also reduce the number of grids. Considering the large number of grids required to simulate the flow field, it is difficult to get the required results in a short time. This paper design the ship model with the ratio of 1:10. According to the symmetry of the ship, the ship model was taken half to do the calculation to ensure the results as well as reduce the number of grids. Based on the analysis of the flow field and the references^{[8][9]}, the computational domain selected is $10L \times 2L \times 2.5L$, the towing tank entrance from the bow $2L$, depth $1.25L$.

The division of the computational domain grid not only have to consider the quality of grid, but also should consider the flow characteristics of the flow field. HEXPRESS adapt hexahedral unstructured mesh grid to divide the whole ship. First step: the initial mesh generation, Second step: the initial mesh refinement. Mesh refinement is only effective to the initial mesh unit near the surface. The initial mesh units which need refinement should be marked, then continuous resolution should be done to the marked mesh units according to specified refinement criterion. Every time do the resolution,

mesh units outside the computational domain need to be eliminated. And then figure out whether another resolution is necessary. Eliminate the mesh units which intersect with the surface to form a ladder distribution grid near the surface. The hull geometry file imported into HEXPRESS generate grid as shown in figure 4:

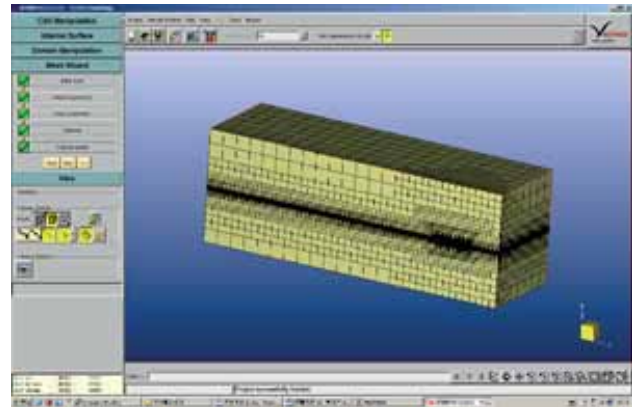


Fig.4 Mesh

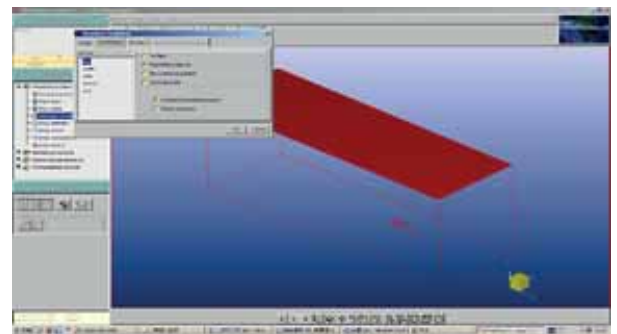


Fig.5 Set grid boundary conditions

BOUNDARY CONDITION

Save the mesh file and imported it into FINE/Marine to do parameter settings. The calculation parameters mainly include the state parameters, boundary conditions, body definition, body motion parameters, initialization parameters, parameters of controlling calculation and numerical method parameters. The selection of boundary conditions should be consistent with the actual situation, so as to ensure that the numerical simulation is close to the actual. The FINE/Marine boundary condition include three types: solid wall and flow field boundary and the symmetric boundary (Fig. 5). The solid wall boundary condition includes slip wall, nonslip wall and wall function. In this paper, the deck is set to slip wall, the hull surface is set to wall function. FINE/Marine provides four boundary definition for calculation outside the boundary conditions: far field, prescribe pressure, zero pressure gradient and wave generator. The boundary conditions in the calculation area in this paper is: the top and bottom of the computational domain are set to pressure conditions; the

other direction is set to speed far field boundary. As a result of the calculation by half ship model, so the symmetry plane set for symmetric boundary.

RESULTS

Using FINE/Marine with the watershed division method and boundary condition definition method, in the scale 1:10, the ship speed is 20 KN, the resistance of simulation is 48.36 N, is close to the result of real ship model experiment: 50.17 N. Therefore the method mentioned above can be used to do numerical simulation analysis for trimarans with different characteristic parameters to predict resistance.

THE EFFECT OF DIFFERENT SIDE HULL DISPLACEMENT

This paper did four sets of numerical simulation calculation with different displacement volume ratio, respectively, using the method mentioned above. The scaling factor is 1:10, the ship speed is 20 KN, four schemes of ship model resistance are shown in Table 3:

Tab. 3. four schemes of ship model resistance

Scheme	one (9%)	two (12%)	three (15%)	four (18%)
resistance (N)	49.134	49.428	51.816	50.954

Through comparison, it is found that resistance value is small when the side hull displacement volume accounts for 9% of the total displacement volume. At the same time, the resistance value of the second scheme is close to the resistance value of the first scheme. Therefore, the resistance performance is better when the displacement volume of side hull accounted for 9% to 12% of the total displacement volume. The main hull and side hulls can produce favorable interference within the ratio range.

STUDY ON DIFFERENT POSITION OF SIDE HULLS

Considering the initial metacentric height and stability are affected due to the small side hull in Scheme One, This paper took the Scheme Two: Ratio 12% to study the impact of different side hull position on the resistance performance. The three longitudinal position: middle, postmedian, tail. The transverse space b value for 3.9 m, 4.05 m, 4.2 m, 4.4 m.

When transverse space $b = 4.05$ m, The analytical results of CFD numerical simulation are shown in Table 4 with three groups of different longitudinal positions:

Tab. 4. ship model resistance under different longitudinal position

longitudinal positions	Middle (l=0m)	Postmedian (l=3.175m)	Rear (l=6.35m)
resistance (N)	55.298	56.624	49.428

Through comparison with the resistance of three groups of different longitudinal positions, It is found that, the value of resistance is minimum when the stern transom plate of side hulls are flush with the stern transom plate of main hull. Four sets of numerical simulation calculation were done with different transverse position, the scaling factor is 1:10, the ship speed is 20 KN, four schemes of ship model resistance are shown in Table 5:

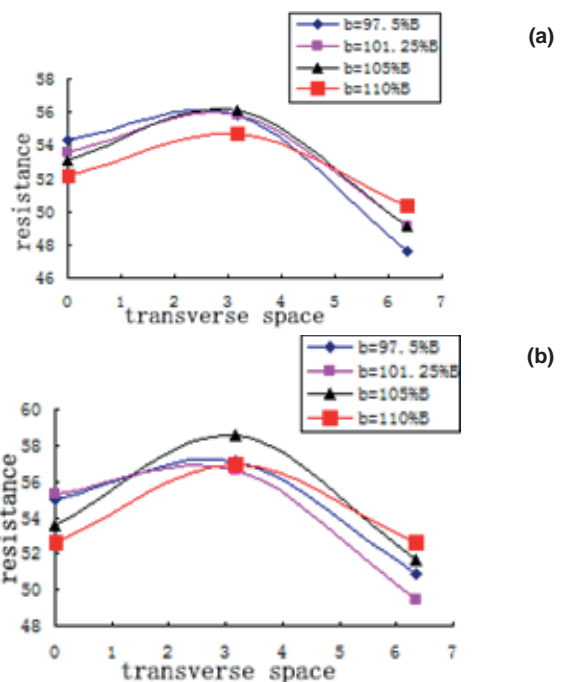
Tab. 5. ship model resistance under different transverse position

transverse position (m)	3.9	4.05	4.2	4.4
resistance (N)	50.886	49.428	51.632	52.610

From four transverse space calculation results showed, with the gradually increase of the transverse space, resistance values decreased at beginning and then increased. The resistance value minimum when the transverse space $b = 4.05$ m. Therefore the resistance performance is best when transverse space $b = 4.05$ m. Through comparison, the resistance performance is best when the stern transom plate of side hulls are flush with the stern transom plate of main hull and the transverse space is 101.25 % b .

THE GENERATION OF RESISTANCE CHART

Due to the side hull, interference resistance exists between the main hull and the side hull. Up to now, there are no charts nor formulas to estimate the resistance of trimarans. This paper did simulation calculation with combination of the ratio of displacement 9%, 12%, 15%, 18% and transverse space $b = 97.5\% B$, 101.25 % B , 105 % B , 110 % B with side hull in middle, postmedian and rear tail. The scaling factor is 1:10, Froude number = 0.73. The resistance chart (Fig.6).



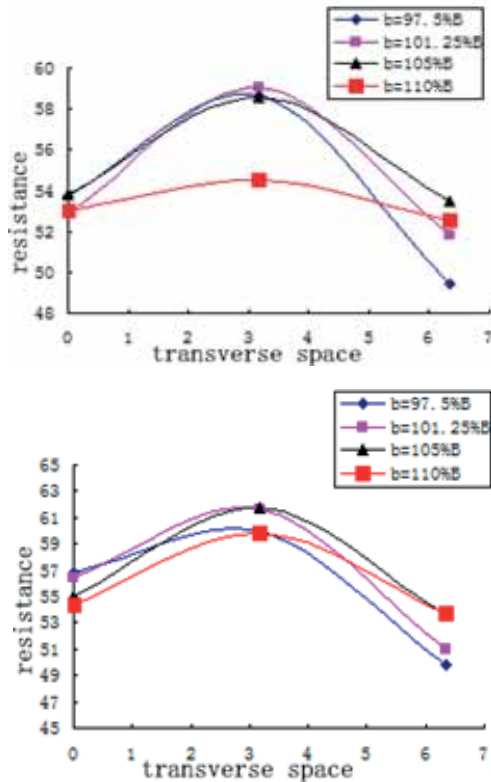


Fig.6. resistance chart: (a) volume ratio 9%; (b) volume ratio 12%; (c) volume ratio 15%; (d) volume ratio 18%

4 CONCLUSION

Operation and maintenance ships are necessary for offshore wind farms. The good performance of ships are very important for completing the operation mission in rough sea conditions. This paper used the ratio of displacement and relative position as characteristic parameters to do numerical simulation analysis, obtained the following conclusions:

(1) when the displacement of side hull is 9% ~ 12% of total displacement, the resistance performance of trimaran is better.

(2) when the stern transom plate of side hulls are flush with the stern transom plate of main hull, transverse space is 101.25 % B, the resistance performance of trimaran is better.

(3) the numerical simulation method used in this paper is more credible, the resistance chart obtained has reference value in the estimation of trimaran.

REFERENCES

1. Wang Xianjun [D]. of Harbin Engineering University master's degree thesis of engineering calculation of shallow water body resistance, 2006.3

2. Li Peiyong. Multi hull Ph.D. performance and conceptual design of [D]. dissertation of Shanghai Jiao Tong University, 2002.1
3. Cai Xingong, Wang Ping, Xie Xiaomin. The layout of the resistance calculation and experimental study on [J]. hydrodynamics of trimaran optimization, 2007,22 (2)
4. Wang, Lu Xiaoping, Zhan Jinlin. New progress in the study of water dynamics and ship [J]. trimaran ship mechanics, 2011,15 (7)
5. Jiang Zongyu, Zong Zhi, Jia Jingbei yinglang. Under the condition of the trimaran heave and pitch motion parameters of [J]. Chinese shipbuilding, 2010,51 (4)
6. Zheng Cong Gang, Wang Yaohui. Law, three side optimization design of [J]. ship body position, 2012,23 (4)
7. China Shipbuilding Industry Corporation. Ship design practical manual [M]. National Defence Industry Press, 1998.12
8. Deng Rui, Huang De-bo, Li Jia, Cheng Xuan-Kai, Lei Yu. Discussion of Grid Generation for Catamaran Resistance Calculation[J]. Journal of Marine Science and Application 2010,9:187-191.
9. Xie Yunping, Yao Weiet al. Study on numerical simulation method of wave resistance of high speed ships with numerical wave tanks [J]. ship engineering, 2013, 35 (2).

SEMI-ANALYTICAL SOLUTION OF OPTIMIZATION ON MOON-POOL SHAPED WEC

W.C. ZHANG,

H.X. Liu,

X.W. ZHANG,

L. ZHANG

College of Shipbuilding Engineering, Harbin Engineering University, Harbin, China

ABSTRACT

In order to effectively extract and maximize the energy from ocean waves, a new kind of oscillating-body WEC (wave energy converter) with moon pool has been put forward. The main emphasis in this paper is placed on inserting the damping into the equation of heaving motion applied for a complex wave energy converter and expressions for velocity potential added mass, damping coefficients associated with exciting forces were derived by using eigenfunction expansion matching method. By using surface-wave hydrodynamics, the exact theoretical conditions were solved to allow the maximum energy to be absorbed from regular waves. To optimize the ability of the wave energy conversion, oscillating system models under different radius-ratios are calculated and comparatively analyzed. Numerical calculations indicated that the capture width reaches the maximum in the vicinity of the natural frequency and the new kind of oscillating-body WEC has a positive ability of wave energy conversion.

Keywords: wave energy; eigenfunction expansion; moon pool; conversion ability; optimization

INTRODUCTION

With worldwide demand for energy and electricity unabated, over the past decades, so much considerable attention and effort have been devoted to the problem of extracting energy from the ocean waves and to investigating theoretically and experimentally several types of devices in order to maximize their efficiency. The major concern in extensively today is to continue to improve the oscillating bodies and the oscillating water columns which are the two main types of devices containing the oscillating system and PTO (power take-off) mechanism.

Oscillating-body WEC reflects a simple but robust technology, especially for the point absorbing WEC, which consists of buoys or floating bodies to capture the waves

heaving motion. Oscillating-body WEC can take advantage of the body with resonant and periodic motion caused by the ocean waves with large forces at slow speeds to capture energy. Comparing to other types of WECs, the oscillating body is usually small in size and often used in arrays. Due to the immense potential and prospect of wave energy technology, a number of wave conversion devices have been designed and analyzed by researchers. Budal K et al [1] developed a kind of buoy, consisting of a spherical floater which could perform heaving oscillations relative to a strut connected to an anchor on the sea bed through a universal joint and the buoy could be phase-controlled by latching and was equipped with an air turbine. Weinstein et al. [13] outlined a project of developing the Makah Bay pilot offshore power plant, which used Aqua Energy's point absorber wave energy conversion device Aqua

BUOY. The device represented the next generation of the technology that combines the Swedish Hose-Pump and the IPS Buoy technologies to generate clean energy from ocean waves. Margheritini et al. [9] described concept of the sea slot-cone generator (SSG) WEC and the studies behind the process that led to the construction of such wave energy conversion system. There has been a turning point in structure with moon-pool in accordance with the advent of extracting energy from the ocean waves. In the present work, we focus on need for a new kind of oscillating-body WEC which is cylindrical structures with a moon pool with a restricted entrance associated with a smaller disk inner.

To being with we will provide a brief background on the study of waves around cylindrical cylinders. The pioneer work on the semi-analytical solution of the oscillating system can be traced to MacCamy and Fuchs [8] on the simplest case of a vertical cylinder standing on the seabed. Since Miles and Gilbert [11] formulated the problem of the scattering of the surface waves by a circular dock and obtained a variational approximation to the far field, a number of works have been done for different types of vertical cylinders (truncated and composed of different diameters) by using so called eigenfunction matching method which consists of dividing the fluid domain into several cylindrical subdomains and matching the eigenfunction expansions in different subdomain. Many research studies have been carried out on this topic such as Liu et al. [7] for a series of different configurations of a single cylinder. The central issue in all above studies is the analytical method based on the series expansion of eigenfunctions which satisfy Laplace equation and are used to evaluate the velocity potentials around cylindrical structures and to compute the wave loads. The fluid domain around the complex structure hull is divided into an army of cylindrical subdomains. In each domain, the different expansions of eigenfunctions are developed and the unknown coefficients of expansion series are determined by the boundary condition on cylinder hull and the continuous conditions through the control surfaces which separate the domains.

The cylindrical structure with moon pool which contains resonance frequency is developed by Garrett [5], a bottomless cylinder which is equivalent to a cylinder with fully opened moon pool. Mavrakos and Chatjigeorgiou [10] have solved wave loads on a stationary floating bottomless cylinder with a finite wall thickness. Very recently, Chen et al. [2] introduced the free surface dissipation for wave diffraction of cylindrical structures with moon pool of restricted entrance using the semi-analytical solution and the positive agreement of the free-surface elevation on the center of moon pool with measurements in model test is indicative of the instructional significance to engineering design.

An additional difficulty is related to the conception of the PTO which should allow the production of usable energy. Considerable efforts have been made by several authors to investigate the performance of the point absorber WEC with a linear damping. Eriksson et al. [3] investigated the coupling behavior of the linear generator and the floating buoy in the frequency domain. Price et al. [12] studied the

capture width of WECs in detail and discusses the effects of the PTO control on the capture width. Yeung et al. [16] utilizes both the theoretical and mathematical models to obtain the hydrodynamics properties of the floating buoy and studies the performance of the UC-Berkeley WEC via experimental approach. Special attention was paid on power take-off performance and design, and on the control of the system. Henderson [6] described the hydraulic power take-off system employed in the Pelamis WEC and the process of the systems development was also presented, including simulation and laboratory tests at 1/7th and full scale. Falcao [4] presented a general method of modeling oscillating-body WECs with hydraulic power take-off and gas accumulator. With the assumption of linear PTO and linear surface-wave hydrodynamics, Wu et al. [14-15] derived a reciprocal relationship between the spring stiffness, damping coefficient and diffraction properties, and a general expression for time-averaged power output was also presented.

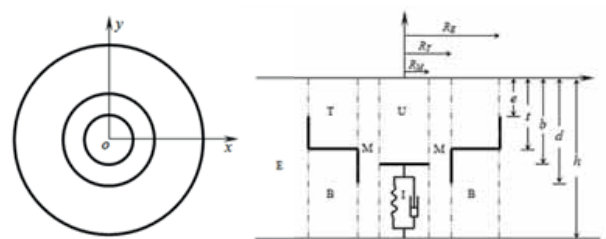


Fig. 1 Cylindrical structures with a moon-pool with a restricted entrance associated with smaller disk inner

This paper focuses on the performance analysis and geometrical optimizations of a newly proposed two-body oscillating wave energy converter which contains a submerged moon-pool shaped paddock and a coaxial disk. The damper installed on the paddock and activated by the bodies' oscillations contains a linear spring and controllable velocity dependent impedance. The plane wave theory based upon the eigenfunction matching method considering the complex boundary conditions is used for the hydrodynamic analysis of the structures in frequency domain. The expressions of the diffracted and radiated velocity potentials in each subdomain are analytically established. The linear wave excitation forces and hydrodynamic coefficients are further obtained. Finally, the numerical results of the wave forces, hydrodynamic coefficients and captured width radii are illustrated considering different geometries of the paddocks.

METHODS

The oscillating-body WEC considered in this work is shown in Fig.1. At the water depth of e , a barrel shaped structure of radius R_E with a moon pool of radius R_T at the bottom center is submerged vertically in the fluid of constant depth h . The heights of the barrel and moon pool are denoted by $(t-e)$ and $(b-e)$ respectively. A circular quality disk (the oscillating body) of smaller radius R_M is assumed to be installed vertically and coaxially with the moon pool under the undisturbed free surface of d . It is further assumed that a bottom-mounted

nonlinear PTO device is installed at the bottom of the circular disk for energy extraction, and the thicknesses of the barrel, the moon pool wall and the circular plate are all thin and are set to zero in developing the theory.

We defined the cylindrical coordinated system (r, θ, z) by its origin located at the center of the cylinder and on the mean plane of the free surface. The axis oz is vertically upward. By assuming that the fluid is perfect and flow irrotational, fluid velocity $V(r, \theta, z, t)$ can be represented by the gradient of a potential function $\Psi(r, \theta, z, t)$ which satisfies the Laplace's equation:

$$\nabla(r, \theta, z, t) = \nabla\Psi(r, \theta, z, t) \text{ with } \nabla^2\Psi(r, \theta, z, t) = 0 \quad (1)$$

in the fluid domain. Considering a linear surface wave of small amplitude A propagates along the positive x -axis direction, given the above assumptions, the flow field can be described by a velocity potential:

$$\Psi(r, \theta, z, t) = \Re\{\Phi(r, \theta, z)e^{-i\omega t}\} \quad (2)$$

On the mean free surface $z = 0$, the combined kinematic and dynamic boundary condition is given by:

$$-f^2\Phi + \partial_z\Phi = 0 \quad (3)$$

in which $f^2 = \omega^2/g$ with ω as wave frequency and g the acceleration due to gravity.

On the hull is expressed by:

$$\partial_n\Phi = V_n \quad (4)$$

where V_n is the cylinder's velocity in the direction normal to the hull. In the same way, the boundary condition on the sea bed is $z = -h$ is $\partial_z\Phi = 0$. In addition, we have to a radiation condition requiring that all perturbation due to cylinders disappears at infinity, i.e.

$$\Phi \rightarrow \Phi_0 \text{ at } r \rightarrow \infty \quad (5)$$

to ensure the uniqueness of the solution, where Φ_0 representing the velocity of incoming waves is given as:

$$\Phi_0 = -Ag/\omega \cdot \cosh k_0(z+h)/\cosh k_0h \cdot \exp(ik_0r \cos\theta) \quad (6)$$

in which (A, ω, k_0) stand for the amplitude, frequency and wavenumber, respectively, the wave number k_0 defined by k_0 and $k_0h = f^2$ incoming waves propagating along the positive x -axis.

POWER TAKE-OFF MECHANISM

In order to calculate the optimal extraction efficiency of the WEC, we consider the simple case of the body with a single-degree of freedom, oscillating in heave. To know the optimal relationship between the quadratic PTO device and key hydrodynamic parameters, a linear PTO and iterative method will be introduced. Given the flow field environment of the

oscillating body, the governing equation can be condensed into the following expression:

$$m\ddot{Z} = F_d + F_r + F_m \quad (7)$$

where m is the proper mass of the oscillating body, Z is the displacement and the dot denotes the differential of time t . F_d is the vertical force produced by the incident waves on the assumedly fixed body (excitation or diffraction force), F_r is the hydrodynamic force due to the body oscillation in otherwise calm water (radiation force), F_m is the vertical component of the force applied on the oscillating body by the PTO mechanism.

In the case of regular waves of frequency ω , the excitation force F_D and displacement Z are both simple harmonic functions of time t and for convenience, we can write $Z(t) = ze^{-i\omega t}$ and $F_d(t) = f_d e^{-i\omega t}$. Here, z and f_d are the complex amplitudes respectively. It is convenient to decompose the radiation force as inertial force and wave making damping, which can be expressed as $F_r = \mu\ddot{Z} - \lambda\dot{Z}$. Here μ is the added mass and λ is the radiation damping coefficient (λ cannot be negative according to physical reasons). The PTO mechanism force F_m contains spring restoring force and damping which is associated with the energy extraction and for linear damping can be expressed as $F_m = -kZ - c\dot{Z}$. Here k is the spring rigidity coefficient and c is the damping coefficient.

For bodies with a vertical axis of symmetry oscillating in heave, by combining the expressions of the above forces, we find that $z = f_d/[-\omega^2(m+\mu) - i\omega(\lambda+c)+k]$. Based upon the governing equation of the oscillating body in frequency domain, the time-averaged absorbed power can be calculated and given as:

$$\bar{P} = c/2 \cdot f_d f_d^* / \{[k/\omega - \omega(m+\mu)]^2 + (\lambda+c)^2\} \quad (8)$$

where the asterisk denotes the conjugate. This show that, for a given body and given incident wave (i.e., fixed ω, λ and f_d), the time-averaged absorbed power will reach the peak when the values of k and c satisfy $\partial_k \bar{P} = \partial_c \bar{P} = 0$. Combining the Eq. (12), we have $k_{opt} = \omega^2(m+\lambda)$, $c_{opt} = |\lambda|$. Here k_{opt} and c_{opt} are the optimum PTO coefficients. Furthermore, we will get the maximum time averaged absorbed power $\bar{P}_{max} = f_d f_d^* / 8|\lambda|$. In order to calculate the power take-off efficiency η , we need to know the time-power in unite wavelength and in the width of the oscillating body, which can be expressed as:

$$\bar{P}_0 = \rho g^2 A^2 R_m / 2\omega \cdot (2k_0h + \sinh 2k_0h) / (1 + \cosh 2k_0h) \quad (9)$$

Then the maximum power take-off efficiency η of the WEC can be obtained:

$$\eta = \bar{P}_{max} / \bar{P}_0 = \omega f_d f_d^* / (4|\lambda| \rho g^2 A^2 R_m) \cdot (1 + \cosh 2k_0h) / (2k_0h + \sinh 2k_0h) \quad (10)$$

SEMI-ANALYTICAL SOLUTION OF HYDRODYNAMIC COEFFICIENTS

In order to obtain semi-analytical solution of hydrodynamic coefficients μ, λ and f_d , the diffraction velocity potential Φ_r

and radiation velocity potential for heave mode Φ_3 around a new kind of oscillating-body WEC can be expressed as:

$$\begin{aligned}\Phi_7(r, \theta, z) &= -\frac{Ag}{\omega} \sum_{l=0}^{\infty} \phi_l(r, z) \cos l\theta \\ \Phi_3(r, \theta, z) &= \phi_3(r, z)\end{aligned}\quad (11)$$

The appropriate expression of $\phi(r, z)$ composed of eigenfunctions should be obtained by considering the boundary conditions in a cylindrical domain of fluid. The fluid domain surrounding structures is divided into six cylindrical subdomains as shown in Fig.1. In such case, the diffraction velocity potential Φ_7 and radiation velocity potential for heave mode Φ_3 around the structure in each of the aforementioned subdomains, namely, $\Phi_{7,3E}$ in the exterior subdomain E, $\Phi_{7,3T}$ in the above subdomain T, $\Phi_{7,3B}$ in the underneath subdomain B, $\Phi_{7,3M}$ in the middle subdomain M, $\Phi_{7,3U}$ in the inner above subdomain U, $\Phi_{7,3L}$ in the inner underneath subdomain L. Following Garrett (1970), the velocity potential in the exterior domain E is written as:

$$\begin{aligned}\phi_{7E}^l(r, z) &= a_0^l Z_0(k_0, z, h) \mathbf{H}_l(k_0 r) + \sum_{n=1}^{\infty} a_n^l Z_n(k_0, z, h) \mathbf{H}_l(k_n r) + \phi_0^l(r, z) \\ \phi_{3E}^l(r, z) &= \phi_{7E}^0(r, z)\end{aligned}\quad (12)$$

with $Z_n(k_n, z, h) = \cos k_n(z+h) / (2k_n h + \sin 2k_n h)$ and k_n defined by $k_n \tan k_n h = -f^2$ for $n \geq 1$. In the above subdomain T, the velocity potential ϕ_{7T}^l is written as:

$$\begin{aligned}\phi_{7T}^l(r, z) &= b_0^l Z_0(\gamma_0, z, d) \mathbf{J}_l(\gamma_0 r) + \sum_{n=1}^{\infty} b_n^l Z_n(\gamma_n, z, d) \mathbf{I}_l(\gamma_n r) + \tilde{b}_0^l Z_0(\gamma_0, z, d) \mathbf{H}_l(\gamma_0 r) + \sum_{n=1}^{\infty} \tilde{b}_n^l Z_n(\gamma_n, z, d) \mathbf{K}_l(\gamma_n r) \\ \phi_{3T}^l(r, z) &= \phi_{7T}^0(r, z) + (z\omega^2 + g) / \omega^2\end{aligned}\quad (13)$$

with the wave number defined by $\gamma_0 \tanh \gamma_0 t = f^2$ and $\gamma_n \tan \gamma_n t = -f^2$ for $n \geq 1$. In the subdomain B, the velocity potential ϕ_{7B}^l can be expressed by:

$$\begin{aligned}\phi_{7B}^l(r, z) &= c_0^l P_0^l(r) + \sum_{n=1}^{\infty} c_n^l \cos \lambda_n(z+h) [\mathbf{K}_I^{nl} \cdot \mathbf{I}_I(\lambda_n r) - \mathbf{I}_I^{nl} \cdot \mathbf{K}_I(\lambda_n r)] + \tilde{c}_0^l \tilde{P}_0^l(r) + \sum_{n=1}^{\infty} \tilde{c}_n^l \cos \lambda_n(z+h) [\mathbf{I}_E^{nl} \cdot \mathbf{K}_I(\lambda_n r) - \mathbf{K}_E^{nl} \cdot \mathbf{I}_I(\lambda_n r)] \\ \phi_{3B}^l(r, z) &= \phi_{7B}^0(r, z) + [2(z+h)^2 - r^2] / [4(h-t)]\end{aligned}\quad (14)$$

in which the function P_0^l and \tilde{P}_0^l are defined by

$$\begin{aligned}P_0^l(r) &= \ln(r/R_I) / \ln(R_E/R_I), \quad \tilde{P}_0^l(r) = \ln(R_E/r) / \ln(R_E/R_I) \text{ with } l=0 \\ P_0^l(r) &= [(r/R_I)^l - (R_I/r)^l] / [(R_E/R_I)^l - (R_I/R_E)^l], \quad \tilde{P}_0^l(r) = [(R_E/r)^l - (r/R_E)^l] / [(R_E/R_I)^l - (R_I/R_E)^l] \text{ with } l > 0\end{aligned}\quad (15)$$

The constants $\{\mathbf{K}_I^{nl}, \mathbf{I}_I^{nl}, \mathbf{K}_E^{nl}, \mathbf{I}_E^{nl}\}$ are given by:

$$\begin{aligned}\{\mathbf{K}_I^{nl}, \mathbf{I}_I^{nl}, \mathbf{K}_E^{nl}, \mathbf{I}_E^{nl}\} &= \{\mathbf{K}_I(\lambda_n R_I), \mathbf{I}_I(\lambda_n R_I), \mathbf{K}_I(\lambda_n R_E), \mathbf{I}_I(\lambda_n R_E)\} / C_{IE}^{nl} \\ C_{IE}^{nl} &= \mathbf{K}_I(\lambda_n R_I) \mathbf{I}_I(\lambda_n R_E) - \mathbf{K}_I(\lambda_n R_E) \mathbf{I}_I(\lambda_n R_I) \quad \text{with } n \geq 1 \text{ and } l \geq 0\end{aligned}\quad (16)$$

in which, the wave number λ_n is defined by $\lambda_n = n\pi / (h-t)$ to satisfy the boundary condition $\partial_z \phi_B^l = 0$ on both surfaces $z = -h$ and $z = -t$. In the middle subdomain M, the velocity potential ϕ_{7M}^l can be expressed by:

$$\begin{aligned}\phi_{7M}^l(r, z) &= d_0^l Z_0(k_0, z, h) \mathbf{J}_l(k_0 r) + \sum_{n=1}^{\infty} d_n^l Z_n(k_n, z, h) \mathbf{I}_l(k_n r) + \tilde{d}_0^l Z_0(k_0, z, h) \mathbf{H}_l(k_0 r) + \sum_{n=1}^{\infty} \tilde{d}_n^l Z_n(k_n, z, h) \mathbf{K}_l(k_n r) \quad n \geq 1 \\ \phi_{3M}^l(r, z) &= \phi_{7M}^0(r, z)\end{aligned}\quad (17)$$

In the inner above U, the velocity potential ϕ_{7U}^l can be expressed by:

$$\begin{aligned}\phi_{7U}^l(r, z) &= f_0^l (r/R)^l + \sum_{n=1}^{\infty} f_n^l \cos \lambda_n(z+h) \mathbf{I}_l(\lambda_n r) \\ \phi_{3U}^l(r, z) &= \phi_{7U}^0(r, z) + [2(z+h)^2 - r^2] / [4(h-d)]\end{aligned}\quad (18)$$

In the inner underneath I, the velocity potential ϕ_{7I}^l can be expressed by:

$$\begin{aligned}\phi_{7I}^l(r, z) &= f_0^l (r/R)^l + \sum_{n=1}^{\infty} f_n^l \cos \lambda_n(z+h) \mathbf{I}_l(\lambda_n r) \\ \phi_{3I}^l(r, z) &= \phi_{7I}^0(r, z) + [2(z+h)^2 - r^2] / [4(h-d)]\end{aligned}\quad (19)$$

for $n \geq 1$. In the eigenfunction expansion for the velocity potentials, the unknown coefficients are to be determined by taking advantage of the orthogonality, in the so-called Garrett's method (Garrett, 1971), according to matching the potential and its normal derivative on the juncture boundaries surfaces shared by subdomains. Once the velocity potential is known, the diffraction wave force and hydrodynamic coefficients on the heave direction can be obtained by the integration of the

pressure on the disk hull:

$$f_3^d = i2\pi\rho g A \int_0^{R_M} \{\phi_{7U}^0(r, -d) - \phi_{7L}^0(r, -d)\} r dr$$

$$\mu_{33} + i\lambda_{33}/\omega = 2\pi \int_0^{R_M} \{\phi_{3U}(r, -d) - \phi_{3L}(r, -d)\} r dr \quad (20)$$

RESULTS

In this section, to examine the advantage of the moon pool and optimize the wave energy conversion ability of the WEC, hydrodynamic analysis of a certain disk with several cases of moon pools is considered. As a measure of wave energy conversion ability, the magnification η/η_0 of the optimal power take-off of the disk with moon pool relative to the single disk is also calculated. In the solving process, to reduce the computational complexity and highlight the key variables, some geometrical dimensions such as $h = 60$ (m), $e = 3$ (m), $t = 5$ (m), $b = 11$ (m) and $R_m = 4.0$ (m) are confirmed.

As shown in Fig.2~4, the hydrodynamic coefficients in a dimensionless representation and connected wave energy conversion ability are plotted versus dimensionless wave period $T^* = (g/R_M)^{1/2}T$ ($R_M =$ disk radius, $T = 2\pi/\omega =$ wave period) for various geometries of the moon pools. No spring is assumed to be present, i.e. $k = 0$ as the optimal spring calculated before cannot be realized in fact. It is observed from Fig.2 that the geometry of the moon pool has great influence on the hydrodynamic performance of the disk. The non-dimensional added mass in heave of the disk is friendly period-dependent and nearly stays the same at longer period and decrease with the increase of R_T/R_M .

The non-dimensional heave damping is highly period-dependent with a higher peak damping occurs at the same period for a smaller R_T/R_M . In addition, it will be negative when the period is long enough. The non-dimensional amplitude of excitation force in heave direction is highly dependent on wave period and approaches zero for very short and long high period. The wave periods where the peak of excitation force occurs are same and the bigger R_T/R_M results in a lower peak. The wave energy absorption magnification η/η_0 is highly dependent on period with inconspicuous peak which is inversely related with the value of R_T/R_M .

Fig.3 depicts the hydrodynamic coefficients of disk and energy absorption magnification with a higher $R_E/R_M = 2.5$. The added mass in heave increases rapidly at short wave period and nearly stays the same at long period for a certain R_T/R_M , and stays nearly the same with the increase of R_T/R_M at short wave period. The non-dimensional heave damping is highly dependent on period and a higher peak damping occurs at a longer wave period for a smaller R_T/R_M . The non-dimensional amplitude of excitation force in heave direction is highly dependent on wave period and approaches zero for very short and long high period. The wave period the peak occurs and the peak decrease with the increase of R_T/R_M . The wave energy absorption magnification η/η_0 is highly dependent on period and approaches zero at very long period for bigger R_T/R_M , and null points occur for smaller R_T/R_M . The wave period bandwidth where the magnification is greater than one is highly dependent on the geometry of the moon pool and decrease with the increase of R_T .

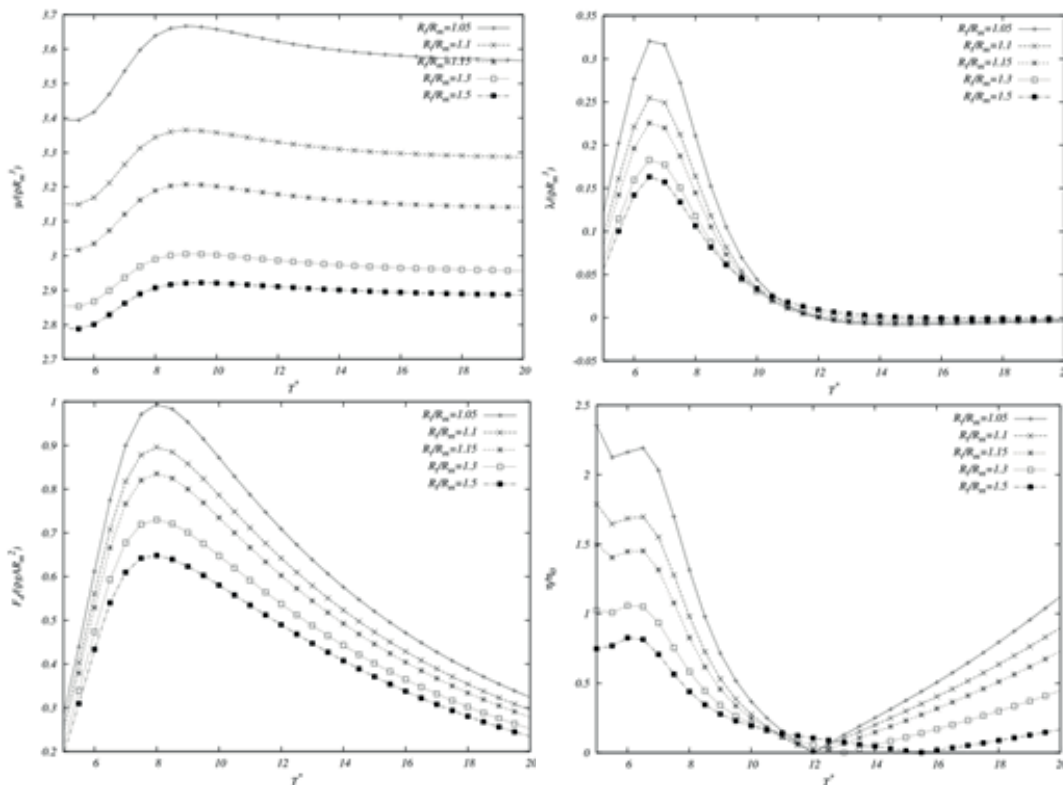


Fig. 2 Hydrodynamic analysis and energy magnification for various R_T/R_M with certain $R_E/R_M = 1.5$

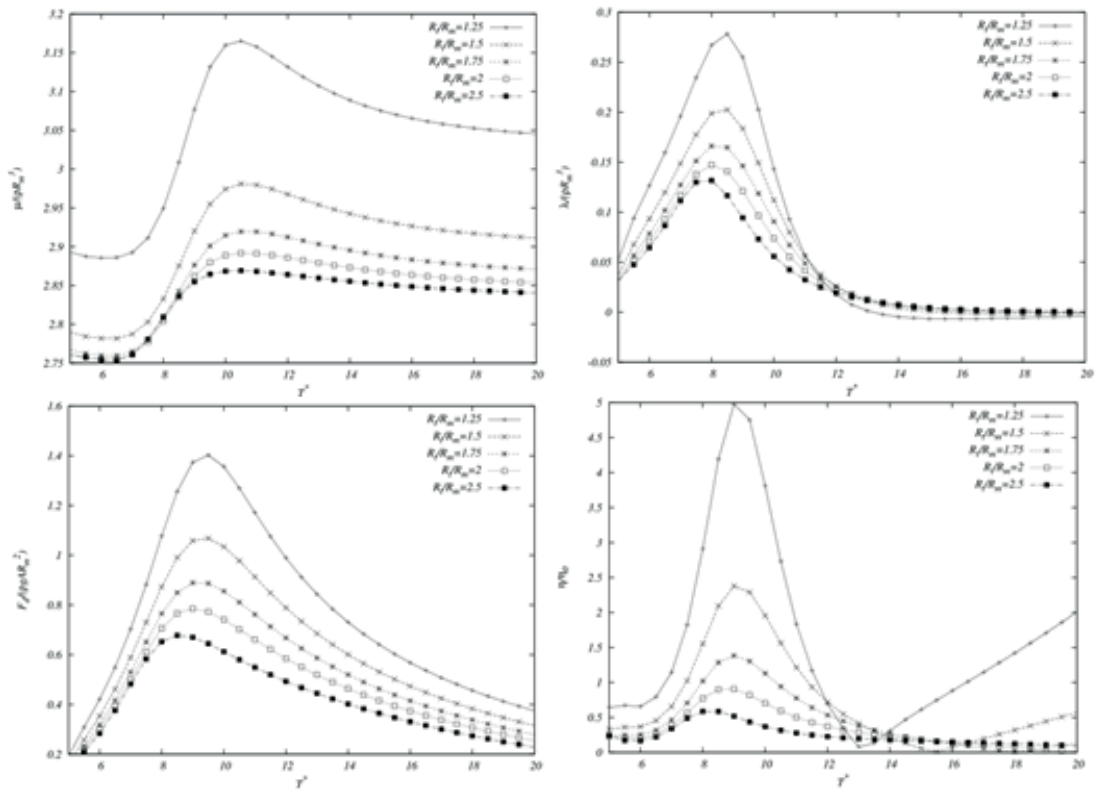


Fig. 3 Hydrodynamic analysis and energy magnification for various R_l/R_M with certain $R_E/R_M = 2.5$

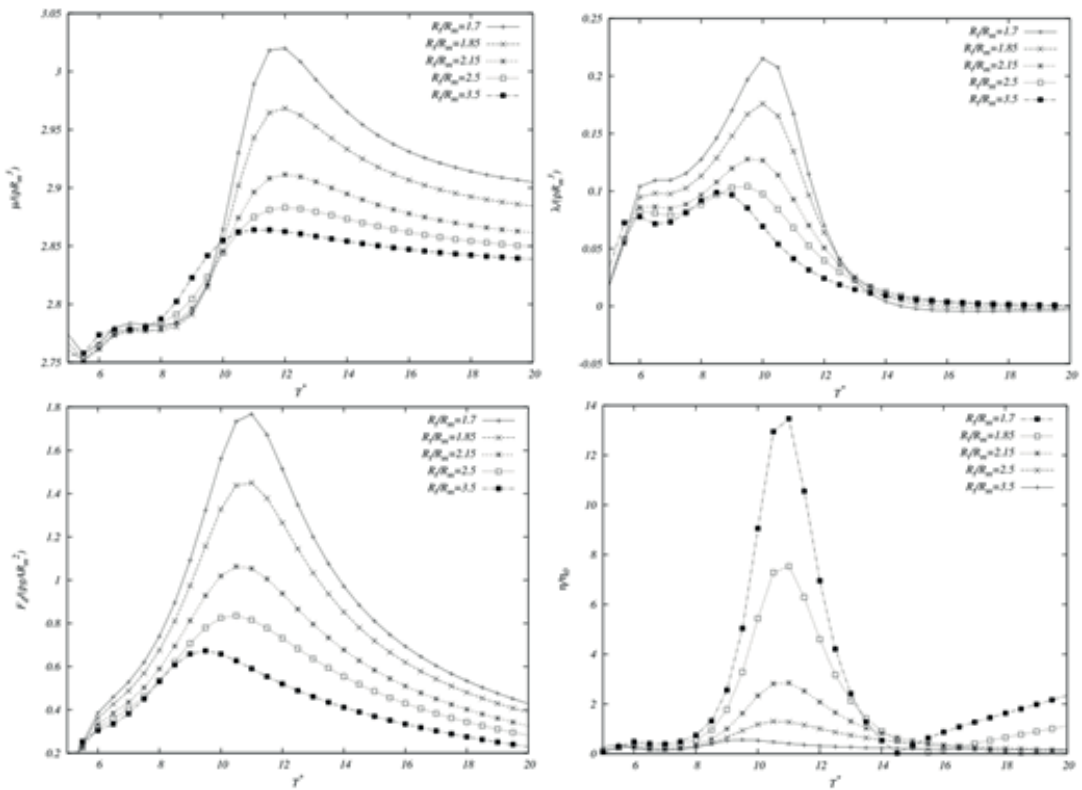


Fig. 4 Hydrodynamic analysis and energy magnification for various R_l/R_M with certain $R_E/R_M = 3.5$

CONCLUSIONS

Although the hydrodynamic frequency-domain analysis of the WECs is based on some assumptions and ignorance of some affects such as the non-linearity in this paper, the presented analytical approximation provides an efficient solution for the fundamental research. Despite the negative effect caused by the assumption, the analysis of the effects for different geometries especially for the fixed water depth is good, from which we can have a good understanding of the effects of different geometries for fixed mass on the hydrodynamic performance.

In the research for the ability of WECs for the energy conversion, a series of geometries based on the fixed water depth are considered respectively, from which we find that the geometry of the moon pool have great effect on the ability of energy conversion and when the radius of moon pool is closed to that of disk, the conversion ability will be the best.

REFERENCES

1. Budal K, Falnes J, Iversen LC, Lillebekken PM, Oltedal G, Hals, et al. (1982) The Norwegian wave-power buoy project. In: Proceedings of 2nd International Symposium on Wave Energy Utilization, Trondheim, Norway, 323-44.
2. Chen XB, Liu HX, Duan WY (2015) Semi-analytical solutions to wave diffraction of cylindrical structures with a moon pool with a restricted entrance. *Journal of Engineering Mathematics*, 90(1), 51-66.
3. Eriksson M, Isberg J, Leijon M (2005) Hydrodynamic modeling of a direct drive wave energy converter. *Int. J. Eng. Sci.*, 43: 1377C1387.
4. Falcao AFO (2007) Modeling and control of oscillating-body wave energy converters with hydraulic power take-off and gas accumulator. *Ocean Engineering*, 34(14-15), 2021-2032.
5. Garrett CJR (1971) Waves forces on a circular dock. *J. Fluid Mech.* 46, 129-39.
6. Henderson, R (2006) Design, simulation, and testing of a novel hydraulic power take-off system for the Pelamis wave energy converter. *Renewable Energy*, 31(2), 271-283.
7. Liu HX, Duan WY, Chen XB (2012) Analytical solution of wave loads on cylindrical structures. *Proc. ICMT2012*, Harbin (China).
8. MacCamy RC, Fuchs RA (1954) Wave forces on piles: a diffraction theory. US Army Corps of Engineers, Beach Erosion Board Tech. Memo. No. 69.
9. Margheritini L, Vicinanza D, Frigaard P (2009) SSG wave energy converter: design, reliability and hydraulic performance of an innovative overtopping device. *Renewable Energy*, 34(5), 1371-1380.
10. Mavrakos SA, Chatjigeorgiou IK (2006) Second-order diffraction by a bottom-seated compound cylinder. *Journal of Fluids and Structures* 463-492.
11. Miles JW, Gilbert JF (1968) Scattering of gravity waves by a circular dock. *J. Fluid Mech.* 34, 783-793.
12. Price AAE, Dent CJ, Wallace AR (2015) On the capture width of wave energy converters. *Applied Ocean Research*, 31(4), 251-259.
13. Weinstein A, Fredrikson G, Parks MJ, Nielsen K (2004) Aqua-BUOY: the off-shore wave energy converter numerical modeling and optimization In: Proceedings of MTTTS/IEEE Techno-Ocean., 04, 1854C1859, Kobe, Japan.
14. Almar, R; Almeida, P; Blenkinsopp, C; Catalan (2016), P. Surf-Swash Interactions on a Low-Tide Terraced Beach. *Journal of Coastal Research*. SI 75, 348-352.
15. Wu BJ, Lin HJ, You YG, Feng B, Sheng SW (2010) Study on two optimization methods of oscillating wave energy conversion device. *Acta Energiæ Solaris Sinica*, 31(6), 769-774, Chinese.
16. Yeung RW, Peiffer A, Tom N (2012) Design, analysis and evaluation of the UC-Berkeley wave-energy extractor. *J. Offshore Mech. Arct.*, 134(2): 02190

CONTACT WITH AUTHOR

H.X. Liu

College of Shipbuilding Engineering,
Harbin Engineering University,
Harbin 150001,
China

email: liuhengxu@hrbeu.edu.cn;
15045630022@139.com

ANALYSIS OF THE START-UP OF NATURAL BIO-FILM COLONIZATION OF CONSTRUCTED RAPID INFILTRATION SYSTEM

Wenlai Xu

Ju Yang

Jing Wang

Yue Jian

Min Tang

State Key Laboratory of Geohazard Prevention and Geoenvironment Protection,
Chengdu University of Technology, Chengdu, China

ABSTRACT

Abstract: this paper studied the start-up of natural bio-film colonization under the conditions where wet-to-dry ratio was 1:6, hydraulic load was $0.8\text{m}^3/\text{m}^2\cdot\text{d}$, and water temperature was 10°C - 15°C , it took 25d in total to become mature, after the success of bio-film colonization, the removal rate of COD and NH_4^+-N can be stabilized at 80%, and the removal rate of NH_4^+-N can reach 90% above. The microorganism was divided into the following stages during bio-film colonization: 1. Reversible adhesion of cell on the surface of the carrier, 2. Irreversible adhesion of cell on the surface of the carrier, 3. Division of cell adhering to the surface of the carrier and formation of microcolony adhering to the surface of the carrier, 4. Growth of microcolony adhering to the surface of the carrier to be mature bio-film with three-dimensional structure. The process of natural bio-film colonization can be judged comprehensively according to removal rate of NH_4^+-N and COD, effluent pH as well as color of microbial film.

Keywords: Constructed Rapid Infiltration System, start-up of natural bio-film colonization, removal rate, COD

INTRODUCTION

Constructed Rapid Infiltration System (CRI system) is a new wastewater treatment system developed from Rapid Infiltration (RI system), which works on the basis of purification of wastewater using interaction between infiltration media and microorganisms in the CRI system through a series of physical, chemical and biological actions. It is especially suitable for wastewater treatment in small towns and farmer concentrated residential areas[1]. It has the advantages of low cost, low energy consumption, easy to operate, good effluent quality, etc. However, the total removal rate of nitrogen is not up to standard. Study suggested that the pollutant removal in the CRI system mainly relied on the biological mechanism, supplemented by non-biological

mechanism[2]. So the quality of bio-film in the CRI system determined the level of pollutant removal capacity in the CRI system. The bio-film colonization methods mainly adopted at present include: natural bio-film colonization method[3], artificial inoculation bio-film colonization method [4] and compound bio-film colonization method[5]. This paper adopted the natural bio-film colonization method for the CRI system, analyzed the change in COD, ammonia nitrogen and other index during bio-film colonization as well as correlation with bio-film colonization process, thus providing theoretical basis for natural bio-film colonization method of the CRI system.

EXPERIMENTAL DEVICES AND MATERIALS

EXPERIMENTAL DEVICES

The experimental devices are as shown in the figure, the column adopted organic glass column with diameter D of 150mm, column height h was 1500 mm, where the supporting layer adopted cobblestone with height of 100 mm, filtering material height H was 1000 mm, consisting of 10% marble sand + 5% zeolite sand + 85% river sand.

The artificial rapid process was adopted, wastewater was fed from the top and flew downward, where the inlet layer height h_1 was 300 mm, the first flow layer height h_2 was 100 mm, and a sampling port was set every 200 mm, Fig. 1 shows the experimental devices.

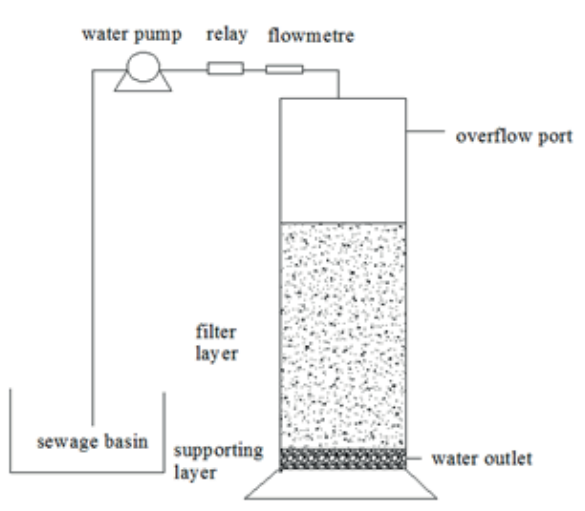


Fig. 1. Experimental Devices

EXPERIMENTAL WATER QUALITY

Experimental raw water adopted the configured wastewater, making up of glucose, soluble starch, sodium acetate, ammonium chloride, peptone, beef extract, ammonium sulfate, potassium dihydrogen phosphate, sodium bicarbonate and tap water, Table 1 shows the experimental water quality, and experimental methods for all water quality adopted the national standard methods.

Tab. 1. Experimental water quality

	COD /mg·L ⁻¹	NH ₄ ⁺ -N /mg·L ⁻¹	NO ₂ -N /mg·L ⁻¹	NO ₃ -N /mg·L ⁻¹	TN /mg·L ⁻¹	pH
Mean	206.1	46.8	1.3	12.4	86.3	6.73

EXPERIMENTAL METHODS

NH₄⁺-H: Nessler's reagent photometric method

COD: Potassium dichromate method

pH: Glass electrode method

EXPERIMENTAL STARTING METHODS

This experiment adopted the natural bio-film colonization, which was started under the conditions where wet-to-dry (the ratio between water distribution and drying time of CRI[6]) ratio was 1:6, hydraulic load was 0.8m³/m²·d, and water temperature was 10°C-15°C.

Around one week after the start-up of natural bio-film colonization, dotted yellow green bio-film that was visible to the naked eyes appeared, and white filamentous film appeared at the outlet pipe orifice.

Around two weeks after the start-up of natural bio-film colonization, the area of the dotted yellow green bio-film that was visible to the naked eyes increased, and color deepened, and the white filamentous film at the outlet pipe orifice changed to black brown.

Around 25 days after the start-up of natural bio-film colonization, the color of filler surface became green-black, and the water quality index showed stable removal effect of COD and ammonia nitrogen, indicating successful natural bio-film colonization.

ANALYSIS OF EXPERIMENTAL RESULTS

REMOVAL EFFECT OF COD DURING NATURAL BIO-FILM COLONIZATION

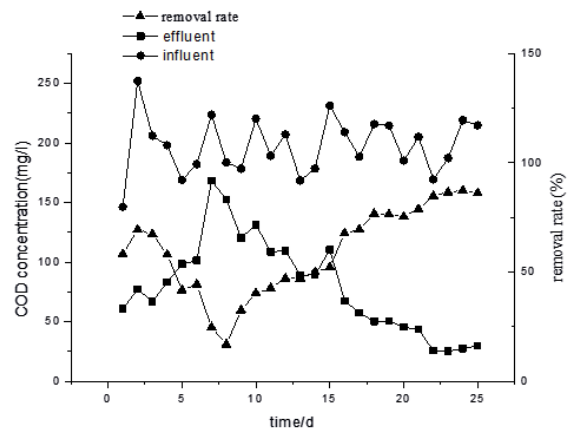


Fig. 2. Removal Effect of COD During Natural Bio-film colonization

It can be seen from Fig. 2, the removal effect of COD during natural bio-film colonization was not stable, around one week before the start-up of natural bio-film colonization, the removal effect of COD decreased gradually, and reached its minimum level at 8d, adsorption rate was only 16.9%.

Then it reached stability gradually at 80% above from low to high.

This was because that around one week before the start-up of natural bio-film colonization, microbial film had not been formed, so the removal of COD in the CRI system mainly relied on the physical functions like interception and adsorption, study [7] has found that the theoretical maximum adsorption capacity of pollutants in wastewater by river sand at room temperature is 1893.706 mg·kg⁻¹.

The adsorption capacity of pollutants by filtering material decreased gradually with the decreasing of adsorption point position of filtering material, so the removal rate of COD decreased gradually, however, after one week, the bio-film of the CRI system gradually formed, which decomposed organic matters in pollutants adsorbed, and slowly released the adsorption point position of filtering material, allowing gradual increasing of adsorption capacity of organic matters by filtering material, by adsorbing organic matters during the flooding period and decomposing organic matters and releasing adsorption point position and synthesising its own material during the drying period allowed constant development and maturation of bio-film in the CRI system while increasing the removal effect of COD and stabilized it gradually.

REMOVAL EFFECT OF NH₄⁺-N DURING NATURAL BIO-FILM COLONIZATION

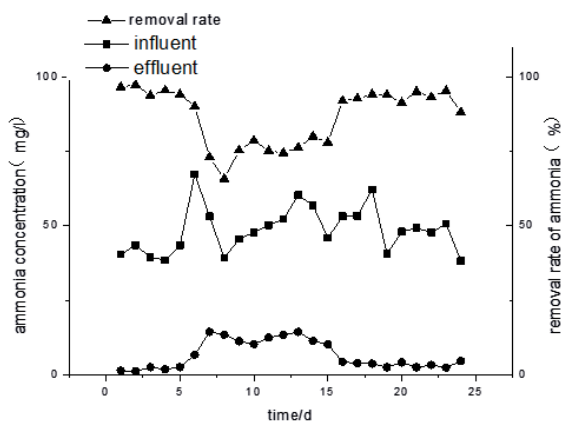


Fig. 3. Removal Effect of NH₄⁺-N during Natural Bio-film Colonization

It can be seen from Fig.3, the removal rule of ammonia nitrogen at earlier stage of natural bio-film colonization basically coincided with that of COD, the removal rate of ammonia nitrogen at earlier stage of natural bio-film colonization was reduced on some degree when the saturation of adsorption point position of filtering material was reached by interception and adsorption by filtering material, however, the minimum removal rate of ammonia nitrogen reached up to 65%, and the average removal rate of ammonia nitrogen reached up to 86.8% during natural bio-film colonization.

This was because that the infiltration media may have more than one adsorption point position for ammonia nitrogen[8], in addition, the infiltration media were negatively charged, while NH₄⁺-N was positively charged, so it was easy to be intercepted and adsorbed by filtering material[9].

Meanwhile, the filtering material contained 5% of zeolite sand, which had good adsorption effect for ammonia nitrogen[10].

With the formation of bio-film, the removal of ammonia nitrogen mainly relied on the absorption and transformation of ammonia nitrogen by nitrifying bacteria.

The growth condition suitable for most nitrifying bacteria was: temperature 25-30°C, pH 7.5-8.0.

Since this experiment was started at early March, the bio-film began to gradually form around the second week, and the temperature cannot reach the optimum temperature for nitrifying bacteria in mid-March, so the nitrifying bacteria grew slowly, during which the removal rate of ammonia nitrogen basically maintained around 75%, which reached around 90% with the rise of climate temperature and became stable with the maturity of bio-film.

CHANGE IN PH DURING NATURAL BIO-FILM COLONIZATION

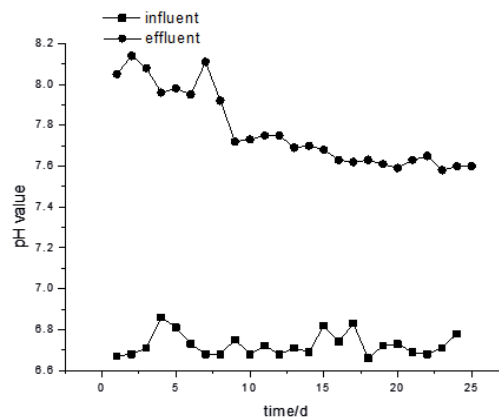


Fig. 4. Change in pH during Natural Bio-film Colonization

It can be seen from Fig.4 that the influent pH basically maintained around 6.7 and the effluent pH basically maintained around 8.1 in the first week, and then pH began to gradually decrease and became stable, and finally basically became stable at around 7.5.

This was because that the adding of 10% marble sand in the CRI system provided a certain alkalinity for the CRI system, at earlier stage of natural bio-film colonization, there were few microorganisms in the CRI system, wastewater entered the CRI system, and ran from top to bottom and contacted with marble sand, which allowed increasing of effluent pH in the CRI system.

However, around the second week, the microorganisms in the CRI system began to grow slowly, whose nitrification required consumption of alkalinity, theoretical alkali consumption of was 7.07g/(CaCO₃/NH₄⁺-N)[11], thus allowing gradual decreasing of effluent pH, and the alkali consumption reached stable with the formation of bio-film, so the effluent pH gradually became stable.

CONCLUSION

1 The natural bio-film colonization of the CRI system under the conditions where the wet-to-dry rate was 1:6, water temperature was 10°C-15°C, and hydraulic load was 0.8m³/m²·d can succeed at about 25d.

2 The success of natural bio-film colonization of the CRI system can be judged comprehensively according to pH, removal rate of COD and removal rate of ammonia nitrogen as well as color of microbial film.

After the success of natural bio-film colonization of the CRI system, the removal rate of COD can maintain stable at 80%, and the removal rate of $\text{NH}_4^+\text{-N}$ can reach 90% above.

3 The forming process of bio-film can be divided into the following stages: 1. Reversible adhesion of cell on the surface of the carrier, 2. Irreversible adhesion of cell on the surface of the carrier, 3. Division of cell adhering to the surface of the carrier and formation of microcolony adhering to the surface of the carrier, 4. Growth of microcolony adhering to the surface of the carrier to be mature bio-film with three-dimensional structure, 5. Shedding of part of cells from the bio-film[12-13].

According to the analysis of removal rate of COD and ammonia nitrogen as well as change in pH during natural bio-film colonization, it can be simply judged that the bio-film of the CRI system was in the first two stages of bio-film formation around the first week, the third stage of bio-film formation from the second week to around the third week, and basically the fourth stage of bio-film formation around the fourth week.

ACKNOWLEDGEMENTS

The research was funded by the Natural Science Foundation of China (No. 41502333), the State Key Laboratory of Geohazard Prevention and Geoenvironment Protection Foundation (No. SKLGP2015Z012, SKLGP2014Z001), the specialized research fund for the doctoral program of colleges and universities (No. 20135122120020), the scientific research plan of education department of Sichuan Province (No. 14ZB0073).

REFERENCES

1. Yang Xiaomao et al., Application Research of Constructed Rapid Infiltration Technology in Water Pollution Control in Rural Areas in Our Country. *Environmental Engineering*, 2012(S2): Page 91-96.
2. Cui Chengying et al., Pollutant Removal Mechanism by Constructed Rapid Infiltration System. *Environment Pollution and Control*, 2007(02): Page 95-98.
3. Li Yafeng, Zhang Juan, Zhang Peize, Bai Yuanbo, Analysis of the Start-up of Natural Bio-film Colonization of Biological Aerated Filter. *Shenyang Architectural University Journal (JCR Science Edition)*, 2008.24(6): Page 1035-1038.
4. Yang Jingwen, Jiang Shuangying and Liu Zhaoli, Low Temperature Starting Test of Up-flow Biological Aerated Filter. *Water Treatment Technology*, 2011(01): Page 112-115.
5. Wang Jianhua, Chen Yongzhi, Peng Yongzhen, Bio-film Colonization and Start-up of Nitrification Biological Aerated Filter. *Chinese Journal of Environmental Engineering*, 2010(10): Page 2199-2203.

6. GuoJinsong et al., Influence on Decontamination Property of Constructed Rapid Infiltration System by Wet-to-dry Ratio, *China Water and Wastewater*, 2006(17): Page 9-12+17.
7. XuWenlai and Zhang Jianqiang, Adsorption and Dynamics of Organic Matter in Wastewater. *Water Treatment Technology*, 2011. 37(5): Page 30-32, 36.
8. Wang Lu, Yu Zhiping, Zhao Zhijie, Ammonia Nitrogen Removal Mechanism of Constructed Rapid Infiltration System. *China Environmental Science*, 2006.26 (4): Page 500-504.
9. XuWenlai, Pollutant Removal Mechanism and Dynamics Research of Constructed Rapid Infiltration System. Southwest Jiaotong University. Page 127.
10. You Shaohong, Tong Xiaowei and Zhu Yinian, Absorption and Influencing Factors of Ammonia Nitrogen by Natural Zeolite. *Water Resources Protection*, 2010. 26(1): Page 70-74.
11. ZhengPingxu, Xiang Yang, Hu Baolan, Theory and Technology of Novel Biological Dinitrification. 2004: Science Press.
12. Choi, BH (Choi, Byung Ho); Yuk, JH (Yuk, Jin-Hee); Kim, KO (Kim, Kyeong Ok), Integral Tide-Surge-Wave Model of the Yellow Sea for Understanding Local Sediment Transport. *Journal of Coastal Research*. 2016. SI(75): Page 208-212.
13. Qi Hanying et al., Exploration of Mechanism and Influencing Factors of Bio-film Formation. *Journal of Microbiology*, 2013(04): Page 677-685.

CONTACT WITH AUTHOR

Ju Yang

State Key Laboratory of Geohazard Prevention
and Geoenvironment Protection,
Chengdu University of Technology,
Chengdu 610059,
China

email:12487616@qq.com

SPATIAL ECONOMICS MODEL PREDICTING TRANSPORT VOLUME

Bo LU

Institute of Electronic Commerce and Modern Logistics, Dalian University

ABSTRACT

It is extremely important to predict the logistics requirements in a scientific and rational way. However, in recent years, the improvement effect on the prediction method is not very significant and the traditional statistical prediction method has the defects of low precision and poor interpretation of the prediction model, which cannot only guarantee the generalization ability of the prediction model theoretically, but also cannot explain the models effectively. Therefore, in combination with the theories of the spatial economics, industrial economics, and neo-classical economics, taking city of Zhuanghe as the research object, the study identifies the leading industry that can produce a large number of cargoes, and further predicts the static logistics generation of the Zhuanghe and hinterlands. By integrating various factors that can affect the regional logistics requirements, this study established a logistics requirements potential model from the aspect of spatial economic principles, and expanded the way of logistics requirements prediction from the single statistical principles to an new area of special and regional economics.

Keywords: Spatial economics, Logistics requirements potential model, Regional logistics prediction

INTRODUCTION

The logistics requirements prediction is to predict the changes of the logistics requirements and its development trend by virtue of judgment, technical method and model according to the past and current requirements of the logistics markets and the relationship among the factors that affect the changes in the logistics market requirements.

The regional logistics requirements prediction was firstly proposed in the 1990s [2]. After nearly 20 years of development, it has made great progress. By sorting out comprehensive overview about existing method, most researchers deal with them as a regression problem. According to the development process and the level of intelligence, it can be roughly divided into three stages:

The prediction method based on statistics in the first stage. Main methods include regression analysis [4], elasticity coefficient method [1], freight intensity method, clustering method, gray theory model [5], Markov chain [3], input-output model [7], space-time multi-term probability model and decision support system, etc [9]. The major features of this type of methods can process the sequencing and linear data, and explain the construct models effectively. With the deepening of the study, many defects of the research methods are exposed: firstly, there are very few regional logistics requirements data samples, which are difficult to be collected and is harmful for the validation of the prediction method. Secondly, it is not ideal for processing the regional logistics requirements data with high dimension, non-linear relationship, non-normal distribution and chronological

order [32]. Thirdly, lack of flexibility, which cannot guarantee the learning and generalization ability and will process all data in the same way whether it is required or not.

The prediction method based on artificial intelligence in the second stage. Later on, to enhance the prediction accuracy, the researcher [10] adopted the artificial intelligence method, such as the artificial neural network (ANN) and its improvement model. By introducing the artificial intelligence factors into the traditional method, such as the learning and generalization ability of neural networks, expert system inference rules, etc, then the regional logistics requirements prediction accuracy can be improved. However, there are still the following problems: firstly, it cannot guarantee the generalization capability of the prediction model, which makes it no stable prediction effect for the new logistics requirements data sets for the prediction model after training. Secondly, when the number of study samples is limited, the learning process error is easy to converge to local minima, hence the learning accuracy is difficult to guarantee; when there is more sample variables, it will come to the “disaster of dimensionality” [32]. Thirdly, it mainly relies on the empirical risk minimization principle, and its main defects are: to select the decision-making function with the empirical risk instead of the expected risk is not subject to strict testifying and full demonstration, which is only a reasonable way; it is easy to lead to “over-learning”. It is an inevitable result by blind pursuit of small errors, which causes decrease in the generalization ability [21].

The prediction methods based on statistical learning theory is the third stage. To further enhance the accuracy and stability of the prediction models, in recent years, the researchers started to explore the prediction method based on the principle of structural risk minimization [8]. Such methods are represented by the support vector machine (SVM). Although certain achievements have been made, some urgent problems still exist in the regional logistics requirements prediction [11], mainly as follows: first, when the quantity of learning samples is limited, the learning process error is easy to converge to a local minimal point, and the learning accuracy is difficult to guarantee; when there are many learning sample variables, they fall into the “dimension disaster” [23]. Second, mainly rely on the empirical risk minimization principle. Therefore, the generalization capability of the prediction model cannot be guaranteed from theory, which makes the predictive models after training to have no stable prediction effect for the new logistics requirements data set. Third, since the concept of regional logistics has been introduced to China for not a long time, many logistics standards are not unified, and also lack of direct statistical data. The historical data for researching prediction have to be substituted by the related cargo quantity, which affect the empirical study of the prediction methods [12]. Especially in china, most of the literatures [6, 13] are only an overview of the method, and almost no actual regional logistics data are used for predictive analysis [15], which makes many studies lack of practical significance. Fourth, the selection method of

indicators of regional logistics mainly which support the prediction [14, 16], relies on the experiences of the industry researchers and practitioners, the principal component analysis, factor analysis and other traditional methods, hence they are lack of new research method. Fifth, among these methods, although the artificial intelligence methods and support vector machine method have certain advantage in the prediction of accuracy, it still cannot explain the models effectively [31].

As seen from the above analysis, the researches in the present stage are mainly restricted by the non-unified logistics standard. Under the condition of lack of direct statistical data, to continue the logistics requirements prediction from the perspective of regression statistics cannot guarantee the prediction accuracy, nor explain the models effectively [22].

Regional logistics requirements is a derived requirements determined by the level of regional economic development, therefore, the indicators that affect the regional logistics requirements prediction such as economic factors (mainly including: the overall level and scale of the regional economy, industrial structure and product structure of the regional economy and the spatial layout of the regional economy, etc), logistics industry factors (mainly including: logistics facilities and services, changes in logistics costs, etc.), environmental factors (mainly including: technological progress, economic policies and institution, etc), as well as other factors (mainly including: regional geographic location, emergency factors, etc.), will directly or indirectly affect the growth or reduction of the regional logistics requirements [17].

Therefore, by integrating various factors that affect the regional logistics requirements, this study explores the logical relationship between the regional logistics requirements and many other relevant factors based on the spatial economics and new economic geography, etc, and from the perspective of market potential in the space economic principles [27-29], then this study established the logistics requirements gravity model and expanded the logistics requirements prediction way from the single statistical principles to the new area of space economics and regional economics, to enrich the research method of the regional logistics requirements.

In recent years, among the relevant study in spatial economics, the theoretical breakthrough made by the economists [24] brought a new wave of the industrial clustering study [26]. But regrettably, there is still very less experiences and empirical support in the logistics industry clustering and logistics requirements prediction [19]; therefore, this study expects to make some efforts in this area.

The paper is structured as follows: after the introductory section of Chapter 1, there will be followed by the description of the logistics requirements potential model. In so doing, the research procedure is included in Chapter 2. Moreover, the research scope and logistics requirements prediction in Chapter 3. Finally, conclusions are drawn in Chapter 4.

RESEARCH METHOD

LOGISTICS REQUIREMENT POTENTIAL MODEL

The concept of market potential was firstly proposed by Harris [17], which can be described that, as a place of production, the decision of region depend on the easy accessibility of market in this area. The measurement on the accessibility is the market potential index, which can be expressed by the formula: $M_j = \sum_k Y_k g(D_{jk})$, where, M_j is the market potential of place j ; Y_k is the incomes of the all regions; $g(D_{jk})$ is the decay function of distance; D_{jk} is the distance between place j and place k . Harris' market potential model, however, has no micro-structure, which only showed that the market potential is proportional to market purchasing power of various places (i.e. the market scale), and inversely proportional to the distance from this place to the market.

But the theoretical innovation on this issue as a special field was originated from the early 1990s when Krugman and Fujita, et al built the New Economic Geography [18, 20]. The economists represented by Krugman studied the business location choice behavior to maximize the profits, and proposed the market potential model based on the monopolistic competition, increasing returns to scale and iceberg transport cost, general equilibrium framework including the enterprise subject decision behaviors. [25] claimed that two forces determine whether the economic behavior and economic factors are convergent or diffusive in spaces in the model: centripetal force and centrifugal force. The centripetal force makes the economic activities and economic elements to reflect the industrial agglomeration in the spatial distribution in the industry level, which is why the new economic geography and spatial economics attaches great importance to industrial agglomeration [26].

However, [19] who proposed the potential model just from the perspective of economic scale and regional economic agglomeration. On the basis of the market potential model, this paper has introduced the related logistics factors, including a series of related indicators such as overall level and scale of the regional economy, regional cargo output, and economic distance, to construct the logistics requirements potential model:

$$P_i = k_{ij} \frac{M_i^{a_i} M_j^{a_j}}{ED_{ij}^b} \quad (1)$$

Where, P_i is the potential value between city i and j , k_{ij} is the weight, which reflects the contribution rate of the city i on the centripetal force; M_i, M_j respectively represent the scale of two cities (such as gross national product, logistics volume, population, etc.), a_i, a_j are the indices, which reflect the space liquidity difference, ED_{ij} is the economic distance between the two geographic locations, and b is the friction coefficient of distance.

Since the two cities have different contributions to the centripetal force, it is required to calculate its contribution

on the centripetal force when calculating the potential of city i according to the following formula:

$$k_{ij} = \left[\frac{GDP_i}{GDP_i + GDP_j} \right] \times \left[\frac{Q_{(total-i)}}{Q_{(total-i)} + Q_{(total-j)}} \right] \times \left[\frac{Q_{(industry-i)}}{Q_{(industry-i)} + Q_{(industry-j)}} \right] \quad (2)$$

Where, GDP_i and GDP_j are respectively the GDP of cities i and j ; $Q_{(total-i)}$ and $Q_{(total-j)}$ are respectively the production of goods of cities i and j ; $Q_{(industry-i)}$ and $Q_{(industry-j)}$ are respectively the production of goods of the dominant and leading industry in cities i and j .

According to assumptions (Li, 2008), in this paper, the $\sqrt{(Q_i \times Q_j)}$ (the product of cargo quantity) represents the city size; the combined proportion of highway, railway and waterway is used to calculate the economic distance:

$$ED_{ij} = \alpha \times C_{highway-ij} \times D_{highway-ij} + \beta \times C_{railway-ij} \times D_{railway-ij} + \gamma \times C_{waterway-ij} \times D_{waterway-ij} \quad (3)$$

Where, C is the transportation cost, D is the spatial distance between two cities, α, β, γ are transport weights calculated by three transport modes. According to (Luo, 2010), this paper has set the distance friction coefficient to 2.

Therefore, the formula of the logistics requirements potential model can be changed as:

$$P_i = k_{ij} \frac{\sqrt{Q_i \times Q_j}}{ED_{ij}^2} \quad (4)$$

RESEARCH PROCEDURE

By constructing the model of the logistics requirements potential, this paper has predicted the logistics requirements of Zhuanghe, which not only avoids the double counting of the cargo quantity, but also calculate the logistics requirements potential value of Zhuanghe, and sort the logistics requirements potential values in various cities within the system.

Let Zhuanghe as the research center, this study, firstly, need identify the cities which have high relevance with logistics of Zhuanghe to jointly constitute a logistics system. Then, based on the leading industry of Zhuanghe, this study could predict the cargo output of each city in these industries by data fitting.

When predicting the logistics requirements based on the logistics requirements potential model, this study, firstly, need calculate five parameters which are the GDP weight, weight of the cargo quantity, weight of the industry cargo quantity, weight of the city logistics scale, and economic distance; then the study should respectively calculate the logistics requirements of the leading industries in each city, that is, by applied with the logistics requirements potential model, this study, firstly, calculates the logistics potential value of the leading industry in each city, and by normalization processing, the weight of the potential value

can be obtained, and then multiply the total production of cargo of this industry within the system, to obtain the logistics requirements of each industry within the system in each city. The formula is:

$$\text{Logistics Requirements of City}_i \text{ Industry}_j = \frac{\text{Potential Value Weight} \times \text{Total Output of Industry}_j \text{ Within System}}{\text{Total Output of Industry}_j \text{ Within System}} \quad (5)$$

RESULT ANALYSIS

RESEARCH SCOPE

The study is centring on city of Zhuanghe, scope of I, II, III area surrounding, I area is as per radius of 100 kms, II area is as per radius of 100~300 kms, III area is as per radius of 300~500 kms, and IV area are the cities along the “east-railway”.



Figure 1: Radiation area of research scope

Definition of I, II, III surrounding areas is as following: central city: Zhuanghe; I area: Wafangdian and Pulandian; II area: Yingkou, Dandong, Dalian, Anshan, Panjin, Jinzhou and Huludao; III area: Shenyang, Fushun, Tieling, Fuxin, Chaoyang, Yantai, Weihai, Tonghua and Baishan; IV area: Hegang, Jiamusi, Shuangyashan, Yanji, Jixi, Mudanjiang and Qitaihe.

PREDICTION FOR STATIC CARGO QUANTITY

Zhuanghe is located between Dalian and Dandong, the centre of the Northeast Asia economic circle. With the advantage of location, resources and industry, it is one of the windows for the opening-up in Liaodong Peninsula. As the construction of eastern border railway in Northeast, HD-highway, ZG-highway, ZX-railway, Binhai National Road

and the national first level ports in Zhuanghe, Zhuanghe will become an important sea port city in Northeast eastern region, and also an important node for commodity exchange in the Northeast to Japan, South Korea and North Korea.

In addition to the geographic advantages, the rapid economic development of Zhuanghe has direct correlation with its industrial structure. The major industry in Zhuanghe is the second industry with relatively complete category, including its three superior industries: agro-food processing industry, machinery and equipment manufacturing and furniture manufacturing, which account for a large proportion of the industrial added value. In addition, the rapid development of the above-scale general equipment manufacturing industry, transportation equipment manufacturing industry & communications equipment, computer & other electronic equipment manufacturing industry will bring a large quantity of logistics requirements.

Economic development speed of Zhuanghe has direct correlations with its industrial structure. By combining with the status of economic development, this study has mainly analyzed the following 16 industries which are Farming, Animal husbandry, Aquatic products, Food processing, Food manufacturing, Textile and apparel, Furniture manufacturing, Plastic products, Special equipment manufacturing, Fabricated metal products, General equipment manufacturing, Transportation equipment manufacturing, Electrical machinery manufacturing, Communications and electronic equipment, and Flow of commerce.

Based on data collection of site survey, statistical yearbooks and bulletins, this study, firstly, has calculated the static cargo quantity of 16 industries of Zhuanghe and surrounding four areas by means of data fitting, $Q_n = Q_0 \times (1+x)^{n-1}$. It is shown in table 1.

PREDICTION FOR DYNAMIC LOGISTICS REQUIREMENTS

Within the system (four area) composed by 26 cities centering Zhuanghe, Zhuanghe is located in the narrow space. Therefore, it is required to accurately calculate the logistics in the environment, and it is also critical to carry out accurate logistics industry positioning under the competitive environment.

When predicting the logistics requirements based on the logistics requirements potential model, this study firstly should calculate the five parameters which include: GDP weight, weight of cargo quantity, weight of industry cargo quantity, weight of city logistics scale, and economic distance.

The predicting values of GDP in year 2015, and economic distance between Zhuanghe and other cities have been summarized in table 2 and table 3, respectively.

Within the 26 cities, each city has its different key industry type, therefore, the production and consumption have different features. Judging the leading industry based on Zhuanghe, this study has predicted the logistics requirements of these industries in each city. Firstly this study has calculated the potential value of logistics requirements of the leading industry in each city.

Tab. 1. Predicting cargo quantity results of each city in 2015

Industry	City		Z.H.	W.F.D.	
	Z.H.	W.F.D.			
Farming	185.44	426.76			
Animal Husbandry	63.49	114.89			
Aquatic Products	74.09	11.82			
Food Processing	187.57	51.57			
Food Manufacturing	78.51	23.29			
Textile & Garment	1.56	1.32			
Furniture Manufacturing	370.69	93.46			
Plastic Products	13.15	12.46			
Special Equipment Manufacturing	1.78	2.37			
Fabricated Metal Products	100.46	16.56			
General Equipment Manufacturing	6.31	4.17			
Transportation Equipment Manufacturing	18.14	31.21			
Electrical Machinery Manufacturing	1.61	5.83			
Communications and Electronic Equipment	1.17	0.42			
Flow of Commerce	42.24	50.79			
P.L.D.	Y.K.	D.D.	D.L.	A.S.	P.J.
206.74	275.39	191.64	644.47	518.36	334.25
126.52	42.66	90.01	296.69	159.77	43.89
57.19	74.47	106.09	249.43	--	64.85
32.41	86.56	200.92	322.82	742.30	268.60
16.63	41.26	173.94	182.97	75.38	18.12
0.99	2.29	5.42	10.65	2.43	0.08
73.22	169.83	131.44	673.38	76.48	2.85
7.95	23.14	187.53	83.01	89.27	42.45
1.40	4.03	66.05	21.53	31.45	33.66
8.90	79.01	39.27	447.10	16.26	5.64
2.87	7.14	115.28	37.03	54.89	1.80
19.57	56.21	110.95	195.65	55.05	27.05
3.90	9.85	211.57	53.49	123.85	8.75
0.22	3.56	10.07	16.98	4.11	4.57
41.57	126.18	121.27	317.69	169.53	72.08
J.Z.	H.L.D.	S.Y.	F.S.	T.L.	F.X.
764.53	375.64	1075.67	72.76	886.01	323.03
293.86	68.50	431.18	43.96	267.17	651.60
79.47	77.41	27.01	--	--	1.89
275.63	190.84	1460.33	315.08	261.54	90.02
174.74	147.46	155.73	30.82	151.75	57.68
5.57	4.92	4.85	0.99	4.78	1.84
165.11	165.64	117.85	31.13	129.34	55.31
6.56	5.85	175.64	37.90	244.11	2.16
93.05	67.75	61.86	13.35	84.49	33.20
38.15	29.90	35.16	6.66	33.65	12.56
162.41	118.24	107.97	23.30	150.05	57.95
145.90	118.59	99.49	23.36	111.91	48.99
266.98	262.25	189.72	50.42	208.73	89.39
9.68	7.43	9.01	1.69	8.57	3.18
136.69	106.73	375.03	108.93	134.14	115.07
C.Y.	Y.T.	W.H.	T.H.	B.S.	H.G.
920.06	984.30	249.42	272.15	16.85	133.65
279.22	232.80	58.33	136.87	49.44	25.29
--	178.32	164.55	--	--	0.48
198.43	221.41	271.70	48.06	42.80	72.12
117.89	151.21	0.98	23.77	20.80	49.00
3.72	24.19	56.27	1.33	1.20	1.68
101.60	106.82	51.47	95.64	86.50	43.49
189.25	27.00	10.40	12.84	10.80	2.20
66.75	0.30	0.15	2.43	1.95	31.45
26.10	3.35	1.46	41.28	13.82	34.74
146.68	7.22	0.77	4.22	4.07	85.11
88.06	61.88	126.92	31.61	25.85	42.87
163.98	0.11	13.23	5.90	5.17	73.47
6.64	520.86	149.285	1.21	0.35	6.39
169.80	298.54	113.97	98.19	58.81	52.83
J.M.S.	S.Y.S.	Y.J.	J.X.	M.D.J.	Q.T.H.
897.77	383.60	44.60	327.47	341.68	252.96
119.06	125.76	7.30	28.39	76.76	31.66
3.82	0.62	--	3.00	3.14	--
324.07	42.86	60.62	90.13	133.22	25.80
6.98	116.57	14.49	64.53	116.12	0.12
1.08	2.02	1.41	2.22	3.70	6.46
0.87	61.04	25.01	57.45	86.83	5.98
0.27	2.59	4.23	4.45	4.42	1.16
1.13	41.30	22.14	33.30	59.89	0.04
2.53	23.30	13.93	22.16	35.74	0.21
4.48	71.80	41.50	57.91	104.43	0.18
0.14	60.80	37.12	56.07	75.42	20.75
19.88	72.07	72.25	96.73	141.31	1.35
--	3.18	5.92	3.62	6.73	165.40
127.79	71.19	26.49	99.59	363.69	42.76

Tab. 2. Predicting GDP results of each city in 2015

City				Z.H.
GDP				
W.F.D.	P.L.D.	Y.K.	D.D.	D.L.
1539.18	927.89	2343.36	1393.76	10546.39
A.S.	P.J.	J.Z.	H.L.D.	S.Y.
4447.38	1543.76	1543.76	1051.56	10212.62
F.S.	T.L.	F.X.	C.Y.	Y.T.
1734.42	1880.96	885.07	1833.49	7985.08
W.H.	T.H.	B.S.	H.G.	J.M.S.
3840.16	1544.63	1284.77	535.48	958.94
S.Y.S.	Y.J.	J.X.	M.D.J.	Q.T.H.
922.65	446.14	808.02	1572.03	799.45

Tab. 3. Economic distance from Zhuanghe to other Cities

From Zhuanghe to other Cities				
Economic distance				
W.F.D.	P.L.D.	Y.K.	D.D.	D.L.
2275.29	2481.53	3535.49	1005.71	4830.57
A.S.	P.J.	J.Z.	H.L.D.	S.Y.
8927.40	8937.06	41031.00	49188.79	17509.48
F.S.	T.L.	F.X.	C.Y.	Y.T.
20037.82	22769.72	22749.33	52573.22	12100.51
W.H.	T.H.	B.S.	H.G.	J.M.S.
12544.52	2162.25	2652.25	6642.25	10261.69
S.Y.S.	Y.J.	J.X.	M.D.J.	Q.T.H.
12723.84	13947.61	17715.61	16205.29	17768.89

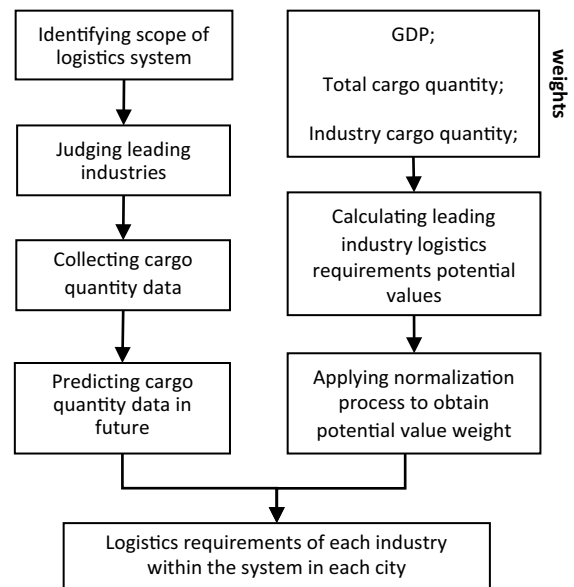


Fig. 2. Research procedure

By applying the normalization process, the weight of the potential value could be obtained. Then, the logistics requirements of each industry within the system in each city, can be calculated by the weight of the potential value multiply by total cargo quantity of this industry within the system. The predicting logistics requirements of Zhuanghe

in 2015, have been summarized in table 4, and the following observations can be made.

Tab. 4. Predicting logistics requirements of Zhuanghe

Industry	C.Q.	Log.R.	Var.	Rank
Farming	185.44	245.99	60.55	13
Animal H.	63.49	95.15	31.66	12
Aquatic P.	74.09	90.99	16.9	4
Food P.	187.57	259.06	71.49	8
Food M.	78.51	87.62	9.11	6
T. & A.	1.56	3.30	1.74	14
F. M.	370.69	429.23	58.54	3
Plastic P.	13.15	36.58	23.43	10
Special E. M.	1.78	9.48	7.7	16
F. M. P.	100.46	105.05	4.59	3
General E. M.	6.31	22.34	16.03	15
T. E.M.	18.14	25.07	6.93	15
E. M. M.	1.61	11.67	10.06	25
C. & E.E.	1.17	13.47	12.3	16
F. C.	42.24	51.76	9.52	15
Sum	1146.21	1486.76	340.55	--
C.Q.: Cargo quantity.				
Log. R.: Logistics requirements				
Var.: Variation.				

The column and row totals represent, respectively, the static cargo quantity, dynamic logistics requirements of Zhuanghe and the variation in 2015 year.

It is clear from table 4 that, the static cargo quantity yields lower than the dynamic logistics requirements in each industry. This result indicates that the logistics potential value is greater than average level, therefore the variation is positive. However, in sort order of industries competitive power, most industries of Zhuanghe are disadvantageous, except the industry of Aquatic Products, Food Manufacturing, Furniture Manufacturing and Fabricated Metal Products, thus indicating that the four leading industries has played the role of logistics engine, and Zhuanghe municipal government would need give policy support to them.

CONCLUSIONS

As a gathering node of logistics companies and logistics devices, logistics parks has become an important theme pushed forward by provinces and zones. According to incomplete statistics, there are several hundreds of logistics park, logistics base or logistics centre being planned and constructed at present. With its status confirmed on a national level, especially its important role in the service industry, logistics industry is one of the key items planned and developed by all levels of governments and is served as a new economic growth point in many zones.

Northeastern old industrial base reconstruction brings historical development chance and policy advantage for development of logistics industry in Zhuanghe. The state has intensified support for infrastructure construction in Liaoning Regions so that such tangible infrastructures as

communication, road traffic and urban infrastructures have an obvious improvement. Especially the improvement of transportation conditions is a powerful precondition for the development of the logistics industry. Zhuanghe has accelerated construction of logistics infrastructures continuously in recent years, such as logistics parks.

However, it is not all logistics parks have well played the role of logistics engine expected by us. In fact, there are no enterprises settling in most logistics parks and the vacancy rate is as high as 60%, resulting in huge wasting of resources. Therefore, construction of logistics parks should follow a uniform planning and should not be repeated. Because of that, a scientific prediction is a basic work for proper planning of logistics parks, which is also important to analyze the proper construction scale of logistics parks.

Furthermore, from the prospective of macro economic development of industries, the various regional logistics development strategies and regional logistics plan cannot be formulated without a quantitative analysis of regional logistics requirements. The first question occurred in logistics planning is the prediction for the scale of macro logistics market. Prediction of regional logistics requirements could provide a basis in theory for national and regional economic administrations. In addition, according to prediction of regional logistics requirements, the government could evaluate the contribution of the logistics industry to local economic development which is useful in helping the government to formulate for the logistics industry and guide optimum configuration of resources in the logistics market.

From a micro perspective, logistics enterprises should properly configure limited resources according to the prediction of logistics requirements in order to minimize investment risks and maximize benefits. Thus, a scientific prediction of regional logistics requirements is a very important task.

ACKNOWLEDGMENTS

This work was supported by the National Natural Science Foundation of China (71573028); 2014 Liaoning BaiQianWan Talents Program (2014Q013); Liaoning Social Science Planning Fund Plan (L14CJY041); Liaoning Provincial Education Department (WJQ2015004); Dalian science and technology project (2015D21ZC001;2014D11ZC117); Program for Liaoning Excellent Talents in University (WJQ2015004); Dalian Jinzhou Science and technology project (RXYJ-RXSK-2015-002); Liaoning educational scientific research management think tank project (ZK2015090).

REFERENCES

1. Adolf K.Y. Ng, Flavio Padilha, Athanasios A. Pallis, (2013). Institutions, bureaucratic and logistical roles of dry ports: the Brazilian experiences [J] Journal of Transport Geography, Vol. 27, No. 2, Pages 46–55, 2013.
2. Andrawis, R. R., Atiya, A. F., El-Shishiny, H., (2011).

- Combination of long term and short term forecasts, with application to tourism demand forecasting [J] *International Journal of Forecasting*, Vol. 27, Pages 870–886, 2011.
3. Anna, B., Maurizio, C., Claudio, F., Alessio T., (2014). Ports and regional development: A spatial analysis on a panel of European regions [J] *Transportation Research Part A: Policy and Practice*, Vol. 65, Pages 44-55, 2014.
 4. Babai, M.Z., Ali, M., Nikolopoulos, K., (2012). Impact of temporal aggregation on stock control performance of intermittent demand estimators: empirical analysis. [J] *International Journal of Management Science*, Vol. 40, Pages 713–721, 2012.
 5. Bacchetti, A., Saccani, N., (2012). Spare parts classification and demand forecasting for stock control: investigating the gap between research and practice [J] *International Journal of Management Science*, Vol. 40, Pages 722–737, 2012.
 6. Bandyopadhyay, S., Bhattacharya, R. (2013). A generalized measure of bullwhip effect in supply chain with ARMA demand process under various replenishment policies [J] *International Journal of Advance Manufacturing Technology*, Vol. 68, Pages 963–979, 2013.
 7. Briant, A., Combes, P.–P., Lafourcade, M., (2010). Dots to boxes: do the size and shape of spatial units jeopardize economic geography estimations? [J] *Urban Economics*, Vol. 67, No. 3, Page 287–302, 2010.
 8. Cang, S., Yu, H., (2014). A combination selection algorithm on forecasting [J] *European Journal of Operational Research*, Vol. 234, Pages 127–139, 2014.
 9. Chris Jacobs–Crisioni, Piet Rietveld, Eric Koomen, (2014). The impact of spatial aggregation on urban development analyses [J] *Applied Geography*, Vol. 47, Pages 46–56, 2014.
 10. Colin Wren, (2012). Geographic concentration and the temporal scope of agglomeration economies: an index decomposition [J] *Regional Science and Urban Economics*, Vol. 42, Issue 4, Pages 681–690, 2012.
 11. Crone, S. F., Hibon, M., Nikolopoulos, K., (2011). Advances in forecasting with neural networks? empirical evidence from the NN3 competition on time series prediction [J] *International Journal of Forecasting*, Vol. 27, Pages 635–660, 2011.
 12. David A. Hensher, Truong P. Truong, Corinne Mulley, Richard Ellison, (2012). Assessing the wider economy impacts of transport infrastructure investment with an illustrative application to the north–west rail link project in Sydney, Australia [J] *Journal of Transport Geography*, Vol. 24, No. 9, Pages 292–305, 2012.
 13. Dongya Li, Yi Lu, Mingqin Wu, (2012). Industrial agglomeration and firm size: evidence from China [J] *Regional Science and Urban Economics*, Vol. 42, Issues 1–2, Pages 135–143, 2012.
 14. Dixit, A.K., Stiglitz, J.E., (1977). Monopolistic competition and optimum product diversity [J] *American Economic Review*, Vol. 67, Pages 298–302, 1977.
 15. Echeverri–Carroll, E., Ayala, S.G., (2010). Gender wage differentials and the spatial concentration of high–technology industries [J] *Progress in Spatial Analysis*, Pages 287–309, 2010.
 16. Eric Nitzsche, Stefan Tscharaktschiew, (2013). Efficiency of speed limits in cities: a spatial computable general equilibrium assessment [J] *Transportation Research Part A: Policy and Practice*, Vol. 56, No. 10, Pages 23–48, 2013.
 17. Feo–Valero, M., García–Menéndez, L., Sáez–Carramolino, L., Furió–Pruñonosa, S., (2011). The importance of the inland leg of containerized maritime shipments: an analysis of modal choice determinants in Spain [J] *Transportation Research Part E*, Vol. 47, Pages 446–460, 2011.
 18. Frank P.van den Heuvel, Peter W.de Langen, Karel H.van Donselaar, Jan C.Fransoo, (2013). Regional logistics land allocation policies: stimulating spatial concentration of logistics firms [J] *Transport Policy*, Vol. 30, Pages 275–282, 2013.
 19. Frank, P., Liliana, R., Karel, H., Jong, A., Yossi, S., Peter, W., Jan, C., (2014). Relationship between freight accessibility and logistics employment in US counties [J] *Transportation Research Part A: Policy and Practice*, Vol. 59, Pages 91–105, 2014.
 20. Frémont, A., Franc, P., (2010). Hinterland transportation in Europe: combined transport versus road transport [J] *Journal of Transport Geography*, Vol. 18, No. 4, Pages 548–556, 2010.
 21. Fujita M, Krugman P., (2004). The new economic geography: Past, present and the future [J] *Regional Science*, Vol. 83, Pages 139–164, 2004.
 22. Garcia–Alonso, L., Sanchez–Soriano, J., (2010). Analysis of the evolution of the inland traffic distribution and provincial hinterland share of the Spanish port system [J] *Transport Reviews*, Vol. 30, No. 3, Pages 275–297, 2010.
 23. Gianmarco I.P. Ottaviano, (2012). Agglomeration, trade and selection [J] *Regional Science and Urban Economics*, Vol. 42, Issue 6, Pages 987–997, 2012.
 24. Hyok–Joo Rhee, Sanggyun Yu, Georg Hirte, (2014). Zoning in cities with traffic congestion and agglomeration economies [J] *Regional Science and Urban Economics*, Vol. 44, No. 1, Pages 82–93, 2014.

25. Ingrid Ott, Susanne Soretz, (2010). Productive public input, integration and agglomeration [J] *Regional Science and Urban Economics*, Vol. 40, Pages 538–549, 2010.
26. Lei Fan, William W. Wilson, Bruce Dahl, (2012). Congestion, port expansion and spatial competition for US container imports [J] *Transportation Research Part E: Logistics and Transportation Review*, Vol. 48, Issue 6, Pages 1121–1136, 2012.
27. Marufuzzaman, M., Eksioglu, S.D., Li, X.P., Wang, J., (2014). Analyzing the impact of intermodal-related risk to the design and management of biofuel supply chain [J] *Transportation Research Part E: Logistics and Transportation Review*, Vol. 69, Pages 122-145, 2014.
28. Tomasicchio, GR; D'Alessandro, F. Wave energy transmission through and over low crested breakwaters [J] *Journal of Coastal Research*. SI 65, Pages 398-403, 2013.
29. Zastempowski, M; Bochat, A. Mathematical modelling of elastic deflection of a tubular cross-section [J] *Polish Maritime Research*. Vol. 22(2), Pages 93-100, 2015.
30. Masahisa Fujita, Nobuaki Hamaguchi, (2001). Intermediate goods and the spatial structure of an economy [J] *Regional Science and Urban Economics*, Vol. 31, Issue 1, Pages 79–109, 2001.
31. Masahisa Fujita, Tomoya Mori, (1996). The role of ports in the making of major cities: self-agglomeration and hub-effect [J] *Development Economics*, Vol. 49, Pages 93–120, 1996.
32. Krugman, Paul, (1991). Increasing returns and economic geography [J] *Political Economy*, Vol. 99, Pages 483–499, 1991.

CONTACT WITH AUTHOR

Bo LU

Research center of electronic commerce
& modern logistics,
Xuefu road #10,
Dalian economic technological development zone,
116022, China.

E-mail: lubo_documents@hotmail.com

EXTENDED ELLIPTIC MILD SLOPE EQUATION INCORPORATING THE NONLINEAR SHOALING EFFECT

XIAO Qian-lu ^{a,b}

LI Chun-hui ^a

FU Xiao-yan ^a,

WANG Mei-ju ^a

^aKey Laboratory of Coastal Disaster and Defence, Ministry of Education, Hohai University, Nanjing, China;

^bCollege of Harbour, Coastal and Offshore Engineering, Hohai University, Nanjing, China

ABSTRACT

The transformation during wave propagation is significantly important for the calculations of hydraulic and coastal engineering, as well as the sediment transport. The exact wave height deformation calculation on the coasts is essential to near-shore hydrodynamics research and the structure design of coastal engineering. According to the wave shoaling results gained from the elliptical cosine wave theory, the nonlinear wave dispersion relation is adopted to develop the expression of the corresponding nonlinear wave shoaling coefficient. Based on the extended elliptic mild slope equation, an efficient wave numerical model is presented in this paper for predicting wave deformation across the complex topography and the surf zone, incorporating the nonlinear wave dispersion relation, the nonlinear wave shoaling coefficient and other energy dissipation factors. Especially, the phenomenon of wave recovery and second breaking could be shown by the present model. The classical Berkhoff single elliptic topography wave tests, the sinusoidal varying topography experiment, and complex composite slopes wave flume experiments are applied to verify the accuracy of the calculation of wave heights. Compared with experimental data, good agreements are found upon single elliptic topography and one-dimensional beach profiles, including uniform slope and step-type profiles. The results indicate that the newly-developed nonlinear wave shoaling coefficient improves the calculated accuracy of wave transformation in the surf zone efficiently, and the wave breaking is the key factor affecting the wave characteristics and need to be considered in the nearshore wave simulations.

Keywords: nonlinear dispersion relation; nonlinear shoaling coefficient; extended elliptic mild slope equation; surf zone; wave transformation

INTRODUCTION

Waves propagate from deep waters to shallow waters with wave heights changing due to shoaling, refraction, diffraction, reflection, bottom friction and breaking. The transformation above during wave propagation is significantly important for the calculations of hydraulic and coastal engineering, as well as the sediment transport. The breaking waves not only produce large forces on coastal structures but also give rise to near-shore currents which influence the beach topographies [5][10][15]. The exact wave height deformation calculation on the coasts is essential to near-shore hydrodynamics research

and the structure design of coastal engineering.

Wave numerical models based on mild slope equation involving breaking have been proposed by many scholars [3][6][8][11][16-17][19][21-23] and the commonly used method is a wave energy dissipation coefficient for wave breaking, which is applicable to arbitrary reflective boundary conditions. Watanabe and Maruyama applied the time dependent mild slope equation to simulate the wave transformation in the surf zone, and found that the wave height was underestimated at the breaking point when applying a linear wave shoaling coefficient. To overcome this shortcoming of the linear mild slope equation, Black and Rosenberg [17] raised a

semi-empirical formula, but it is difficult to calculate the combined wave transformation on the coasts. Shuto's empirical nonlinear shoaling equations is applied by Tsai[19] to deduce the wave shoaling coefficient and improve the mild slope equation, which produced better wave heights prediction but emerge restrictions when Ursell number is less than 30.

In this paper, the empirical nonlinear shoaling equations proposed by Shuto are utilized to develop the nonlinear wave shoaling coefficient corresponding to the nonlinear wave dispersion relation. The extended elliptic mild slope equation is modified with the nonlinear wave dispersion relation, the corresponding nonlinear wave shoaling coefficient, the wave frictional energy dissipation coefficient and the wave breaking energy loss coefficient to calculate the wave transformation in the complicated topographies and the surf zone. Compared with the linear wave model, the accuracy of the numerical calculations of modified wave model is improved and the computed wave heights under these topographies conform to the experimental results preferably.

WAVE DISPERSION RELATION

The nonlinear dispersion relation with higher precision could be expressed as[9]

$$\sigma^2 = gk(1 + p\varepsilon^2) \tanh(kh + q\varepsilon) \quad (1)$$

Where, σ is the frequency of wave, g is the acceleration of gravity, k is the wave number, h is the water depth and the parameters p , q and ε could be written as

$$p = \tanh(kh) \quad q = \left[\frac{kh}{\sinh(kh)} \right]^2 \quad \varepsilon = \frac{kH}{2} \quad (2)$$

Where H is the wave height. With simple transformations and arrangements, another form of eq.(1) could be expression as follow

$$L = \frac{gT^2(1 + p\varepsilon^2)}{2\pi} \tanh(kh + q\varepsilon) \quad (3)$$

Where L is the wave length and T is the wave period. According to the formula structure of eq. (3), when the ratio of water depth and wave length is larger than 0.5 or the wave belongs to the deep water wave, eq. (3) could be written as

$$L_0 = \frac{gT^2(1 + \varepsilon_0^2)}{2\pi} \quad (4)$$

Where, L_0 is the wave length in deep water and $\varepsilon_0 = k_0 H_0 / 2$. k_0 and H_0 are the wave number and the wave height in deep water, respectively. Combining eq. (3) and eq. (4), namely

$$L = L_0 \frac{1 + p\varepsilon^2}{1 + \varepsilon_0^2} \tanh(kh + q\varepsilon) \quad (5)$$

Dividing by the wave period T at both ends of eq.(5), the relational expression of the wave phase velocity C and C_0 in deep water could be indicated as

$$\frac{C}{C_0} = \frac{1 + p\varepsilon^2}{1 + \varepsilon_0^2} \tanh(kh + q\varepsilon) \quad (6)$$

On the basis of the definition of wave group velocity, the expression of wave group velocity would be written as

$$C_g = d\sigma / dk \quad (7)$$

Taking the derivative of the wave number for both ends of eq. (1), and substituting into eq. (7), the wave group velocity could be expressed as

$$C_g = \frac{C}{2} + \frac{2p\varepsilon^2 + kh\varepsilon^2 / \cosh^2(kh)}{1 + p\varepsilon^2} \frac{C}{2} + \frac{C}{\sinh(2kh + 2q\varepsilon)} [kh + q\varepsilon + \frac{2\varepsilon k^2 h^2}{\sinh^3(kh)} (\sinh(kh) - kh \cosh(kh))] \quad (8)$$

Adopting eq. (2) to simplify eq. (8) further, namely

$$C_g = \frac{C}{2} + \frac{2p\varepsilon^2 + hk\varepsilon^2(1 - p^2)}{1 + p\varepsilon^2} \frac{C}{2} + \frac{C}{2\sinh(2kh + 2q\varepsilon)} [kh + \varepsilon q(3 - \frac{2kh}{p})] \quad (9)$$

Then, the relational expression between wave group velocity C_g and the wave phase velocity C could be shown as

$$C_g = CN \quad (10)$$

Where, the ratio N could be written as

$$N = \frac{1}{2} + \frac{p\varepsilon^2 + hk\varepsilon^2(1 - p^2)/2}{1 + p\varepsilon^2} + \frac{1}{2\sinh(2kh + 2q\varepsilon)} [kh + \varepsilon q(3 - \frac{2kh}{p})] \quad (11)$$

When the wave locates in the deep water, eq. (11) could be simplified as

$$N = \frac{1}{2} + \frac{\varepsilon_0^2}{1 + \varepsilon_0^2} \quad (12)$$

WAVE ENERGY EQUATION

WAVE SHOALING EFFECT

Wave energy equation is the foundation of wave transformation calculation[4]. In the process of monochromatic wave propagation, one dimension steady energy equation could be given by [1]

$$\frac{d}{dx} (EC_g) = -NfE \quad (13)$$

Where, E is the wave energy per unit area of the water body, f is the coefficient of combined energy dissipation, and x is the horizontal axis of the Cartesian coordinate perpendicular to the coastline. The wave energy dissipation on the right-hand side of eq. (13) could be equal to zero if the energy was assumed without any loss, such as outside the surf zone[19]. According to the Airy wave theory, $E = \rho g H^2 / 8$ and the wave shoaling coefficient could be shown as

$$f_s = \frac{H}{H_0} = \sqrt{\frac{C_0}{2nC}} \quad (14)$$

Where, f_s is the wave shoaling coefficient and n is the ratio of wave group velocity and the wave phase velocity due to the linear dispersion relation. If applying the nonlinear dispersion relation eq. (1), combining eq. (1) with eq. (13), yields

$$\frac{1}{8} \rho g H_0^2 C_0 \left(\frac{1}{2} + \frac{\varepsilon_0^2}{1 + \varepsilon_0^2} \right) = \frac{1}{8} \rho g H^2 C N \quad (15)$$

After further arrangement, namely

$$f_s = \frac{H}{H_0} = \sqrt{C_0 \left(\frac{1}{2} + \frac{\varepsilon_0^2}{1 + \varepsilon_0^2} \right) / CN} \quad (16)$$

Substituting eq. (11) into eq. (16), the wave shoaling coefficient in the linear wave shoaling theory with nonlinear dispersion relation could be expressed as

$$f_s = \sqrt{C_0 \left(\frac{1}{2} + \frac{\varepsilon_0^2}{1 + \varepsilon_0^2} \right) / CN} = \sqrt{\left(\frac{1}{2} + \frac{\varepsilon_0^2}{1 + \varepsilon_0^2} \right) \frac{1 + \varepsilon_0^2}{N(1 + p\varepsilon^2) \tanh(kh + q\varepsilon)}} \quad (17)$$

Thus the liner wave shoaling conclusion proposed by Shuto can be evolved as

$$\left\{ \begin{array}{l} \frac{H}{H_0} = \sqrt{\left(\frac{1}{2} + \frac{\varepsilon_0^2}{1 + \varepsilon_0^2} \right) \frac{1 + \varepsilon_0^2}{N(1 + p\varepsilon^2) \tanh(kh + q\varepsilon)}} \quad U_r \leq 30 \\ Hh^{\frac{2}{7}} = const. \quad 30 < U_r \leq 50 \\ Hh^{\frac{5}{2}} (\sqrt{U_r} - 2\sqrt{3}) = const. \quad U_r > 50 \end{array} \right. \quad (18)$$

Based on the relational expressions as follow

$$\frac{d}{dx}(EC_g) = \frac{d}{dh}(EC_g) \frac{dh}{dx} = -\frac{d}{dh}(EC_g) \tan \beta_{po} = -f_s k (EC_g) \quad (19)$$

Combining eq. (10), eq. (13) and eq. (19), the expression of wave shoaling coefficient could be shown as

$$f_s = \left(\frac{dC}{dh} + \frac{C}{N} \frac{dN}{dh} + \frac{C}{E} \frac{dE}{dh} \right) \tan \beta_{po} \quad (20)$$

Where, β_{po} is the bottom slope along the wave transformation direction. Namely, the solution of eq. (20) is the derivation of three differential terms expressed by the wave characteristics.

In eq. (20), the derivative of wave velocity C with respect to the water depth h could be shown as

$$\frac{dC}{dh} = \frac{d}{dh} \left(\frac{\sigma h}{kh} \right) = \frac{\sigma kh - \sigma h \frac{d(kh)}{dh}}{(kh)^2} \quad (21)$$

Due to the nonlinear dispersion relation equation (1), yields

$$\sigma^2 = g(1 + p\varepsilon^2) \tanh(kh + q\varepsilon) \frac{\partial(kh)}{\partial h} + gkh \tanh(kh + q\varepsilon) \frac{\partial(1 + p\varepsilon^2)}{\partial h} + gkh(1 + p\varepsilon^2) \frac{\partial[\tanh(kh + q\varepsilon)]}{\partial h} \quad (22)$$

Expanding and arranging the derivatives of composite functions in eq. (22), namely

$$\frac{\partial(kh)}{\partial h} + \frac{1}{1 + p\varepsilon^2} (2p\varepsilon^2 + \frac{kh\varepsilon^2}{\cosh^2(kh)}) \frac{\partial(kh)}{\partial h} + \frac{2}{\sinh(2kh + 2q\varepsilon)} [kh + q\varepsilon + \frac{2\varepsilon(kh)^2}{\sinh^3(kh)}] \frac{\partial(kh)}{\partial h} = k + \frac{2kp\varepsilon^2}{1 + p\varepsilon^2} + \frac{2kq\varepsilon}{\sinh(2kh + 2q\varepsilon)} \quad (23)$$

Combining eq. (11) and eq. (23), the derivative of kh could be written as

$$\frac{d(kh)}{dh} = \frac{k}{2N} + \frac{kp\varepsilon^2}{(1 + p\varepsilon^2)N} + \frac{kq\varepsilon}{N \sinh(2kh + 2q\varepsilon)} \quad (24)$$

Substituting eq. (24) into eq. (21), yields

$$\frac{dC}{dh} = \frac{C}{h} \left[1 - \frac{1}{2N} - \frac{p\varepsilon^2}{(1 + p\varepsilon^2)N} - \frac{q\varepsilon}{N \sinh(2kh + 2q\varepsilon)} \right] \quad (25)$$

In eq. (20), the derivative of ratio N with respect to the water depth h could be shown as

$$\frac{dN}{dh} = \frac{1}{2(1 + p\varepsilon^2)^2} [(1 + p\varepsilon^2) \frac{\partial}{\partial h} (2p\varepsilon^2 + \frac{kh\varepsilon^2}{\cosh^2(kh)}) - (2p\varepsilon^2 + \frac{kh\varepsilon^2}{\cosh^2(kh)}) \frac{\partial}{\partial h} (1 + p\varepsilon^2)] + \frac{1}{\sinh^2(2kh + 2q\varepsilon)} [\sinh(2kh + 2q\varepsilon) \frac{\partial}{\partial h} (kh + q\varepsilon + \frac{2\varepsilon k^2 h^2}{\sinh^3(kh)} (\sinh(kh) - kh \cosh(kh))) - (kh + q\varepsilon + \frac{2\varepsilon k^2 h^2}{\sinh^3(kh)} (\sinh(kh) - kh \cosh(kh))) \frac{\partial}{\partial h} (\sinh(2kh + 2q\varepsilon))] \quad (26)$$

Expanding and arranging the derivatives of composite functions in eq. (26), namely

$$\frac{dN}{dh} = K_{w1} \frac{d(kh)}{dh} + K_{w2} \quad (27)$$

Where, the parameter K_{w1} could be written as

$$K_{w1} = \frac{1}{1 + p\varepsilon^2} \left[\frac{2p\varepsilon^2 - p^3 q\varepsilon + (\varepsilon + \varepsilon^2) p^2 q}{kh} - \frac{[2p\varepsilon^2 + \varepsilon^2 p^2 q / (kh)]^2}{2kh(1 + p\varepsilon^2)^2} + \frac{1}{\sinh(2kh + 2q\varepsilon)} (1 - \frac{14q\varepsilon}{p} + \frac{9q\varepsilon}{kh} - 2qkxh + \frac{kh}{p^2}) - \frac{2 \cosh(2kh + 2q\varepsilon)}{\sinh^2(2kh + 2q\varepsilon)} (1 + \frac{3q\varepsilon}{kh} - \frac{2q\varepsilon}{p}) (kh + 3q\varepsilon - \frac{2kh\varepsilon}{p}) \right] \quad (28)$$

And the parameter K_{w2} could be written as

$$K_{w2} = \frac{-1}{1+p\epsilon^2} \left[\frac{2p\epsilon^2}{h} + \frac{\epsilon q p^2}{2kh} \right] + \frac{[2p\epsilon^2 + \epsilon^2 p^2 q / (kh)] p \epsilon^2}{h(1+p\epsilon^2)^2} - \frac{1}{\sinh(2kh+2q\epsilon)} \left(\frac{q\epsilon}{kh} + 2q\epsilon \frac{p-kh}{p} \right) + \frac{2q\epsilon \cosh(2kh+2q\epsilon)}{\sinh^2(2kh+2q\epsilon)} (kh+q\epsilon+2q\epsilon \frac{p-kh}{p}) \quad (29)$$

On the basis of eq. (5), the relational expression of the wave numbers in the coasts and in deep waters could be expressed as

$$k_0 / k = \frac{1+p\epsilon^2}{1+\epsilon_0^2} \tanh(kh+q\epsilon) \quad (30)$$

Substituting eq. (30) into eq. (27), the parameters K_{w1} and K_{w2} could be written respectively as

$$K_{w1} = \frac{1}{1+p\epsilon^2} \left[\frac{2p\epsilon^2 - p^3 q \epsilon}{kh} + \frac{(\epsilon + \epsilon_0^2) p^2 q}{k^2 h^2} - \frac{[2p\epsilon^2 + \epsilon^2 p^2 q / (kh)]^2}{2kh(1+p\epsilon^2)^2} \right] + \left(1 - \frac{14q\epsilon}{p} + \frac{9q\epsilon}{kh} - 2q\epsilon kh + \frac{kh}{p^2} \right) \frac{k_0(1+\epsilon_0^2)}{2k(1+p\epsilon^2)\sinh^2(kh+q\epsilon)} - \frac{k_0^2(1+\epsilon_0^2)^2 + k^2(1+p\epsilon^2)^2}{2k^2(1+p\epsilon^2)^2 \sinh^2(kh+q\epsilon)} \left(1 + \frac{3q\epsilon}{kh} - \frac{2q\epsilon}{p} \right) (kh+3q\epsilon - \frac{2kh\epsilon}{p}) \quad (31)$$

$$K_{w2} = \frac{-1}{1+p\epsilon^2} \left[\frac{2p\epsilon^2}{h} + \frac{\epsilon q p^2}{2kh} \right] + \frac{[2p\epsilon^2 + \epsilon^2 p^2 q / (kh)] p \epsilon^2}{h(1+p\epsilon^2)^2} - \frac{k_0(1+\epsilon_0^2)}{2k(1+p\epsilon^2)\sinh^2(kh+q\epsilon)} \left(\frac{q\epsilon}{kh} + 2q\epsilon \frac{p-kh}{p} \right) + (kh+q\epsilon+2q\epsilon \frac{p-kh}{p}) \frac{q\epsilon [k_0^2(1+\epsilon_0^2)^2 + k^2(1+p\epsilon^2)^2]}{2k^2(1+p\epsilon^2)^2 \sinh^2(kh+q\epsilon)} \quad (32)$$

In eq. (20), the derivative of wave energy E with respect to the water depth could be shown as

$$\frac{C}{E} \frac{dE}{dh} = \frac{C}{H^2} \frac{d(H^2)}{dh} \quad (33)$$

According to eq. (19), the expression of wave height is $H_s \sqrt{\frac{1+\epsilon_0^2}{2} \frac{1+\epsilon_0^2}{1+\epsilon_0^2} \frac{1+\epsilon_0^2}{N(1+p\epsilon^2)\tanh(kh+q\epsilon)}}$ when the Ursell number is no larger than 30, and eq. (33) could be shown as

$$\frac{C}{E} \frac{dE}{dh} = \frac{C}{H^2} \frac{d(H^2)}{dh} = -\frac{dC}{dh} - \frac{C}{N} \frac{dN}{dh} \quad (34)$$

When value range of the Ursell number is $30 < U_r \leq 50$, $H = C_{w1} h^{-2/7}$ and C_{w1} is the coefficient. Namely,

$$\frac{C}{E} \frac{dE}{dh} = \frac{C}{H^2} \frac{d(H^2)}{dh} = -\frac{4}{7} \frac{C}{h} \quad (35)$$

When the Ursell number is larger than 50, $Hh^{5/2}(\sqrt{U_r} - 2\sqrt{3}) = C_{w2}$ and C_{w2} is the coefficient. Substituting the expression of the Ursell number, $U_r = gHT^2 / h^2$, into the relational expression of wave height, yields

$$Hh^{5/2} (T\sqrt{gH} / h - 2\sqrt{3}) = C_{w2} \quad (36)$$

Taking the derivative of the water depth h for both ends of eq. (36), then

$$\frac{3}{2} H^2 h^{3/2} T g^{1/2} \frac{1}{dh} \frac{dH}{dh} + \frac{3}{2} H^2 h^{1/2} T g^{1/2} - 2\sqrt{3} (h^2 \frac{dH}{dh} + \frac{5}{2} h^{3/2}) = 0 \quad (37)$$

After the arrangement, eq. (37) could be transformed as

$$\frac{dH}{dh} = -\frac{H}{h} \frac{1.5\sqrt{U_r} - 5\sqrt{3}}{1.5\sqrt{U_r} - 2\sqrt{3}} \quad (38)$$

Substituting eq. (38) into eq. (34), yields

$$\frac{C}{E} \frac{dE}{dh} = -\frac{C}{h} \frac{3\sqrt{U_r} - 10\sqrt{3}}{1.5\sqrt{U_r} - 2\sqrt{3}} \quad (39)$$

Combining eq. (25), eq. (27), eq. (34), eq. (35), eq. (39) with eq. (20), the wave nonlinear shoaling coefficient corresponding to the wave nonlinear dispersion relation raised by Li et al. [13] could be expressed as

$$f_s = \begin{cases} 0 & U_r \leq 30 \\ \left(\frac{C}{h} \right) \left[\frac{3}{7} - \frac{K_{w3}}{k} + \frac{hK_{w3}K_{w1}}{N} + \frac{hK_{w2}}{N} \right] \tan \beta & 30 < U_r \leq 50 \\ \left(\frac{C}{h} \right) \left[\frac{-4.5\sqrt{U_r} - 12\sqrt{3}}{1.5\sqrt{U_r} - 2\sqrt{3}} + \frac{h(K_{w3}K_{w1} + K_{w2})}{N} - \frac{K_{w3}}{k} \right] \tan \beta & U_r > 50 \end{cases} \quad (40)$$

Where, the parameters K_{w1} and K_{w2} could be expressed as eq. (31) and eq. (32), respectively. The parameter K_{w3} could be written as

$$K_{w3} = \frac{k}{2N} + \frac{kp\epsilon^2}{(1+p\epsilon^2)N} + \frac{kq\epsilon}{N \sinh(2kh+2q\epsilon)} \quad (41)$$

Eq. (40) would be adopted as the wave shoaling coefficient by the extended elliptic mild slope equation in this paper.

WAVE BREAKING EFFECT

The breaking index considering the bottom slope is following [15]

$$\xi_o = \frac{\tan \beta_{po}}{\sqrt{H_o / L_o}} \quad (42)$$

$$\xi_b = \frac{\tan \beta_{po}}{\sqrt{H_b / L_o}} \quad (43)$$

$$\begin{aligned} \xi_b \geq 2.0 & \quad \text{Or} \quad \xi_o \geq 3.3 & \quad \text{surging breaking} \\ 0.4 \leq \xi_b < 2.0 & \quad \text{Or} \quad 0.5 \leq \xi_o < 3.3 & \quad \text{plunging breaking} \\ \xi_b < 0.4 & \quad \text{Or} \quad \xi_o < 0.5 & \quad \text{spilling breaking} \end{aligned} \quad (44)$$

Based on the convenience of programming and the distinct classification, the breaking index proposed by Battjes

would be adopted in the mild slope equation in this paper. The hydraulic jump model is used to compute the energy loss after the wave breaks. Subscribing the index above into wave energy equation, we can get the wave breaking energy dissipation coefficients:

$$d(EC_g)/dx = -0.01875\rho g(H^2\sqrt{gh} - 0.16h^2\sqrt{gh})/h \quad (45)$$

$$f_d = \frac{0.15}{kh} \left(1 - \frac{0.04}{\gamma_a^2}\right) \quad (46)$$

WAVE FRICTIONAL EFFECT

In the most coasts, the energy dissipation produced by the bed frictions would be the primary cause compared with those by the permeability loss and the mud surface wave resistance loss.

According to the wave boundary layer theory, the work of the bed friction could be indicated as

$$D_f = f_b k (EC_g) \quad (47)$$

Where, D_f is the unit bed surface energy loss and f_b is the wave frictional energy dissipation coefficient. And the unit bed surface energy loss could be shown as

$$D_f = \overline{U_b \tau_b} = \frac{1}{T} \int_0^T \frac{1}{2} \rho f_w U_b^2 |U_b| dt = \frac{1}{2} \rho f_w U_{bm}^3 \left(\frac{1}{T} \int_0^T |\cos^3(\sigma)| dt\right) \quad (48)$$

Where $U_b = U_{bm} \cos(kx - \sigma) = A_m \sigma \cos(kx - \sigma) = (\pi H / T \sinh(kh)) \cos(kx - \sigma)$. Combing eq. (47) and eq. (48), yields

$$D_f = \frac{2\pi^2}{3} \rho f_w \frac{H^3}{T^3 \sinh^3(kh)} \quad (49)$$

$$f_b = \frac{2f_w}{3\pi} \frac{H\sigma^2}{Ng \sinh^3(kh)} \quad (50)$$

Eq. (50) would be adopted in this paper for the wave energy dissipation due to the bed frictions.

THE WAVE MODEL BASED ON EXTENDED ELLIPTIC MILD SLOPE EQUATION

The extended elliptic mild slope equation involving the energy dissipation stated above is applied to calculate the wave transformation. The governing equation of the extended elliptic mild slope equation [11] could be expressed as

$$\nabla(CC_g \nabla \Phi) + k^2 CC_g (1 + if) \Phi + [f_1 g \nabla^2 h + f_2 (\nabla h)^2 g k] \Phi = 0 \quad (51)$$

Where

$$f_1 = \frac{-4kh \cosh(kh) + \sinh(3kh) + \sinh(kh) + 8(kh)^2 \sinh(kh)}{8 \cosh^3(kh) [2kh + \sinh(2kh)]} - \frac{kh \tanh(kh)}{2 \cosh^2(kh)} \quad (52a)$$

$$f_2 = \frac{\sec^2(kh)}{6[2kh + \sinh(2kh)]^3} [8(kh)^4 + 16(kh)^3 \sinh(2kh) - 9 \sinh^2(2kh) \cosh(2kh) + 12(kh)(1 + 2 \sinh^4(kh))(kh + \sinh(2kh))] \quad (52b)$$

Where $\nabla = (\partial/\partial x, \partial/\partial y)$ is the horizontal operator; Φ is the velocity potential function of the harmonic wave; ∇ and ∇^2 are the bottom slopes and bottom curvatures in the x and y directions, respectively; and x and y are the two horizontal coordinates; $f = f_s + f_d + f_b$ is the combined energy dissipation factor, and f_s , f_b and f_d are calculated with eq.(41), eq.(49-1) and eq.(56) respectively. The nonlinear wave dispersion relation is adopted with eq. (1).

In order to verify the present model and test the computational accuracy, the classical and the slope flume experiments would be used including the Berkhoff single elliptical topography, sinusoidal varying topography, and uniform slope and composite slopes topography tests in the flume. In terms of reflecting the modification, the computed values of RIDE model established by Maa et al.[11], which adopted the linear wave theory, would be used to contrast with the present model.

BERKHOFF SINGLE ELLIPTICAL TOPOGRAPHY

Berkhoff et al.[2] conducted the wave propagating and transforming experiment on the ideal uniform slope topography with a single ellipse, and obtained the measured data of eight cross sections. In the numerical simulation, the height of incident wave is 0.0232 m, the period is 1.0 s and the direction is along the positive coordinate. The comparisons among computed values of the linear wave model of Maa et al., calculated results of the present model and experimental data in the cross section 1# ~ 8# are shown in Fig.2. The horizontal coordinate is the cross section, and the vertical coordinate is the ratio of local wave height and incident wave height. The black solid points in Fig.2 represent the experimental wave height data, the black dashed lines represent computed values of the linear wave model of Maa et al. and the black solid lines represent the calculated results of the present wave model. On the basis of the contrasts in Fig.2, although there are some obvious deviations in some locations, such as the significant error at 17m nearby in the 7# cross section, yet the calculated results of the present model coincide to the experimental results overall and the computed precision is preferable than the linear wave model of Maa et al.. Fig.3 shows the contrast about the computed wave height distribution fields between the linear wave model of Maa et al. and the present model. And the left figures are the computed values of the linear wave model of Maa et al., and the right figures are the calculated results of the present model. Based on the comparison of wave height distribution field, the calculated results of the present model make the wave energy more disperse after the single ellipse.

The calibrations indicate that the nonlinear wave dispersion relation and the corresponding wave shoaling coefficient in the present model are able to improve the wave refraction and diffraction effects apparently under the complex topography.

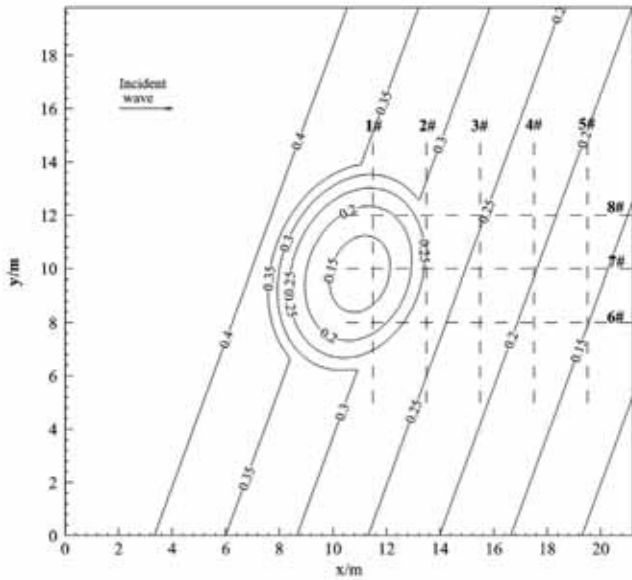


Fig. 1. The single elliptical topography and arrangement of cross sections

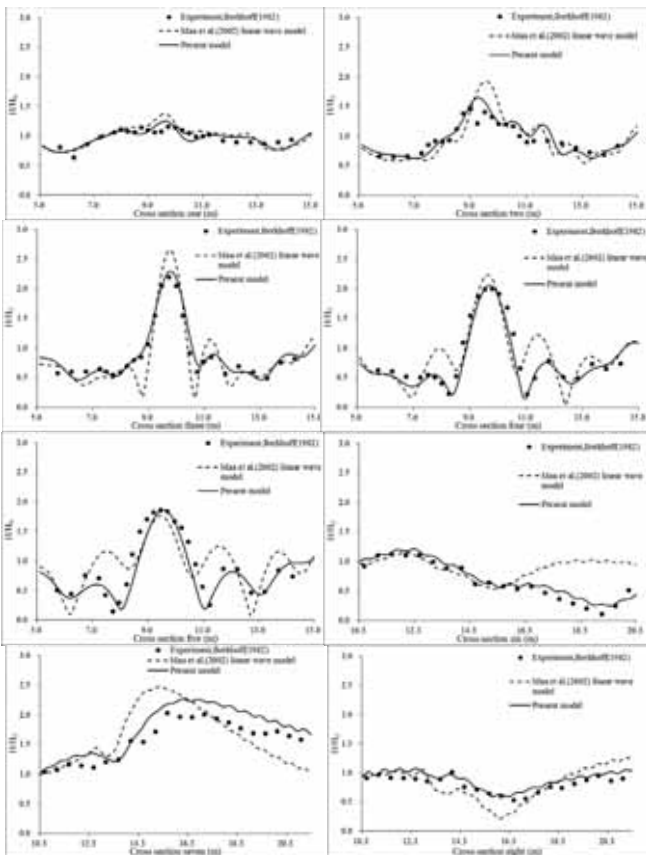


Fig. 2. Compared computed values of the linear wave model of Maa et al. and calculated results of the present model with experimental wave height data in the eight different cross sections

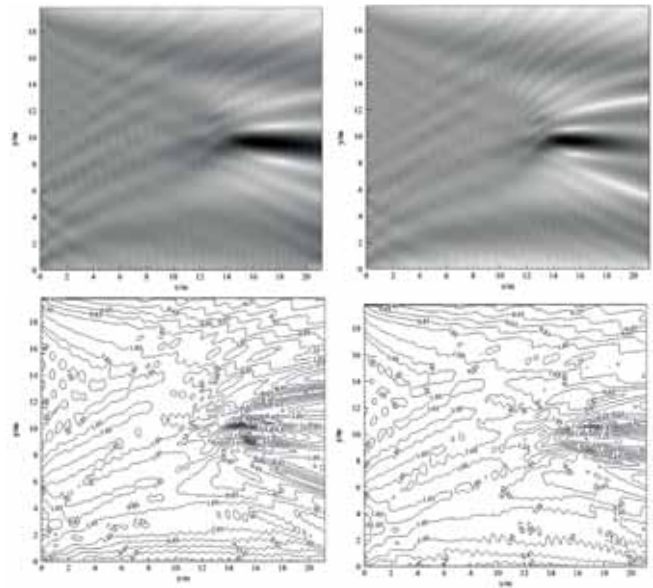


Fig. 3. Compared computed wave height distribution field of the linear wave model of Maa et al. (left) with calculated wave height distribution field of the present model (right)

SINUSOIDAL VARYING TOPOGRAPHY

Davies and Heathershaw[20] carried out a series of experimental research on the wave transformation under various sand ripple numbers and water depth conditions. The wave situation with ten sand ripples is simulated by the present model. In the numerical simulation, the wave height of incident wave is 0.02 m, the period is 1.31 s, and the direction is along the positive coordinate. The fully absorbing condition is situated at $x = 30$ m. The comparisons between observed data and computed values under sinusoidal sand ripples terrain are listed in Fig.5. The horizontal coordinate is the distance from the wave incident position, and the vertical coordinate is the wave amplitude of local wave (Half of local wave height). The black solid points in Fig.5 represent the observed wave amplitude data, and the black solid lines represent the calculated results of established wave models. In the light of the verifications in Fig.5, the calculated results of the wave mathematical model could coincide to the experimental data generally, and is capable of reflecting the tendency of wave deformation under the sinusoidal varying topography.

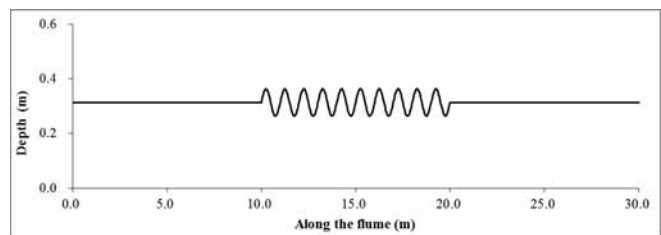


Fig. 4. Sinusoidal varying topography profile when ripple wavenumber equals to ten

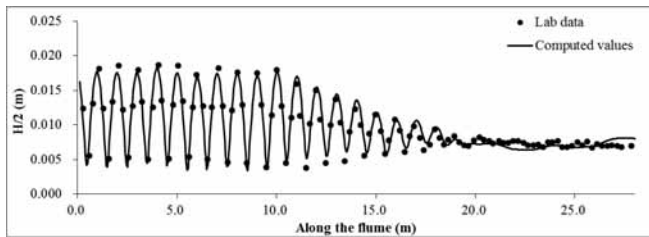


Fig. 5. Compared experimental wave height data observed in the flume with computed values of the present model

COMPOSITE SLOPES TOPOGRAPHY

The wave transformation experiment under the complex bar-type beach profile caught out by Nagayama[12] is applied to verify the present model, the topography profile is shown in Fig.6(a). The wave height of incident wave is 0.07 m, and the wave period is 1.18s. The numerical results of the present model are compared with the computed values of the linear wave model of Maa et al. and the experimental data, which are shown in Fig.6(b). Both the solution of the linear wave model of Maa et al. and the present model predict a second wave breaking at the tailing section of the 1/20 slope. For under this bar-type topography, the wave deformation includes the wave shoaling effect, wave frictional effect, wave decaying effect, wave recovery and the second breaking. It is found that the present model is in better agreement with the experimental results and of higher accuracy.

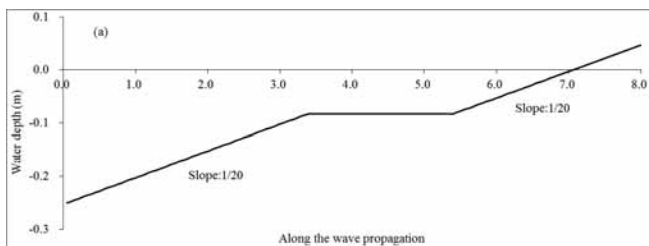


Fig. 6(a). Composite slopes topography profile with fronting and tailing slope 1/20

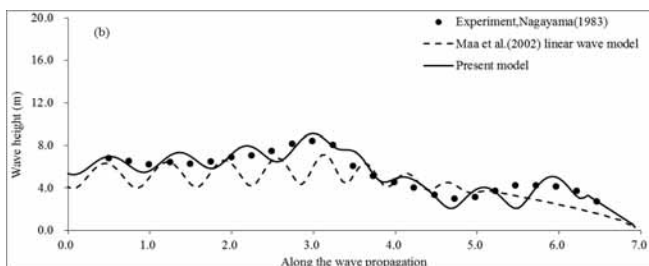


Fig. 6(b). Compared computed values of the linear wave model of Maa et al. and calculated results of the present model with experimental wave height data along the wave propagation

CONCLUSION

The mild slope equation models applied in this paper have contained various modifications for the computations of combined wave shoaling, refraction, diffraction, reflection, bottom friction and breaking. In the surf zone, linear wave

dispersion relation and linear wave shoaling coefficient have been adopted to improve the accuracy of wave height calculation. To overcome the error of the linear dispersion relation, the empirical nonlinear shoaling relation equations are utilized to develop the nonlinear wave shoaling coefficient corresponding to the nonlinear wave dispersion relation. The extended elliptic mild slope equation is modified with the nonlinear wave dispersion relation, the corresponding deduced nonlinear wave shoaling coefficient, the wave frictional energy dissipation coefficient and the wave breaking energy loss coefficient to calculate the wave transformation in the complicated topographies and the surf zone. The Berkhoff classical single elliptic topography experiment, some uniform slope and composite slope flume tests are applied to verify the modified wave model, and the calculated results coincide to the experimental data overall.

ACKNOWLEDGEMENTS

This work was supported by the Foundation of Jiangsu Province in China ordinary graduate student research innovation project for 2015(Grant No. KYZZ15_0143).

REFERENCES

1. Akbarpour Jannat, M. R., & Asano, T. (2007). External forces of sediment transport in surf and swash zones induced by wave groups and their associated long waves. *Coastal Engineering Journal*, 49(02), 205-227.
2. Berkhoff, J. C. W., Booy, N., & Radder, A. C. (1982). Verification of numerical wave propagation models for simple harmonic linear water waves. *Coastal Engineering*, 6(3), 255-279.
3. Cerrato, A., González, J. A., & Rodríguez-Tembleque, L. (2016). Boundary element formulation of the Mild-Slope equation for harmonic water waves propagating over unidirectional variable bathymetries. *Engineering Analysis with Boundary Elements*, 62, 22-34.
4. Chang, G., Ruehl, K., Jones, C. A., Roberts, J., & Chartrand, C. (2016). Numerical modeling of the effects of wave energy converter characteristics on nearshore wave conditions. *Renewable Energy*, 89, 636-648.
5. Chella, M. A., Bihs, H., Myrhaug, D., & Muskulus, M. (2015). Hydrodynamic characteristics and geometric properties of plunging and spilling breakers over impermeable slopes. *Ocean Modelling*.
6. Hamidi, M. E., Hashemi, M. R., Talebbeydokhti, N., & Neill, S. P. (2012). Numerical modelling of the mild slope equation using localised differential quadrature method. *Ocean Engineering*, 47, 88-103.

7. [7] Korotkevich, A. O., Dyachenko, A. I., & Zakharov, V. E. (2016). Numerical simulation of surface waves instability on a homogeneous grid. *Physica D: Nonlinear Phenomena*, 321, 51-66.
8. [8] Lin, X., & Yu, X. (2015). A finite difference method for effective treatment of mild-slope wave equation subject to non-reflecting boundary conditions. *Applied Ocean Research*, 53, 179-189.
9. Li, R. J., Zhang, Y., & Gao, H. S. (2004). A wave nonlinear dispersion relation and its application. *Ocean Eng./Haiyang Gongcheng*, 22(3), 20-24.
10. Lupieri, G., & Contento, G. (2015). Numerical simulations of 2-D steady and unsteady breaking waves. *Ocean Engineering*, 106, 298-316.
11. Maa, J. Y., Hsu, T. W., & Lee, D. Y. (2002). The RIDE model: an enhanced computer program for wave transformation. *Ocean Engineering*, 29(11), 1441-1458.
12. Nagayama, S. (1983). Study on the change of wave height and energy in the surf zone. Bachelor thesis, Yokohama National University, Japan (in Japanese).
13. Rincon, M. A., & Quintino, N. P. (2016). Numerical analysis and simulation for a nonlinear wave equation. *Journal of Computational and Applied Mathematics*, 296, 247-264.
14. Salmon, J. E., & Holthuijsen, L. H. (2015). Modeling depth-induced wave breaking over complex coastal bathymetries. *Coastal Engineering*, 105, 21-35.
15. Salmon, J. E., Holthuijsen, L. H., Zijlema, M., van Vledder, G. P., & Pietrzak, J. D. (2015). Scaling depth-induced wave-breaking in two-dimensional spectral wave models. *Ocean Modelling*, 87, 30-47.
16. Sharma, A., Panchang, V. G., & Kaihatu, J. M. (2014). Modeling nonlinear wave-wave interactions with the elliptic mild slope equation. *Applied Ocean Research*, 48, 114-125.
17. Stockdon, H. F., Holman, R. A., Howd, P. A., & Sallenger, A. H. (2006). Empirical parameterization of setup, swash, and runup. *Coastal engineering*, 53(7), 573-588.
18. Thompson, D. A., Karunarathna, H., & Reeve, D. (2016). Comparison between wave generation methods for numerical simulation of bimodal seas. *Water Science and Engineering*, 9(1), 3-13.
19. Tsai, C. P., Chen, H. B., Hwung, H. H., & Huang, M. J. (2005). Examination of empirical formulas for wave shoaling and breaking on steep slopes. *Ocean Engineering*, 32(3), 469-483.
20. Yu, J., & Zheng, G. (2012). Exact solutions for wave propagation over a patch of large bottom corrugations. *Journal of Fluid Mechanics*, 713, 362-375.
21. Zhao, L., Panchang, V., Chen, W., Demirbilek, Z., & Chhabbra, N. (2001). Simulation of wave breaking effects in two-dimensional elliptic harbor wave models. *Coastal Engineering*, 42(4), 359-373.
22. Yoon, BI; Woo, SB. (2013). Tidal asymmetry and flood/ebb dominance around the Yeomha channel in the Han River Estuary, South Korea. *Journal of coastal research*, 65, 1242-1246.
23. Chen, M; Han, DF. (2015). Multi-grid model for crowd's evacuation in ships based on cellular automata. *Polish maritime research*, 22(1), 75-81.

HEATING CONTROL OF HEATED TWIN RADIOSONDE HUMIDITY SENSOR BASED ON DMC

SUN Ning^{a,b}
ZHANG Ying-chao^{a,b}
ZHANG Wei-guo^a
CHENG En-lu^a
LIU Yun-ping^{a,b}

^aKey Laboratory of Meteorological Disaster of Ministry of Education,
Nanjing University of Information Science and Technology, Nanjing, China

^bSchool of Information and Control.

Collaborative Innovation Center on Forecast and Evaluation of Meteorological Disasters,
Nanjing University of Information Science and Technology, Nanjing, China

ABSTRACT

In order to effectively solve condensation and icing problems of radiosonde in low-temperature environment at high altitude, humidity sensor heated automatic alternately to remove pollution and improve the measurement accuracy. Heat experiments obtained the curve of rising temperature and responsible time on heated twin humidity sensor in normal temperature and pressure, by expanded responsible curve to obtain heated model of twin heated humidity sensor and by the analysis of heating model, use DMC and PID control for heating respectively. Simulation results show that the DMC control meets the practical requirements of measure at high altitude.

Keywords: DMC; twin heated humidity sensor; expanded responsible curve; Heating Control

INTRODUCTION

Altitude humidity with height has greater spatial resolution, sounding humidity sensor should have a high sensitivity, response speed, small size and other characteristics [1]. The humidity sensor is susceptible to clouds, rain and other humid hypothermia environments. Especially, when encountering with cold water, it prone to be frozen, thus, the measurement of humidity is likely influenced. Conventional approach is to heat the radiosonde humidity sensor to eliminate environmental impacts during the process of rising [2].

PID control method is widely used in process control because of its simple and reliable principle, as well as advantages like astatic property and cheap price. Meanwhile, it is a relatively mature classic controller [6-8]. However, this

system is based on a non-linear model (saturated, latency, backlash, etc.), and its uncertainty makes it difficult to achieve an expected result under certain conditions. Moreover, traditional PID control algorithm is difficult to predict the effect of control. Disadvantages like low control accuracy and poor robustness also exists [9-11]. Fuzzy control is flexible and adaptable because it does not require accurate mathematical model of the object. However, regardless the types of pure fuzzy controller, every controller is essentially a non-linear PD control that actually does not play an integral role in controlling. Sometimes the control process is not smooth, and the steady-state error is also hard to be reduced to a desired level [12-16].

Dynamic Matrix Control (DMC) is a predictive control algorithm based on the step response of the object, which is suitable for asymptotic stability of linear objects, in a rolling optimization and online error correction to ensure the control of accuracy and the parameter, environmental change of robustness. The whole algorithm includes a predictive model, rolling optimization and feedback correction [12-14]. It is directly based on the model of the step response of the object, thus can avoid parameter identification in the usual transfer function or state space equation model. DMC is a kind of optimal control technology because this control algorithm can effectively solve problems of delay process by using multi-step predictive value technology. Meanwhile, according to the predictive value of output with a given value of minimum deviation of the quadratic performance index is implemented to control. It has the advantages of simple algorithm, small computational amount and strong robustness, which can be applied to the stability of linear systems. In addition, the dynamic characteristics of the system with pure lag or non-minimum phase are not affected by the direct application of the algorithm [17-21]. For resolving issues related to rain (cloud) drops soaked, freezing and other conditions that causing the humidity sensor to detect inaccurate moisture signals, a dual heating radiosonde humidity sensor was proposed in this paper based on the traditional heating control method, which effectively reduces the impact of humidity measurement accompanied with external environment [22-29].

THE OUTLINE OF HEATING PRINCIPLE

System's humidity sensor uses humicap to measure. The main advantages of Humicap includes high sensitivity, fast response, low hysteresis humidity, etc. In the upper-air sounding, when the ambient temperature is below -30 °C, water diffusion becomes quite difficult to film in the humidity, as a result, the response speed and accuracy will be reduced. The principle diagram of dual heat humidity sensor heating is given in Figure 1, which is constituted by four layers including the measuring humidity level, the measuring temperature level, the heating level and the substrate level. The dual heated humidity sensor consists of two humidity sensors with humidity sensors automatically rotate two alternate work. When humidity sensor A is heating, sensor B measures the humidity. When A completed the heating to measure, B switch heated.

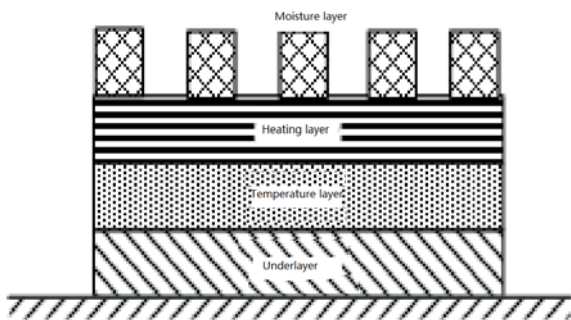


Fig. 1. Sensor heating principle structure

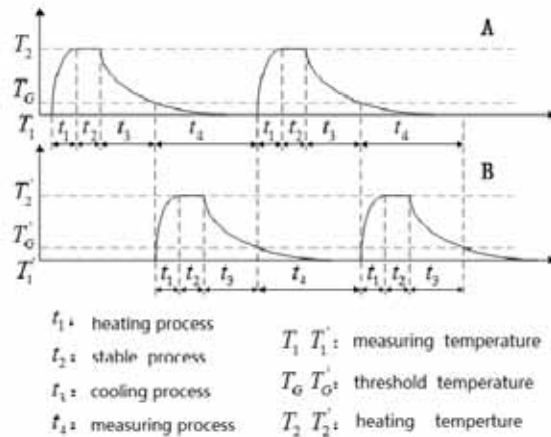


Fig. 2. The work process of pairs of heat and humidity sensors

As shown in Figure 2, when dual heating and humidity sensors are heating alternately, the measurement cycle can be simply divided into heating link t_1 , stable link t_2 , cool link t_3 and measuring link t_4 . Heating the plate in the heating part of the humidity sensor brings a temperature rise from ambient temperature T_1 to a target temperature T_2 . During the stable process, the temperature of the sensor at T_2 is maintained by the heating resistance in the chip. In the cooling part, the sensor is cooled by natural convection. Finally, the humidity is measured in the measurement part. Select the variability in Y-axis direction as the temperature drop threshold criteria T_G , when the temperature is lower than value of T_G , it will be similar to that temperature will not change. Therefore, the cooling process is divided into cool link and measurements link.

Interdigital sandwich structure is used in the layer of measuring wet. This structure increases the capacitance values of wet sense capacitance and the sensitivity of sensor. In the middle of the electrode, polyimide film is taken as Humicap media. According to the semi-empirical relationship of Looyenga:

$$\epsilon = \left[V(\epsilon_2^{1/3} - \epsilon_1^{1/3}) + \epsilon_1^{1/3} \right]^3 \quad (1)$$

where ϵ , ϵ_1 and ϵ_2 are complex, PI is the dielectric constant of water, V is the volume percentage of PI-absorbent that is related to RH. Greater the humidity would result in more adsorbed water molecules by the PI film. Besides, the greater the V, the greater the dielectric constant ϵ .

Then, the capacitance value of the humidity sensor is:

$$C = \frac{A\epsilon_0\epsilon_r}{d} \quad (2)$$

In this formula, C is the total capacitance value, d is the thickness of the dielectric film polyimide and ϵ_r is a dielectric constant of the polyimide depending on humidity variations.

ESTABLISHING HEATING MODEL

THE EXPANSION RESPONSE CURVE METHOD

The size of the humidity sensor selected in this paper is 6 mm × 4 mm × 0.625 mm. Two titanium material heating plate is integrated on the heating layer, with the length, width and thickness are 5200 μm, 400 μm and 200 nm, respectively. When the sensor is added to the measurement circuit at a constant voltage 9 V, the measured sensor temperature T and the heating time t is shown in Figure 3.

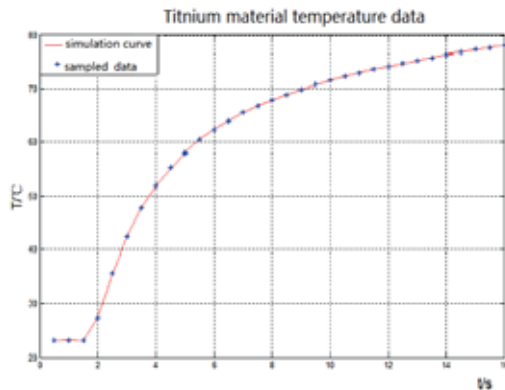


Fig. 3. Sensor temperature versus time curve

As shown in Figure 3, the heating process of the sensor can be approximately expressed by a first-order inertia link and a pure lag link, which is

$$G(s) = \frac{Ke^{-Ts}}{T_s + 1} \quad (3)$$

where, K is a static gain, T is the equivalent time delay, τ is the equivalent time constant. The unit step response is shown in Figure 2 (a). The parameter K can be determined by the ratio of output and input in the steady-state. τ and T can be calculated by a simple way based on the area of measurement according to equation (4):

$$\begin{cases} T + \tau = \frac{A_{01} + A_{02}}{k} \\ T = \frac{eA_1}{k} \end{cases} \quad (4)$$

Where A_{01} , A_{02} and are area which can be measured by Figure 4.

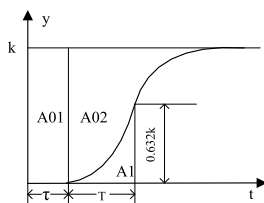


Fig. 4. The model parameters determined by Ziegler and Nichols method

ESTABLISHING HEATING MODEL

According to experimental data, K = 46, T = 2.8, $\tau = 1.2$ can be obtained using the expansion response curve. Thus, the transfer function $G(s) = \frac{46e^{-1.2s}}{2.8s + 1}$ can be determined for the heating plate, with the frequency characteristic given in Figure 5.

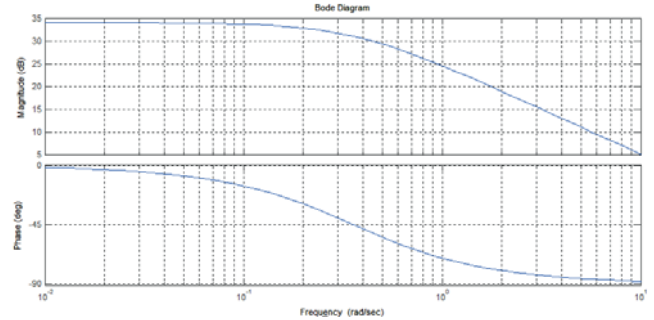


Fig. 5. The frequency characteristics of humidity sensor heating control system

Figure 5 can be obtained from the frequency characteristics of the system. The amplitude stability margin is $+\infty$, phase stability margin is -90° . When the humidity sensor heating plate open-loop frequency characteristic is greater than 0 dB logarithmic frequency domain, the number of phase curve for the -180° line crossing the both positive and negative is 0, so the closed-loop system is stable.

THE IMPLEMENTATION OF CONTROL ALGORITHM

PREDICTION MODEL

DMC Algorithm is a step response model of the system as a predictive model. When coupled with an input of the system step response, the sampling time at the $t = T, 2T, 3T, \dots, NT$ can be measured separately a sequence of sample values at the output of the system, with dynamic coefficients represented as $a_1, a_2, a_3, \dots, a_N$. Where N is the cut-off point of the step response, which is called the length of the time domain model. The choice of N should make a_i ($i > N$) close to its steady state value a_∞ . In proportion to the additive nature of the linear system and the use of this model, the output in the future of the system can be predicted according to the input control increment. The prediction model is given in equation formula (5)

$$\tilde{y}_{PM}(k) = \tilde{y}_{P0}(k) + A\Delta u_M(k) \quad (5)$$

where,

$$\tilde{y}_{PM}(k) = \begin{bmatrix} \tilde{y}_M(k+1|k) \\ \vdots \\ \tilde{y}_M(k+P|k) \end{bmatrix}, \quad \tilde{y}_{P0}(k) = \begin{bmatrix} \tilde{y}_0(k+1|k) \\ \vdots \\ \tilde{y}_0(k+N|k) \end{bmatrix}, \quad \Delta u_M(k) = \begin{bmatrix} \Delta u(k) \\ \vdots \\ \Delta u(k+M-1) \end{bmatrix}, \quad A = \begin{bmatrix} a_1 & 0 & \dots & 0 \\ a_2 & a_1 & \dots & 0 \\ \vdots & \vdots & \dots & \vdots \\ a_p & a_{p-1} & \dots & a_{p-M+1} \end{bmatrix}$$

Here, P is the prediction domain length. Generally, $M \leq P \leq N$, where M is the control horizon length, and N is the length of the time-domain model.

ROLLING OPTIMIZATION

DMC is a control strategy algorithm based on optimization. At sampling time $t = kT$, the optimization performance index is given by formula (6),

$$\min J(k) = \sum_{i=1}^P q_i \left[\omega(k+1) - \tilde{y}_M(k+i|k) \right]^2 + \sum_{j=1}^M r_j \Delta u^2(k+j-1) \quad (6)$$

Where q_i and r_j are the weight coefficients.

At different times, the optimization performance indicators are not the same, but their relative forms are consistent. The so-called "rolling optimization" refers to the optimization time-domain goes forward with time constantly. Introducing vector and matrix notation as $w(k) = [w(k+1) \dots w(k+P)]^T$ and $Q = \text{diag}(q_1, \dots, q_p)$, $R = \text{diag}(r_1, \dots, r_M)$, then the optimization performance index of formula (6) can be rewritten as,

$$\min J(k) = \left\| \omega_p(k) - \tilde{y}_{PM}(k) \right\|_Q^2 + \left\| \Delta u_M(k) \right\|_R^2 \quad (7)$$

Where, Q and R are error weighting matrix and control matrix.

Without considering the input and output constraints, the time at $t = kT$, $\omega_p(k)$ and $y_{p0}(k)$ are both known, so that J(k) can achieve the minimum $\Delta u_M(k)$ by taking the extreme conditions necessary $dJ(k)/d\Delta u_M(k)$

$$\Delta u_M(k) = (A^T Q A + R)^{-1} A^T Q (\omega_p(k) - \tilde{y}_{p0}(k)) \quad (8)$$

FEEDBACK CORRECTION

Because of the model error, weakly nonlinear characteristics and other uncertain factors that exist in the actual process, the open-loop optimal control formula (8) based on prediction model equation (5) does not necessarily guarantee a system output following closely to the expectations. Moreover, the object being disturbed can not be taken into account. Therefore, we should use the error information in time during this process to correct the predicted value of output, instead of waiting until the M controls are implemented and making incremental correction. Therefore, the output of the system should be on the basis of output of predicted model, and use the actual output error correction, namely

$$\tilde{y}_{cor}(k+1) = \tilde{y}_{N1}(k) + h e(k+1) \quad (9)$$

Where

$$\tilde{y}_{cor}(k+1) = \begin{bmatrix} \tilde{y}_{cor}(k+1|k+1) \\ \vdots \\ \tilde{y}_{cor}(k+N|k+1) \end{bmatrix} \text{ is the output at } t = (k+1) \text{ (} i = 1, \dots, N \text{)}$$

of predicted system after error correction at $t=(k+1)T$. $h = [h_1, h_2, \dots, h_N]^T$ is the vector of error correction, where $h_1=1$, $e(k+1)$ is prediction error.

ANALYSIS OF SIMULATION RESULTS

From the angel of fluid dynamics (CFD) simulation that when the two humidity sensors are separated by more than 3 mm, it will not affect the temperature and humidity around the field of another when a sensor is heating, which means the measurement is valid in this case, the low- altitude mode and high-altitude mode are proposed in this paper. Specially, at the low-altitude mode (0 ~ 20 km), when the power is 0.6 W and the temperature rise is 46 °C, the surface temperature rise time is 5.8 s. On the contrary, at the high- altitude mode (20 km ~ 30 km), when the power is 0.4 W and the temperature rise is 40 °C, the high-altitude rise time is 5.8 s.

Sensor in the rising process and not in a straight line rise, in order to make the model more close to the real joined the cross wind effects of simulated rotation rising effect. At the same time, the sensor fully contact with the air. Due to the actual situation, the size of the sensor spacing of pitch angle research will not affect the study. Therefore, the final selected spacing is 3.5 mm, sea level and climatic conditions, pitch angles in Figure 6 are in 35°,40°,45° and 45° as the research object. Because of frictional resistance to the wall cutting area to be the force, and the wall boundary layer flow solver, the sensor and the air full contact friction, the larger inevitable, so use the model of wall shear should force (shear stress) as the reference variable.

Figure 6 shows cloud image of wall shear stress of the two sensors at a distance of 3.5 mm. From Figure 6 (a) available sensor surface shear stress 0.375 Pa, on its boundary is part of the region have different values. With the shear stress 0.432 Pa, sensors in Figure 6 (b) have different changes and the sensors of the shear stress distribution is different. In Figure 6 (c), surface shear stress distribution is uniform and the edge changes are also approximate symmetrical. Figure 6 (d) reveals a sensor surface shear stress change slowly, when humidity measurement error is larger.

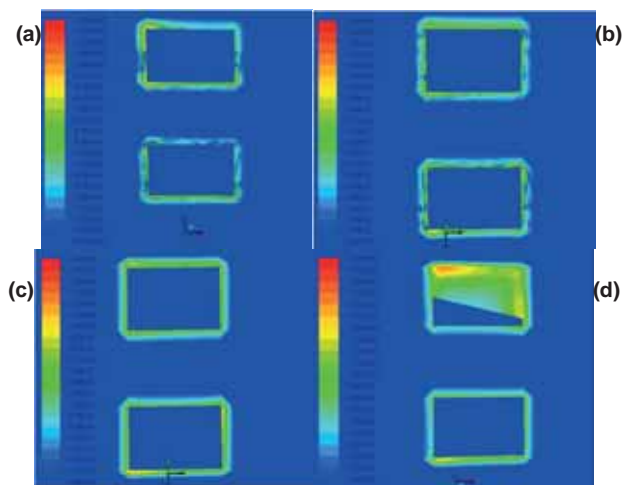


Fig. 6. Angle simulation diagram (a) pitch angle of 35° (b) pitch angle of 40° (c) pitch angle of 45° (d) pitch angle of 50°

When the sensor spacing is 3.5 mm, pitch angle is 45°, from the XY scatter diagram of the numerical distribution of the two sensors are more coincident, by the resistance of the air is basically the same, distribution interval of 0.1~1.7 Pascal, due to the presence of larger jump numerical variations, in addition to this part mainly concentrated in the 0.6 ~ 1 Pascal, the sensor surface shear should force change range is small and the values are pitching angle of 45°, 40° large on the boundary, as shown in Figure 7. Therefore, the choice of pitch angle, rolling angle and yaw angle are 45°, 90°, and 0°, respectively.

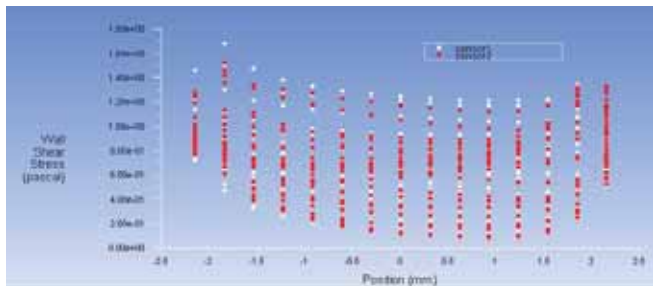


Fig. 7. Shear stress distribution in the wall of the pitching angle 45 degrees

Based on the control requirements discussed above, when the heating plate temperature rose from 0 °C to 46 °C, sampling period is taken as 20 s. The predictive control parameters were chosen as $T_s = 5, P = 10, M = 1, N = 30, \alpha = 2$. The value of system output feedback coefficient is $h = [h_1, h_2, \dots, h_N]^T$, and $h_1 = 1$. Because the system is a first-order inertial system, weighting matrix Q and R may be selected in accordance with the $Q = I$ (Unit matrix), to determine R in the real-time control process. The step response output curve of the system is shown in Figure 10.

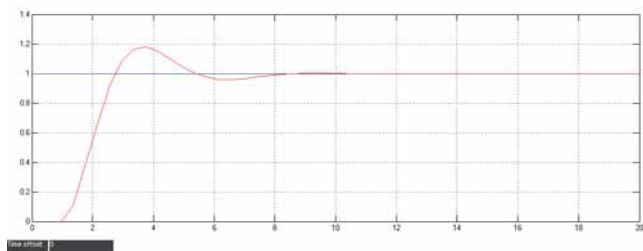


Fig. 8. PID temperature control heating film simulation results

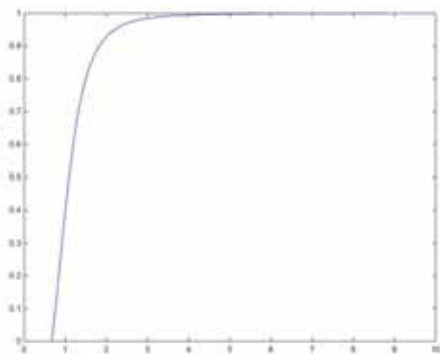


Fig. 9. Fuzzy temperature control heating film simulation results

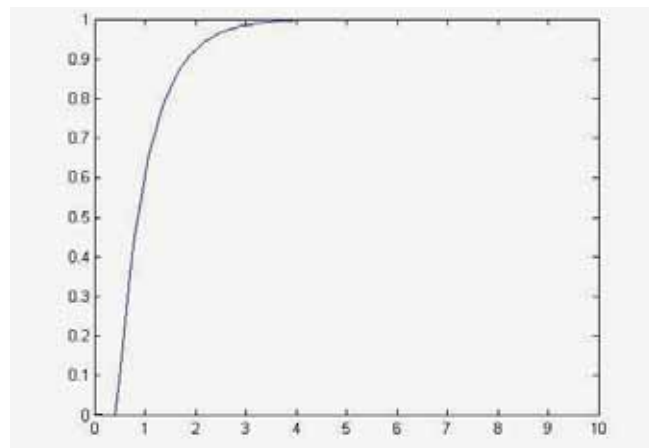


Fig. 10. DMC heating plate temperature control simulation results

The results of simulation shows that the control of DMC is faster than PID control (smaller overshoot, and settling time $t = 3.6$ s), which meets the heating requirements of low-altitude mode. Considering the limit conditions, high altitude heating model is difficult to establish, and the time of sensor response is very long (60 to 200 seconds) in the following -60 °C. Cooling time after heating is long at low pressure. Water in the cloud exists in the form of small ice crystals at this point, which means frost is less likely to generate on the sensor surface, therefore the heat treatment cannot be finished.

CONCLUSION

This paper studied the heating control process of dual heated sounding humidity sensor and built the relationship between the temperature and humidity, with its stability analyzed in details. DMC, Fuzzy and PID were used to control, heating and simulate. Results show that the control method in this paper has great stability, with stabilization time determined as 3.6 s, which meets the requirements of sounding humidity measurement. However, the model is relatively easy with some simplifications: since the heating layer is very thin, temperature of measurement temperature layer is considered to be equivalent to measurement humidity layer. The physical properties of the sensor itself is ignored after heated, which is also a hot point and difficult point of MEMS. In future studies, the model will be refined to make it better to meet the timeliness and accuracy of the altitude humidity detection.

ACKNOWLEDGMENTS

This work is supported by Public Welfare Industry (Meteorological) Special Funding Scientific Research Projects(GYHY201106040), the National Natural Science Foundation of China (51405243), the National Science Foundation of Jiangsu province (BK20130999), Supported by National Natural Science Foundation of China (61271395)

REFERENCE

1. Wei, Zhao Peitao, Guo Qiyun, et al. 2011. The international radiosonde intercomparison results for China-made GPS ra-diosonde. *Journal of Applied Meteorology (in Chinese)*, 22(4):453–462
2. Ye X I, Liao J I , Gao , D X , Wang F F .based on PSO support vector machine humidity sensor temperature compensation [J] *Instrument Technique and Sensor*, 2013 (11): 14-30.
3. Liu Q Q,Dai W,Yang R K,et al. Fluid dynamics analysis on solar radiation error of radiosonde temperature measurement. *Plateau Mete-orology*,2013; 32(4) : 1157—1164
4. Ciesielski P E,Johnson R H,Wang J H. Correction of humidity bia-ses in Vaisala RS80-H sondes during NAME. *Journal of Atmospheric and Oceanic Technology*,2009; 26: 1763—1780
5. Indrajit Mukherjee,Srikanta Routroy, Comparing the Performance of Neural Networks Developed by Using Levenberg-Marquardt and Quasi-Newton with the Gradient Descent Algorithm for Modelling a Multiple Response Grinding Process [J] *Expert Systems with Ap-plications*,2012(39) : 2397 - 2407
6. Stuart Bennett. The past of PID controllers[J]. *Annual Reviews in Control*, 2001, 25: 43-53.
7. I. Cervantesa, J. Alvarez-Ramirezb. On the PID tracking control of robot manipulators. *Systems and Control Letter*,vol. 42, no. 1, pp. 37–46, 2001.
8. KAYA I. IMC based automatic tuning method for PID controllers in a Smith predictor configuration [J]. *Computers and Chemical Engineering*, 2004, 28(3): 281–290.
9. HAN J Q. Form PID to active disturbance rejection control [J]. *IEEE Transaction on Industrial Electronics*, 2009, 56(3): 900–906.
10. ASTROM K J, HAGGLUND T. The future of PID control [J]. *Control Engineering Practice*, 2001, 9: 1163–1175.
11. LI Y, KIAM H A, GREGORY C Y. Patents, software and hardware for PID Control [J]. *IEEE Control Systems Magazine*, 2006, 26(1): 42–54.
12. LI H X, GATLAND B H, GREEN A W. Fuzzy variable structure control [J]. *IEEE Trans Sys, Man, Cybern B*, 1997, 27(2): 306– 312.
13. Zadeh L. Fuzzy Sets[J]. *Journal of Information and Control*, 1965, 8: 338-353.
14. L. Peng, P. Y. Woo. Neural-fuzzy control system for robotic manipulators. *IEEE Control Systems Magazine*, vol. 22,no. 1, pp. 53–63, 2006.
15. H. F. Ho, Y. K. Wong, A. B. Rad. Robust fuzzy tracking control for robotic manipulators. *Simulation Modeling Practice and Theory*, vol. 15, no. 7, pp. 801–816, 2007.
16. Z. J. Sun, R. T. Xing, C. S. Zhao, W. Q. Huang. Fuzzy auto-tuning PID control of multiple joint robot driven by ultrasonic motors. *Ultrasonics*, vol. 46, no. 4, pp. 303–312, 2007.
17. Simminger J,Peterson T.Constrained multivariable nonlinear model predictive control based on iterative QDMC.IFAC advanced control of chemical processes,To ulonse,France,1991,1: 149-154.
18. Liuyou Fei, Wu Gang, Wei Heng Hua, Sun Demin stepped Dynamic Matrix Control and Its Application in Temperature Control System [J] *University of Science and Technology of China*, 2005 (6): 347-352.
19. Wang Shihu,Shen Jiong,Li Yiguo. Multi-model control method and research progress [J] *Industrial instrumentation and Automation*,2008,(1) : 13-17
20. Abderrahim A.Dynamic matrix control(DMC) of rolling mills[J].*Mterials and manufacturing processes*,2007,22(7):909-915.
21. zhou J.Z,Li X,Zhu H.T.Application and simulation of DMC controller in time delay inertial system[C].2008 Chinese control and decision conference,2008:640-654.
22. NOAA, NASA, USAF, et al. U. S. Standard Atmosphere[M]. Washington, D. C. :U. S. Government Printing Office, 1976:53-63.
23. Bhajneet Singh, Sukanta K. Dash. Natural convection heat transfer from a finned sphere[J]. *International Journal of Heat and Mass Transfer*. 2015,81(2):305-324.
24. Y.Y. Qiu, C. Azeredo-Leme, L.R. Alcacer, et al. A CMOS humidity sensor with on-chip calibration[J]. *Sensors andActuatorsA*. 2001, 92:80-87.
25. Kalyan Phani Tangirala, J. Robert Heath, Arthur Radun. A Handheld Programmable-Logic-Device-Based Temperature and Relative-Humidity Senso, Processor, and Display System Platform forAutomation and Control of Industry Process [J]. 2010, 46(4):1619-1629.
26. Elbisy, MS. Sea Wave Parameters Prediction by Support Vector Machine Using a Genetic Algorithm [J]. *Journal of Coastal Research*. 2015, 31(4): 892-899.

27. Gu .L, Qin.M,Huang .Q.A, CMOS integrated capacitive humidity sensor [J] Instrument Technique and Sensor, 2003, (06): 7-11.
28. Watson, PJ. Development of a Unique Synthetic Data Set to Improve Sea-Level Research and Understanding [J]. Journal of Coastal Research. 2015, 3(3): 758-770.
29. Liu .Q.Q, Yang J, Yang R.K and other dual heating humidity sensor CFD Analysis and Design of heating strategies [J] Sensing Technology, 201 225 (08): 1039-1044.

CONTACT WITH AUTHOR

SUN Ning

Key Laboratory of Meteorological Disaster
of Ministry of Education,
Nanjing University of Information Science
and Technology,
Nanjing 210044,
China

School of Information and Control.
Collaborative Innovation Center on Forecast
and Evaluation of Meteorological Disasters,
Nanjing University of Information Science
and Technology,
Nanjing 210044,
China

email:sunning0908@126.com

AUTO MISSION PLANNING SYSTEM DESIGN FOR IMAGING SATELLITES AND ITS APPLICATIONS IN ENVIRONMENTAL FIELD

Yongming He

Yuan Wang

Yingwu Chen

Lining Xing

National University of Defense Technology, College of Information System and Management, Sanyi Road, Changsha, China

ABSTRACT

Satellite hardware has reached a level of development that enables imaging satellites to realize applications in the area of meteorology and environmental monitoring. As the requirements in terms of feasibility and the actual profit achieved by satellite applications increase, we need to comprehensively consider the actual status, constraints, unpredictable information, and complicated requirements. The management of this complex information and the allocation of satellite resources to realize image acquisition have become essential for enhancing the efficiency of satellite instrumentation. In view of this, we designed a satellite auto mission planning system, which includes two sub-systems: the imaging satellite itself and the ground base, and these systems would then collaborate to process complicated missions: the satellite mainly focuses on mission planning and functions according to actual parameters, whereas the ground base provides auxiliary information, management, and control. Based on the requirements analysis, we have devised the application scenarios, main module, and key techniques. Comparison of the simulation results of the system, confirmed the feasibility and optimization efficiency of the system framework, which also stimulates new thinking for the method of monitoring environment and design of mission planning systems.

Keywords: systems engineering, imaging satellite, meteorological monitoring, space-ground integration

INTRODUCTION

Half a century ago, the Union of Soviet Socialist Republics (USSR) successfully launched the first artificial earth satellite (AES) in the world, which represents the coming era of human exploration and utilization of space resources to serve human productivity and life. According to statistics, China have launched 139 on-orbit satellites until 2014, and this quantity ranks second only to the United States. As an important branch of the satellite family, imaging satellites have found application in major activities such as finding earth resources, meteorological and geological disasters relief support, and supporting agricultural activities. However, the increase in the quantity of satellites and the improving hardware level has led people's expectations in terms of devices relying

on satellite to increase. At the same time, there has been a realization that traditional ground-planning systems and mission planning techniques and instrumentation of imaging satellites need to improve.

A traditional imaging satellite is only a command executor in an application process; for example, the Earth observation system (EOS) as shown in Fig. 1. The user delivers the satellite image request to the task-dispatching center according to different work requirements, and after rearranging all user requests the dispatching center standardizes complicated user requests before generating the mission planning scheme and sending the scheme to both the monitoring center and ground station. The monitoring center then compiles the satellite action code and uploads it to the satellite. In addition, they also monitor the satellite status information, such as

information relating to the position and satellite sources, and they load the working conditions. The ground station adjusts the antenna to receive data at a specified time according to the plan.

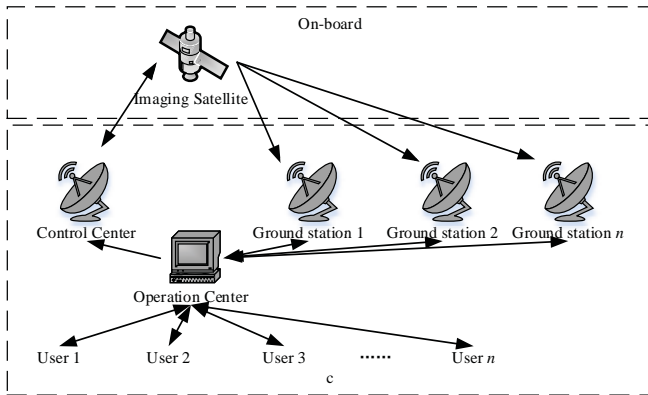


Fig. 1. Earth observation system (EOS) of traditional imaging satellite

Therefore, it is obvious that the mission planning for a traditional imaging satellite involves a process of off-line scheduling with simple loading data, a time during which the satellite cannot acquire working information and guide decisions⁴. As the satellite hardware level continues to improve, users also demand enhanced image quality and response speed of an imaging satellite. Moreover, the development of image processing and pattern recognition techniques has enabled satellites to perceive image characteristics and support mission planning.

In the face of increasingly complicated imaging demands, the trend is for future imaging satellites to use multi-satellite united imaging to fulfill complicated missions. The mission-planning model for traditional imaging satellites is unable to satisfy the fast-response demand, and cannot overcome the limitations of existing monitoring ability. In addition, because of its low monitoring efficiency in terms of the planning scheme, it is unable to function effectively in the complicated and complex space environment, which means that the traditional mission-planning model is unable to adapt to future imaging instrumentation. As a result, the auto mission planning system emerges in response to the needs of times.

The new type of imaging satellite has the following characteristics: high-resolution ratio, high agility, multi-sensor and satellite data processing and decision abilities, all of which present a new challenge to satellite mission planning: an expanded question range, greater decision variety and constraints, more complex object function, etc. A mission planning system is quite similar to the „brain” of a satellite because it needs to co-ordinate all satellite resources and its intelligence needs the support of each commonly developed module, such as satellite image processing, pattern recognition, and parameter adaptive technology. With the support of these other technologies, the “brain” can make accurate judgments and decisions so as to improve overall system reliability. How to fully apply information acquired by the satellite and planning auto mission tasks so as to enhance the actual profit of the

satellite mission-dispatching scheme has become a major research challenge for all space system researchers.

The design goal for a satellite auto mission planning system is to enable the satellite to acquire the environment and status automatically, and to enable it to generate a scientific scheme to improve the utilization rate of satellite resources. Many organizations and scholars are currently studying satellite autonomous management controlling techniques, such as that designed by Chien in the form of an order for EO-1 named CASPER, which can accept instructions based on an actual situation. He also proposed an iterative repair algorithm capable of adjusting the mission-planning scheme according to the changing targets and constraints. The Verification of Autonomous Mission planning Onboard a Spacecraft (VAMOS) project proposed by the German Aerospace Center (DRL) can realize satellite resources automation inspection and adjustment; it can also realize the re-planning based on actual resources usage and task demand generated autonomously by the satellite. The experiment named “Autonomy Generic Architecture: Test and Applications (AGATA)” is projected by the Centre National d’Etudes Spatiales (CNES), and it is a kind of general system architecture demonstration and verification platform that supports spacecraft in comprehensive capabilities such as planning, monitoring, and diagnosing and is still in the testing period. Beaumet has designed a satellite mission planning system and it is also applied to the Pleiades satellite, a French technology experiment satellite. This system is mainly based on the real-time state of the satellite and environmental information with the aim of proposing satellite action for decision-making and to choose a strategy for each action at any time, based on a greedy algorithm of random iteration as its core. The different loads carried by each satellite and the need to realize different functions require the design of special planning processes and algorithms. These systems need to be designed with certain intelligence, yet each satellite functions independently and has different standards, which is not conducive to completing complex task observation quickly and reliably.

In this paper, the satellite mission planning system applies to image satellites with different loads, different capabilities, and different orbits. Reorganization of the functions and correlation of different modules enables the key technology for all modules to be abstracted. Finally, the feasibility of this system was confirmed by performing a case analysis for a typical application scenario, which shows the advantages of autonomous planning in future satellite instrumentation.

HOLISTIC DESIGN

SYSTEMATIC OBJECTIVES

The process shown in Fig. 1 allows us to easily establish the characteristics and limits of traditional satellite mission-planning systems. It is these reasons that lead to the difficulties in applying imaging satellite to the environment area. Reasons as follow:

(1) Off-line planning and controlling (dispatching). Currently, it is difficult for imaging satellites to realize real-time

communication with the ground station; this means the ground station can only plan once according to predicted information. This causes conflicting or contradictory problems, such as hardware control or practical constraints, while the satellite is carrying out instructions, which reduces the efficiency of the satellite.

(2) Low information utilization ratio. Real-time information about the satellite can eliminate uncertainty and would be convenient for satellite mission scheduling and controlling. Traditional imaging satellites carry a single load; thus, it uses little information. Satellite mission scheduling has complicated constraints; for example, the imaging effect for an optical imaging satellite is affected by clouds, fog, and haze, and if we do not analyze and respond to this information, the imaging results may be useless.

(3) Decision making is negatively affected. In the traditional satellite mission planning process, the planning is finished at the ground station, and the satellite only accepts executive instructions after simple data processing, after which the results are transferred to the ground station for decision-making. This lowers the speed at which the satellite responds to tasks, which means that important and emergency tasks are affected.

Generally speaking, the performance of the traditional imaging satellite is satisfactory in terms of producing useful information from the perspective of space, but with low efficiency. In view of the above limitations, this thesis proposes design objectives for a new imaging satellite auto mission planning system as follows:

- (1) Realize autonomous information acquisition and re-organization for satellites.
- (2) Realize autonomous mission scheduling and decision making for satellites.
- (3) Realize real-time tasks re-scheduling for satellites.

FUNCTIONAL REQUIREMENTS

Combined with the new operational requirements for satellites and considering that satellite users have different requirements for different missions, we propose the following functional requirements for new imaging satellites:

(1) The capability to autonomously acquire dynamically changing and uncertain information and the ability to effectively process information accordingly. A satellite mission planning process is noted for uncertainties, such as demands that change dynamically, constraints, judgment, and uncertainties in the environment and the availability of resources. The satellite requires the ability to respond to these factors to ensure optimal results under any circumstances and in any environment.

(2) The capability for fast data processing. Satellite mission planning is a complicated process and is highly demanding in terms of temporal efficiency. This would require us to raise the system calculation and processing ability depending on the hardware capabilities. Thus, we need to design the scheduling algorithms reasonably to improve the convergence rate of results and to ensure that a feasible solution is obtained in an acceptable period of time.

(3) The capability to analyze satellite observation results. Increasingly complicated satellite missions make it difficult to process many users' requirements by simply splitting a single imaging task. Each task requires multi-stage decision-making in which decisions in the second stage are based on the results of the previous stage. Therefore, satellites require the ability to process results to allow the plan to be adjusted according to the results obtained in the previous step.

TYPICAL APPLICATION SCENARIOS

The traditional satellite operational process involves splitting complicated tasks into several single images with certain coordinates. New imaging satellites have to satisfy higher-level demands with the following typical applications.

IDENTIFYING TARGET CHARACTERISTICS

Application objective: to acquire target characteristic information as much as possible to improve the success rate of identifying the object. In this application scenario, task completion time can be seen as a common constraint to guarantee the effectiveness of the information.

General procedure: When one target is defined as the most important, the mission-planning system dispatches satellites to finish multi-observations in different directions for a period of time until all characteristics to be acquired can be successfully obtained by the satellite and we have high assurance that the attributes for these characteristics have been identified.

Typical scenario: Some region is threatened by geological disaster; however, the government cannot effectively control it because of limited access to the stricken area. Decisions are required in terms of arranging rescue, estimating losses, and further controlling the disaster situation by comprehensively considering multi-dimensional information such as the nature of the hazard, topographic conditions, vegetation conditions, land use situation, current weather conditions, and the density of the population. However, due to the restricting conditions in all respects, it is more effective to use a satellite to acquire this information. This requires reasonable scheduling and dispatching of satellite resources so as to accomplish tasks effectively and timeously.

SEARCHING FOR AN UNCERTAIN TARGET

Application objective: to locate eligible targets as much as possible in the stipulated time.

General procedure: First, define the area within which the target exists, and then search its terrain by specifying target characteristics according to the information programming search strategy.

Typical scenario: Forest fire is one of a costly natural hazard, and it really spawned a great number of economic loss each year. Government is devoted to monitoring forest fire in a region and hopes to find it and control them effectively. Because the use of alternative methods is ruled out due to limitations in terms of cost and technology, an imaging satellite is the best tool to conduct target searching in this region in a short

period of time. A satellite is characterized by a high target recognition rate, wide coverage, and a unique perspective, it can perform general searching in the specified region and find the possible target, and then checking and confirming one by one until all targets are finally found.

TRACKING A MOVING TARGET

Application objective: continuously tracking the target from beginning to end.

Working procedure: The satellite defines the starting point for one target, and then predicts the target location in the next phase and performs continuous observation and tracking. During the tracking process, the satellite adjusts the parameters according to the actual target location and predicted location to ensure the target is always in the detected area.

Typical Scenario: In a sparsely populated area, a serious mobile pollution source is moving. The officer obtained the current position for the source through other means and now they need it to be continuously tracked for final capture. The satellite starts from the current location of the source and forecasts the possible location for the next step and adjusts the observation angle. In this process, the satellite may face many different situations, for example, there might be a large difference between the predicted direction/speed and reality; it may also encounter disruptions such as target loss, or a false target. This requires us to be fully prepared to overcome the changing conditions.

CHARACTERISTICS

The load carried by image satellites is constantly being upgraded, as is its imaging capability. A non-agile satellite would not be able to finish acquiring the image of a river course that is not parallel to the satellite orbit, whereas an agile satellite would be able to do so. The following new requirements in mission planning and scheduling are proposed for these new satellites:

(1) Diversity in mission demand. Traditional mission planning systems preset a profit through analyzing the completion of each mission, and determine the planning system according to the total profit. Traditional planning systems simplify a mission as a point with a single imaging model and mission demand, which means that a plan with a high profit target may not be reasonable. New imaging satellites need to comprehensively consider the requirements of different users such as time-effectiveness and image resolution.

(2) Changes in the environment influence different tasks in different ways³³. Because of the diversity in imaging demands, the influence of the environment on different tasks is not exactly the same, and the constraints for each task can also change accordingly. For example, given the following two tasks, one of which is to acquire the outline of some architecture, whereas the other is to acquire the color of this architecture. When using an imaging satellite to analyze the image, the degree of difficulty is apparently not the same under different weather conditions.

(3) Higher requirement in mission planning time effectiveness. Traditional mission planning usually takes much more time due to the communication links. The timeliness of information directly affects its value. As a means of information acquisition, the time required for the planning process directly affects the value of the information. Especially for emergencies, if the satellite cannot acquire information and report it to the user in time, it will cause great losses. Meanwhile, the existence of many uncertainties in the planning process leads to error accumulation, which negatively affects the outcome or could even result in task failure.

(4) Requirements in terms of efficiency and reliability for satellite-borne processing algorithms have improved.

In the current satellite mission planning system, the speed at which hardware is upgraded does not correspond to the growth rate for constraints and demands; at the same time, the wide range of uses of satellites in human life means that the satellite mission observation density also continues to increase. The problem associated with agile satellite mission planning has already been proven to be an NP-hard problem. In view of this, a more effective solution is required for the satellite-borne processing algorithm, with a more reliable outcome.

DETAILED DESIGN

FUNCTIONAL MODULES OF AUTO MISSION PLANNING SYSTEM

The satellite auto mission planning system can receive the status and resource information from other subsystems, and integrate these data to arrange the imaging task demands. Based on the analysis of the working process of the satellite, the function of the mission planning system is divided into seven modules. Table 1 presents a comparison of the functions of each module in traditional and autonomous satellites.

Tab. 1. Comparison of features of modules in mission planning system

Modules	Autonomous satellite	Traditional satellite
User requirements integration	Diverse tasks	Single source
Environmental information analysis	On-board	On ground station
Imaging task planning	Flexible process	Fixed routine
Action control and prediction	Online formation	Off-line operation
Load data processing	Big-Capacity Data Disposal	Without it
Data transmission and signal communication	Real-time upload and return	Batch transmission
Structure and parameter adaptation	Automatic adjustment	Manual adjustment

The following schematic diagram incorporates the characteristics proposed above for an on-board mission planning system for future imaging satellites.

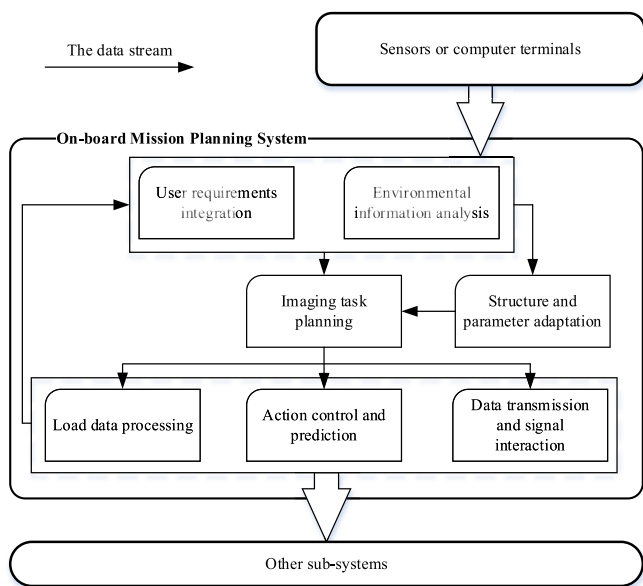


Fig. 2. Structure of proposed on-board mission planning system

Next, the function of each module and the mutual relations between modules are described in detail.

User requirements integration: with the deepening of research on collaborative multi-satellite operations and the developments in hardware and software design of imaging satellites, the reception of multi-source task information is an increasing trend in the future application of imaging satellites. Multi-source task information refers to information from many different devices, such as ground stations, mobile terminals, other satellites, and other loads. As user demands are becoming increasingly complex with increasing uncertainties, the process of requirement integration has to be completed on-board. It includes requirement generation, requirement decomposition, strip division, and other tasks, with all of the requirements ultimately included in a unified standard satellite mission planning system.

Environmental information analysis: Environmental information refers to the attributes that influence the completion of a satellite-imaging mission, including the external and internal environments. Weather conditions, light conditions, and the distribution of facilities (such as ground stations and the positions of other satellites) constitute the external environment of the satellite, which is usually determined through a communication link on the exterior of the satellite or calculated and analyzed based on known information internal to the satellite. The internal environment refers to storage space, the use of electricity, the health state of the satellite, etc., and can be read directly from the other modules of the satellite. It can realize two functions based on the provided information: One is to determine whether the system needs to adjust the task planning scheme by checking the environmental information according to the set rules, the second is to reduce the size of the solution domain occupied by mission planning for the satellite to improve the operational efficiency and to ensure that the mission planning scheme can be executed for final profit.

Imaging task planning: The purpose of this module is to generate a feasible plan for guiding satellite movement by analyzing all valuable information. Mission planning usually needs a relatively optimal solution considering all feasible solutions to strengthen the reliability and shorten the planning time and heighten the benefit. This is a multiple objective planning process; however, there are many practical constraints when the planning module is working on-board, in which case it is impossible to optimally reach all objects. The computation efficiency and optimization results of the different algorithms is also different under different kinds of constraints; thus, mission planning algorithms should be self-determined according to the requirements of different environments, in order to improve the overall optimization effect.

Action control and prediction: The action sequence of a satellite can be generated based on the constraints imposed by satellite actions and environmental information. Implementation of satellite action involves monitoring and control by other sub-systems of the implementation of the directive, and monitoring the feedback of information to this module. There are a wide variety of satellite actions, and there are some specific relationships between actions, which requires the appropriate action sequence to be determined based on these relationships. In addition, the module also scientifically predicts the actions of resource consumption, including feedback to the task planning system to assist decision-making. The resource consumption of each action is also an important factor in affecting the task-planning scheme and is difficult to predict; therefore, determination of the parameter in the predictive function has to correspond to the implementation of the actual action at each time, to finally improve the prediction accuracy.

Load data processing: Through the analysis and processing of the information obtained from different loads, some useful knowledge can be extracted from the image, which can lead to new task requirements. For example, by processing the signals received by the satellite, such as electronic loads and infrared loads, the satellite can determine whether the target is a current suspicious target or not, and generates the observation mission to the suspicious object. The satellite can also be used in the planning process of the potential demand generated by processing the load data. For example, the use of an optical or multi-spectral imaging load can be used to quickly sense imaging regional meteorological conditions, and determine whether it will affect the imaging planning task scheme and need corresponding adjustment.

Data transmission and signal communication: Due to the limited data link facilities, the present satellite communication system is composed of an oriented high-speed network and an un-oriented low-speed network. If the satellite transmits data by the high-speed network, advance request for transmission to the relevant object is essential; in contrast, a low-speed network can transfer instructions at any time, because the orientation of the antenna attitude is unlimited, but the transmission rate is slower. The satellite can communicate or transmit data and information to the ground unit or other satellite data and information through both methods. This

module design can reasonably use limited transmission data resources to realize effective communication between the satellite and ground station. It enables the satellite to transmit data while relative positions are changing dynamically, as well as while all kinds of required information is obtained from other facilities.

Structure and parameter adaptation: The complexity and variety of the environment on the satellite means that there are many parameters and models that need to be adjusted according to the actual situation. However, resources and constraints cannot be accurately predicted, so the system needs to be able to select the appropriate structure and system parameters flexibility and automatically. In the face of complex task demands, especially under conditions of multi-source information, the system processing flow is not exactly the same for different task demands. This requires the algorithm structure and parameters to be selected according to the actual situation.

FUNCTIONAL STRUCTURAL DESIGN OF SATELLITE OPERATION

Based on the idea of the integration of satellite and ground operations, this paper proposes the framework for the Earth observation system of a new imaging satellite shown in Fig. 3.

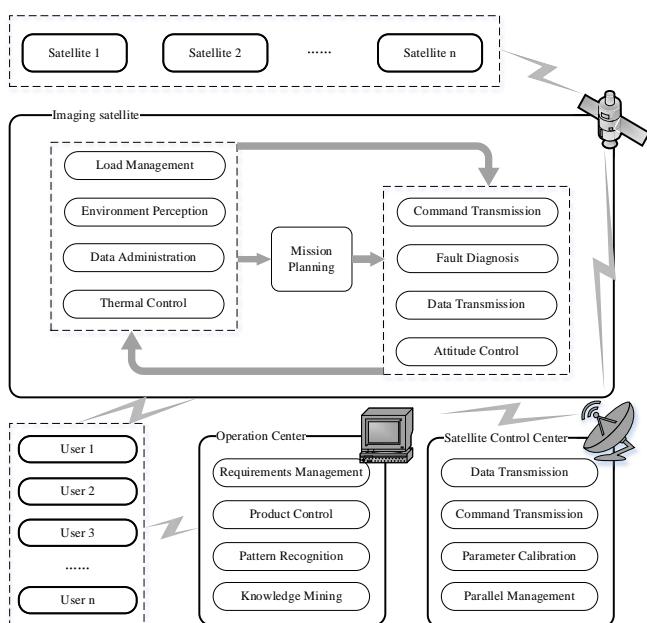


Fig. 3 Framework of the proposed Earth observation system

As shown in Fig. 2, the role of the satellite has been converted from that of a simple instruction executor into an agent with decision-making ability. The satellite can adapt to changes in the environment and resources and realize operations such as task processing, mission planning, and real-time adjustment on board, before deciding whether to carry out the task of planning according to the observation results and the environment. This is a so-called event-oriented program structure: different events can trigger the operation of different modules in the program. Meanwhile, addressing

the diversity of the environment and demands requires the satellite to have the ability to base its calculations on a variety of structures and a variety of algorithms. Although computational resources are precious on the satellite, the task planning system cannot cover all operational processes, and it still needs many functions in other sub-systems as support. (e.g., the status information for other subsystems and the part function needs to be supplemented by the ground system). The ground station can establish and maintain some knowledge base (planning algorithms library, general function library, system structure pattern database, etc.) in order to reduce the cost of learning on board and achieving flexible task planning as well. In this system framework, demands upload by means of the “mission-type” instead of the “instruction-type,” avoids a considerable amount of unnecessary processing by the ground station, thereby greatly reducing the fractional pressure, and taking advantage of the realization of the features in the auto mission planning system.

KEY TECHNIQUE

EXPENDABLE DYNAMIC DATA DESCRIPTION FRAMEWORK

Next generation agile EOSs face a more complex and uncertain mission environment, which is quite different from those faced by current EOSs. Thus, considering the strict environment, like the concept of “JIT”, next generation EOSs should have the ability rapidly respond to the dynamic environment by using dynamic mission information collected from different data sources.

This aim can be achieved by implementing a unique expandable data description framework to transfer mission data (i.e., in text, image, and video format) from different data sources, including analyzing these data to generate information and ensuring an efficient mission execution plan. This framework can offer any data source (e.g., an environment detection satellite) in the EOS control system the ability to exchange data with other data source and process mission data under a unique data framework. In addition, this framework ensures that systems using the framework have the ability to process data described under this framework irrespective of the data source and to ensure a similar result when the same data is processed by different process units. Finally, this framework should be expendable to reduce costs once external detectors are included in this system.

FLEXIBLE EARTH OBSERVATION MISSION PREPROCESS TECHNOLOGY

According to our research, the time cost of earth observation mission preprocesses can significantly affect the efficiency of mission planning and scheduling software. Moreover, the process precision can also affect the final observation profit. Thus, the preprocessing technology is also very important. Current mission preprocess technology divides all of the earth observation demands into n different meta-tasks, which are

studying volcanoes). It should be noted that because data mining is computationally intensive in terms of resources, most of these processes will be operated off-board. Plugins will be constructed to enable the final output of the data mining process to be uploaded to the EOS onboard operation system.

APPLICATION EXAMPLE

TEST SCENE DESIGN

Some imaging satellites carry two loads: the main load is the imaging camera, which acquires the image information and the secondary load is a cloud detector, which can detect real-time weather conditions 10 minutes ahead of the flight of the satellite. The satellite parameters for the simulation test are provided in Table 2, whereas its load parameters are listed in Table 3.

Tab. 2. Satellite parameters

Parameter	Value
Semi-major axis /(km)	6928.14
Height/(km)	550
Eccentricity	0
Inclination /(°)	97.5976
Perigee /(°)	0
Lon. Acnsn. Node/(°)	135
Storage/(GB)	100

Tab. 3. Sensor parameters

Type	Parameter		
	Shape	Vertical half-angle	Horizontal half-angle
Cloud detector	Rectangle	45	75
Imaging lens	Rectangle	45	45

Table 4 lists a batch of required properties for satellite mission planning in a period of time, including task types of identifying, searching and tracking. The task id was uniformly numbered by the transport control center; image time is determined by objective conditions such as user demand and environmental information; the image time window (imaging starting and ending time) is calculated by using the orbit parameter of this satellite and each of the task coordinates; cloud level means the cloud thickness detected by the probe during an imaging task (usually the more cloud the worse the image quality).

Traditional satellite mission planning systems cannot acquire cloud cover information; hence, it requires integration of demand with resources on the ground to generate a feasible plan, which would then have to be uploaded to satellite via a high-speed network. A high-speed data transmission network has directionality and is related to the distribution of ground stations. In these experiments, we assume two time windows for data transmission as below:

Tab. 4. Task attributes received by imaging satellite

Task id	Imaging time /(s)	Starting Time	End Time	Task Arrival Time	Cloud Level
1	10	02:14:30	02:17:58	00:00:00	2
2	16	02:17:50	02:21:15	00:00:00	3
3	15	02:27:50	02:31:10	00:00:00	4
4	14	02:35:39	02:39:02	00:00:00	5
5	08	02:21:41	02:25:12	00:00:00	1
6	06	04:11:28	04:14:50	00:00:00	2
7	12	03:51:56	03:55:21	00:00:00	4
8	14	03:52:47	03:56:11	02:12:00	8
9	06	03:51:52	03:55:15	02:12:00	2
10	10	03:50:46	03:54:10	02:12:00	2
11	14	04:08:33	04:11:58	02:12:00	9
12	12	04:09:46	04:13:10	02:45:30	3
13	09	05:32:30	05:35:56	02:46:12	7
14	06	05:32:33	05:35:55	02:46:12	2
15	08	05:53:26	05:56:51	02:59:28	8
16	10	05:52:58	05:56:22	02:59:45	2
17	06	05:53:57	05:57:21	03:00:07	1
18	06	05:40:47	05:44:07	03:00:22	3
19	08	05:39:18	05:42:40	03:00:24	5
20	10	05:39:17	05:42:39	03:00:24	6

Tab. 5. Ground station information

g	orb	FST	FET
1	1	01:37:23	01:43:47
2	1	01:40:20	01:46:39

An autonomous satellite mission planning system would have no need for information processing throughout such as upload orders or codes, because each task carries a small data volume. This would enable us to use a low-speed monitoring network, or to repeat satellite communication, to use a short message, and other forms of upload instructions to realize satellite autonomous planning and management.

Because of the limited range of the cloud probe, the mission planning system will be event-driven in autonomous mode, thereby ensuring that planning occurs within the range of the cloud probe. We compared the test results of different algorithms in a framework based on two systems by applying an improved dynamic programming (IDP) algorithm and depth-first search (DFS) algorithm in the two frames. This enabled us to obtain the results in a different frame with a different algorithm.

ANALYSIS FOR TEST AND RESULTS

We combined the processes in Sec. 5.1 by using C++ language in Visual Studio 2010 to build the testing platform and installed this system in a computer with the following configuration: processor model core i5 (2.6 GHz), memory 8 GB, 64-bit Windows 7 operating system. Next, we input the original data for testing, after which we obtained the final mission plan and simulation result for the completion of each task. This allowed us to generate an index for the direct evaluation of system planning. The utilization rate for return resources, dynamic task response rate, environmental change response rate, and program running time are as follows:

Utilization rate for return resources: In all returned data, the proportion for valuable data. In reality, the value of data is related with many factors. In this test, if the cloud level is over 5, then we consider the image to be worthless.

further divided into different observation windows based on the cost of resources. This method ignores the differences between different earth observation demands, and may not be able to support complex earth observation missions in the future.

Addressing this problem requires the use of flexible earth observation mission preprocess technology. This technology is intended to support different demand types (pre-ordered mission, dynamic arrived mission, and rapid response mission) with different types of preprocessing methods considering the responsiveness requirement (i.e., in the case of rapid response missions, some of the highly time-consuming processes, e.g., the mission merging process, can be eliminated). Furthermore, flexible preprocessing technology has the ability to forecast the strict mission constrains in the next planning horizon, based on current onboard resource conditions, when new mission requirements are uploaded. This facilitates efficient planning by the mission planning software. Finally, this technology should have the ability to eliminate redundancy requirements to ensure the efficient division of limited onboard computational resources.

CONFIGURABLE MISSION PLANNING AND SCHEDULING ALGORITHM

The importance of the mission planning and scheduling algorithm to increase the effectiveness of earth observation missions is undeniable. Currently, satisfying the increasing demand for earth observation with limited earth observation resources is problematic. Thus, a flexible and configurable (i.e., capable of supporting different types of earth observation missions under fluctuating environmental conditions) mission planning and scheduling algorithm to solve this problem is obviously important.

The method could use machine-learning methods to extract information from past mission sets to forecast the conditions of future mission areas. Then, it could dynamically configure its mission planning and scheduling operators to fit the future mission environment. This method focuses on the dynamic factors of an earth observation mission and thus can be expected to achieve an increase in mission planning efficiency. Note that because the adjustments made to this method are intended to enable it to fit a dynamic mission set, the machine-learning process can be accomplished off-board. However, this method also needs past mission information to extract mission area characteristics of different situations.

EOS OPERATION SYSTEM ONBOARD RECONFIGURATION TECHNOLOGY

Next generation EOSs face the requirement of cooperation with other EOSs in an EOS network to complete complex earth observation missions. In special situations, an EOS may communicate and cooperate with other EOSs in different EOS networks. Thus, next generation EOSs should have the ability to perform a partial onboard reconfiguration (especially the communication and mission planning mechanism) to fit the requirements of different EOS networks. On the other

hand, onboard system reconfiguration would also be able to solve some onboard hardware errors owing to the wide application of FPGA and onboard EOS hardware health monitoring technologies. When an onboard hardware error occurs, the FPGA will be activated and the onboard system will be reconfigured in real time to ensure uninterrupted operation of the other parts. This technology would reduce the maintenance costs and increase the error tolerance ability of next generation EOSs.

“PLATFORM PLUS PLUGINS” SYSTEM FRAMEWORK

Current EOS operation systems are mostly unchangeable once they are built. However, next generation earth observation missions require the EOS operation system to change the functions of its subsystems to meet special observation requirements. Moreover, it is noticeable that in most of the life cycle of an EOS, the onboard computational resources are not completely used. In addition, the function of a computational resource may not remain unchanged during the life cycle of the EOS (e.g., the function of EO-1 has been changed from a high-resolution EOS to an EOS network pathfinder). As a result, a “platform plus plugin” system framework is needed. When the EOS mission environment is changed, this framework would make it possible to upload some new plugins to the onboard operation system to help it accommodate the new environment. This technology is expected to reduce the development and maintenance costs of the EOS.

4.6 USER DEMAND AUTONOMOUS MINING TECHNOLOGY

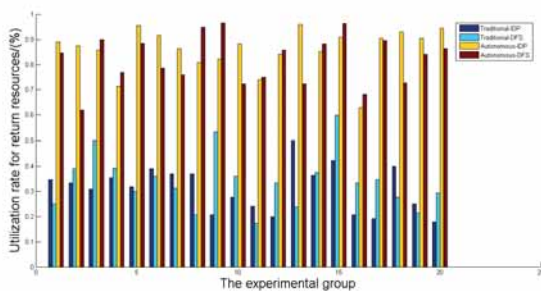
Current earth observation missions are mostly offered by professional EOS users, who are familiar with the constraints and abilities of the EOSs they want to use. However, this situation is expected to change in next generation earth observation activates. The users of next generation EOSs will mostly be nonprofessional users, and most of them would have little knowledge as to how an EOS functions. Thus, they would not have the ability to offer a standard earth observation mission. This problem would have to be addressed by equipping the EOS mission control system as well as the EOS onboard operation system with the ability to perform autonomous user demand mining. Some of these demands (but not limited to) could be: help users to divide their requirement into standard earth observation missions; help users to find the specific high-value information in which they are interested (e.g., users who are concerned about wildfires would obviously find the infrared information valuable); to help important users build their own knowledge database based on the missions they offer; decision making technology based on key mission information, which means that the EOS operation system could autonomously produce earth observation missions based on a user’s knowledge database (i.e., when EOS receives an alert that a volcano may erupt, a new observation mission will be produce autonomously to offer rapid response information to institutional users

Dynamic task response rate: Generally, task processing and planning are considered to occur in real time shortly after task arrival.

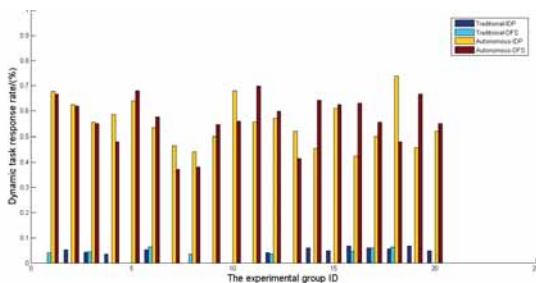
Environmental change response rate: it is the ratio between the task of automatically adjusting the imaging strategy when detecting the related environmental information and total task quantity.

Program running time: it is the total time required for a full simulation when program initiation to all tasks is included.

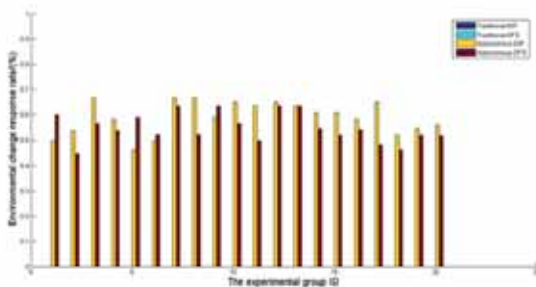
Parameter input was accomplished by using a pseudo-random function, as a result of which we designed 20 sets of input data with different quantities and characteristics. The results in Fig. 4 were generated by performing a simulation and analysis on these datasets.



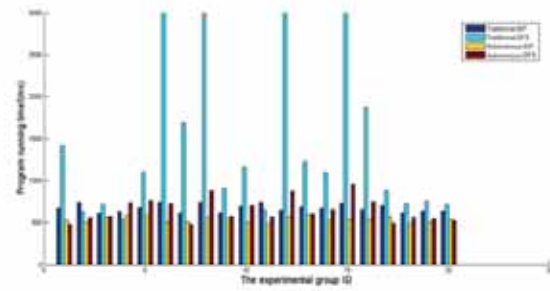
(a) Utilization rate for return resources



(b) Dynamic task response rate



(c) Environmental change response rate



(d) Program running time

Fig. 4. Comparison of the results obtained for the traditional system and simulation systems.

Figure 4(a) indicates that the data transmission utilization rate has greatly improved in the case of the auto mission planning system. This is attributed to the ability of the auto mission planning system to actively avoid clouds in the process of observation arrangement, during which it will choose low cloud level as the priority task. In fact, tasks conducted in the presence of high cloud level might not be useless; thus, if the satellite is equipped with a mature model recognition algorithm, it can arrange imaging and returning for all resources and time window conditions allowed to avoid neglecting to acquire some useful information. It can autonomously decide which information is useful and needs to be returned to the ground station after imaging.

In Fig. 4(b), it can be seen that the autonomous mission-planning model can effectively and timely process tasks dynamically upon arrival. In contrast, traditional satellite mission planning systems are only capable of conducting real-time planning in the data transmission time window; hence, their dynamic task response rate is 0. When we require imaging in the event of an emergency, a traditional satellite mission planning system would not necessarily be able to respond.

Figure 4(c) shows that a traditional satellite cannot respond to dynamic environmental change because it cannot detect and analyze the influence of weather conditions on mission planning. Even if the ground station succeeds in re-planning after receiving the real-time satellite running environment information it would be unable to upload the orders or instructions to the satellite in time. An autonomous satellite mission planning system is equipped with an additional module to detect and process environmental information. This capability enables it to proactively avoid the impact of poor environmental conditions and to improve the overall planning.

In Fig. 4(d), it can be seen that the auto mission planning system generally requires less time to run than the non-autonomous system, but this conclusion would have to be confirmed by investigating the influence of the different structures of the two planning systems on the program running time by performing additional testing. Because of the complexity of the problem, we decided to set the maximum elapsed time as 3000 ms to prevent a situation of plugging

into a local optimum. Traditional planning systems using a DFS algorithm to artificially set a desired target value will stop running when the desired target is achieved; otherwise they continue searching the solution space. In the autonomous system, the problem is decomposed into several sub-problems according to the time, thereby greatly reducing the solution space and simultaneously reducing the running time of the program to within a controllable range. The use of different algorithms in the system has an impact on the time efficiency and the optimization effects, which differ accordingly. Establishing the relationship between the algorithm and the input parameters is a problem that needs to be solved in the next step of system design.

CONCLUSION

This thesis elaborates a design frame for an auto mission planning system for imaging satellites. The new application environment and new task requirements divide the satellite mission planning system into two subsystems: the satellite and ground station systems. The imaging satellite needs to realize four main functional requirements and the system was applied to three typical scenarios to solve problems encountered in the practical applications of satellites to constantly improve its system design in different scenarios. In the future, we plan to mainly focus on enabling the six key technologies to improve the effectiveness of the imaging satellite as a tool to obtain information on a variety of human activities.

In reality, China's satellite network is becoming increasingly complex. Thus, once users have proposed an imaging task, they do not necessarily understand the characteristics and constraints of each satellite; neither do they care about how the system allocates resources for the operation. Under the proposed system framework, users only need to put forward their desired results, whereupon the system would determine how to arrange the resources to achieve these results. Finally, the simulation test conducted with both the traditional and new autonomous satellite mission planning systems, indicated that the new satellite mission planning system can optimize the satellite mission planning time complexity and resource utilization efficiency with higher stability and faster convergence speed.

ACKNOWLEDGEMENT

First and foremost, I would like to express my deepest gratitude to my school, the National University of Defense Technology, who provided me with a perfect intellectual atmosphere, such that I could write this article successfully. This research is supported by the National Natural Science Foundation of China (Grant Nos. 71331008 and 71101150). Finally, I want to thank all my schoolmates, especially each person working in my lab, for their encouragement and support.

REFERENCES

1. J. C. Li, Album of world satellites in orbit, Beijing: National Defense Industry Press, 1-32. (In Chinese) (2014).
2. B. N. Zhang, Survey on technical development of optical remote sensor on Chinese resource satellite, Chinese Space Science and Space Exploration Society of Professional Committee of Twenty-Sixth National Symposium on Space Exploration, 327-333(In Chinese) (2013).
3. S. Baek, S. Han, K. Cho, et al., "Development of a scheduling algorithm and GUI for autonomous satellite missions." *Acta Astronaut.* 68(7), 1396-1402 (2011).
4. C. Pralet, G. Verfaillie. "Using Constraint Networks on Timelines to Model and Solve Planning and Scheduling Problems," in ICAPS 8, 272-279 (2008).
5. L. Shumin, Z. Zheng, C. Kai-Yuan. Robust task scheduling of multi-satellite parallel test. *Control Conference (CCC), 2011 30th Chinese.* IEEE, 2152-2157 (2011).
6. S. Chien, R. Sherwood, D. Tran, et al., "Using autonomy flight software to improve science return on Earth Observing One," *J. Aeros. Comp, Inf. Commun.* 2(4), 196-216 (2005).
7. S. J. Delany, S. Ontañón. Case-based reasoning research and development, 8th International Conference on Case-Based Reasoning. Washinton, USA. 20-23 (2009).
8. Z. Lian, Y. Tan, Y. Xu, Static and Dynamic Models of Observation Toward Earth by Agile Satellite Coverage, *Proceedings of International Workshop on Planning and Scheduling for Space.* Darmstadt, Germany: ESOC. 1-6 (2011).
9. R. L. Sherwood, S. Chien, D. Tran et al., *Intelligent systems in space: the EO-1 Autonomous Sciencecraft.* Pasadena, CA: Jet Propulsion Laboratory, National Aeronautics and Space Administration (2005).
10. H. J. You, W. N. Chen, X. G. Zhou et al., "Scalable architecture model for Spacecraft's electronic system," *Syst. Eng. Electron.* 35(2):263-269 (2013) (In Chinese).
11. S. Laubach. Calculation of Operations Efficiency Factors for Mars Surface Missions, *SpaceOps 2014,* Pasadena, CA. AIAA, 1778-1786 (2014).
12. M. L. Pinedo, *Scheduling: theory, algorithms, and systems.* Springer Science & Business Media, 252-374 (2012).
13. R. Knight, G. Rabideau, S. Chien et al. "Casper: Space exploration through continuous planning," *Intelligent Systems, IEEE* 16(5), 70-75 (2001).

14. S. Chien, D. Tran, G. Rabideau et al., "Planning Operations of the Earth Observing Satellite EO-1: Representing and reasoning with spacecraft operations constraints," (2009).
15. F. Ip, J. M. Dohm, V. R. Baker et al., "Flood detection and monitoring with the Autonomous Sciencecraft Experiment onboard EO-1," *Remote Sens. Env.* 101(4), 463-481 (2006).
16. G. Rabideau, R. Knight, S. Chien, A. Fukunaga, A. Govindjee, Iterative Repair Planning for Spacecraft Operations in the ASPEN System, International Symposium on Artificial Intelligence Robotics and Automation in Space, Noordwijk, The Netherlands, (1999).
17. B. Zhukov, E. Lorenz, D. Oertel et al., "Spaceborne detection and characterization of fires during the bi-spectral infrared detection (BIRD) experimental small satellite mission (2001–2004)," *Remote Sens. Env.* 100(1), 29-51 (2006).
18. G. Ruecker, E. Lorenz, A. A. Hoffmann et al., High Resolution Active Fire Monitoring for Global Change Analysis: The Upcoming FireBIRD Satellite Mission, The 5th International Wildland Fire Conference, Sun City, South Africa. 134-144 (2011).
19. W. Jiang, H. C. Hao, Y. J. Li, "Review of task scheduling research for the Earth observing satellites," *Syst. Eng. Electron.* 35(9):1878-1885 (2013) (In Chinese).
20. M. A. Gleyzes, L. Perret, P. Kubik, "Pleiades system architecture and main performances," *Int. Arch. Photogramm. Remote Sens. Spat. Inf. Sci.*, 39: B1, 537-542 (2012).
21. D. Greslou, F. de Lussy, J. M. Delvit, et al., "Pleiades-HR innovative techniques for geometric image quality commissioning," *Int. Arch. Photogramm. Remote Sens. Spat. Inf. Sci.*, 39: B1, 543-547 (2012).
22. G. Beaumet, G. Verfaillie, M. C. Charmeau, "Autonomous planning for an agile earth-observing satellite," in *iSAIRAS*, pp. 1-6, (2008).
23. M. K. Griffin, K. B. Hsiao-hua, D. Mandl et al., Cloud cover detection algorithm for EO-1 Hyperion imagery, *AeroSense 2003. International Society for Optics and Photonics* 483-494 (2003).
24. Y. H. Guo. Research on the key technology of combining multiple types of EOSs with multiple types of data transmitting resources. Changsha: National University of Defense Technology, 2009. (In Chinese)
25. A. G. Davies, S. Chien, D. Tran et al., "The NASA Volcano Sensor Web, advanced autonomy and the remote sensing of volcanic eruptions: a review," *Geological Society, London, Special Publications* 426, SP426. 3 (2015).
26. G. Beaumet, G. Verfaillie, M. C. Charmeau, "Feasibility of autonomous decision making on board an agile earth-observing satellite," *Comput. Intelligence*, 27(1): 123-139, (2011).
27. D. Izzo, L. Pettazzi, "Autonomous and distributed motion planning for satellite swarm," *J. Guid. Control Dynam.* 30(2), 449-459 (2007).
28. Y. Long, P. Wang, Z. Zhang et al., "Uplink Task Scheduling Model and Heuristic Algorithm of Satellite Navigation System," *Adv. Inf. Sci. Service Sci.* 4(16), 450-461 (2012).
29. G. Beaumet, "Continuous planning for the control of an autonomous agile satellite," *ICAPS 2006*, 13 (2006).
30. N. Chen, X. Wang, X. Yang, "A direct registry service method for sensors and algorithms based on the process model," *Comp. Geosci.* 56, 45-55 (2013).
31. D. S. Qiu, J. J. Wang, C. B. Wu et al., "Emergency scheduling method of earth observation satellites based on task merging," *Syst. Eng. Electron.* 35(7), 1430-1437 (2013) (In Chinese).
32. S. Bernardini, M. Fox, D. Long, et al. Autonomous Search and Tracking via Temporal Planning, *ICAPS*. 481-489 (2013).
33. S. A. Chien, R. Knight, A. Stechert et al., Using Iterative Repair to Improve the Responsiveness of Planning and Scheduling, *AIPS*. 300-307 (2000).
34. G. Beaumet, G. Verfaillie, M. C. Charmeau, "Decision-making on-board an autonomous agile Earth-observing satellite," *ICAPS (SPARK)* (2008).
35. A. Altinok, D. R. Thompson, B. Bornstein et al., "Real-Time Orbital Image Analysis Using Decision Forests, with a Deployment Onboard the IPEX Spacecraft," *J. Field Robot* (2015).
36. M. Lemaître, G. Verfaillie, "Interaction between reactive and deliberative tasks for on-line decision-making", in *International Conference on Automated Planning and Scheduling, ICAPS'07 Workshop on Planning and Plan Execution for Real-World Systems*, Providence, RI, USA (2007).
37. P. F. Maldague, A. Y. Ko, JIT planning: an approach to autonomous scheduling for space missions, *Aerospace Conference, 1999. Proceedings. 1999 IEEE*. IEEE, 1: 339-349 (1999).
38. R. Knight, S. Chien, Producing Large Observation Campaigns Using Compressed Problem Representations, *International Workshop on Planning and Scheduling for Space*, Space Telescope Science Institute, Maryland (2006).

39. S. Chien, R. Knight, G. Rabideau, An empirical evaluation of the effectiveness of local search for replanning. Springer Berlin Heidelberg (2001).
40. E. Gat, "On three-layer architectures," Artificial intelligence and mobile robots, 195: 210 (1998).
41. Adnan, F.A.F.; Hamylton, S.M.; Woodroffe, C.D., Surf-Swash Interactions on a Low-Tide Terraced Beach, Journal of Coastal Research, SI75, 348-352 (2016).
42. D. R. Thompson, A. Altinok, B. Bornstein, et al., "Onboard machine learning classification of images by a cubesat in Earth orbit," AI Matters, 4, 38-40 (2015).
43. Zieja, M; Wazny, M. A model for service life control of selected device systems. Polish Maritime Research, 21(2) 45-49 (2014).

CONTACT WITH AUTHOR

Lining Xing

National University of Defense Technology,
College of Information System and Management,
Sanyi Road,
Changsha 410073,
China

E-mail: xing2999@qq.com

OPTIMAL CONFIGURATIONS OF WAVE ENERGY CONVERTER ARRAYS WITH A FLOATING BODY

Wanchao Zhang,
Hengxu Liu,
Xuewei Zhang,
Liang Zhang,
Muhammad Aqeel Ashraf,

College of Shipbuilding Engineering, Harbin Engineering University, Harbin, China
Faculty of Science and Natural Resources, University Malaysia Sabah 88400 Kota Kinabalu Sabah,
Malaysia

ABSTRACT

An array of floating point-absorbing wave energy converters (WECs) is usually employed for extracting efficiently ocean wave energy. For deep water environment, it is more feasible and convenient to connect the absorbers array with a floating body, such as a semi-submersible bottom-moored disk, whose function is to act as the virtual seabed. In the present work, an array of identical floating symmetrically distributed cylinders in a coaxial moored disk as a wave energy device is proposed. The power take-off (PTO) system in the wave energy device is assumed to be composed of a linear/nonlinear damper activated by the buoys heaving motion. Hydrodynamic analysis of the examined floating system is implemented in frequency domain. Hydrodynamic interferences between the oscillating bodies are accounted for in the corresponding coupled equations. The array layouts under the constraint of the disk, incidence wave directions, separating distance between the absorbers and the PTO damping are considered to optimize this kind of WECs. Numerical results with regular waves are presented and discussed for the axisymmetric system utilizing heave mode with these interaction factors, in terms of a specific numbers of cylinders and expected power production.

Keywords: Wave energy; cylinder array; power take-off; hydrodynamic analysis

INTRODUCTION

The slow-speed periodic waves with large forces can cause periodic resonant motion of buoys relative to a reactant through which the wave energy can be extracted. This oscillating bodies utilizing heave mode which have small horizontal dimensions compared with the incident wave length have been defined as the simplest point-absorber wave energy converters. In the real sea, especially in deep water, the absorbers are often deployed in arrays connected to a bottom moored disk which makes them more stable, reliable and cost-effective. However, in such case, within the absorbers array, the interactions between the bodies due to diffracted waves and waves radiated by the oscillations of the bodies will occur. The wave energy conversion ability of the WECs array

can be strongly impacted by these interactions depending on the incident waves, separating distances between the bodies and array layouts, as well as the PTO damping.

The pioneer work of studying the interactions that affect the WECs array can be traced to Budal [1] who put forward an interaction factor to assess the effect of the interaction depended on the array configurations and the separating distances between the bodies. For his study, the absorbers are assumed to be small to neglect the scattered wave. Subsequent work are carried out by Falnes and Budal [2] who affirmed that whether the effect is constructive depends on the incident wave frequencies and the array layouts. Based upon their theories, McIver [3] analyzed the wave power absorption performance of the array by setting unequal spacing of devices and constraining the amplitudes of device motions

through surge or heave motions. He found that the wave power absorption performance of the array is dramatically depended on the incidence wave directions in heave and less sensitivity to that in surge. Fitzgerald and Thomas [4] proceeded further in this direction, studying the effect of the variations of array geometries and incident wave directions on the wave power conversion performance of a five hemispheres array. The interaction factor is found to be equal to unity over all the incident wave directions $0 \sim 2\pi$. The most recent studies on the interactions correspond to researchers [5-12] Weller et al. [6] examined the interaction factors of the floaters array through experiment measurement in regular and irregular waves and found that whether the interaction is positive depends on the displacements of the floaters, incident wave periods and the performance of adjacent devices. Child and Venugopal [7] optimized a generic point absorbers array by adjusting the incident wave directions and the array layouts through two different methods (parabolic intersection and genetic algorithm methods). Babarit [8] examined two two-body oscillating WECs with heave or surge motions and demonstrated that when the separating distance is over 2000 m, the interactions are wake and can be negligible which is very important in the preliminary design of a WECs farm in the real sea. Most of the latest studies carried out on the WECs array and power optimization correspond to [13-17]. Andres et al. [14] exceed further in this kind of two-body oscillating WEC through varying the array layout, the separating distance, the number of WECs and the wave directions. Their results suggested that the wave directions and number of WECs are major factors to make the interactions constructive and the triangular array layout may be more adaptable in irregular waves. Finally, Goteman et al. [16] made it more extreme on the study of the number of WECs. They optimized a wave energy park which contains over 2000 point absorbers including global geometries, number of devices, separating distance between devices and sea states by using an approximate analytical method.

Most of the WEC devices considered in the former studies are isolated and installed directly connected to the sea floor which makes them possible with typical large separating distances of few hundreds of meters. However, for practical reasons (limitation of sea area and economic cost for example), the arrays of WECs cannot be isolated and sparse especially in such water depth. It may be more credible and adaptable to connect the absorbers array with a floating moored disk on which the PTO mechanism can be installed. Therefore it is particularly significant and necessary to analyze the interaction factors under the constraint of the disk such as the separating distances, array layouts and PTO damping. As a matter of fact, the PTO damping also has a great effect on the wave energy conversion performance even though few of researchers have paid their attention to the PTO damper (linear or nonlinear). The special work can correspond to Sheng et al. [19], Sheng and Anthony [20,21] who optimized the PTO damper considering the variation of PTO damping coefficients and velocity index.

The aim of this paper is to investigate the potential for wave energy extraction with an array of WECs at intermediate

water depth considering different incident wave directions, array layouts, separating distances and PTO dampers. As the absorbers should work against the reactant to activate the actuator which is difficult to be installed on the seabed in such water depth, a moored reactant is needed. Thus, in this work, arrays of identical vertical floating absorbers symmetrically distributed over and sliding along some guides attached to a coaxial moored semi-submersible disk were proposed as a WEC device for extracting wave energy as shown in Fig.1. Numerical results concerning for the hydrodynamic coefficients and the wave excitation forces in heave are presented for a specific case of four identical cylinders over a plate considering different incident wave angles. Three special array layouts with varying wave directions, separating distances and linear PTO damper are conducted to examine the effect of these factors on the wave power absorption performance. Emphasis is given on the optimization of captured wave energy by choosing the appropriate PTO damping coefficients and velocity indexes.

MATHEMATICAL MODEL

The array of WECs employed in this paper is illustrated in Fig.1 which contains a semi-submersible disk and N ($N=1, 2, \dots$) floating absorbers. The multi-body oscillating system with mooring system is thought to be in static equilibrium in still water, and their vertical oscillations are measured relative to their positions of static equilibrium in this paper. Consistent with a frequency-domain treatment, sinusoidal incident waves at frequency ω are assumed. The linear superposition of diffraction and radiation forces follows from the small-amplitude assumption. Straightforward application of Newton's laws leads to the equations of motion for system in Fig.1.

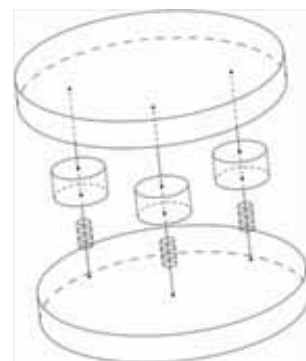


Fig.1. Sketch of the device

We denote the masses of the cylinders and the disk as m_q ($q=0, 1, \dots, N$). Here and hereafter, the subscript q ($q=0, 1, 2, \dots, N$) denotes body q of this complex system. It represents the semi-submersible disk when $q=0$ and the q -cylinder when $q=1, 2, \dots, N$. In such case, the hydrostatic restoring force stiffness of body q can be denoted as $k_q = \rho g S_q$. Here, ρ denotes the density of sea water, g denotes the acceleration due to gravity and S_q denotes the water plane area of body q . In this paper, the bottom structure of the disk is through to be

a submerged plate. The support columns where the cylinders are installed are assumed to be small-scale components and have little effect on the hydrodynamic performance. In such case, the water plane areas of the disk are assumed to be zero. Further, we define the controllable resistive load coefficient as c_q which comprise the q -actuator activated by the cylinder q ($q = 1, \dots, N$) and the disk ($q = 0$). The equation of heave motion in regular waves for this system is

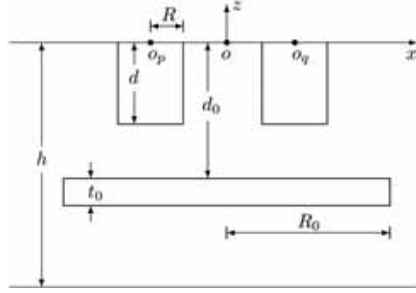


Fig.2. Simplified model and geometries

$$\mathbf{M}\ddot{\mathbf{Z}} = \mathbf{F}_{ex} + \mathbf{F}_r + \mathbf{F}_s + \mathbf{F}_t + \mathbf{F}_{PTO}$$

with: $\mathbf{Z} = \Re(\bar{Z}e^{-i\omega t})$ and $\dot{\mathbf{Z}}, \ddot{\mathbf{Z}}$ being, respectively, the velocity and acceleration vectors of the system in heave (1)

$\mathbf{M} = \text{diag}(m_0, m_1, \dots, m_N)$, the inherent mass matrix of the system

$\mathbf{F}_{ex} = \Re(\bar{F}e^{-i\omega t})$, the excitation force vector per unit of wave amplitude, associated to the action of incident and diffracted wave fields upon the WECs

$\mathbf{F}_r = -\mathbf{M}_\omega \dot{\mathbf{Z}} - \mathbf{B}_\omega \mathbf{Z}$, the radiation force vector due to the bodies' oscillation in the otherwise calm water, in which $M_\omega(p, q) = \mu_{pq} = \mu_{qp}$ and $B_\omega(p, q) = \lambda_{pq} = \lambda_{qp}$. Here, μ_{pq} and λ_{pq} ($p, q = 0, 1, \dots, N$) denote the added mass and damping coefficients of body p due to the oscillation of body q .

$\mathbf{F}_s = -\mathbf{K}_s \mathbf{Z}$, the hydrostatic force vector of the system with $\mathbf{K}_s = \text{diag}(k_0, k_1, \dots, k_N)$.

$\mathbf{F}_t = -\mathbf{K}_t \mathbf{Z}$, the force vector of possible moorings. In this study, it was neglected, i.e. $\mathbf{K}_t = 0$.

$\mathbf{F}_{PTO} = -\mathbf{B}_{PTO} \dot{\mathbf{Z}}$, the force vector of the actuators activated by the absorbers' and the disk's oscillations. \mathbf{B}_{PTO} is the PTO damping coefficients matrix and $B_{PTO}(q, q) = c_{q-1}$, $B_{PTO}(1, q) = B_{PTO}(q, 1) = -c_{q-1}$ with $q = 2, \dots, N+1$ and $\mathbf{B}_{PTO}(1, 1) = \sum_{q=1}^N c_q$ with $c_q = C_{PTO} |\omega \bar{Z}_0 - \omega \bar{Z}_q|^\alpha$. The superscript α is the velocity index. In this study, both the linear ($\alpha = 0$) and nonlinear ($\alpha > 0$) PTO damping forces are considered. The not listed elements in this matrix are zero.

In such case, in regular waves, the time-averaged wave power extracted by each absorber in the array per unit of wave amplitude can be calculated and expressed as

$$\bar{P}_q = 1/2 \omega^2 c_q (\bar{Z}_q - \bar{Z}_0)(\bar{Z}_q - \bar{Z}_0)^* \quad (2)$$

with $q=1, \dots, N$ and the asterisk denotes the conjugate complex. For the whole array, the mean absorbed power is

$$\bar{P} = \sum_{q=1}^N \bar{P}_q \quad (3)$$

To obtain the excitation forces, added mass and radiation damping coefficients in heave, for linear water wave theory, it is convenient to decompose the velocity potentials in the fluid around the device as

$$\Phi = \Phi_D + i\omega \sum_{p=1}^N A_p \Phi_p \quad \text{with} \quad \Phi_D = \Phi_I + \Phi_S \quad (4)$$

Where Φ_D is the diffracted velocity potential which contains incident wave velocity potential Φ_I and scattered wave velocity potential Φ_S . Φ_p stands for radiated velocity potential in heave of body p ($p = 0, 1, \dots, N$). According to the potential flow theory, the velocity potentials should satisfy:

Laplace's equation:

$$\nabla^2 \Phi_{D,p} = 0 \quad (\text{in fluid}) \quad (5)$$

Free surface condition:

$$-f^2 \Phi_{D,p} + g \partial_z \Phi_{D,p} = 0 \quad (z = 0) \quad (6)$$

Bottom condition:

$$\partial_z \Phi_{D,p} = 0 \quad (z = -h) \quad (7)$$

Radiation condition:

$$\lim_{r \rightarrow \infty} \sqrt{r} (\partial_r \Phi_{D,p} - ik \Phi_{D,p}) = 0 \quad (8)$$

Hull boundary condition on $S^{(p)}$:

$$\partial_{n_p} \Phi_q = \delta_{pq} n_3^q, \quad \partial_{n_p} \Phi_D = 0 \quad (9)$$

Here the subscripts and superscripts p, q ($p, q = 0, 1, \dots, N$) denote the body p and body q , $f^2 = \omega^2/g$ with ω as the wave frequency and g the acceleration due to gravity. The wave number k is defined by the dispersion equation $k \tanh kh = f^2$ which is obtained by satisfying the boundary conditions. Here and hereafter, $\partial n(\cdot)$ denotes the derivative in the direction of the outward unit normal vector n to the mean wetted surface $S^{(p)}$ of the body p , δ_{pq} is the Kronecker's symbol and n_3^q is the normal component in the vertical direction.

Thus the non-dimensional first order force in heave direction is given by integrating the pressure on the hull and expressed by

$$F_p = -i\omega/g R_p^2 \int_{S^{(p)}} \Phi_D n_3^p ds \quad (p = 0, 1, \dots, N) \quad (10)$$

The added mass and the damping coefficients of body p by body q 's oscillation can be defined by

$$\mu_{pq} + i\lambda_{pq}/\omega = 1/R_p^3 \int_{S^{(p)}} \Phi_q n_3^p ds \quad (p, q = 0, 1, \dots, N) \quad (11)$$

ADDED MASS, RADIATION DAMPING AND WAVE FORCING

As mentioned before, this paper is focus on accessing the factors that influence the wave energy conversion performance and optimizing the WECs array. The water depth and the geometries of the structures are not included in these influence factors though they may have a great influence on the calculated results. For simplicity of hydrodynamic

calculation, the upper structures of the disk are assumed to be out of water and the bottom ones are simplified as a submerged plate in this wave power capturing process. In such case, the water depth and the geometries of the structures as shown in Fig.2 should be confirmed and given as $h = 50$ m, $R/h = 0.04$, $R_0/R = 4.0$, $d/R = 2.5$, $d_0/R = 4.0$ and $t_0/R = 0.5$ in this study.

A four cylinder array over a plate is considered in this paper and the array layouts are shown in Fig.3. Layout (a) is a square configuration consisting of two lines of absorbers. Layout (b) is a rhombus configuration consisting of two equilateral triangles. Finally, layout (c) is an equilateral triangle configuration with another absorber at the central point. Above all the three array layouts, the geometric center of the configurations and the center of the plate are coincident.

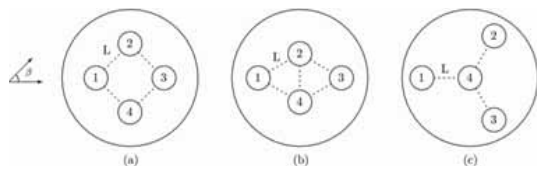


Fig.3. Layouts of the absorbers array

To provide the hydrodynamic coefficients M_ω , B_ω and F_ω for the optimization, a BEM based FORTRAN code is used. The calculated hydrodynamic coefficients are plotted in Fig.4 in the case of array layout (a) with incident wave direction $\beta = 0^\circ, 45^\circ$ and separating distance $L/R = 0.5, 1.5$. The illustrated added mass gives an expected result that the cross coupled added mass decreases with the increase of the separating distance. However, the added mass caused by the cylinder's own oscillation also shows the same trend. Particular attention should be given that the frequency-dependent amplitude reduction of the added mass seems to be the same except those happen in the range of $[0.7, 2.5]$ rad/s. In this frequency range, we notice a great change in the amplitude reduction with the variation of the separating distances. In the upper-right subgraph in Fig.4, the radiation damping stays the same outside this frequency range, and shows great change in the frequency range especially when the frequency $\omega = 1.8$ rad/s with different separating distances.

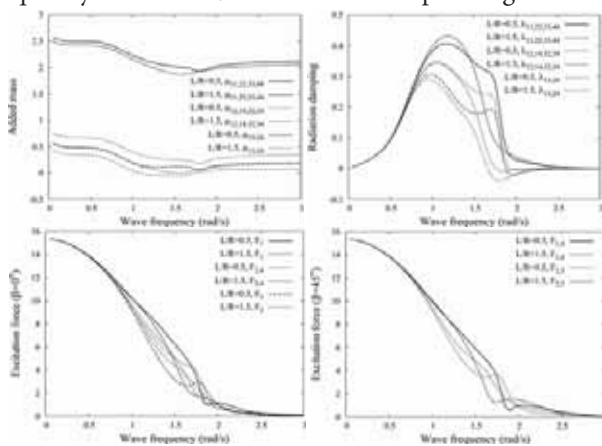


Fig.4. Non-dimensional added mass (upper-left), radiation damping (upper-right) and wave excitation force (below) in array layout (a) with incident wave direction ($\beta = 0^\circ, 45^\circ$) and separating distance ($L/R = 0.5, 1.5$)

About the excitation forces, the similar phenomenon also occurs. The incidence angles and separating distances play major roles in determining the degree of hydrodynamic interference in the same frequency range. On these evidences, the effect of incident wave direction and separating distance are not significant outside this frequency range and therefore might reasonably be neglected when estimating damping and excitation forces which are highly correlated to the wave energy conversion.

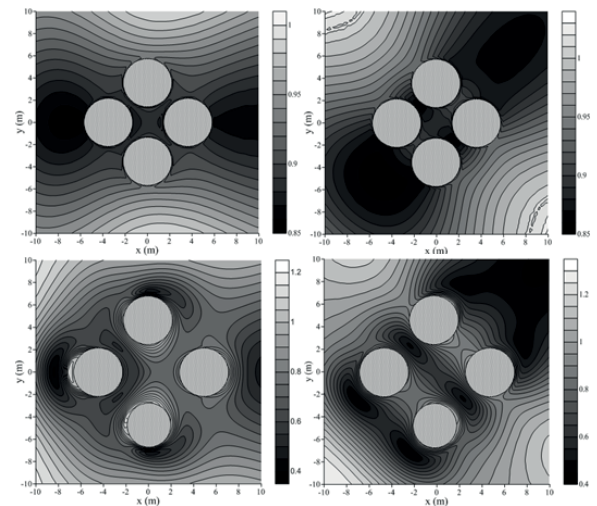


Fig.5. Non-dimensional elevations at the free surface in array layout (a) with incident wave direction ($\beta = 0^\circ, 45^\circ$) and separating distance ($L/R = 0.5, 1.5$)

NUMERICAL RESULTS

This section will deal with the factors that affect the wave energy conversion performance and optimizing this kind of WECs array. As mentioned before, the factors include the array layout, the separating distance, the incidence wave direction and the PTO damping. Of all the four factors, the PTO damping's effect includes the effect of the PTO damping type (linear and nonlinear) and that of the damping coefficient value. In such case, in the study of the first three factors, the PTO damping is assumed to be linear and the coefficient is set to be 10 kN/s/m.

As is known to all, the wave energy conversion performances of oscillating-typed WECs are usually highly dependent on the incident wave frequency and natural frequencies of the oscillators in the analysis based upon the potential flow theory. In addition, the resonance condition is that the natural frequency of the absorber approaches the frequency of the incident wave. Thus, the undamped natural frequency ω_n of the absorber should be an important reference condition for the following analysis and defined as $\omega_n^2 = k/(m+\mu)$. Here, k , m and μ denote the hydrostatic restoring force stiffness, the inherent mass and added mass of the absorber respectively. In such case, the range of the natural frequencies of the absorbers for the considered array layouts with different separating distances can be obtained and recorded in table 1.

As shown in table 1, the natural frequency ranges are almost the same and in such case, the frequency being choose to analyze the factors will be near this frequency range [1.2,

1.3]. Fig.5~7 show the wave energy conversion performance with separating distance for the considered three array layouts at frequency $\omega = 1.0, 1.25$ and 1.5 rad/s with different incident wave directions.

Table 1 Range of the natural frequencies

Layout No.	L/R=0.5	L/R=1.0	L/R=1.5	L/R=2.0
(a)	[1.216, 1.255]	[1.218, 1.258]	[1.220, 1.259]	[1.222, 1.260]
(b)	[1.217, 1.251]	[1.220, 1.256]	[1.223, 1.258]	[1.225, 1.260]
(c)	[1.220, 1.256]	[1.223, 1.258]	[1.226, 1.260]	[1.229, 1.261]

SEPARATING DISTANCE

Considering the area restriction of the disk, the separating distance L/R considered in this study is set in the range of [0.5, 2.0]. Analyzing the following Fig.6~8, it is noticeable that the separating distance shows amazing effect on the wave conversion performance of this kind of WEC. For the considered array layouts, the effect of the distance are highly depend on the incident wave frequency. All the curves show more or less a similar pattern for the considered wave frequencies respectively. As shown in the left subgraphs in Fig.6~8, the captured power decrease first and then increase with the increase of the separating distance at the frequency $\omega = 1.0$ rad/s though it is not so obvious in the rhombus array layout. While at the frequency $\omega = 1.25$ rad/s as shown in the middle subgraphs, the captured power keeps increasing with the increase of the distance. The right subgraphs give an opposite trend with the left ones: increase first and then decrease.

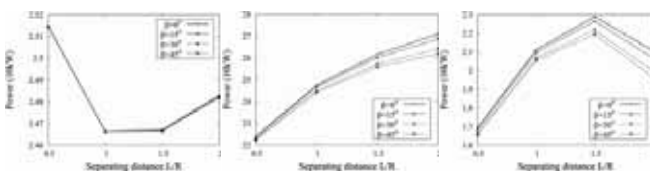


Fig.6. Captured wave power for array layout (a) with separating distance at different wave frequencies; Left: $\omega = 1.0$ rad/s; Middle: $\omega = 1.25$ rad/s; Right: $\omega = 1.5$ rad/s

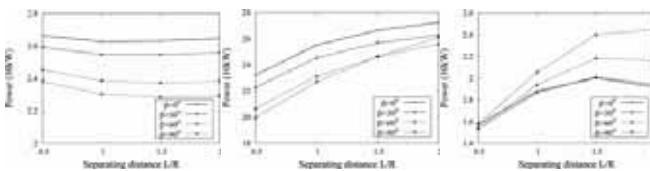


Fig.7 Captured wave power for array layout (b) with separating distance at different wave frequencies; Left: $\omega = 1.0$ rad/s; Middle: $\omega = 1.25$ rad/s; Right: $\omega = 1.5$ rad/s

ARRAY LAYOUT

It can be observed from Fig6~8 that the behaviors of the WECs related to the array layouts are highly depended on the incident waves and the separated distances. As shown in the left subgraphs, the rhombus layout shows better conversion

performance than the other two layouts just considering the maximal value though the square layout shows better stability. While at the wave frequency $\omega = 1.25$ rad/s as illustrated in the middle subgraphs, at a smaller separating distance such as L/R=0.5, the triangular array layout shows better conversion ability. However, with the increasing distance, the square layout shows better performance not only in the value of captured power but also in the stability with incidence wave direction. The right subgraphs depict the captured wave power at wave frequency $\omega = 1.5$ rad/s with different separated distances. It is noticeable that when the distance is small, the triangular array layout shows better performance, however, with the increasing distance, the rhombus one is better especially when the incident angle is 90° . Particular attention should be given to that the square layout shows excellent performance not only in the value of captured power but also in the stability with incidence wave direction.

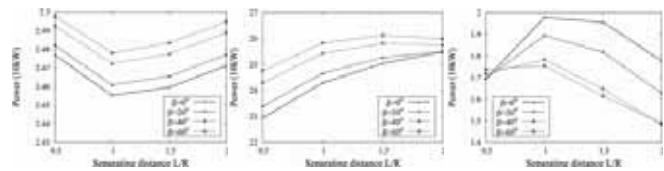


Fig.8 Captured wave power for array layout (c) with separating distance at different wave frequencies; Left: $\omega = 1.0$ rad/s; Middle: $\omega = 1.25$ rad/s; Right: $\omega = 1.5$ rad/s.

4.3 INCIDENCE WAVE DIRECTION

The effects of the incident wave angles are so obvious in all the subgraphs and depend on the layouts. In such case, the analysis should be performed taking into account each layout. For the square array layout, at a lower wave frequency, the angle shows little effect, while at higher wave frequencies, the captured wave power decreases with the increasing incident angle in the considered entire separated length range. For the rhombus layout, at the frequencies $\omega = 1.0$ and 1.25 rad/s, the captured wave power decreases with the increasing incident angle. The difference, however, is that when the separating distance L/R is larger than 1.5, the incident angle $\beta = 90^\circ$ leads to more excellent performance than $\beta = 60^\circ$. While at higher frequency $\omega = 1.5$, the captured wave power increases with the increasing incident angle. There is something special that the incident angle has little effect on the conversion ability when the angles are small. For the triquetrous layout, a larger incident angle leads to more excellent conversion performance when the wave frequencies $\omega = 1.0$ and 1.25 rad/s, while at the frequency $\omega = 1.5$ rad/s, the smaller incident angle shows better performance.

PTO DAMPING

As mentioned before, the influence of the PTO damping contains the influence of the PTO damping coefficient C_{PTO} and that of the damping type embodied in the velocity index. In such case, we analyze their influence from these two aspects

in the case of array layout (a) with separating distance $L/R=2.0$ and incident wave angle $\beta = 0^\circ$.

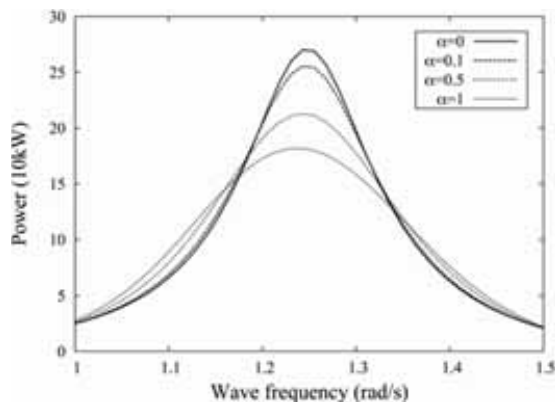


Fig.9. Captured wave power with wave frequencies when $C_{PTO}=10$ kN/s/m

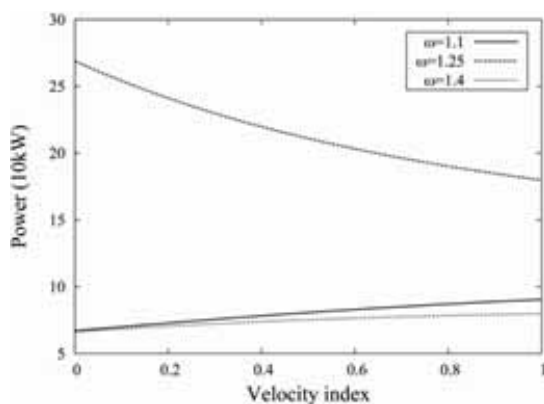


Fig.10. Captured wave power with velocity indexes when $C_{PTO}=10$ kN/s/m

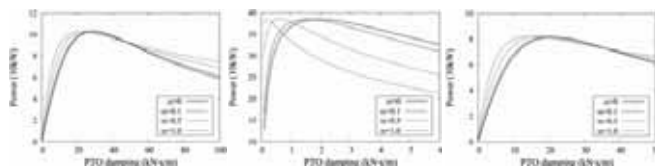


Fig.11 Captured wave power with PTO damping coefficients in case of layout (a); Left: $\omega = 1.1$ rad/s; Middle: $\omega = 1.25$ rad/s; Right: $\omega = 1.4$ rad/s

- Velocity index: Fig.9 depicts the captured wave power of square array layout with different velocity indexes when the PTO damping coefficient $C_{PTO} = 10$ kN/s/m. It is observed that the velocity index has a great effect on the wave energy conversion performance. In the frequency ranges $[1.0, 1.17]$ rad/s and $[1.33, 1.5]$ rad/s, the higher index shows better performance, such as $\alpha = 1$ (quadratic). However, in the range of $[1.17, 1.33]$ rad/s, the lower velocity index shows better performance, such as $\alpha = 1.0$ (quadratic PTO). Special attention should be given to the frequency where the peak value of the power occurs. There is a slight left shift in the peak frequency with the increasing velocity index. The Fig.9 shows the effect of velocity index on the captured power with considered three frequencies which further affirms the previous conclusions.

- PTO damping coefficient: The effect of the coefficient value can be seen from Fig.11. It is noticeable that the wave

energy conversion abilities are highly depended on the PTO damping coefficients and the incident wave frequencies. The captured power increases first and then decreases with the increasing PTO damping coefficients. The damping coefficient where the peak value of the power occurs decreases with the increasing velocity index though the peak values are the same. However, at lower frequencies (such as $\omega = 1.1$ rad/s) and higher frequencies (such as $\omega = 1.4$ rad/s), the curves of corresponding higher velocity indexes are seen to be more smooth and the corresponding captured powers stay relative high in a larger range of the damping coefficients. At the frequencies around the natural frequency of the absorber such as $\omega = 1.25$ rad/s, the conversion performance seems to be more excellent as the values of the captured power are relative high in the considered range of PTO damping coefficients.

DISCUSSION AND CONCLUSION

A four absorbers array connected to a semisubmersible disk is composed as a wave energy converter to extract ocean wave energy in this study. The interactions of the hydrodynamics and PTO mechanisms between the bodies are accounted for in the proposed corresponding coupled equations in frequency domain. A BEM based FORTRAN code is programmed to calculate the hydrodynamics of the oscillating system. The separating distance, array layout, incident wave direction and the PTO damping are considered for the optimization of the proposed WEC. The calculation results show that:

- (1) The hydrodynamic characteristics of the disk combined WEC show good stability at very low and high frequencies. In particular, the frequency-dependent amplitude of the added mass decreases with the increasing separating distance and the reduction seems to be the same at these frequencies. However, in the frequency range $[0.7, 2.5]$ rad/s, they are highly affected by the separating distances and the incident wave directions for each considered array layout.

- (2) The effects of the separating distance on the wave energy conversion performance are highly depended on the incident wave frequency. The captured wave powers decrease first and then increase with the increasing separating distance at the frequency $\omega = 1.0$ rad/s and shows the opposite trend when $\omega = 1.5$ rad/s. While at the frequency $\omega = 1.25$ rad/s, the captured power keeps increasing with the increase of the distance. Thus, the separating distance should be determined by the frequencies in its operation sea area.

- (3) The square array layout shows better performance than the rhombus and triangular ones not only in the value of captured power but also in the stability with incidence wave direction. However, at the frequencies $\omega = 1.25$ and 1.5 rad/s, the triangular one shows better performance when the separating distances are small. In summary, the square array layout is more appropriate considering the restriction of the disk.

- (4) The incidence wave direction affects the conversion ability depending on the choice of the array layout and the wave frequency. The square one is not sensitive to changes in the incident wave angle. The rhombus and triangular ones show the opposite trend.

(5) The influence of the PTO damping is reflected in two aspects, the damping type (velocity index) and the damping coefficient. The higher velocity index shows better applicability in the real random sea area. For different velocity indexes, the captured power can reach the maximum value by changing the damping coefficient.

ACKNOWLEDGEMENT

This paper is financially supported by the National Natural Science Foundation of China (No.51106034, No.51579055 and No.51509048).

REFERENCE

1. Budal K (1977). Theory for absorption of wave power by a system of interacting bodies. *Journal of Ship Research*, 21:248-253.
2. Falnes J, Budal K (1982). Wave-power absorption by parallel rows of interacting oscillating bodies. *Applied Ocean Research*, 4:194-207.
3. McIver P (1994). Some hydrodynamic aspects of arrays of wave energy devices. *Applied Ocean Research*, 19:283-291.
4. Fitzgerald C, Thomas G (2007). A preliminary study on the optimal formation of an array of wave power devices. In: *Proceedings of the 7th European Wave and Tidal Energy Conference*, Porto, Portugal.
5. Garnaud X, Mei CC (2010). Comparison of wave power extraction by a compact array of small buoys and by a large buoy. *IET Renewable Power Generation*.4 (6):519-530.
6. Weller SD, Stallard TJ, Stansby PK (2010). Experimental measurements of irregular wave interaction factors in closely spaced arrays. *IET Renewable Power Generation*.4 (6):628-637.
7. Child BFM, Venugopal V (2010). Optimal configurations of wave energy device arrays. *Ocean Engineering*, 37:1402-1417.
8. Babarit A (2010). Impact of long separating distances on the energy production of two interacting wave energy converters. *Ocean Engineering*, 37:718-729.
9. Borgarino B, Babarit A, Ferrant P (2012). Impact of wave interactions effects on energy absorption in large arrays of wave energy converters. *Ocean Engineering*, 41:79-88.
10. Wolgamot HA, Taylor PH, Taylor RE (2012). The interaction factor and directionality in wave energy arrays. *Ocean Engineering*, 47:65-73.
11. Heikkinen H, Lampinen MJ, Boling J (2013). Analytical study of the interaction between waves and cylindrical wave energy converters oscillating in two modes. *Renewable Energy*, 50:150-160.
12. Sharkey F, Bannon E, Conlon M, Gaughan K (2013). Maximising value of electrical networks for wave energy converter arrays. *International Journal of Marine Energy*, 1:55-69.
13. Goteman M, Engstrom J, Eriksson M, Isberg J, Leijon M (2014). Analytical and numerical approaches to optimizing fluid-structure interactions in wave energy parks. [Iwwwfb.naoe.eng.osaka](http://www.naoe.eng.osaka).
14. Andres AD, Guanche R, Meneses L, Vidal C, Losada IJ (2014). Factors that influence array layout on wave energy farms. *Ocean Engineering*, 82:32-41.
15. Goteman M, Engstrom J, Eriksson M, Isberg J, Leijon M (2014). Methods of reducing power fluctuations in wave energy parks. *Journal of Renewable and Sustainable Energy*, 6: 043103.
16. Goteman M, Engstrom J, Eriksson M, Isberg J (2015). Optimizing wave energy parks with over 1000 interacting point-absorbers using an approximate analytical method. *International Journal of Marine Energy*, 10:113-126.
17. Konispoliatis DN, Mavrakos SA (2016). Hydrodynamic analysis of an array of interacting free-floating oscillating water column (OWC's) devices. *Ocean Engineering*, 111:179-197.
18. Adnan, FAF; Hamylton, SM; Woodroffe, CD (2016). Surf-Swash Interactions on a Low-Tide Terraced Beach, *Journal of Coastal Research*, SI75: 348-352.
19. Sheng WN, Alcorn R, Lewis A (2015). Optimising power take-offs for maximizing wave energy conversions. In: *the 30th International Workshop on Water Waves and Floating Bodies*, Bristol, UK.
20. Jakubowski, M (2015). Influence of pitting corrosion on fatigue and corrosion fatigue of ship and offshore structures, part II: load - PIT -crack interaction. *Polish Maritime Research*, 22(3): 57-66.
21. Sheng WN, Lewis A (2016). Power takeoff optimization for maximizing energy conversion of wave-activated bodies. *IEEE Journal of Oceanic Engineering*, 2016:1-12.

CONTACT WITH AUTHOR

Hengxu Liu
E-mail: liuhengxu@hrbeu.edu.cn

COUPLING MECHANISM AND COUPLING DEGREE MEASUREMENT MODEL OF SHIPBUILDING INDUSTRY CLUSTER

SU Yi^{a,b},

Wang Fa-yin^a,

AN Xiao-li^a

^{a)} School of Economics and Management, Harbin Engineering University, P.R.China, 150001

^{b)} School of Economics and Management, Tsinghua University, P.R.China, 10010

ABSTRACT

This article was aimed to analyse the working condition of the coupling mechanism in Chinese shipbuilding industry cluster. Literature review was conducted to unveil the coupling mechanism of shipbuilding industry cluster, providing analysis of the present development of shipbuilding industry. A theoretical model was proposed by using the efficacy function and the capacity of the coupling coefficient while measuring the coupling of the shipbuilding industry cluster. Four coupling characteristics were found including relevant, systemic, diversity, and collaborative in the shipbuilding industry cluster. The shipbuilding industry cluster has two levels of coupling mechanism including the core layer coupling mechanism and the support layer coupling mechanism respectively. The improvement through coupling the core layer, support layer, and the coupling between two levels, is an effective way to achieve long-term stable development in Chinese shipbuilding industry cluster.

Keywords: coupling mechanism, coupling degree measurement model, shipbuilding industry cluster

INTRODUCTION

Chinese Shipbuilding Industry is the supporting industry of Chinese maritime transportation, ocean development and national defense construction, and strategic industry of combination of military and civilian. It has important significance to the national defense capability and the national economic growth. The construction of shipbuilding industrial cluster is an effective way to enhance the competitiveness of shipbuilding industry, and the appropriate coupling mechanism can make positive synergy effect on shipbuilding industry cluster. The industrial clusters of shipbuilding industry can take appropriate measures to improve the coupling degree to make the cluster maintain high coupling operation in a state of highly efficient operation, and make

greater contribution to military and civilian. Shipbuilding industry cluster is an effective way for the development of shipbuilding industry as a strategic tool (Huang, 2006)[1]. Scholars focus on the studies on development elements (Cao and Liu, 2007)[2], development models (Tao and Yang, 2007; Li, 2008; Hu and Yu, 2013)[3-5], the formation mechanism of shipbuilding industrial cluster (Tao, 2005; Zhao, 2007; Wang, 2010)[6-8], and the life cycle of South Korea's shipbuilding industry cluster (Shin et al., 2011)[9], shipbuilding industry cluster development theoretical model (Zong, 2013)[10], development opportunities and challenges of shipbuilding industry cluster (Zhang and Zeng, 2014)[11], etc. However, the literatures rarely involve the study of the complex mechanism of the shipbuilding industry cluster. The coupling theory provides a new theoretical support for this field of research.

The coupling theory is applied to the study of the complex relationships within the systems, which is mainly used in manufacturing industry and other related fields. Li and Li (2005) presented that the equipment manufacturing industry cluster coupling contains three layers coupling mechanisms, namely the manufacturing enterprise's coupling mechanism, coupling mechanism of industry cluster and regional social network coupling mechanism, proposed the coupling degree model of equipment manufacturing industry cluster, analyzed the influence factors of equipment manufacturing industry cluster coupling degree and coupling mechanism, and finally made empirical analysis on Shenyang equipment manufacturing industry cluster[12]. Ruan and Zuan (2010) put forward the coupling degree model of manufacturing industry cluster, and made empirical analysis of the coupling degree on Qingdao manufacturing industry cluster[13]. Yuan et al. (2012) divided the network structure of the manufacturing industry into core manufacturing layer, industry matching layer, service support layer and analyzed coupling mechanism among layers[14]. Fu et al. (2012) made the research on the coupling of multiple wastewater using network design to achieve agile manufacturing[16]. Du et al. (2012) established the coupling coordination model about the industrial technology innovation ability. The model mainly includes three basic parts, the efficiency function, the coupling degree model and the evaluation index system. This coupling coordination model was used to evaluate whether the coal resource cities should develop some leading industries, and took Qitaihe as an example[17]. Liu and Sun (2014) established the coupling degree measurement model of knowledge innovation and technology innovation in high-end equipment manufacturing industry, and proved the validity of the coupling degree measure model from the empirical point of view[15]. Zou et al. (2014) analyzed the development trend of the equipment manufacturing industry in Liaoning by using factor analysis method, and proposed the coupling development "Trilogy" of technology innovation and technological upgrading of Liaoning province equipment manufacturing industry combined with technological innovation and technological upgrading coupling improvement mechanism, respectively, exploration and development model, the leading domestic development model and international development model[18]. The research of the coupling mechanism and coupling degree measurement model of shipbuilding industry cluster can provide theoretical guidance and decision-making basis for the industrial cluster of shipbuilding industry, which has important significance to both theoretical and practical development.

DEVELOPMENT STATUS QUO OF CHINESE SHIPBUILDING INDUSTRY

CHINA REMAINED THE WORLD'S LARGEST SHIPBUILDING COUNTRY

The data of Figure 1 and 2 are obtained from China Association of the National Shipbuilding Industry Website. The new orders of China, South Korea, and Japan already occupied more than 90% of the world shipbuilding total

completion. The market share of China was more than 45% both in the year of 2013 and 2014, followed by South Korea and Japanese with the market share of about 30% and 20% respectively.

The new received orders in China kept the world's first in 2013 and 2014. From the perspective of market share, China, South Korea and Japan are the world shipbuilding countries led by China. China's shipbuilding industry development is quite superior and stability.

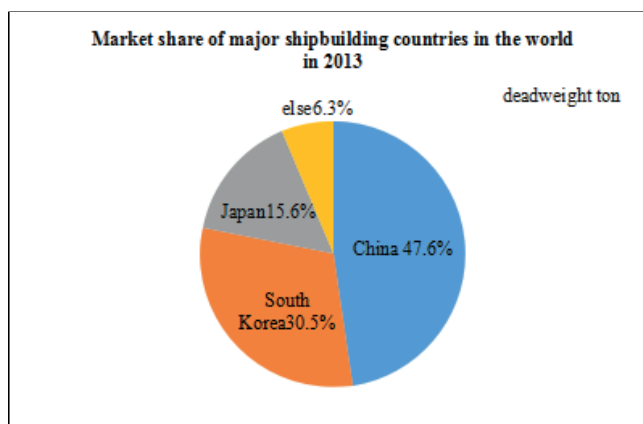


Fig.1. Market share of major shipbuilding countries in the world in 2013

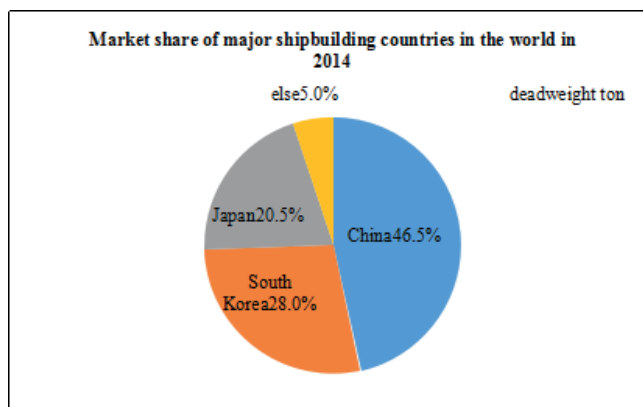


Fig.2. Market share of major shipbuilding countries in the world in 2014

THE THREE MAJOR INDICATORS OF CHINESE SHIPBUILDING INDUSTRY ARE SHOWING AN OVERALL UPWARD TREND

From 2001 to 2014, China's annual shipbuilding output, the new received orders, the overall holding orders had showed a rising trend, and reached the highest value in 2012, 2007 and 2008, respectively. China's annual shipbuilding output had been declining in the last three years, but the degree of declining has slowed. The number of new received orders had increased significantly, and then fell slightly. China's annual shipbuilding output, the new received orders, and the overall holding orders had been showing a fluctuation states, however the general trends are still upward.

INDUSTRIAL CONCENTRATION HAS BEEN INCREASED, AND THE COMPREHENSIVE STRENGTH HAS BEEN GREATLY IMPROVED

In the year of 2014, there were more than 90 percent orders has been completed in the three major shipbuilding bases, which were in the place of the Bohai Bay region, Yangtze River Delta and Pearl River Delta. The concentration degree of top 10 enterprises, top 20 enterprises and top 30 enterprises was up to 50.6%, 71.6% , 83.8%, respectively, which increased 3.2%, 5.9% and 7.4% respectively comparing to the year of 2013. This means the degree of industrial concentration has been significantly improved. There has been formed a group of key enterprises in China, and four of them are the world's top ten enterprises, in terms of new orders. We can obtain that Chinese shipbuilding enterprises' market competitiveness and the international status had been improved.

MARKET DEMAND IS NOT BALANCED, AND THE DEVELOPMENT POTENTIAL IS SLIGHTLY INADEQUATE

In the year of 2014, China's new receive orders quantity maintained a high level, which was about 60 million deadweight tons. The quantity of new receive orders was showing a quarterly decline trend, which was 25 million deadweight tons, 14 million deadweight tons, 11 million deadweight tons and 7 million deadweight tons, from first quarter to the fourth quarter, respectively. Except the first quarter, the situation of shipbuilding enterprises had deteriorated significantly in the year of 2014. The main reason is as following: first of all, shipping market supply and demand contradictions problems have not been fundamentally resolved, and the order quantity is gradually reduced. Secondly, as a significant reduction in international oil prices, which dampened the enthusiasm of the enterprise to manufacture energy-saving ships, and postponed dismantling of old ships, the market demand for new ships continued to decrease. In recent years, the Chinese shipbuilding output has reached 20 million tons. Facing the depressed market, China's shipbuilding industry capacity utilization efficiency is not high, and does not reach a reasonable level of the industry.

THE COUPLING CONNOTATION AND CHARACTERISTICS OF SHIPBUILDING INDUSTRY CLUSTER

THE COUPLING CONNOTATION OF SHIPBUILDING INDUSTRY CLUSTER

As a typical large-scale equipment manufacturing industry, shipbuilding industry enterprises have many characteristics such as long industrial chain involved and high requirements for supporting industry [4]. A mature shipbuilding industry cluster should include the shipping core manufacturing enterprises, the ship supporting enterprises, the ship parts production enterprises, and the service oriented institutions.

Unique symbiotic cluster of shipbuilding industry enterprises was formed through the exchange of knowledge, information, human resources, equipment and capital of each subject in the cluster. On one hand, from the ecological point of view, the shipbuilding industry cluster is a industry species ecological system; on the other hand, from the innovation economics point of view, shipbuilding industry cluster is a special kind of regional innovation system [19]. This paper argues that the shipbuilding industry cluster refers to taking ship manufacturing enterprises as the center, and united the related enterprises or organizations of ship industry, such as: supporting enterprises, universities, research institutions, vocational training institutions and shipbuilding industry association, gathering together to form an organic system in a particular geographic location [8][20]. The industry cluster, which has complete industrial structure, robust support system, can be formed through specialization and depth cooperation of subjects within the cluster. Initially coupling is a physical concept, which has been widely used in the field of system science and social sciences. The concept of coupling is used to explore or describe the relationship, mutual influence and common cooperation and evolution process of various systems. In physics, coupling refers to the phenomenon that two or more than two of the circuit elements or the input and output of the electrical network are closely matched with each other, and the transmission of energy from one side to the other side through the interaction. In this article, the coupling is defined as a dynamic relationship formed by positive interaction, matching and coordination among system elements or subsystems to achieve the coordinated development. The coupling of Chinese shipbuilding industry cluster is a kind of dynamic relationship and synergistic action process among the related enterprises and organizations of shipbuilding industry. The coupling of shipbuilding industry cluster is not only coordination among the agents, but is also on collaborative development, so as to achieve the purposes, such as complementary advantages, mutual promotion and coordinated development.

THE COUPLING CHARACTERISTICS OF SHIPBUILDING INDUSTRY CLUSTER

Shipbuilding industry cluster has the characteristics of relevance, systematic, diversity, collaborative etc. Firstly, correlation. The coupling agents including core ship manufacturing enterprises, the ship supporting enterprises, the ship parts production enterprises, and the service organizations are interrelated and interact with each other. Shipbuilding industry cluster is not a closed static system. Obviously, Chinese shipbuilding industry cluster has the prerequisites for application of coupling theory. Secondly, systematic. The main subjects or elements in the coupling system form a new system through cooperating with each other according to certain rules. The main bodies of Chinese shipbuilding industry cluster form the new system of shipbuilding industry cluster through cooperating with each other according to the rules and regulations, such as cooperation contract, contract etc. Thirdly, diversity. Each

coupled subsystem has its own organizational characteristics. The links between the elements of the subsystems are complicated, which constitute a variety of coupling modes. Each subject of shipbuilding industry cluster has its own organization and management mode and characteristics, so the links of enterprises and support service agencies are very complex, and the relationship between them is dynamic. Finally, collaborative. The coupled subsystems in shipbuilding industry cluster interact with each other through the way of complementary advantages to achieve the collaborative development of the entire system [21].

THE COUPLING MECHANISM OF SHIPBUILDING INDUSTRY CLUSTER

Large ship manufacturing enterprises are the core of agglomeration of Chinese shipbuilding industry cluster, and a series of related businesses (ship matching enterprises, ship parts production enterprises and shipbuilding supporting enterprise) and service organizations (such as scientific research institutions, intermediary institutions, government agencies, educational institutions, and shipbuilding industry association) are derived from the large ship manufacturing enterprise. These service institutions provide the related services, such as technical, information, policy guidance and coordination for the cluster. Chinese Shipbuilding Industry Cluster coupling structure contains two levels of coupling mechanisms: the core layer coupling mechanism, and the support layer coupling mechanism [12]. The coupling of the shipbuilding industry cluster is the complex combination of the two levels of coupling mechanisms rather than a simple superposition. The two coupling layers are closely linked to each other based on knowledge sharing and economic transactions, but independent of each other. The coupling dynamics of one level will have an effect on the other coupling layer, thus affecting the overall function of the cluster. A positive effect is produced by the good coupling of two levels, to promote the formation of a high coupling degree of the entire cluster, so as to maintain sustainable competitiveness.

COUPLING MECHANISM OF CORE LAYER

The core layer coupling mechanism is mainly the coupling of the core ship manufacturing enterprises, the ship matching enterprises, the ship spare parts manufacturing enterprises and the shipbuilding supply enterprises. In this coupling layer, the cooperation of the enterprises is not only between supply and demand, but the matching of the upstream and downstream enterprises in the product, service and manpower, etc, based on the complete vertical industrial chain. Industrial connection is a prerequisite for the coupling of industry cluster, and the information flow in unobstructed and timely manner are the conditions of realizing the benign coupling. Shipbuilding industry cluster is a typical vertical industry chain agglomeration model, which is longer, involving a wide range of services, with high requirements for matching services. The ship spare parts manufacturing

enterprises, the ship matching enterprises, and the ship core manufacturing enterprises are closely linked to form a vertical industrial chain.

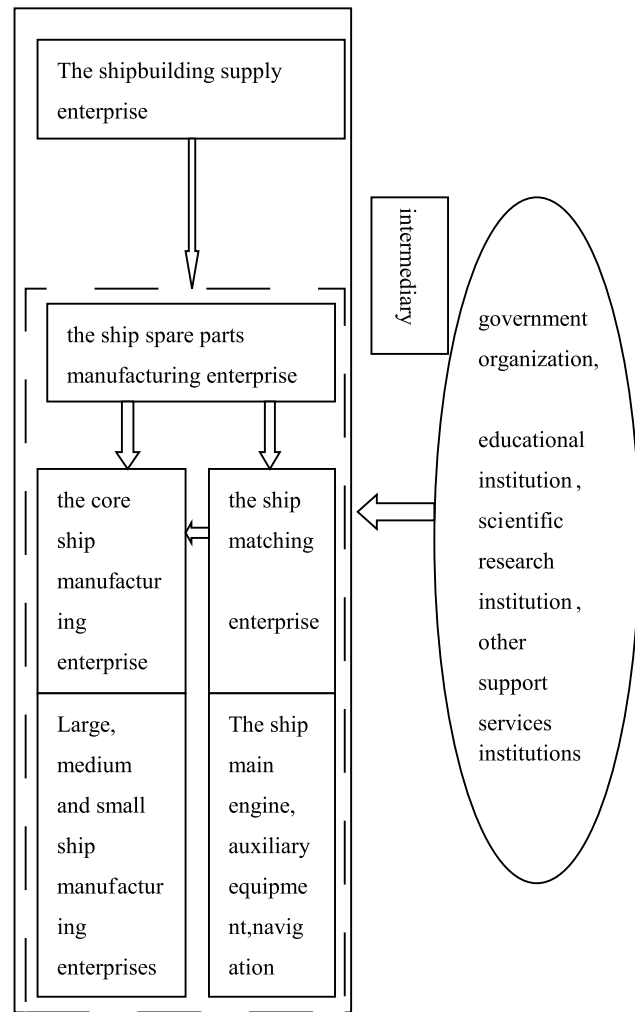


Fig.3. The coupling structure of shipbuilding industry cluster core layer

The main contents of the core layer coupling mechanism are ship manufacturing enterprises, which are the core of the shipbuilding industry cluster and play the role of the components supplied by the supporting enterprises to be assembled into the ship. The matching enterprises and the ship spare parts manufacturing enterprises provide the ship core manufacturing enterprises with spare parts and necessary components of the ship. Of course, the ship spare parts production enterprises also provide spare parts for the ship matching enterprises. Shipbuilding supply enterprises provide the cores of ship manufacturing enterprises, the ship matching enterprises and ship spare parts production enterprises with all kinds of raw materials for shipbuilding. These adaptation stages are the initial stage of coupling, and the closely and efficiently cooperation and interaction among the enterprises are the key points. Each enterprise needs follow-up and support of other links as key link in the vertical industry chain, and the benign interaction among enterprises to produce the adhesive effect, so as to achieve the coordinated

development and the coupling. Good coupling mechanism can promote the formation of positive coupling effect bundle. The positive effect of the coupling effect bundle is amplified to achieve positive cycle.

COUPLING MECHANISM OF SUPPORT LAYER

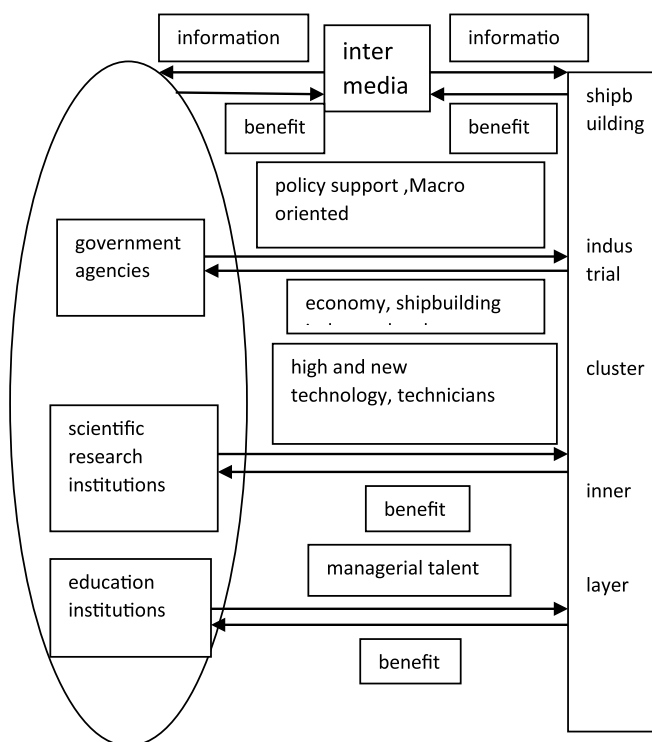


Fig.4. The support coupling layer structure of shipbuilding industrial cluster

Support coupling mechanism is also the outer coupling mechanism, mainly provides technology information, resource, policy guidance and other services for shipbuilding industry cluster. The coupling layer mainly includes the relation and coupling between some support service institutions and the inner cluster. The inner cluster includes the shipping core manufacturing enterprises, the ship matching enterprises, the ship spare parts production enterprises and the shipbuilding supply enterprises. This coupling layer is important, but can easily be neglected. Support service institutions, which are parts of support coupling layer, include government agencies, intermediary institutions, scientific research institutions, education institutions, financial institutions and shipbuilding industry association, etc. In general, these support service institutions support cluster inner layer. Support coupling layer structure is as follows.

The main contents of support layer coupling mechanism are government agencies involving in shipbuilding industrial cluster coupled by providing policy support, macro-environment creation, etc. for cluster inner layer. Government agencies play a guiding role on the behavior of all the subjects in the cluster inner layer by industrial preferential policies, tax policies to bring the cluster to benign coupling. Intermediary agencies provide information

services for the cluster, playing the role of middle bridge and avoiding low coupling degree of cluster caused by the non-smooth information. Scientific research institutions include universities and research institutes, which are the most important innovation institutions of knowledge and technology. Shipbuilding industry cluster inner layer can cooperate with scientific research institutions, such as forming the Research Alliance to continue to learn new technologies, to absorb shipbuilding talents. Scientific research institutions become the birthplace of the high-tech and technical talents of the cluster inner layer in this way. Education and training institutions train managers, so cluster coupling degree is improved by the managers by making the scientific management more effectively in the cluster inner layer. Financial institutions provide funding for enterprises. Shipbuilding industry associations offer a variety of social services for shipbuilding industry cluster, and maintain the legitimate rights of interests of the member units and the industry. The overall effect is much greater than their respective effect, resulting in efficiency overflow proliferation and positive effect on the whole cluster, thus forming a virtuous circle, expanding the overall positive effect of the cluster, so as to achieve benign coupling by support service institutions coordinating with cluster inner layer, and producing synergistic effect in dynamic interaction.

CONSTRUCTION OF COUPLING DEGREE MEASUREMENT MODEL OF SHIPBUILDING INDUSTRIAL CLUSTER

Previous research illustrates the coupling mechanism of shipbuilding industry cluster. In reality, it is necessary to measure the coupling degree of shipbuilding industry cluster scientifically in order to clear the coupling condition of shipbuilding industrial cluster. Then relevant institutions can take pertinent measures to improve cluster coupling degree. Construction process of coupling degree measurement model of shipbuilding industry cluster is as follows.

EFFICIENCY FUNCTION OF SHIPBUILDING INDUSTRIAL CLUSTER

Set variable $(i=1,2,\dots,n)$ is the order parameter of the shipbuilding industry cluster. The core ship manufacturing enterprise, the ship matching enterprise, the ship spare parts manufacturing enterprise, the shipbuilding supply enterprise, and support service institution are the five order parameters. u_{ij} is the j -index of i -parameter, the value is X_{ij} ($i=1,2,\dots, n$). A_{ij} , B_{ij} are the upper and lower limits of order parameter of shipbuilding industry cluster steady state. And efficiency function of the core ship manufacturing enterprise, the ship matching enterprise, the ship spare parts manufacturing enterprise, the shipbuilding supply enterprise, and support service institution orderly to shipbuilding industrial cluster system can be expressed by:

$$u_{ij} = \begin{cases} (X_{ij} - B_{ij}) / (A_{ij} - B_{ij}) \\ (A_{ij} - X_{ij}) / (A_{ij} - B_{ij}) \end{cases} \quad (1) \quad \begin{matrix} u_{ij} \text{ has a negative effect} \\ u_{ij} \text{ has a positive effect} \end{matrix}$$

The u_{ij} is the efficiency contribution size of variable X_{ij} to the system. u_{ij} represents the satisfaction degree of each index reaching the goal, u_{ij} is between 0 and 1, reaching to 0 for the most unsatisfied, closing to 1 for the most satisfactory. The core ship manufacturing enterprise, the ship matching enterprise, the ship spare parts manufacturing enterprise, the shipbuilding supply enterprise and support service institution are mutually connected and influenced subsystems, the total contribution of each index to subsystems is achieved by integrated method, and the linear weighted method is generally used[22].

$$\begin{aligned} u_i &= \sum_{j=1}^m \lambda_{ij} u_{ij} \\ \sum_{j=1}^m \lambda_{ij} &= 1 \end{aligned} \quad (2)$$

u_i is the contribution of subsystem to total system order degree. m is the number indicators of subsystem, λ_{ij} is index weights. The weights of each index can be determined by analytic hierarchy process and entropy weight method[22][23].

COUPLING DEGREE FUNCTION OF SHIPBUILDING INDUSTRY CLUSTER

The calculation of the coupling degree of shipbuilding industry cluster draw lessons from the concept of capacity coupling and capacity coupling coefficient model in physics[24]. In this paper, it is extended to the coupling degree measurement model of multiple systems.

$$C_n = n \{ (u_1 \cdot u_2 \cdots u_n) / \prod (u_i + u_j) \}^{\frac{1}{n}} \quad (3)$$

According to the above equation, the core layer consists of four sub-systems, namely the core ship manufacturing enterprise, the ship matching enterprise, the ship spare parts manufacturing enterprise, the shipbuilding supply enterprise. Support layer consists of five subsystems, namely the core ship manufacturing enterprise, the ship matching enterprise, the ship spare parts manufacturing enterprise, the shipbuilding supply enterprise and support service institution. The core layer coupling degree measurement model and the support layer coupling degree measurement model are constructed with subsystem number instead of n of the formula. The value of C is between 0 and 1, 1 represents subsystem coupled with maximum degree and the coupling condition of subsystems benign. 0 represents subsystems coupled with minimum degree, and the subsystems are independent.

Coupling degree C is an important parameter to judge the coupling state of the subsystems, but it is difficult to reflect the overall effect of the cluster coupling in some cases, especially in the cluster contrast study. Due to the development strategy, the characteristics of each shipbuilding industry cluster are different. For example, development stages of cluster A and cluster B are different, but the coupling degree is the

same. Therefore, it is obviously not a good reflection of the shipbuilding industry cluster synergy and the overall effect only using the coupling degree to evaluate the development of the cluster. In this case, the significance of conclusion by using the coupling degree to the development of cluster is not obvious. The modified coupling degree measurement model of shipbuilding industry cluster is[25-27]:

$$\begin{cases} C' = (C \cdot T)^{\frac{1}{2}} \\ T = au_1 + bu_2 + cu_3 \cdots \end{cases} \quad (4)$$

where, C is coupling degree; C' is modified coupling degree; T is subsystem comprehensive harmonic index of shipbuilding industrial cluster, which reflects the overall synergistic effect of shipbuilding industrial cluster; a, b, c , etc. are undetermined coefficients, which can be determined by absorbing the experts' advice. The modified coupling is divided into four levels. Coupling layer of shipbuilding industrial cluster is in the low coordination coupling stage, if $0 < C' \leq 0.4$. Coupling layer of shipbuilding industrial cluster is in the moderate coordination coupling stage, if $0.4 < C' \leq 0.6$. Coupling layer of shipbuilding industrial cluster is in the high coordination coupling stage, if $0.6 < C' \leq 0.8$. Coupling layer of shipbuilding industrial cluster is in the extreme coordination coupling stage, if $0.8 < C' \leq 1$.

CONCLUSIONS

Through the review of the prior literature on the Chinese shipbuilding industrial cluster and manufacturing, this paper focuses on the current development of the Chinese shipbuilding industry and related concepts. The shipbuilding industrial cluster includes two basic coupling mechanism layers: the core layer and support layer on top of the prior papers, this paper developed a new coupling degree measurement model. In order to achieve the long-term stable development of the shipbuilding industry cluster, the following aspects were proposed.

First of all, the ship matching enterprises play an important role in the shipbuilding industry cluster. Accelerated development of matching industries is useful for improving the coupling degree of the core layer, promoting the development of the shipbuilding industry cluster. When the matching capacity cannot catch up with the development of the shipbuilding industry, the ship manufacturing enterprises will not carry out effective production activities, in other words, the core layer coupling degree of shipbuilding industry cluster is delayed by the supporting layer. The development of matching industries can be accelerated by implementing professional operation, e.g. establishing the main auxiliary instrument, machinery and other professional company; concentrating financial resources, material resources, manpower to engage in specialized production[6]. Specialized production can be applied to improve the matching capacity of shipbuilding industry cluster, to promote the establishment of a good coupling mechanism.

Secondly, the support layer coupling can be strengthened by enhancing the flow of knowledge and technological innovation of the shipbuilding industry cluster. As the current spillover of the Chinese shipbuilding industry is still at a lower level, the coupling degree of the support layer is restricted at relative lower level. It is obviously that the improvement of knowledge spillover of shipbuilding industry cluster can optimize the coupling mechanism of the cluster, and promote the development of coupling of shipbuilding industry. Technology innovation can save the cost of shipbuilding for the cluster, but also can make up the in shortage of raw materials in shipbuilding, so that the cluster is more competitive. The knowledge creation and flow can be strengthened through enhancing cooperation of the industry and universities, increasing the flow of talents and enhancing the sharing degree of infrastructure facilities[3].

Thirdly, the two level coupling state of cluster can be promoted by taking measures together and developing producer service industry. Chinese shipbuilding industry can better achieve structural adjustment, and the cluster can better maintain a good coupling state by speeding up the development of producer service industry. Efficient logistic services, perfect marketing and after-sale service network systems are good signs of the core layer coupling status, sound financial services system is a good performance of the support layer coupling status. Accordingly, the coupling degree of the two layers can be improved by the following ways, so that the cluster can maintain a high degree of coupling status. First, the cluster can establish information and intelligent logistic service systems by making full use of modern information technology. Second, it can build brands, and improve market share by establishing and improving the global after-sale services and marketing network systems. Third, Cluster can improve the construction of the ship financial services system to provide better financial support for the development of the shipbuilding industry cluster by strengthening cooperation with domestic and foreign financial institutions, developing multi-channel financing, and improving financing means.

Coupling structure of shipbuilding industry cluster is complicated, this research puts forward the coupling mechanism of the shipbuilding industry cluster, and coupling measurement model was established. However, further empirical research needs to be carried out. The coupling theory will be applied to the empirical research through field survey and secondary data collection based on this research in the future.

ACKNOWLEDGEMENTS

The authors thank reviewers for their insightful comments. This work was supported by National Natural Science Foundation of China(71403066), Doctoral Fund of Ministry of Education of China(20122304120021), China Postdoctoral Science Foundation(2013T60351), Heilongjiang Province Postdoctoral Start Foundation (LBH-Q13050), the Special Foundation of Central Universities Basic Research Fee (HEUCF140907).

REFERENCE

1. Huang Jin. Chinese shipbuilding industry cluster development stratify[D].Hunan University.2006.(in Chinese)
2. Cao Yousheng,Liu Xisong. Research on elemental factors and countermeasures in promoting cluster of China shipbuilding industry[J].Ship Building of China,2007(3):91-95. (in Chinese)
3. Tao Yonghong,Yang Haisong. On development mode and strategy of shipbuilding industrial cluster in Yangtze River Delta[J].Journal of Jiangsu University of Science and Technology(Social Science Edition), 2007(6):33-38. (in Chinese)
4. Li Hao. Research on the Yangtze River Delta ship industry cluster development[D].Lanzhou University.2009. (in Chinese)
5. Hu Wei,Yu Yingying. Research on the development model and strategic of Wuhu ship industrial cluster[J].Machine Design and Manufacturing Engineering,2013(3):22-25. (in Chinese)
6. Tao Yonghong. Formation mechanism and developments research of the shipbuilding industry cluster based on The Symbiosis Theory[D].Nanjing University of Science & Technology.2005. (in Chinese)
7. Zhao Xin. The research on Chinese shipbuilding industry cluster[D].Dongbei University of Finance and Economics.2007. (in Chinese)
8. Wang Lei. The Research on formation and development of the shipbuilding industrial clusters in Yangtze River Delta[D].Shandong University.2010. (in Chinese)
9. Shin,Dong-Ho,Hassink,Robert. Cluster life cycles: the case of the shipbuilding industry cluster in South Korea[J]. Regional study.2011,45(10):1387-1402. (in Chinese)
10. Zong Shengchun. Research on Yantai shipbuilding industrial cluster and its development strategy[D].Ocean University of China.2013. (in Chinese)
11. Zhang Mudan,Zeng Yihui. The development thoughts and countermeasures on the shipbuilding industry cluster in the ecological economic zone of Dongting Lake[J]. Business,2014(2):301. (in Chinese)
12. Li Kai,Li Shijie. Coupling structure of equipment manufacture industrial clusters: a new view on the industrial clusters[J].China Industrial Economy, 2005(2):51-57. (in Chinese)

13. Ruan Yanyan, Qi Zhenfa. The study of coupling degree of manufacturing clusters[J]. Journal of Shandong University of Technology (Natural Science Edition), 2010(11):107-110. (in Chinese)
14. Yuan Yijun, Ren Huanhuan, Zhang Mengmeng. Coupled network analysis and upgrading path of equipment manufacturing industry[J]. Science & Technology Progress and Policy, 2012(5):59-61. (in Chinese)
15. Liu Weiwei, Sun Ru. Research on coupling degree measurement between knowledge innovation and technological innovation of High-End equipment manufacturing enterprises[J]. Science of Science and Management of S.& T., 2014(7):17-22. (in Chinese)
16. Jie Fu, Tianxing Cai, Qiang Xu. Coupling multiple water-reuse network designs for agile manufacturing[J]. Computers and Chemical Engineering, 2012, 45(12):62-71.
17. Du Jiming, Yu Bo, Yao Xilong. Selection of leading industries for coal resource cities based on coupling coordination of industry's technological innovation[J]. International Journal of Mining Science and Technology, 2012, 22(3):317-321.
18. Zou Hua, Sun Jian, Sun Jinliang. Research on the coupling development of technology innovation and technology upgrading of equipment manufacturing industry—a case study of Liaoning[J]. Science & Technology Progress and Policy, 2014(8):76-79. (in Chinese)
19. Wu Dejin. Organizational nature of industrial cluster: property and connotation[J]. China Industrial Economy, 2004(7):14-20. (in Chinese)
20. Wang Hui, Zhang Guangming. Analysis of shipbuilding supply chain structure characteristics and competitive advantage in shipbuilding industry cluster[J]. Marine Technology, 2007(1):4-6. (in Chinese)
21. Li Yong. On Coupling mechanism of regional industry[J]. Business Economy, 2010(5):31-34. (in Chinese)
22. Qiu Guodong, Ma Qiaohui. The endogenous coupling mechanism of technological innovation and institutional innovation: the secret of corporation growth—a case study of Geely and Hyundai[J]. China Soft Science, 2013(12):94-113. (in Chinese)
23. Xu Yulian, Wang Yudong, Lin Yan. Research on coupling coordinated degree evaluation of regional sci-tech innovation and sci-tech finance[J]. Science of Science and Management of S.& T., 2011(12):116-122. (in Chinese)
24. Varile. Dictionary of Physics (in Chinese)[M]. Beijing: Foreign Language Press, 1996.
25. Kowalski, Jakub; Lesniewski, Wojciech; Litwin, Wojciech. Multi-source-supplied parallel hybrid propulsion of the inland passenger ship STAH Research work on energy efficiency of a hybrid propulsion system operating in the electric motor drive mode[J]. Polish Maritime Research, 2013, 20(3): 20-27.
26. Liu Yaobin, Song Xuefeng. Coupling degree model and its forecasting model of urbanization and ecological environment[J]. Journal of China university of Mining & Technology, 2005(1):91-96. (in Chinese)
27. Jiang, Haibo; Tang, Kai; He, Xinlin. Experimental Studies on Reduction of Evaporation from Plain Reservoirs in Drought Areas by Benzene Board Covering Technology[J]. Journal of Coastal Research, 2015, SI73: 177-182.

CONTACT WITH AUTHOR

SU Yi

School of Economics and Management,
Harbin Engineering University,
Harbin 150001,
P.R.China

School of Economics and Management,
Tsinghua University,
Tsinghua, 10010
P.R.China,

E-mail: suyi@hrbeu.edu.cn

NUMERICAL ANALYSIS ON THE INFLUENCE OF THE TWISTED BLADE ON THE AERODYNAMIC PERFORMANCE OF TURBINE

Jianguo Jin

Zhanzhou Wang

Lihua Cao

School of Energy and Power Engineering, Northeast Dianli University, Jilin, Jilin, China

ABSTRACT

With the gradual increase of the thermal power unit capacity, the inlet steam parameters and flow of the turbine also increase gradually, which causes considerable secondary flow loss. Therefore, studying the causes and distribution of secondary flow loss within the level is of great significance to effectively improve the stage internal efficiency of turbine. Take high-pressure stage moving blade of a turbine as the research object, and adopt the $k-\omega$ SST model, the SIMPLEC algorithm to numerically simulate the formation and development process of leakage vortex between the tip clearance of the positive bending twisted blade and its effect on the secondary flow of cascade passage. Results show that relative to the conventional twisted blade, the scope of influence of leakage vortex which the steam flow formed near the suction surface of positive bending twisted blade and the disturbance to passage mainstream become smaller, and the increase of tip clearance has weakened the „C” type pressure gradient of suction surface of the positive bending twisted blade, increased the thickness of the boundary layer at both ends of blades and the loss of the blade end.

Keywords: Turbine, Twisted blade, Leakage vortex, Pressure gradient, Tip clearance.

INTRODUCTION

The bending of turbomachinery twisted blade includes positive bending and reverse bending. The included angle between pressure side of the blade and the superior and inferior end walls is obtuse angle, which is reverse bending, and acute angle is positive bending twisted blade. Positive bending twisted blade can make the steam flow in the blade surface, especially nearby the suction surface form “C” type pressure distribution of the positive radial pressure gradient and the negative radial pressure gradient of the blade tip. The “C” type pressure distribution will help to entrain low energy fluid at the superior and inferior end walls into the mainstream region of the central area, so as to effectively control the secondary flow of fluid in the end wall [1]. A large

number of studies have shown that positive bending twisted blades adopted in the blade design can reduce the flow loss in the cascade passage and improve the performance and operational efficiency of the turbomachinery [2-3].

At present, bending technology of twisted blades has had abundant theoretical analysis and experimental research results. B.T. An, etc [4] studied the turbine cascade flow field under different conditions of bending, and pointed out the small angle positive bending design of blade can make the passage vortex of the end region strengthen, angle area separate and disappear, so as to achieve the effect of reducing the flow loss of the end and improving the aerodynamic performance of the turbine. Through the wind tunnel experimental study of high-pressure annular cascade, Z.M. Feng, etc [5] got appropriate coordination of rear load blade

profile with the positive bending blade, which can further optimize the three-dimensional pressure field inside the cascade, and reduce the profile loss and secondary flow loss. The study of H.W. Lu, etc [6,8] shows that passage vortex strength of positive bending cascade in the compressor increases, the wall vortex intensity weakens, and the structure of the passage vortex generates relatively complex changes. L. Chen, etc [7] studied the comprehensive influence of bending blades on the aerodynamic performance of the turbine, and proposed only if the interaction between blade rows be fully considered, can the best aerodynamic performance scheme of the turbine bending blade design be found.

Based on the computational fluid dynamics software Fluent, the article conducts a numerical simulation on the flow field of high-pressure stage positive bending twisted blades of a turbine with blade tip clearance, probes the formation and development process of tip clearance leakage flow and vortex of the positive bending twisted blades in high-pressure stage environment, and emphatically analyzes the influence of the tip leakage flow of positive bending twisted blades on the secondary flow of the cascade passage under different blade tip clearance.

THE CALCULATION MODEL AND NUMERICAL METHOD

PHYSICAL MODEL AND MESH GENERATION.

This paper selects the high-pressure stage positive bending twisted blade of some domestic turbine as the research object, and basic geometric parameters of the blade are as shown in Table 1.

For the geometrical model and mesh generation of cascade, see Fig. 1. All of the meshes in the blade passage adopt structured hexahedral mesh; the blade tip clearance adopts the H-type mesh, and is locally ciphered, to ensure enough accuracy of the flow field. After the mesh independence verification, the total number of divided meshes is about 630,000, among which, the meshes numbers of the axial, circumference and spanwise of the blade passage are respectively $112 * 50 * 68$, and the meshes number of the labyrinth clearance is $166 * 159 * 10$.

Tab. 1. Basic Geometric Parameters of Moving Blade

Parameters	Numerical Value
Length of blade chord/mm	35.04
Length of axial chord/mm	24.81
Blade height/mm	70.8
Pitch/mm	28.2
Leading edge radius/mm	3.305
Trailing edge radius/mm	0.154
Blade setting angle/°	48.69
Entrance geometrical angle/°	42
Angle of attack/°	0

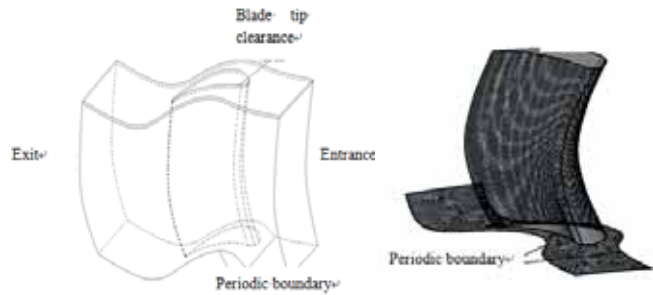


Fig. 1. Geometrical Model and Mesh Generation of Cascade Passage

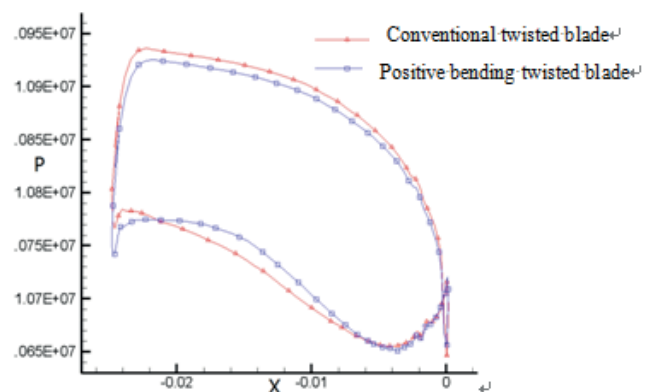
1.2 Numerical Methods and Boundary Conditions

Using the Fluent software to solve the three dimensional steady viscous Reynolds average equations, and using finite volume method based on unit center solves the governing equations. Turbulence model selects $k-\omega$ SST model, and nearby the wall adopts the wall-function method; Use SIMPLEC algorithm to solve the pressure-speed coupling and the discrete set of the convective item of the control equation is the second order upwind scheme. The revolving speed of moving blades is 3,000 RPM. The inlet boundary condition is the pressure entrance, with the pressure of 11.0495 MPa, and the temperature of 750 K; the outlet boundary condition is the pressure exit, with pressure of 10.697 MPa, and the temperature of 734 K. The fluid of the computational domain chooses overheating state seam. In the process of calculation, through the observation of each equation convergence condition, properly adjust relaxation factors, to speed up to calculate the convergence. The residual error to reach convergence of continuity equations, velocity equations, turbulence energy and turbulence dissipation rate is 10^{-3} , and that of energy equations is 10^{-7} .

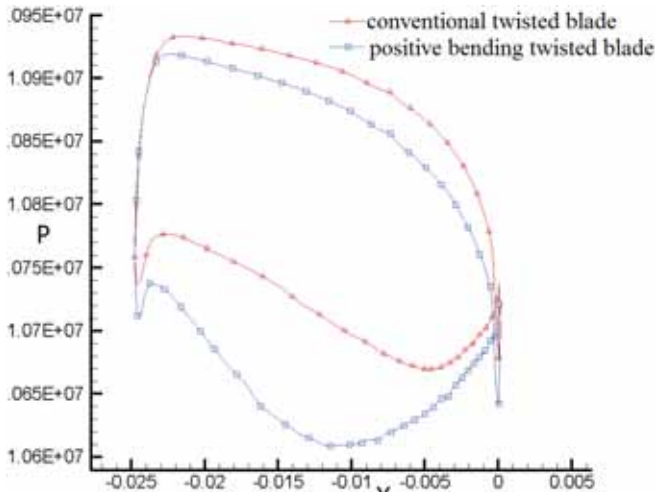
COMPUTATION RESULTS AND ANALYSIS

DISTRIBUTION OF STATIC PRESSURE ALONG BLADE PROFILE IN DIFFERENT BLADE HEIGHT SECTIONS

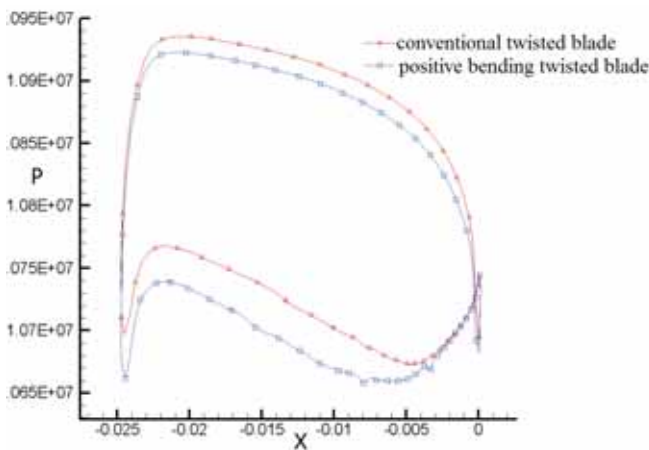
Fig. 2 is distribution of the static pressure of conventional twisted blades and positive bending twisted blades along blade profile in each blade height section.



(a) Distribution of Static Pressure of 10% of the Blade Height Section



(b) Distribution of Static Pressure of 50% of the Blade Height Section



(c) Distribution of Static Pressure of 90% of the Blade Height Section

Fig. 2. Distribution of Static Pressure along Blade Profile in Different Blade Height Sections

As can be seen from Fig. 2, after the steam flow bypassed leading edge point of the blade, the pressure of the pressure surface all gradually reduce along the blade profile; the pressure of suction surface also gradually decreases along the blade profile within the first 80% range of the cascade axial, but within 20% range of the cascade back end, an increase sign appears. This is because in this area, the passage secondary vortex of the cascade flow path under the action of the transverse pressure gradient gathers in the suction surface, and the boundary layer of the suction surface here receives disturbance of the secondary vortex, starts to break away from the suction surface, and mixes together with the passage vortex, which makes the velocity of the steam flow decrease and the pressure increase therewith.

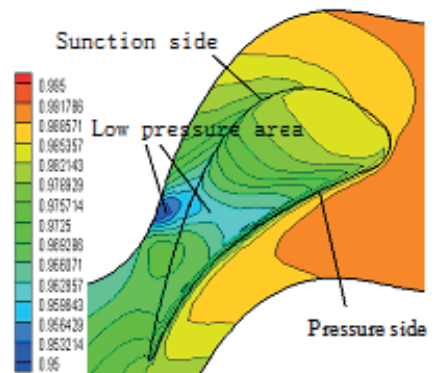
Compared to the Fig. (a), (b), (c) in Fig. 2, we can also see that, relative to the conventional twisted blade, although the change of the transverse pressure gradient of the pressure surface and suction surface of the positive bending twisted blade between the root and the tip of the blade is not big, it is

quite obvious in the middle of the blade. This is due to after the twisted blade bent positively, “C” type pressure distribution is formed both on the suction surface and the pressure surface of the blade, which makes transverse pressure gradient in the middle of the blade increase, the diffusion section of the middle of the suction surface increase, and the transverse pressure gradient at the end of the blade reduce, and the diffusion section at the end of the suction surface reduce.

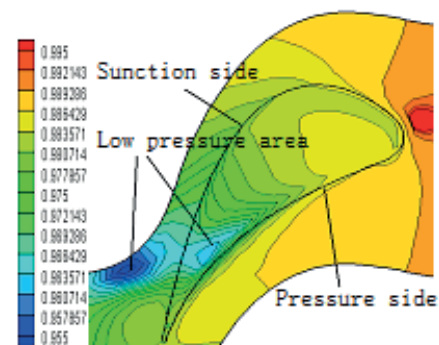
The end secondary flow of the blade is mainly determined by the transverse pressure gradient, so as long as the transverse pressure gradient decreases, the transverse secondary flow of the two ends can be weakened, and then interaction between the secondary flow and the mainstream cascade passage weakens, and the mixing loss caused by the secondary flow reduces.

DISTRIBUTION OF STATIC PRESSURE COEFFICIENT IN THE BLADE TIP CLEARANCE OF POSITIVE BENDING TWISTED BLADES

Fig. 3 is the contour line distribution diagram of static pressure coefficient of positive bending twisted blade clearance section under different blade tip clearances.



(a) $\tau = 1 \text{ mm}$



(b) $\tau = 2 \text{ mm}$

Fig. 3. Distribution Diagram of Static Pressure Coefficient in Blade Tip Clearance

As shown in Fig. 3, due to a larger transverse pressure gradient existing between the pressure side and suction side of the blade, part of steams in the passage will flow from the side

of the pressure side of the tip clearance to the side of suction side under the action of the transverse pressure gradient, forming the leakage flow of blade tip clearance. With the development of the flow, the leakage flow will eventually flow from the suction side of the blade into the adjacent cascade passage, and interblend the mainstream fluid within the passage, and form complex leakage vortex of tip clearance, resulting in the flow loss.

Compared to (a) and (b) in Fig. 3, you can see that with the increase of the tip clearance, the transverse pressure gradient between the pressure side and suction side of the clearance is increasing, which causes the increase of the blade tip clearance leakage rate. In addition, with the increase of the blade tip clearance, the leakage vortex of the blade tip clearance gradually shifts to the downstream of the cascade and gradually gets away from the suction side of the blade. This is because the larger the blade tip clearance, the greater the leakage flow velocity, and the higher the ability to push the mainstream in the cascade passage, at this moment, the leakage loss and the mixing loss caused by the leakage flow are more.

DISTRIBUTION OF STATIC PRESSURE OF THE SUCTION SURFACE OF POSITIVE BENDING TWISTED BLADES

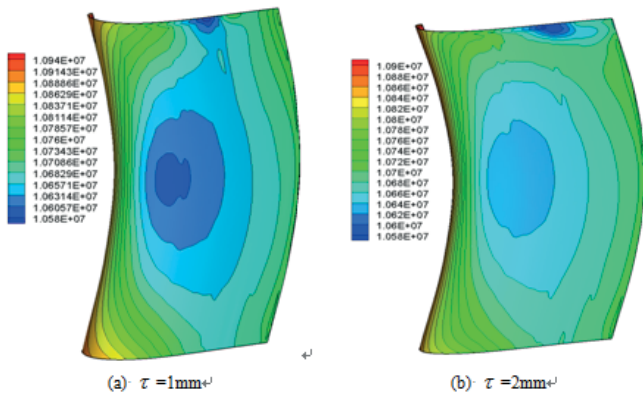


Fig. 4 Distribution Diagram of Static Pressure of the Suction Side

Fig. 4 is the contour line distribution diagram of static pressure of the positive bending twisted blade tip clearance suction surface under different blade tip clearances. From Fig. 4, we can see that with the increase of the blade tip clearance, the scopes of influence of the clearance leakage flow low pressure area in the axial direction and spanwise of the blade somewhat increase. The increase of the low pressure area scope of influence, explains somewhat increase of the loss of pressure of steams, while the increase of leakage loss is just accompanied by the increase of the loss of pressure, thus it can again explain that, the clearance leakage loss caused by the leakage flow increases with the increase of the blade tip clearance.

In addition, the increase of the blade tip clearance, to some extent, weakens the “C” type pressure gradient formed on the suction surface by the positive bending twisted blade. The decrease of “C” type pressure gradient will make reducing of

the power transmitted by low steam energy at both ends of the blade to the central section, so, the low energy steam will be accumulated in the two ends of the blade, which will result in thickness of the boundary layer at the blade end becoming larger, and the end loss can also increase accordingly.

CONCLUSIONS

(1) After the twisted blade positively bends, under the action of “C” type pressure distribution, the transverse pressure gradients at two end of the blade reduce, which helps to reduce the transverse secondary flow at the end, and weakens interaction between the secondary flow and cascade passage mainstream, and thus to reduce the mixing loss of the secondary flow and the passage mainstream.

(2) With the increase of the blade tip clearance, the tip clearance leakage vortex of the positive bending twisted blade gradually transfers to the downstream of the cascade and gradually away from the blade suction surface, the scope of influence in the cascade passage gradually increases, and the corresponding leakage loss and the mixing loss also gradually increase.

(3) The increase of the blade tip clearance weakens “C” type pressure gradient on the suction surface of the positive bending twisted blade, makes the boundary layer thickness at both ends of the blades increase, and causes the increase of the loss of the blade end.

ACKNOWLEDGEMENTS

This work was financially supported by Department of Jilin Province Natural Science Foundation of China(20140101064JC)

REFERENCES

1. H.S.Chen, S. Kang and C.Q. Tan, “Experiment Research on the Influence of Positive bending of the Blade on the Aerodynamic Characteristics of Penetrated Calm Cascade and Blade”, Engineering Thermophysics Newspaper, no. 2, pp. 179-182, 2002,.
2. G Pullan and N.W Harvey, “The influence of sweep on axial flow turbine aerodynamics in the endwall region”, Journal of Turbomachinery, no.130, 2008,.
3. M. H. Vand and S. Wang, “Numerical Study of the Effects of Bowed Blades on Aerodynamic Characteristics in a High-pressure Turbine”, American Society of Mechanical Engineers, pp. 487-496, 2005,.
4. B.T. An, W.J. Han and Z.Q Wang, “Experience Research on Mechanism of Twisted Blades Reducing Losses”, Thermal Energy Power Engineering, no. 15, pp. 498-501, 2000,.
5. Z.M. Feng, W.A. Hang and J.J. Zhong, “Experimental Study on Post-load Positive Bending Cascade Aerodynamic Performance”, Experimental Fluid Mechanics, no. 23, pp.

56-59, 2009,.

6. H.W. Lu, X.X. Kan and J.J. Zhong, etc. :Analysis of the Flow Structure in Positive Bending Compressor Stationary Guide Blade Passageway”, Engineering Thermophysics Newspaper, no. 34, pp. 1828-1832, 2013,.
7. L. Chen, and J. Cheng, “Numerical Investigation on the Influence of Twisted Blades on Turbine Aerodynamic Performance under Stage Environmen”, Aviation Dynamics Newspaper, no. 26, pp. 2765-2711, 2011,.
8. Atkins, RJ (Atkins, Rowland J.); Tidd, M (Tidd, Morgan); Ruffo, G (Ruffo, Gord). “Sturgeon Bank, Fraser River Delta, BC, Canada: 150 Years of Human Influences on Salt Marsh Sedimentation”, Journal of Coastal Research, SI 75, pp. 790-794, 2016,.

CONTACT WITH AUTHOR

Jianguo Jin
email: jinjianguo6503@163.com,

Zhanzhou Wang
wang_zhan_zhou@163.com,

Lihua Cao
email:984066765@qq.com

School of Energy and Power Engineering,
Northeast Dianli University,
Jilin,
China

MODEL OF ECO-WATER DRIVING FORCE AFFECTING THE EVOLVEMENT OF RUNOFF IN THE UPPER MINJIANG RIVER BASIN

JinHuang

WunianYang

Li Peng

Muhammad Aqeel Ashraf

Key Laboratory of Geoscience Spatial Information Technology,

Ministry of Land and Resources of the P.R. China,

Chengdu University of Technology, P. R. China

Faculty of Science and Natural Resources, University Malaysia, Malaysia

ABSTRACT

The amount of eco-water resources reflects the land surface water conservation capability, and the underlying surface condition in the hydrologic cycle. In the upper Minjiang River Basin, the amounts of eco-water resources were retrieved from remotely sensed data during 1992 to 2005. Through regression analysis between the retrieved eco-water data and the climate hydrological data mainly including the temperature, the precipitation, and the runoff in the same period, the model of eco-water driving force affecting the evolvement of runoff was established. The accuracy analysis indicates that the model can well describe the relationship between dry season runoff and its driven factors, the measured data validation proves that the model has high precision and good practicability. The eco-water remote sensing inversion provides a valid method to quantify the land surface water conservation capability, and suggests an interesting approach for the driving function quantitative researches of underlying surface factor in the hydrologic cycle.

Keywords: Eco-water, Remote Sensing Quantitative Retrieval, Upper Minjiang River, Runoff Prediction

INTRODUCTION

The influence of the underlying surface change on hydrological processes should not be ignored, but difficulty of its hydrological effect quantization has been the restriction of hydrological research. Underlying surface mainly includes three layers: the vegetation canopy, vegetation humus layer and soil layer. It is usually studied through three individual experiments respectively at typical sample plots (Liu et al.1989; Ogee and Brunet 2002; Rao et al.2005; Hu et al.2014; Sun et al.2015). However this approach showed its inefficiency and low accuracy, because the sampling method often failed to describe factually and comprehensively the water storage condition of underlying surface. Hence, with the development of modern science and technology, it is desired to find a simple

and effective way to discover the hydrological response to underlying surface change for the modern water science and water management.

The concept of “Eco-water (layer)” emphasizes the important role of underlying surface in hydrologic cycle. It is the extension and coupling of quantitative remote sensing to the hydrologic cycle (Yang et al. 2001; Wan et al. 2004).

Eco-water is the water closely related to the earth’s land surface vegetation, forms the “eco-water layer” centered on vegetation conserved by the vegetation, the vegetation humus layer and the root soil layer after the conversion of atmospheric precipitation. Eco-water serves as a special transfer zone which differs from surface water or groundwater either in existence or in movement form. Functionally, the eco-water is capable of supplementation for both surface

water and groundwater. Although not directly involves in the hydrological cycle processes, eco-water plays an important role of buffering and transformation in the hydrological cycle, that is the driving role of underlying surface factor.

Although subject and study methods are different, eco-water and underlying surface have the same research object (vegetation canopy, humus layer and soil layer) and research purpose (Figure1). Usually, vegetation canopy, humus layer and soil layer were researched respectively to find out that how them intercept and retain water in hydrological cycle. However, although the hydrological effect mechanism of the three is different, they have the same effect to runoff. Therefore, the overarching goal of this study was to take vegetation canopy, humus layer and soil layer as a whole by eco-water, make the effect of underlying surface on runoff quantified with the help of remote sensing technology (Li et al. 2009; Jian et al. 2012; Kyziol, L. 2013), and then build the dry season runoff prediction model from the drive angle.

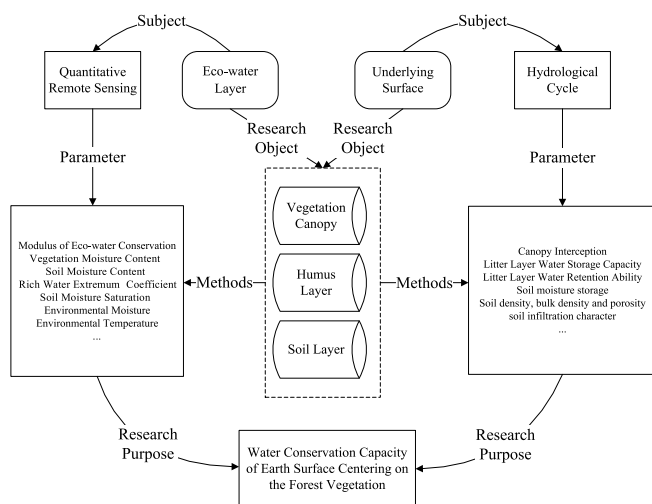


Fig. 1. The relationship of Eco-water Layer and underlying surface

STUDY AREA

The upper Minjiang River Basin, located in the transition region from eastern Qinghai-Tibet Plateau to Sichuan Basin in western China, is an essential tributary to the Upper Yangtze River and important water conservation area for the Chengdu Plain. Good or bad of the ecological environment in western regions of China directly affect the economic development of eastern China: if the western ecological environment deteriorates, water shortages, the east valley will dry up. And the diversification and multilayered of the western ecological environment, is the key to keep the normal operation of the environment in central and eastern China, is also the key to the sustainable development of China economy. The forest in the upper Minjiang River acts as the natural barrier and green reservoir of Sichuan, but due to massive deforestation for hundreds of years, the subsequent ecological environment deterioration has risen serious issues about the water conservation capacity, where the forest vegetation has decreased and thus led to observed reduction of runoff in the

dry season. Thus Chinese water resources research focus on the western region, and the upper Minjiang River basin is one of the most important water resources supply basin in western China.

ECO-WATER REMOTE SENSING QUANTITATIVE RETRIEVAL

Amount of water conserved in the eco-water layer was represented by the modulus of eco-water conservation (MEC). The MEC is related to vegetation and soil water content and represents the water conservation ability of the earth's surface based on vegetation. Vegetation and soil information was extracted by remote sensing technology with high sensitivity and accessibility, thus quantification of each was a precondition for calculating the MEC. The basic research unit of remote sensing image digital processing is a single pixel with MEC following by also utilizing a single pixel as the basic research unit. According to the definition of MEC that the MEC model of pixel(i,j) is as follows:

$$MEC(i,j) = EWTC(i,j) + W(T)(i,j) \quad (1)$$

Where $EWTC(i,j)$ is vegetation water content of the pixel(i,j), $W(T)(i,j)$ is soil water content of the pixel(i,j).

If there are M lines and N rows of the remote sensing image of the study area, the amount of ecological water resource is:

$$MEC = \sum_{i=1}^M \sum_{j=1}^N MEC(i, j) \quad (2)$$

The basic principle of remote sensing quantitative inversion is the reflection spectrums of surface features actually exhibit particular characteristics (Zhang et al. 2010(a)). Vegetation water content has obvious response to spectral characteristics in the wavelength range from near infrared to intermediate infrared. 1600nm indicates a strong moisture absorption band while 820nm indicates a weak moisture absorption band, allowing the vegetation index SR (Simple Ratio) (Equation 3) established by the ratio to effectively highlight the vegetation water content information (Zhang et al. 2010(b); Wang et al. 2011; Yi et al. 2012).

$$SR = R_{1600} / R_{820} \quad (3)$$

Where R_{1600} is spectral reflectivity at 1600 nm, R_{820} is spectral reflectivity at 820nm. Then the measured vegetation spectral data and the measured vegetation biochemistry data were used to establish the vegetation water content model. The highest correlation coefficient model was selected from Regression analysis models (exponential, linear, logarithmic, polynomial, power):

$$EWTC = -0.1126 \times \ln(SR) + 0.2974 \quad (4)$$

Advantages and disadvantages of soil moisture estimation models with optical sensor differ, and after analyzing the characteristics and regression effects with actual soil water

content measurement, SMMRS (Soil Moisture Monitoring by Remote Sensing) (Equation 5) based on soil line was chosen. Soil line is a straight line in a two-dimensional spectral space of red and near infrared generated from a series of pure soil pixels ranged by reflectance. Soil line is a comprehensive reflection of the soil's characteristic in various water conditions (Zhan et al. 2007; Qin et al. 2012).

$$SMMRS = 1 - \frac{1}{\sqrt{M^2 + 1}} (R_{645} + MR_{858}) \quad (5)$$

Where M is the slope of soil line, R₆₄₅ is spectral reflectivity at 645 nm, R₈₅₈ is spectral reflectivity at 858 nm. Then the measured soil spectral data and the measured soil biochemistry data were used to establish the soil water content model, the highest correlation coefficient model was selected from Regression analysis models (exponential, linear, logarithmic, polynomial, power):

$$W(T) = 7.7962 \times SMMRS - 4.7824 \quad (6)$$

Remote sensing data was collected from 1992 to 2005, LANDSAT images were utilized in this study. SR is the ratio of infrared wavelengths (band 5, center wavelength of 1676 nm) and nearly red band (band 4, center wavelength of 840 nm) in remote sensing image inversion of EWTC. The soil line of image must be derived initially to compute SMMRS for the remote sensing image inversion of W(T). The modulus of eco-water conservation of the study area was then retrieved according to the MEC model based on the already retrieved EWTC and W(T).

MODEL OF ECO-WATER DRIVING FORCE AFFECTING EVOLVEMENT OF RUNOFF

Eco-water driving force affecting the evolvement of runoff

The runoff was influenced by two of the driving factors, climate and underlying surface. The climate factors include temperature and precipitation, while the underlying surface factors are represented by vegetation. Because the factors mutual influence and restrict each other, it is hard to understand and simulate the interaction mechanism between them in order to predict the runoff more accurately (Wu et al., 2003; Sansom, 1999). It has always been the difficulties of further research in the hydrologic cycle. Precipitation, temperature, runoff data are available, but the effect of vegetation is difficult to quantify. As early as in the thirties of the 20th century, the experts and scholars had gotten the empirical relationship among hydrological characteristics, climate factors and underlying surface factors with a large amount of observation data, including vegetation type, coverage, spatial pattern and so on. But the precision of this kind of empirical relationship is difficult to guarantee. The amount of eco-water resources not only reflects the water conservation capacity of the earth's surface centered on vegetation, but also comprehensively reflects the general condition of underlying surface in the

instantaneous remote sensing imaging moment. It is a final result after the interaction among climatic conditions and topography, geology, soil, vegetation, human activities, and many other factors. In the original forest, the interception of rainfall by eco-water is around 20% to 40%, the interception volume should not be under estimated. In the process of hydrologic cycle, the amount of eco-water resources affects the transformation and distribution from precipitation to other kinds of water resources, and also affects the length of time of water retention in the stored body. In other words, the amount of eco-water resources represents the efficacy of reducing flood and supplying water shortage in the hydrologic cycle. From a macroscopic perspective provided by remote sensing, the hydrologic cycle driving causes analysis becomes more simple, practical and reasonable, and it is probably that the runoff prediction precision was able to be further improved.

RUNOFF PREDICTION DATA

Climate conditions during the same period should also be considered when studying the influence of ecological water on runoff. Climate data collected for this study included the precipitation and the temperature of years and months in the upper Minjiang River Basin from 1990 to 2005. The precipitation and temperature data was collected from 9 national surface meteorological stations (Songpan, Zoige, Barkam, Hongyuan, Xiaojin, Dujiangyan, Pingwu, Mianyang, Yaan) which were within or adjacent to the river basin and then were interpolated to get derive raster data of the study area. The runoff data of years and months in the Upper Minjiang River Basin from 1992 to 2005 were collected from Zipingpu hydrologic stations.

MODEL OF ECO-WATER DRIVING FORCE AFFECTING THE EVOLVEMENT OF RUNOFF

The statistical features of medium and long term runoff drive factors are relatively complicated in terms of time and space, and the practical application of factor forecast model is difficult to some extent. But, the runoff forecast model based on solid physical causes is recognized as an important development trend of the medium and long term runoff forecast. In this paper, the model of evolvement of runoff was established from driving factors of the precipitation, the temperature and the eco-water. Among the statistical empirical models, the multiple linear regression model is one of the most popular models for runoff predicting. Because the eco-water effect on runoff supplement is generally more observable in the dry season, the annual prediction depth, the annual average temperature and the eco-water depth were taken as the independent variables, and the runoff depth in dry season was taken as the dependent variable. The multiple linear regression was then carried out to establish the runoff prediction mode, modeling process as shown in figure 2.

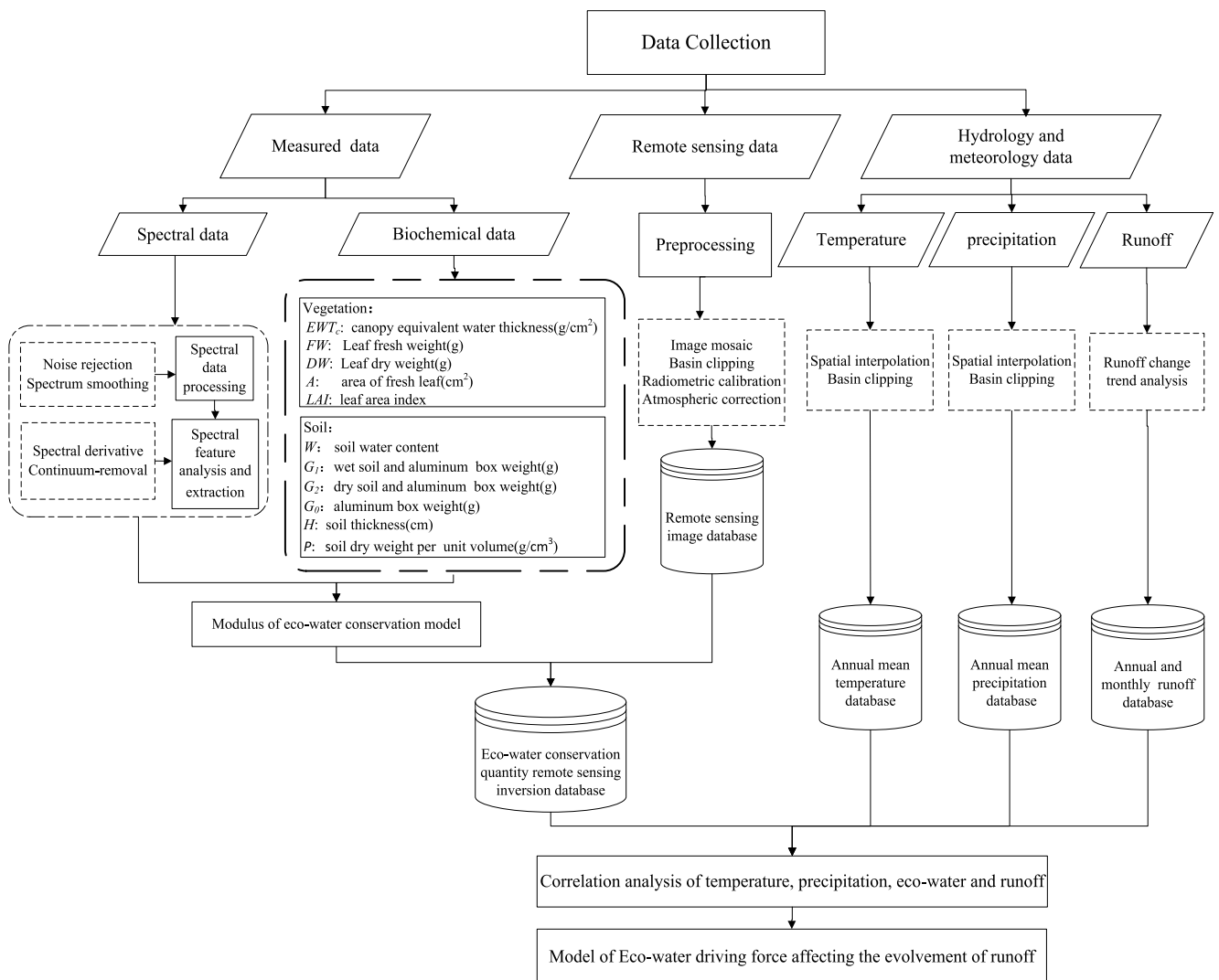


Fig. 2. Modeling flow

The mathematical model of the runoff prediction model is as follows: (7)

$$Y = aX_1 + bX_2 + cX_3 + d$$

Where X_1 is eco-water depth; X_2 is annual precipitation; X_3 is annual temperature; a , b , c , d are undetermined coefficients. The data from 1992 to 2002 were taken as the experimental data to figure out coefficient (table 1), precision analysis and significance testing as shown in table 2 and table 3. From precision analysis, it can be concluded that the correlation coefficient of linear regression model (r) is 0.842 and coefficient of determination (R^2) is 0.709, which means that the model can well reflect the relationship between dry season runoff and its drive factors. From significance testing (F-test), F_0 is 5.690, bigger than critical value of $F_{0.05}(3,9)$ 3.86, the F significant probability test of regression equation is 0.027, smaller than 0.05, mean that the linear relationship between dry season runoff and its drive factors is statistically significant by F-test.

To validate the model, three years prediction values were compared with measured values from 2003 to 2005. According to test result (Table 4), the average relative error is 0.08, presenting a high precision and good practicability.

From significance test of single factors (table 1), probability test of eco-water is 0.006, smaller than 0.05, which means eco-water has significant linear relationship with dry season runoff, while probability test of annual precipitation and annual average temperature are 0.851 and 0.6345, which means they don't have significant linear relationship with dry season runoff. For the precipitation, it is not the mainly supply for runoff yet, there is no high correlation of runoff and precipitation in dry season, as shown in figure 3, the runoff curve changes not as the precipitation in dry season. For the temperature, it has much more complicated relationship with runoff. Temperature influence on precipitation, evapotranspiration and the underlying surface pattern, and finally influence on runoff indirectly. That is why in multiple linear regression model the correlation of temperature and runoff can't be highlight.

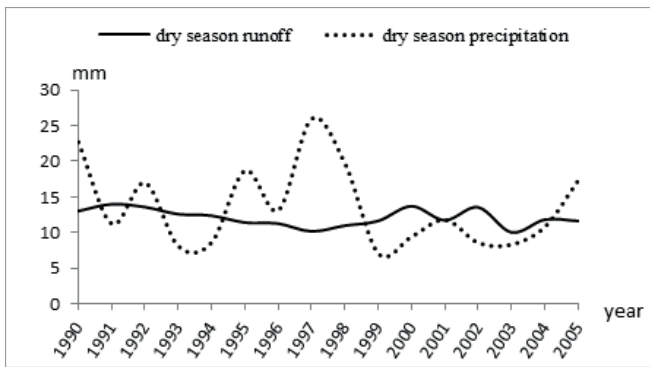


Fig. 3. Change curves of dry season runoff and precipiton

Tab. 1. Model Coefficients

	Unstandardized Coefficients	Standardized Coefficients	Sig.
<i>d</i>	6.258		0.391
<i>a</i>	0.484	0.812	0.006
<i>b</i>	0.000	0.041	0.851
<i>c</i>	-0.268	-0.107	0.634

Tab. 2. Precision of linear regression model

<i>r</i>	<i>p</i> ²	Adjusted <i>p</i> ²	Std.Error of the Estimate
0.842	0.709	0.585	0.6464

Tab. 3. Analysis of linear regression variance

	Sum of Squares	<i>d</i> , <i>f</i>	Mean Square	<i>F</i>	Sig.
Regression	9.686	3	3.229	5.690	0.027
Residual	3.972	7	0.567		
Total	13.658	10			

Tab. 4. Model accuracy test

Year	Dry season measured value	Dry season predicted value (<i>J</i>)	Absolute error	Relative error
2003	10.03375	11.82509	1.791342	0.178532
2004	11.8293	11.37945	-0.44985	-0.03803
2005	11.63487	11.23794	-0.39693	-0.03412

CONCLUSION

In order to solve the difficulties of underlying surface factor quantification, this paper introduces eco-water remote sensing quantitative inversion theory and method to river runoff forecast research. As the water-rich features of eco-water are special, it is difficult to make extraction and quantization with the conventional method, but quantification of underlying surface factor hydrological effect can be realized with remote sensing quantitative inversion technology. Due to eco-water research theory and technology, it is possible to reflect the water conservation function of underlying surface factor more comprehensively, macroscopically and quantitatively, thus providing strong support for researching the influence of underlying surface factor on runoff change. Taking the upper

Minjiang River Basin as the study area, this paper performs inversion of eco-water resources quantity with remote sensing method, and establishes driven runoff forecast model. The accuracy analysis shows that the model of eco-water driving force affecting the evolvement of runoff passed the test of significance and the measured data validation proves that the model has high precision and good practicability, which suggests that the influence of underlying surface on runoff quantified by eco-water is acceptable.

There are still something in need of improvement: Screening and regulating features or feature combination of drive factors sensitive to dry season runoff (such as precipitation/rainy days, the highest temperature, the lowest temperature, wind speed, humidity and so on) will be the further research; Eco-water driven factor was derived by means of quantitative remote sensing inversion. Unlike measurements such as precipitation, temperature, eco-water remote sensing inversion itself has certain accuracy error. Therefore, it is also the basis of increase runoff forecast accuracy by improving the accuracy of the eco-water remote sensing inversion advancing with the times.

ACKNOWLEDGEMENTS

Wunian Yang was sponsored by the National Natural Science Funds (NO. 41071265 and NO.41372340) and the Specialized Research Fund for the Doctoral Program of Higher Education of China (NO. 20105122110006).

REFERENCES

- Liu, X. D., Wu, Q. X., & Su, N. H. 1989 Studies on rainfall interception in canopy, litter and soil hydrological characteristics of forests in Liupanshan mountains. *Scientia Silvae Sinicae*, 25(3), 220-227.
- Kyziol, L. 2013 Stress-corrosion resistance of the EN AW-AlZn5Mg1,5CuZr alloy in different heat treatment states. *Polish Maritime Research*, 20(4), 39-44.
- Ogee, J. & Brunet, Y. 2002 A forest floor model for heat and moisture including a litter layer. *Journal of Hydrology*, 255(1), 212-233.
- Rao, L.Y., Zhu, J. Z. & BI, H. X. 2005 Hydrological effects of forest litters and soil in the Simian mountain of Chongqing city. *Journal of Beijing Forestry University*. 27(1), 33-37.
- Hu, X. Y., YUu, X. Y. 2014 Hydrological characteristics of litters and soil in restoration and succession of Karst forest. *Guangdong Agricultural Sciences*, (23), 150-154.
- Yang, W. N., Yuan, P.X. & Wan, X. N. 2001 The study report: the ecological environment integrative survey and evaluation in the Minjiang upper river based on remote sensing, 863-308-21(6). Chengdu: Chengdu University of Technology Archives.

7. Wan, X. N., Yang, W. N., Wu, B.F., Sun, W. D. & Huang, Q. 2004 Conception of Eco-water sphere and its application. *Adv. Earth Sci*, 6(19), 117–121.
8. Li, Y. X., Yang, W. N., Tong, L., Jian, J. & Gu, X. F. 2009 Remote sensing quantitative monitoring and analysis fuel moisture content based on spectral index. *Acta Optica Sinica*, 29(5), 1403-1407.
9. Jian, J., Yang, W. N., Jiang, H., Wan, X. N., Li, Y. X. & Peng, L. 2012 A model for retrieving soil moisture saturation with Landsat remotely sensed data. *International Journal of Remote Sensing*, 33(14), 4553-4566.
10. Sun, B; Wei, M; Du, J; Ji, W; Wen, MQ. 2015 Multi-attribute Group Decision Making Method of Ecological Water Compensation Program Based on Preference of Decision Makers. *Journal of Coastal Research*, 73, 606-610.
11. Zhang, R. H., Tian J., Li Z. L., Su H. B., Chen S. H. & Tang X. Z. 2010(a) Principles and methods for the validation of quantitative remote sensing products. *Science China(Earth Sciences)*, 53(5), 741-751.
12. Zhang, J. H., Xu, Y., Yao, F. M., Wang, P. J., Guo, W. J., Li, L. & Yang, L. M. 2010(b) Advances in estimation methods of vegetation water content based on optical remote sensing techniques. *Science China Technological Sciences*, 53(5), 1159-1167.
13. Wang, L. T., Wang, S. X., Zhou, Y., Liu, W. L. & Wang, F. 2011 Vegetation water content retrieval and application of drought monitoring using multispectral remote sensing. *Spectroscopy and Spectral Analysis*, 31(10), 2804-2808.
14. Yi, Q. X., Bao, A. M., Luo, Y. & Zhao, J. 2012 Measuring cotton water status using water-related vegetation indices at leaf and canopy levels. *Journal of Arid Land*, 4(3), 310-319.
15. Zhan, Z. M., Qin, Q. M., Ghulan, A. & Wang, D. D. 2007 NIR-red spectral space based new method for soil moisture monitoring. *Science in China(Series D:Earth Sciences)*, 50(02), 283-289.
16. Qin, Q. M., You, L., Zhao, Y., Zhao, S. H. & Yao, Y. J. 2012 Soil line automatic identification algorithm based on two-dimensional feature space. *Transactions of the CSAE*, 28(3), 167-171.
17. Wu, Y., Su, Z. X. & Fang, J. Y. 2003 Study on causes and ecological renewal of arid and warm valley of upper Minjiang river. *Journal of China West Normal University(Natural Sciences)*, 24(3), 276-281.
18. Sansom, A. L. 1999 Upland vegetation management: the impacts of overstocking. *Water Science and Technology*, 39(12), 85-92.

CONTACT WITH AUTHOR

JinHuang
email: jinjin0522@163.com

WunianYang (corresponding author)
email: ywn@cdu.edu.cn

Li Peng
email: pengli@cdu.edu.cn

Muhammad Aqeel Ashraf
email: ashraf@ums.edu.my

Key Laboratory of Geoscience Spatial
Information Technology,
Ministry of Land and Resources of the P.R. China,
Chengdu University of Technology,
Chengdu,
Sichuan, 610059,
P. R. China

Faculty of Science and Natural Resources,
University Malaysia
Sabah 88400
Kota Kinabalu Sabah,
Malaysia

MODELLING AND SIMULATION METHODOLOGY FOR DYNAMIC RESOURCES ASSIGNMENT SYSTEM IN CONTAINER TERMINAL

Bo Lu

Institute of E-Commerce and Modern Logistics,
Dalian University, Xuefu Str. 10, Dalian, China

ABSTRACT

As the competition among international container terminals has become increasingly fierce, every port is striving to maintain the competitive edge and provide satisfactory services to port users. By virtue of information technology enhancement, many efforts to raise port competitiveness through an advanced operation system are actively being made, and judging from the viewpoint of investment effect, these efforts are more preferable than infrastructure expansion and additional equipment acquisition. Based on simulation, this study has tried to prove that RFID-based real-time location system (RTLS) data collection and dynamic operation of transfer equipment brings a positive effect on the productivity improvement and resource utilization enhancement. Moreover, this study on the demand for the real-time data for container terminal operation have been made, and operation processes have been redesigned along with the collection of related data, and based on them, simulations have been conducted. As a result of them, much higher productivity improvement could be expected.

Keywords: Container Terminal, Resources Assignment System, Modelling, Simulation

INTRODUCTION

As the competition among the world ports has become increasingly fierce, every port is striving to increase its investments constantly and lower its operational costs in order to maintain the competitive edge and provide satisfactory services to port users [1]. The unreasoning behavior, however, has induced that substantial waste and inefficiency exists in container port production [9].

Port markets used to be perceived as monopolistic due to the exclusive and immovable geographical location of the port and the unavoidable concentration of port traffic. However, the rapid development of international container and intermodal transportation has drastically changed the market structure from one of monopoly to one where fierce

competition is prevalent in many parts of the world [11]. Many container ports no longer enjoy the freedom yielded by a monopoly over the handling of cargoes from their hinterland. Instead, they have to compete for cargo with their neighboring ports.

To maintain its competitiveness in such competitive condition, [7] claimed that container ports have to invest heavily in sophisticated equipments or in dredging channels to accommodate the most advanced and largest container ships in order to facilitate cost reductions for the container shipping industry [8].

It is important to note, however, that pure physical expansion is constrained by a limited supply of available land, especially for urban centre ports, and escalating

environmental concerns [10]. In addition, the excessive and inappropriate investment also can induce the phenomenon of inefficiency and wasting of resources. In this context, improving the productive efficiency of container port appears to be the viable solution [2].

Realizing the facts, port authorities have shown great interest in efficient port management [12]. Thus, they are continually searching for strategies to meet growing demands by utilizing their resources reasonably [3].

In comparison with the pure physical expansion, more preferable efforts to raise port competitiveness through an advanced operation system are actively being made by virtue of information technology enhancement [5]. With respect to container terminal, the productivity of transfer equipment in the container yard has a significant effect upon the overall productivity [4]. [2] pointed out that the productivity maximization of transfer equipment, minimization of C/C (container crane) and T/C waiting time by effective fulfillment of work order, and remarkable utility rate improvement by dynamic vehicle assignment – all these are essential technologies for state-of-the-art port stevedoring system [13]. Therefore, the development of a dynamic assignment technique (or dynamic operation) based on a real-time location system is needed to increase the efficiency of transfer equipment [20].

Simulations have been widely applied into container terminal production [14]. Majority these terminal simulations are mainly aiming to forecast logistics volume, and to seek an optimal infrastructure and proper equipment combinations, so that they have been used at the planning stage of port construction [17]. The recent researches, however, have turned to develop a new simulator in order to advance an existing port operation system [21]. Therefore, this study utilizes the Arena as a simulation language, and utilizes a visual basic for a linkage to event handling and excel file [22]. In this study, the assignment problems of transfer equipment have been grouped into two ways: there are the existing batch and sequential method and a dynamic assignment method. After that, the simulations for both of them have been performed to measure their quantitative effect respectively [19]. Moreover, this study has divided a simulation model into a current one (As-Is) and a future (To-Be) model. For the purpose of improving the reliability of each simulation model, the current research has collected the operation data of Dalian International Container Terminal for a full year.

The paper is structured as follows: after the introductory section of Chapter 1 and the basic research of Chapter 2, there will be followed by the description of As-Is situation analysis and redesign To-Be model in Chapter 3. In so doing, the initial environment setup for simulation and the required definition of input/output variables have been described in Chapter 4. Simulation modeling of container terminals is derived in Chapter 5. Finally, conclusions are drawn in Chapter 6. The definitions of terms in this study are as follows:

- RTLS: RFID based real-time locating system.
- YT pooling: joint assignment of yard tractors.

- Dynamic operation: optimal assignment of yard tractors based on real-time data.

OPERATION SITUATION OF CONTAINER TERMINAL

In an effort to make a survey of utilization of real-time data, to find out current operational problems, and to listen to the field experts' requirements for improvement, the researcher have visited major container terminals five times from October to December 2011. As the interviewees were composed of managers who have experiences of more than 10 years, they can tell us about the necessity of real-time data and also provide us with the necessary data for simulations. By fact-finding field survey, the researchers have found out the following operational problems and the requirement for advancement.

OPERATIONAL PROBLEMS

In most cases, the bottlenecks in the operational process are usually caused by transfer equipment rather than quay cranes or yard cranes.

In the case of one or two terminals, a pooling system or a dual cycle system has been adopted for the load balance of transfer equipment [23]. But because of inaccurate location recognition and scanty wireless communication infrastructure [24], they have ended up in failure.

In case of most domestic ports, the final job location of a crane can be checked by crane operator's input, consequently lowering the accuracy of input data, and in case of transfer equipment, it is almost impossible to conduct location tracking.

REQUIREMENTS FOR IMPROVEMENT

According to interview [18], equipment on transfer crane for a job completion notice and an automatic sensor for jobs to be done on yard tractor are needed. Tracking of yard tractors is conducive to the enhancement of operational efficiency from the aspect of situational assignment of transfer equipment. In order to show the evidence for effectiveness of dynamic planning, it is necessary to handle more than three berths in making simulation model rather than a small-scale container terminal.

PROCESS ANALYSIS AND REDESIGN

AS-IS ANALYSIS

In the development of a simulation model to test the efficacy of dynamic operation based on RTLS, first of all, this study need to analyze the As-Is business process and also need to design a To-Be business process. The As-Is Y/T (yard tractor) operation method is based on a team unit, that is, a certain number of Y/Ts per C/C (container crane), thus performing the job of loading and unloading for C/C. At this time each

Y/T team can be distinguished by its sign as shown in figure 1.

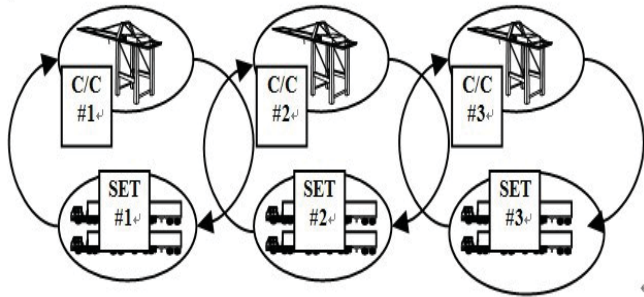


Fig.1 As-Is Y/T Operation Concept

In the sense that this batch and sequential operation of Y/T for shipment on board the ship can be done orderly, it has a positive meaning, but it makes it impossible to exchange mutual cooperation with Y/Ts belonging to the other teams, consequently lowering job flexibility and availability of equipment [27-29].

TO-BE MODEL

Different from the above-mentioned batch and sequential operation of Y/T, a dynamic operation system doesn't have a job team composed of transfer equipment. Instead, Y/Ts freely support the job of several C/Cs. That is to say, Y/T pool can be composed for a ship or for a whole container terminal in figure 2.

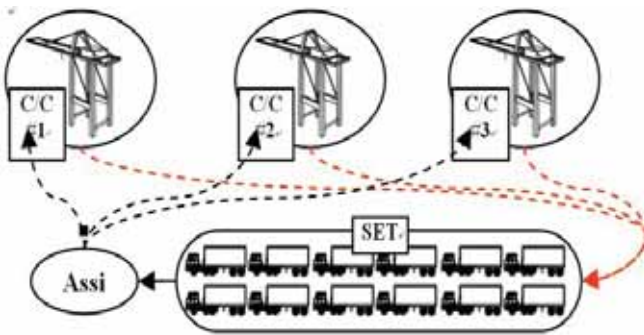


Fig.2 To-Be Y/T operation concept

As this method is FIFO-based assignment of transfer equipment, it can coordinate the imbalanced utility rate of transfer equipment. Also, considering the job situation including the moving distance from the current job place, Y/Ts can be dynamically assigned to the C/C and T/C, thus reducing empty movement considerably.

SIMULATION VARIABLES SETUP

INITIAL ENVIRONMENT SETUP FOR SIMULATION

With regard to environment setup related to job situation, in case of a As-Is model, this study has assumed that one berth has three units of C/C, one C/C has one team organization composed of five Y/Ts, and each team works for 10 hours. Running distance has been counted according to the required time of each movement line of Y/Ts (Figure 3). In case of the To-Be model, most conditions are similar to the As-Is model, but the only difference is that 15 units of Y/Ts have dynamically been assigned to the three units of C/C.

INPUT VARIABLES

In order to produce an input data, the researchers have collected the data of the mother vessel for one year of 2011 at the Dalian International Container Terminal. The data includes: arrival and departure time per mother vessel, work time, number of assigned Q/C, number of Y/T, number of T/C, and storage position of the containers required to be carried. All the average values and probability distribution values have been calculated by input analysis of Arena.

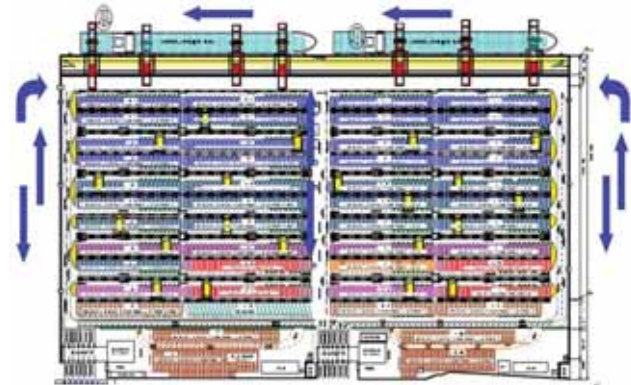


Fig.3 Movement line of Y/Ts

In Table 1, the expression of 3 kinds probability distribution is shown that Gamm means gamma distribution, TRIA means triangular distribution and NORM means normal distribution.

Tab.1 Major simulation input variables

Variable	Type	Value
Service time for ships(from arrival to departure)	Distribution	1+GAMM (2.58,5.48) hrs
Number of C/C	Average value	3 units
Loading time for C/C	Distribution	TRIA (20,30,40) sec
Number of Y/T	Average value	5 units/1GC
Running speed of Y/T	Average value	115 meters/min.
Waiting time for T/C	Distribution	TRIA (0.4,1,1.5) min.
T/C working hours	Distribution	NORM (3,0.2) min.
Y/T running distance	Considering the terminal layout and movement lines, they are converted into meters.	

Y/T's waiting time for T/C, working hours, Y/T's running speed and distance have been calculated according to the judgment of field experts. Table 1 and figure 4 show the values of major input variables.

DEFINITIONS OF OUTPUT VARIABLES

Output variables include: total handling volumes at the same hours, handling volumes per Y/T, and delayed working hours owing to Y/T's waiting.

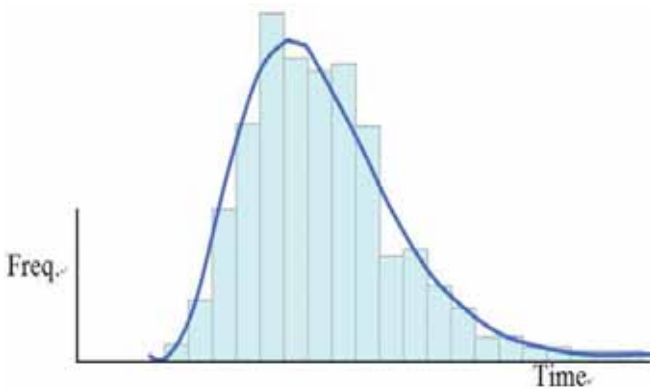


Fig.4 Distribution of Service Time for Ship (1+GAMM (2.58,5.48) hrs)

And then the research on co-relationship between handling volumes and Y/T's working hour delay has been made.

ANALYSIS RESULTS

INPUT VARIABLES

Making the assumption that, this study has conducted modeling based on one ship. The modeling can be divided into three parts. First, if containers come, they needs to be checked whether there are available Y/T or not.

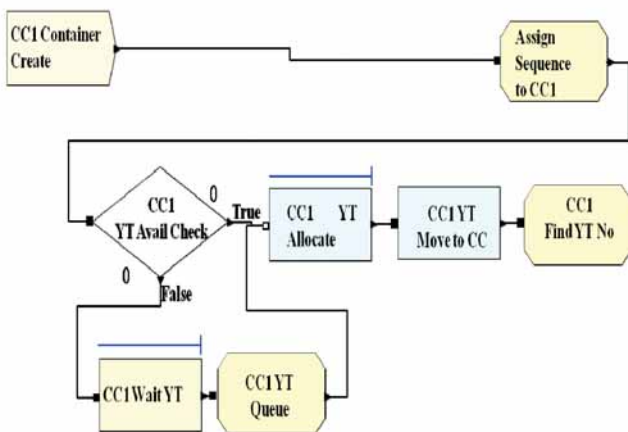


Fig.5 Available Y/T after job completion of C/C

If available, Y/Ts will be assigned to C/C, and if not, C/C is to wait Y/Ts. At this time, the C/C's waiting time for Y/T

is counted as shown in figure 5. 5 Y/Ts per team have been assigned by using the transporter module for C/C of three units which have been summarized as table 2.

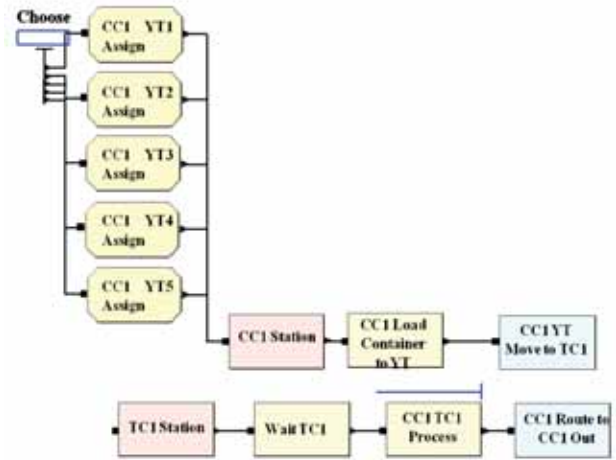


Fig.6 Y/T moves to T/C

Secondly, if Y/Ts are assigned, the corresponding containers will be loaded on the Y/Ts, and move to the T/Cs. At this time, the moving distance of Y/T becomes the movement line's distance to the destination. If T/C is under work, Y/T has to wait as shown in figure 6. At this point, the moving distance of Y/T is measured by a distance module which has been summarized as table 3.

Tab.2 Transporter module

Name	Us	Type	Dis. Set	V. (m/h)	Initial Position	
1	CC1	5	Free Path	CC1 Y/T Distance	10	CC1 Station
2	CC2	5	Free Path	CC2 Y/T Distance	10	CC2 Station
3	CC3	5	Free Path	CC3 Y/T Distance	10	CC3 Station

^a V. is Velocity/ ^b Dis. is Distance/ ^c Us. is Units

Finally, if T/C's storage work is completion, Y/Ts will be released, and containers handling will also be ended as shown in Figure 7.

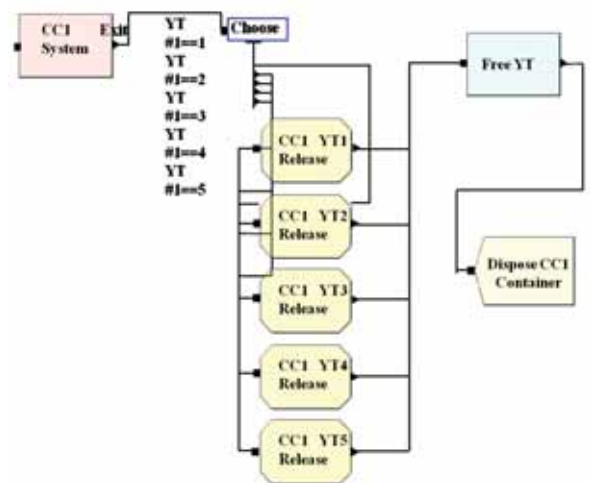


Fig.7 If T/C's storage work is completion, Y/T is released.

If the above-mentioned modules are connected, the modeling for one berth is completed. And this modeling is used for the programming of the container terminal with three berths. A new (or To-Be) model is similar to the As-Is model, but the difference is that Y/T is not assigned to a specific G/C (gantry crane) and also that if Y/Ts are free, they are to be assigned to the nearest G/C. Figure 8 illustrates the difference between the two models.

Tab.3 Distance module

No.	Distance Module Name	Beginning Station	Ending Station	Distance (Meters)
1	Yard Tractor.	CC1 Station	TC1 Station	378
2		TC1 Station	CC1 Exit	621
3	Yard Tractor.	CC2 Station	TC2 Station	351
4		TC2 Station	CC2 Exit	486
5	Yard Tractor.	CC3 Station	TC3 Station	621
6		TC3 Station	CC3 Exit	297

TEST AND RESULTS

In order to enhance the readability of simulation, animation has been made. Moreover, for helping understand the Y/T's flow, the animation has been depicted as shown in the figure 9.

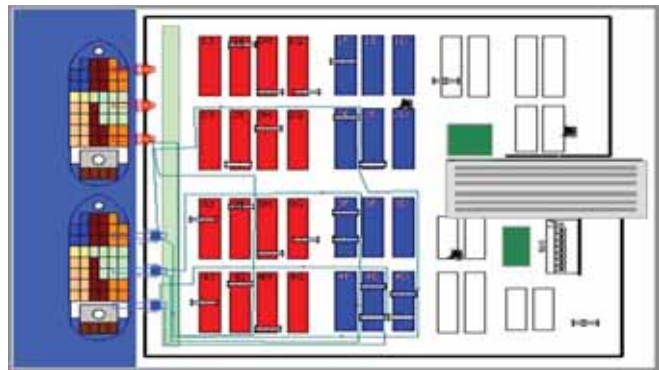


Fig.9 Simulation animation

As a result of this test, the major output values of both the As-Is model and the new model have been summarized as table 4.

Tab.4 Major output values

Output variables	Unit	As-Is model	To-Be model
Total handling volume	TEU	870	1,100
Handling volume per Y/T	TEU	58	73
Avg. Delay Time of C/C in Y/T waiting	Minutes	1.6	0.8

CONCLUSIONS

In the competitive circumstances, most ports were still committed to ongoing investment in the terminal facilities with a view to attracting more commercial vessels for anchorage. This produced an imbalance between inputs and outputs, which, in turn, produced an annual decline in operational efficiency. However, as [6] have claimed that 'Efficiency and productivity are core concepts of economics', and efficiency is also concerned with how to use limited resources more economically for any sort of production.

Moreover, by fact-finding field survey, the researchers have realized that the bottlenecks in the operational process are usually caused by transfer equipment rather than quay cranes or yard cranes. In the case of DITC, a pooling system or a dual cycle system has been adopted for the load balance of transfer equipment. Owing to inaccurate location recognition and scanty wireless communication infrastructure, however, they have ended up in failure. In addition, for most Chinese domestic ports, the final location of a crane can be checked by crane operator's input, consequently lowering the accuracy of input data, and in case of transfer equipment, it is almost impossible to conduct location tracking [25]. Therefore, transfer crane for an operation completion notice and an automatic sensor for operations to be done on yard tractor

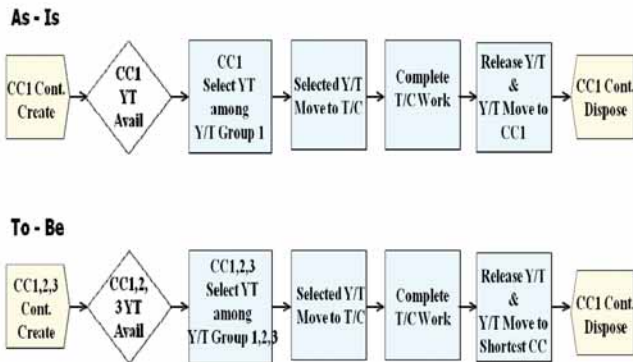


Fig.8 Difference between As-Is and To-Be model

Duplication tests have been made 100 times, and major output variables have been stored in the excel sheet by using VBA (visual basic for applications), and average values have been compared. In case of the As-Is model, it shows that 5 Y/Ts are sequentially assigned to C/C of one unit, and also shows the waiting queue of Y/Ts. In case of the new model, it illustrates that 15 Y/Ts for three C/C are automatically assigned according to resources conditions and shortest distance.

are necessary.

Tracking of yard tractors is conducive to the enhancement of operational efficiency from the aspect of situational assignment of transfer equipment.

As a benchmarking approach to research efficiency, the dynamic resources assignment of transfer equipment based on real-time locating data can increase productivity by more than 25% over the current batch and sequential assignment method. If an error range is reduced by using RFID technology, and also if RTLS is applied not only to the transfer equipment, but also to the yard cranes and containers, much higher productivity improvement could be expected. By doing this, the possible waste of resources and the industry best practice can be identified.

Nowadays, terminal operation systems of many advanced countries are becoming more intelligent and object-oriented, and also tremendous efforts are being made to actively and speedily respond to the rapidly changing environments [26]. Therefore, RTLS is becoming more and more the core technology under production condition in container terminal.

However, this study has a few limitations. As dynamic operation of transfer equipment have a positive effect on container unloading, simulation of this study has been confined to container unloading, and so pooling has also been limited to the ship alone. In this sense, it is not completely safe to say that this study has shown enough proof for the efficiency of a whole container terminal. Moreover, sensitivity analysis on output variables has not been made enough, thus being unable to suggest diverse alternatives. Therefore, more researches will be made in these fields in the future study.

ACKNOWLEDGMENTS

This work was supported by the National Natural Science Foundation of China (71573028); 2014 Liaoning BaiQianWan Talents Program (2014Q013); Liaoning Social Science Planning Fund Plan (L14CJY041); Liaoning Provincial Education Department (WJQ2015004); Dalian science and technology project (2015D21ZC001;2014D11ZC117); Program for Liaoning Excellent Talents in University (WJQ2015004); Dalian Jinzhou Science and technology project (RXYJ-RXSK-2015-002); Liaoning educational scientific research management think tank project (ZK2015090).

REFERENCES

1. Adolf K Y, Ng F P, Athanasios A P 2013 *Journal of Transport Geography* 27(2), 46–55.
2. Albalade D, Bel G, Fageda X 2013 *Ocean Coast Manage*, 71(1), 163–169.
3. Bel G 2011 *Business History* 53(5), 688–705.
4. Bendall H B, Brooks M R 2011 *Transport Logistics* 3(4), 384–405.
5. Blokker E, Vreeburg J, Dijk J 2010 *Journal of Water Resources Planning and Management* 136(19), 19–26.
6. Castillo–Manzano J I, Asencio–Flores J P 2012 *Transport Reviews* 32(4), 519–537.
7. Cullinane, K P B, Song D W, Gray R 2007 *Transportation Research A: Policy and Practice* 36, 743–762.
8. Cullinane K, Wang T F, Song D W 2010 *Transportation Research Part A* 40, 354–374.
9. Cheon S H, David E, Song D W 2010 *Transportation Research Part E* 46, 546–561.
10. De Borger B, De Bruyne D 2011 *Transport Economics and Policy* 45(2), 247–275.
11. Ducruet C, Lee S W, Ng K Y A 2010 *Maritime Policy and Management* 37(1), 17–36.
12. Forsund F R, Sarafoglou N 2010 *Journal of Productivity Analysis* 17, 23–40.
13. Fu Y M, Stuart A 2012 *Regional Science and Urban Economics* 42(3), 473–484.
14. Fan L, William W, Bruce D 2012 *Transportation Research Part E: Logistics and Transportation Review* 48(6) 1121–1136.
15. Ingrid O, Susanne S 2010 *Regional Science and Urban Economics* 40, 538–549
16. Jaipuria S, Mahapatra S 2014 *Expert Systems with Applications* 41, 2395–2408.
17. LU B, Park N K 2010 *Journal of Korean Navigation and Port Research* 34(7) 595–601.
18. Notteboom T E, 2010 *Journal of Transport Geography* 18, 567–583.
19. Rodrigue J P, Debrie J, Fremont A, Gouvernal E, 2010 *Journal of Transport Geography* 18, 519–529.
20. Wei S, Song J, Khan N I 2012 *Hydrological Process* 26, 281–296.
21. Wen–Tai H, Wang P 2012 *Regional Science and Urban Economics* 42(6), 975–986.
22. Woxenius J, Bergqvist R 2011 *Journal of Transport Geography*, 19, 680–688.
23. William G, Szymczak I K, Edward T 2012 *Journal of Aerosol Science* 54(12), 59–76.

24. Wilson W W, Dahl B, Taylor S 2011 *Transport Economics and Policy* 45(1), 129–154.
25. Xiao R, Su S L, Wang J Q, Zhang Z H, Jiang D W, Wu J P 2013 *Applied Geography* 39, 158–171.
26. Lee, J; Yoo, C; Lee, JL.2014. *Journal of Coastal Research*. 72, 81-84.
27. Yang Z, Gu X S, Liang X Y, Ling L C 2010 *Materials and Design* 31, 1042–1049.
28. Du, JQ; Du, SJ; Shen, SL; Yin, ZY. 2015. *Polish Maritime Research*. 22(1), 126-135.
29. Zhu Y H, Drake S, Lü H S, Xia J 2010 *Water Resources Management* 24, 1089–1105.

CONTACT WITH THE AUTHOR

Bo Lu

lubo@ucas.ac.cn

Institute of E-Commerce and Modern Logistics
Dalian University
Xuefu Str. 10, Dalian

CHINA

VERTICAL DISTRIBUTION OF NEARSHORE FLOW VELOCITY

Li Chunhui ^{1,2}

Fu Xiaoyan ^{1,2}

Li Ruijie ^{1,2}

Dai Lu ^{1,2}

Chen Peng ^{1,2}

¹ Key Laboratory of Coastal Disaster and Defense, Ministry of Education, Hohai University, Nanjing 210098, China

² Environment Marine Laboratory, Hohai University, Nanjing, China

ABSTRACT

In this paper, a new exponential formed vertical distribution of nearshore flow velocity is constructed, which is simpler in form and more suitable for engineering application. The physical meaning of the new formula is more specific than that of Soulsby. Compared with those logarithmic formed ones, the new one does not need the maximum velocity and only needs the mean velocity in vertical, which gives it better engineering practicability. Apply the new formula to Jiangsu coastal area and compare the results with that of Soulsby whose results show the new formula agrees better with the measured flow velocity, which reasonably reflects the basic principles of vertical distribution of flow velocity.

Keywords: vertical distribution of flow velocity; Jiangsu Sea; nearshore; exponential formula

INTRODUCTION

The vertical distribution of nearshore flow velocity is an important issue, which is meaningful to oceanography and ocean engineering. Many scholars have been studying on vertical distribution of flow velocity and a variety of formulae are brought forward, such as Prandtl who put forward a logarithmic one by establishing the theory of mixing length [6], Monin [5], Taylor [13], Schauer [8], Soulsby [11], Mattheus[10] and Song Zhiyao [9] who improved Prandtl formula and Karman and Prandtl[13] who proposed an exponential one by dimensional analysis. And Kumbhakar M[3], Xiao Qianlu[16], Jakubowski[15] and He Bingqu[2] also did several studies on it. Most of these formulae are complex in forms and not convenient for application. In 1990, Soulsby[12] brought forward an empirical formula which has been widely used. However it is not distinct enough in physical meaning and it is a piecewise function, which makes

it inconvenient to use. So it is necessary to put forward a new formula for vertical distribution of flow velocity which is simpler, relatively more accurate with definite physical meaning and easier in application.

DERIVATION OF VERTICAL DISTRIBUTION OF FLOW VELOCITY

Ni Jinren et al. [6] found a basic formula after summarizing a variety of velocity profile formulae:

$$F\left(\frac{u}{u_*}, \ln \frac{h}{z}\right) = f(x_1, x_2 \dots) \quad (1)$$

Where, $f(x_1, x_2 \dots)$ is an undetermined function; u is flow velocity; u_* is friction velocity; h is water depth; z is the height above seabed.

A new formula is given through referring to a formula put

forward by Li Ruijie (2012)[4] and the corrective methods for Prandtl formula:

$$\ln \frac{u}{u_*} = A_1 \ln \left(\frac{h}{z} \right) + A_2 \ln z + A_3 \quad (2)$$

Where, A_1, A_2, A_3 are undetermined parameters, and formula (2) could be written as:

$$u = u_* \left(\frac{h}{z} \right)^{A_1} z^{A_2} e^{A_3} \quad (3)$$

According to Prandtl mixing length theory, the friction velocity u_* could be written as (Fang Guo-hong)[1]:

$$u_* = \frac{\kappa U}{\ln(4h/z_0) - 8/3} \quad (4)$$

Where, U is mean velocity in vertical. Formula (3) could be written as:

$$u = e^{A_3} \frac{\kappa U}{\ln(4h/z_0) - 8/3} \left(\frac{z}{h} \right)^{-A_1} z^{A_2} \quad (5)$$

Parameters in formula (5) are determined by using nearshore measured data and the formula works best and the coefficient of correlation reaches 0.985 when z_0, A_1, A_2 and A_3 equal 0.0025, -0.02457, 0.159018 and 2.65953 respectively. Then formula (5) could be written as:

$$u = K \left(\frac{z}{\kappa h} \right)^{\frac{9}{49}} U \quad (6)$$

Where, $K = \frac{4.83}{\ln(1600h) - 8/3} h^{\frac{3}{19}}$

VALIDATION AND COMPARISON OF VELOCITY PROFILE FORMULAE

Apply formula (6) in Jiangsu Sea and compare the results with Soulsby formula (formula 7) which is widely used:

$$u = \begin{cases} \left(\frac{z}{0.32h} \right)^{\frac{2}{7}} U & 0 < \frac{z}{h} < 0.5 \\ 1.07U & 0.5 < \frac{z}{h} < 1 \end{cases} \quad (7)$$

Measured data from 22 stations are used to verify formula (6) and Soulsby formula. Figure 1 shows the comparison between calculation values of formula (6) and measured data, and figure 2 shows the comparison between Soulsby formula and measured data. The figures show that the new formula is better than Soulsby formula in coefficient of correlation, and its distribution is more centralized.

For further comparison and analysis, data of 6 moments of 7 stations are chosen. In the figure, “—” is tide level hydrograph, and “o” is tide level.

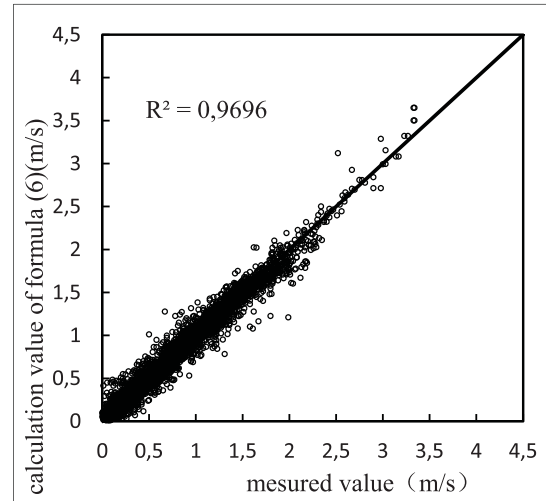


Fig.1 Comparison of formula (6) with measured data

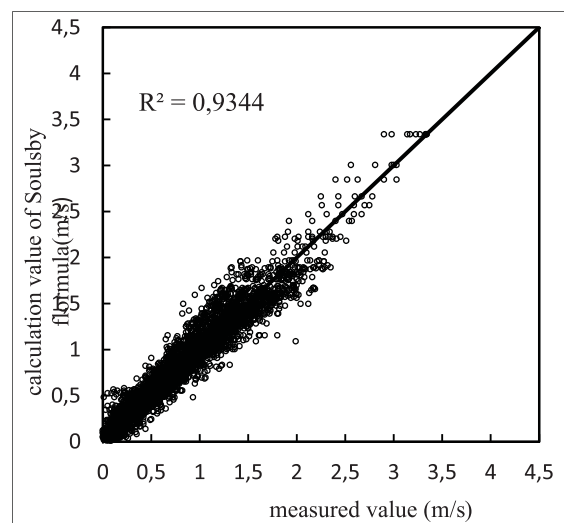


Fig.2 Comparison of Soulsby formula with measured data

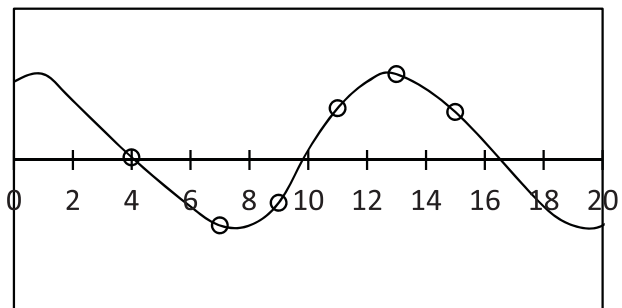


Figure 3 chosen moments for velocity profile verification

Figure 4-10 show comparison between formula (6), Soulsby formula and measured data. The chosen moments are arranged in time order from left to right. “o” stands for measured data of velocity, “—” for calculation value of formula (6) and “- - -” for that of Soulsby formula. Horizontal ordinate stands for $\frac{u}{U}$ and vertical coordinate for $\frac{z}{h}$.

These figures show in different flow regime formula (6) can always reflect the characteristics of velocity profile of different stations. Compared with Soulsby formula, formula (6), a continuous function, works better, and it revises the situation where velocity is fixed when water depth is larger than $0.5h$.

The comparison shows that formula (6) is a continuous function which is similar to Soulsby formula in form but simpler and easier to engineering use. In formula (6) friction velocity in form of Prandtl is introduced to reflect the impact of turbulence caused by bottom shear stress to the whole flow field. Formula (6) which does not need the maximum velocity and only needs the mean velocity in vertical, with more definite

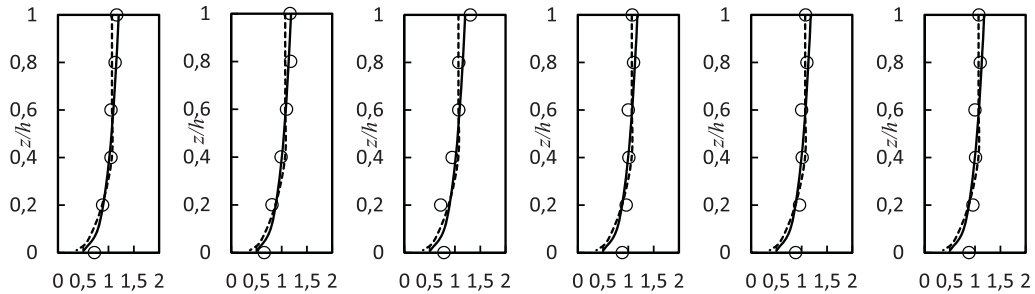


Fig.4 Comparison between formula (6), Soulsby formula and measured data of No.1 station

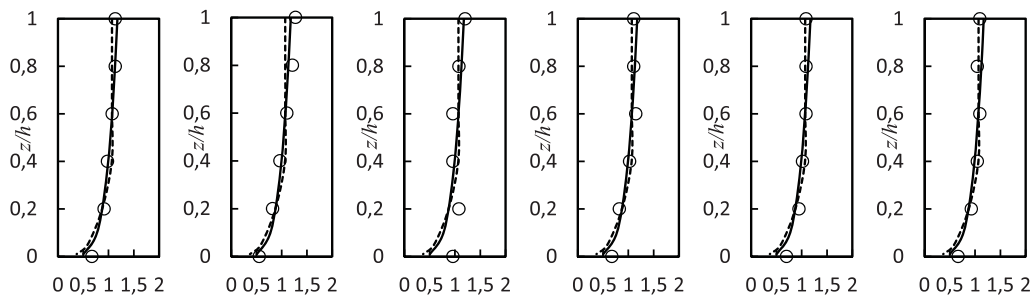


Fig.5 Comparison between formula (6), Soulsby formula and measured data of No.2 station

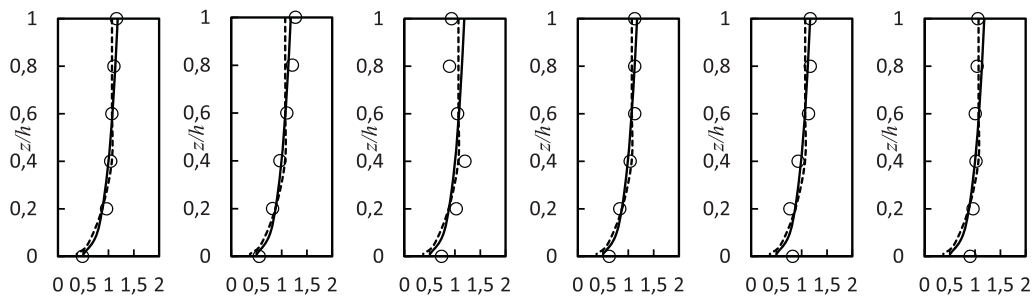


Fig.6 Comparison between formula (6), Soulsby formula and measured data of No.3 station

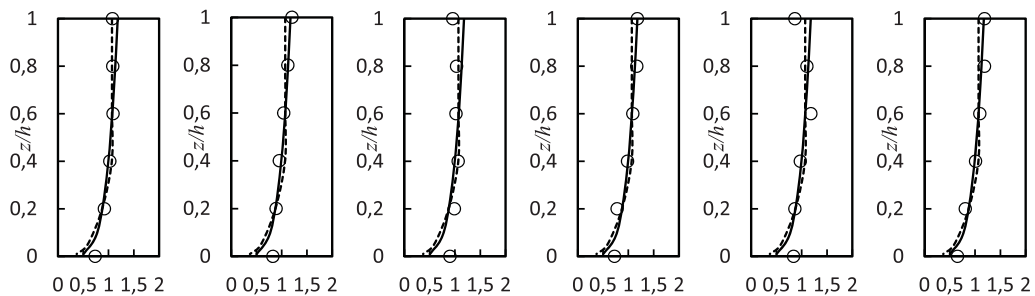


Fig.7 Comparison between formula (6), Soulsby formula and measured data of No.4 station

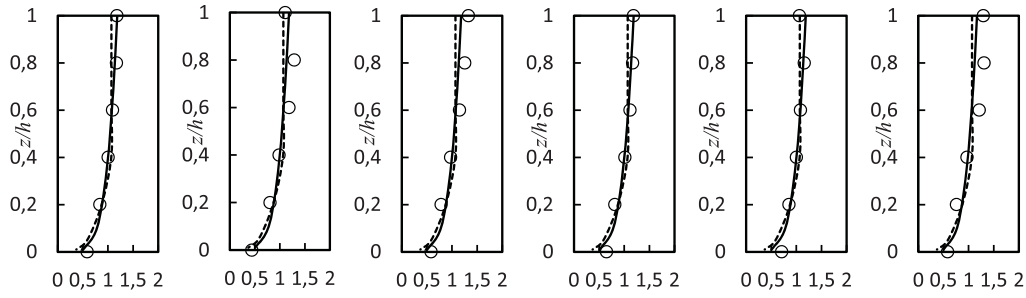


Fig.8 Comparison between formula (6), Soulsby formula and measured data of No.5 station

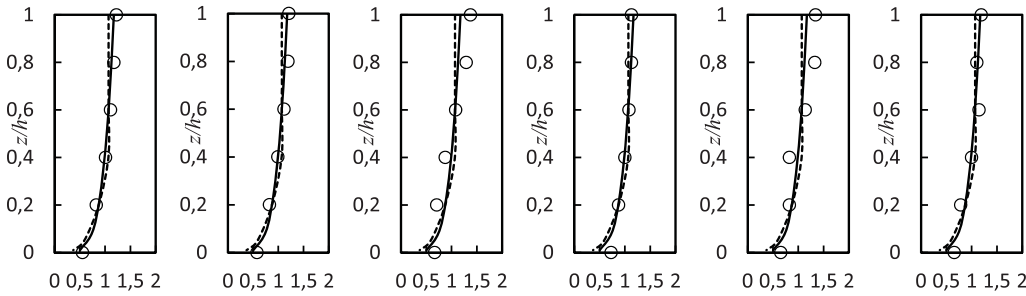


Fig.9 Comparison between formula (6), Soulsby formula and measured data of No.6 station

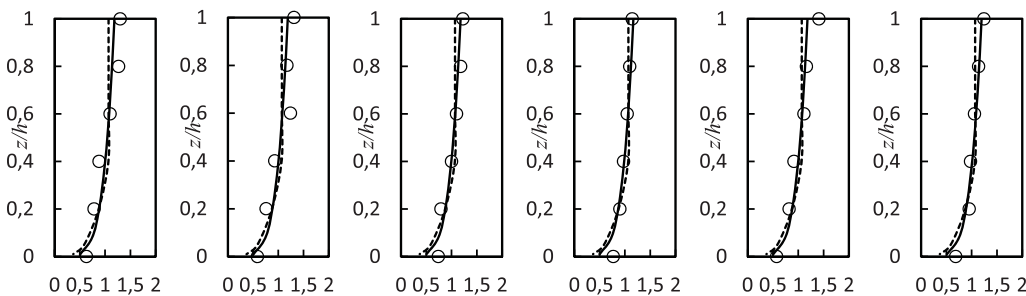


Fig.10 Comparison between formula (6), Soulsby formula and measured data of No.7 station

physical meanings, could show the influences of different flow properties on velocity profile by adjusting Karman constant. In field measurement, it is very difficult to get the maximum velocity within reasonable error control, but getting the mean velocity in vertical is much easier, which gives formula (6) higher applicability. The comparison between formula (6) and Soulsby formula is given in figure 2.

CONCLUSION

In this paper, a new formula of velocity profile which is similar to that of Soulsby but simpler in form and easier to use is constructed. The new formula is a continuous function with specific physical meanings and verified with measured data, which shows the new formula has a high accuracy and can reflect the vertical distribution of flow velocity objectively. As to the estuary region with velocity profile in S form, this formula has some certain errors, which needs further study as well as the applicability of new formula in other sea areas.

Its advantages are as follows:

- a. The new formula is a continuous function,

convenient for engineering application and could be used for further study of vertical distribution of suspended sediment;

- b. Friction velocity in form of Prandtl is introduced to the new formula to reflect the influences of bottom shear stress to the whole flow field, and Karman constant is used to reflect the influence of different flow regime to velocity profile with specific physical meaning.
- c. Compared with logarithmic form, the new formula does only needs the mean velocity in vertical instead of both maximum velocity and mean velocity in vertical, which gives it better engineering practicability.

Apply the new formula in Jiangsu Sea and compare the results with that of Soulsby whose results show the new one has higher accuracy and can reflect the vertical distribution of flow velocity objectively.

As to the estuary region with velocity profile in S form, this formula has some certain errors, which needs further study.

ACKNOWLEDGMENTS

Funded By: the national natural science foundation of China (No.41276017).

REFERENCES

1. Fang Guo-hong, Takashi Ichiye. On the vertical structure of tidal currents in a homogeneous sea [J]. Geophysical Journal of the Royal Astronomical Society, 1983, 73 (1): 65-82.
2. He Bing-ju, Hao Jia-ling. Fractal Study of Vertical Flow Velocity Distribution of Yangtze River Estuary [J]. Water Resources and Power, 2015, 33(12):37-39+31.
3. Kumbhakar M, Ghoshal K. Two dimensional velocity distribution in open channels using Renyi entropy[J]. Physica A: Statistical Mechanics and its Applications, 2016.
4. Li Rui-jie, Feng Qing, Zheng Jun, Jiang Sen-hui. Analysis on vertical distribution of nearshore fluid velocity and sediment concentration [J]. Marine Science Bulletin, 2012, 31(6):607-612.
5. MONIN A S, YAGLOM A M. Stastical fluid mechanics : mechanics of turbulence [M]. Third Edition. Cambridge, MA: The MIT Press, 1977.
6. Ni Jin-ren , Wang Guang-qian, Zhang Hong-wu. The basic theory of solid-liquid two phase flow and its new application [M]. Beijing: Science Press, 1991.
7. Ning Chien, Wang Zhao-hui. Mechanics of sediment transport [M]. Virginia:ASCE Press, 1999.
8. SCHAUER U. Determination of bottom boundary layer parameters at two shallow sea sites using the profile method [J]. Continental shelf Research, 1987, 7(10): 1211-1230.
9. Song Zhi-yao, Yan Yi-xin, Hao Jia-ling, et al. Study on the log-linear velocity profile of near-bed tidal current in estuarine and coastal waters [J]. China Ocean Engineering, 2006, 20(4): 573-584.
10. Mattheus, CR. Climate-Induced Changes in Rates of Headland-Beach Progradation along the Southern Coast of Lake Erie [J]. Journal of Coastal Research, 2014, 30(4): 743-755.
11. Soulsby R L. Dynamics of marine sands [M]. London: Thomas Telford, 1997.
12. Soulsby R L. Tidal -current boundary layer in the sea Ocean Engineering Science [M], Wiley, New York, 1990.
13. TAYLOR P A, DYER K R. Theoretical models of flow near the bed and their implications for sediment transport [R]. New York: Wiley-Inter science, 1977.
14. Van Rijn. Principles of sediment transport in river, estuaries and coastal seas [M]. Amsterdam: Aqua Publication, 1993.
15. Jakubowski, M. Influence of pitting corrosion on fatigue and corrosion fatigue of ship and offshore structures, part II: load - PIT -crack interaction [J]. Polish Maritime Research. 2015, 22(3): 57-66.
16. Xiao Qian-lu, Li Rui-jie. Study of vertical velocity distribution calculation of tidal current in Xiyang Channel of radial sandbanks in South Yellow Sea of China [J]. Yangtze River, 2015, 46(3): 9-13.

CONTACT WITH THE AUTHOR

Li Chunhui

lichunhui35@126.com

Key Laboratory of Coastal Disaster and Defense
Ministry of Education
Hohai University, Nanjing 210098,

Environment Marine Laboratory
Hohai University, Nanjing
CHINA

GROUND LIQUEFACTION AND DEFORMATION ANALYSIS OF BREAKWATER STRUCTURES UNDER EARTHQUAKES

Jie Zhao

Yumei Wang

Gaojie Yun

Muhammad Aqeel Ashraf

Civil Engineering Technology Research and Development Center, Dalian University, Dalian, 116622,
China

Faculty of Science and Natural Resources, University Malaysia Sabah 88400 Kota Kinabalu Sabah,
Malaysia

ABSTRACT

Ground liquefaction and deformation is one of the important causes that damage engineering structures. Chinese current code for seismic design of breakwater is based on the single-level seismic design method as well as code for port and water-way engineering. However, this code can not exactly reflect the seismic performance of breakwater structures which experience different seismic intensities. In this paper, the author used a finite difference software, namely, FLAC3D, to analyze the state and compute seismic responses of breakwater structure. The breakwater foundation's pore pressure ratio and displacement due to different earthquake have been studied. And the result show that: Smaller earthquakes have little influence on serviceability of the foundation, and severe earthquakes can liquefy some parts of the foundation; In the latter case, obvious changes of pores and foundation displaces can be found. Particularly, when seismic peak acceleration reaches 0.2g, Liquefaction appears in the foundation and mainly concentrated in the upper right side of the structure. In addition, the survey of ultra-hole pressure and displacement values of sand layers of the breakwater, manifests when the ultra pore pressure near 1.0, displacement and overturning structure is relatively large, resulting in varying degrees of damage to the structure. This paper's research can provide theoretical and designable reference for similar engineering structures

Keywords: Breakwater, seismic design, liquefaction, excessive pore pressure ratio, displacement

INTRODUCTION

Breakwater port construction has the widespread application in our country, so it has strict requirements for its bearing capacity, suitable for rock and soil, sand and dense clay geological conditions. Since the 1970s, there have been several large earthquakes around the world, many dikes and buildings suffered extensive damages [1]. Liquefaction and ground deformation are the main characteristics of earthquake damage to the breakwater, so breakwater structure for liquefaction and deformation analysis is an important research content of the seismic design. Liquefaction experienced a series of research and development, H.B.Seed, who first proposed the free liquefaction simplified identification method [2]; Fang Yun et al. [3] analyzes the deformation mechanism under conditions

of seismic liquefaction gravity pier design suggestions proposed seismic stability of gravity wharf; Ma Shuo [4] describes the damage types of Japan's Kobe earthquake in harbor pier, river embankment and disaster situation, analyze the reasons for failure, earthquake disaster prevention recommendations proposed wharf, embankment; Wang Li-yan et al. [5] The indirect liquefaction of a single index characterizing breakwater up residual deformation from the physical nature of the relationship between the breakwater obtain function prediction residual deformation and liquefaction degrees. Zhao Jie [12] using effective stress dynamic analysis methods, to obtain a stable ground motion a nuclear diversion dike full coefficient, distribution and post-earthquake liquefaction zone residual deformation. Liu Hanlong et al. [13] In multiple shear

strain space plasticity model for the constitutive relationship of agency landside dock reasonably easy to handle liquefied soil foundation gives advice. Xu Zhiying et al [14] in accordance with the principle of effective stress analysis method is proposed to calculate the two-dimensional dynamic seismic response of saturated soil, considering not only the dynamic shear strain and dynamic non-linear relationship between shear modulus, but also take into account the dynamic pore water pressure gradually effects of growth and change in the nature of power. Ren Jingang et al [15] analyzed the mechanism of liquefaction of saturated sand and sand liquefaction judgment visualization methods.

At present, Chinese water transport project about the breakwater earthquake resistance design, primarily designed [6] in accordance with the relevant provisions of the foundation and the seismic slope, but confined to the limits of the force balance [7]. Fewer domestic and foreign scholars have studied the problem on the liquefaction of the foundation about the breakwater structure [16-18]. In this paper, the finite difference software FLAC3D reclamation project of a large breakwater revetment structure numerical simulation, analysis of the breakwater structure under different seismic pore pressure ratio and changes in the deformation, summed liquefaction and deformation law in breakwater structure and provided theoretical and design reference for similar engineering structures.

NUMERICAL ANALYSIS PRINCIPLES OF FLAC3D

DYNAMIC PORE PRESSURE MODELS

FLAC3D can simulate sand hole in the dynamic action of the pressure accumulation until soil liquefaction, using Finn model to describe the effect of the accumulation of pore water pressure, the essence of the model is to increase the dynamic pore water pressure rises mode based on Moore Coulomb model, and assume dynamic pore water pressure rises with plastic volumetric strain increments on [8].

Located in the sand when the effective stress σ_0' one-dimensional modulus of resilience is E_r , then the relationship under untrained pore pressure increment Δu and $\Delta \epsilon_{vd}$ plastic volumetric strain increments are as follows:

$$\Delta u = \bar{E}_r \Delta \epsilon_{vd} \quad (1)$$

Byrne [9] uses the experimental data of Martin and Seed, proposed a more simple method of calculation about plastic volumetric strain increment:

$$\Delta \epsilon_{vd} = \gamma C_1 \exp(-C_2 \frac{\epsilon_{vd}}{\gamma}) \quad (2)$$

Where: γ is the first N cycles shear strain amplitude; ϵ_{vd} is the cumulative volume strain; C_1, C_2 of D_r and sand relative density and correction standard penetration hammering parameters related to the number of N_p , is calculated as follows:

$$C_2 = \frac{0.4}{C_1}, C_1 = 7600(D_r)^{-2.5} \quad C_1 = 8.7(N_p)_{60}^{-2.5}, D_r = 15(N_p)_{60}^{1/2} \quad (3)$$

LIQUEFACTION STANDARD

In the numerical calculation using the concept of excess pore pressure ratio to describe liquefaction, excess pore pressure ratio represented by $r_u = 1 - \frac{\sigma_m}{\sigma_m^0}$, σ_m^0 driven before calculating the average effective stress σ_m , σ_m is dynamic calculation process mean effective stress. Theoretically, when the excess pore pressure of 1:00, sand liquefaction, but a large number of experimental data indicate that excess pore pressure has not reached 1:00, sandy soil liquefaction phenomenon occurs [7].

DYNAMIC BOUNDARY CONDITIONS

After the process of absorption of seismic reflection seismic waves on the boundary of the calculation model set free field boundary, set the free-field boundary, FLAC3D program will automatically form a free-field around the model grid mesh through the body and free-field Grid earthquake simulation coupling to approximate free field response [7]. Damping in the form of the use of local dampers, which through the node or node structures to increase or decrease the quality of the way to achieve convergence of the vibration cycle, due to the increased quality and reduced unit cell mass are equal, so that the system is to maintain the quality of conservation, the damping is taken as: 0.314.

SEISMIC ANALYSIS BREAKWATER STRUCTURES

DYNAMIC ANALYSIS MODEL

A large land reclamation breakwater structure shown in Figure, the model length 60m, high 50m, 20m thickness direction of the foundation model, the model is partly sand,

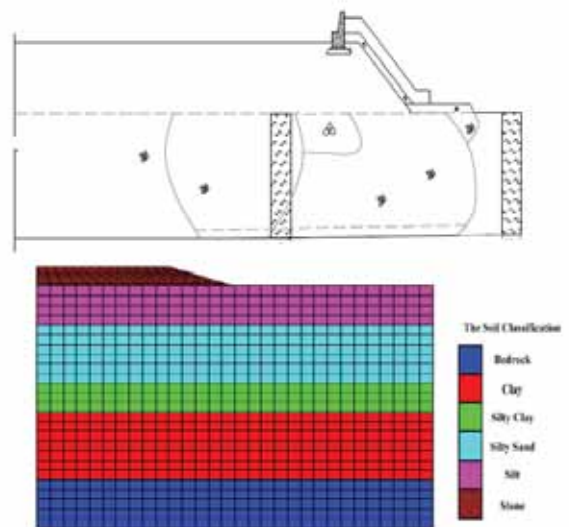


Fig.1 Breakwater structure cross plan and grid model (unit: m)

and a large area, as well as the superstructure 4m high filling section, above the water line is assumed part. Breakwater foundation profiles and meshes structure shown in Figure 1, geotechnical parameters used in calculation of fluid parameters and liquefaction parameters in Table 1, 2.

Tab.1 Geomechanical parameters and fluid and liquefaction parameters for soil liquefaction analysis

Material	The bulk modulus MPa	Shear modulus MPa	Cohesive force	Friction Angle	Poisson's ratio	Density ($10^3 \text{kg} \cdot \text{m}^{-3}$)
Silt	7.9	2.1	10.0	10.6	0.3	1.57
Silty Sand	68.6	26.3	0.00	35.0	0.3	1.94
Silty clay	16.4	5.5	13.0	14.7	0.3	1.97
Clay	173.7	5.8	16.0	16.0	0.3	1.84
Bedrock	1250.0	576.9	0.0	30.0	0.3	2.04
Stone	147.1	56.4	0.0	36.0	0.3	1.80

Tab 2: Fluid and liquefaction parameters for soil liquefaction analysis

Material	Porosity	Permeability coefficient ($\text{cm} \cdot \text{s}^{-1}$)	Damping ratio	Liquefaction parameters
Silt	0.45	1.00E-11	0.314	-
Silty Sand	0.45	1.00E-09	0.314	$C_1=1.2$ $C_2=0.79$ $D_r=0.25$
Silty clay	0.45	1.00E-12	0.314	-
Clay	0.45	1.00E-12	0.314	-
Bedrock	0.45	1.00E-15	0.314	-
Stone	-	-	0.314	-

Assuming the peak horizontal acceleration as 0.1g, 0.15g, 0.2g of EI-Centro seismic loading, to give its dynamic analysis models by 8400 units, 9922 nodes, breakwater foundation dynamic analysis model structure shown in Figure 2.



Fig.2 Dynamic analysis model

SEISMIC INPUT

Our water transport engineering seismic design code (JTS 146-2012) [6] using return period of 475 years (50 years beyond the design basis of the probability of 10%) of the design earthquake, according to building codes considered equivalent fortification earthquake, and only seismic design force from extreme balance, are single-level design; Our reference herein seismic design of buildings (GB50011-2010) [10] regarding the multiple earthquake, fortification earthquake and rare earthquake action time history analysis peak ground acceleration of the relevant provisions of the breakwater structure foundation were time-history analysis, using American EI-Centro seismic waves, seismic waves duration 30s. Figures 3 and 4 are EI-Centro earthquake wave graph and the Fourier spectrum of the curve, it can be seen, seismic wave spectral components more complex, mainly concentrated on the less frequency 5Hz.

The specific dynamic analysis and calculation, bedrock ground motion acceleration input consider three cases, 0.10g, 0.15g and 0.20g, respectively 7 degree earthquake, 7.5 degree earthquake and 8 degree earthquake.

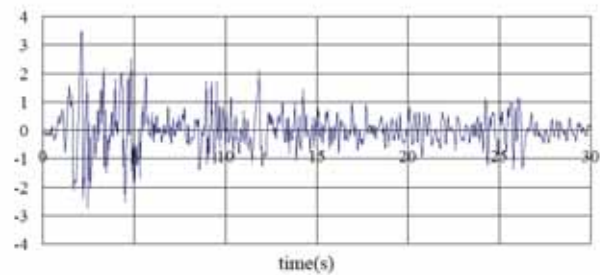


Fig.3 EI-Centro earthquake curve

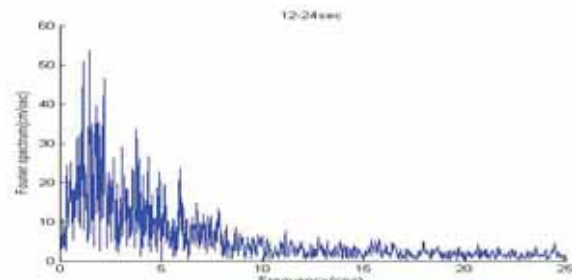


Fig.4 Fourier curve

BREAKWATER LIQUEFACTION AND DEFORMATION ANALYSIS

LIQUEFACTION ANALYSIS UNDER DIFFERENT EARTHQUAKE

In order to determine liquefaction foundation breakwater structure, the calculation of excess pore pressure ratio structure foundation sand layer numerically monitor, Figure 5 shows the position of A, B, C, D four monitoring points, obtained in 0.1 under g, 0.15g and 0.2g peak acceleration, excess pore

pressure at the location of the sand layer is not the same as the ratio of the distribution, over time 0.1g pore pressure ratio in the range of 0.4 to 0.8; when 0.15g excess pore pressure ratio in the range of 0.45-0.94 ; 0.2g when the excess pore pressure ratio of 0.59-1. According to a large number of experimental data that excess pore pressure ratio does not meet the 1:00 also be judged as liquefaction, according to research data [7], this paper take excess pore pressure ratio of 0.7 when it is determined that liquefaction.

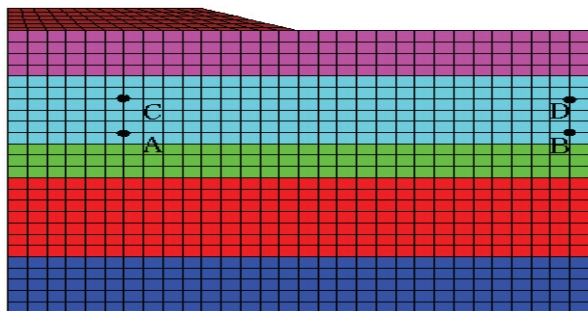


Fig.5 A, B, C, D four monitoring points' position

Tab 3: Different peak acceleration of monitoring points pore pressure ratio

Monitoring stations \ Peak acceleration	A	B	C	D
0.10g	0.41	0.62	0.62	0.83
0.15g	0.45	0.68	0.60	0.94
0.20g	0.59	0.74	0.86	1.00

Table 3 and Figure 6 shows the excess pore pressure ratio value representative monitoring points at different earthquake at the end of breakwater foundation, can be seen, when the earthquake peak acceleration of 0.1g, the excess pore pressure ratio exceeds 0.7 unit is relatively small, indicating that the area is small sand layer liquefaction, liquefaction occurs only surface; When the earthquake peak acceleration of 0.15g, the excess pore pressure ratio exceeds 0.7 unit increase, sandy soil liquefaction region increases, liquefied area can be extended to the lower sand layer, are moderate liquefaction; When the earthquake peak acceleration of 0.2g, the excess pore pressure ratio over 0.7 units increased significantly over the previous two liquefied sand layer significantly increased the area, the lower sand layer liquefaction area is large, it belongs to severe liquefaction zone. With the improvement of the peak ground acceleration, the same soil pore pressure than the unit significantly increased, sand layer of soil liquefaction order is from shallow to deep, as deep soil liquefaction, the excess pore pressure on the casing somewhat lower than that. Moreover, the ratio of the size of the pore pressure can be seen on the right side than the left liquefied sand layer large area, the upper area is larger than the lower liquefaction. Figure 7 shows the different liquefaction area under the peak acceleration.

BREAKWATER CONSTRUCTION GROUND DEFORMATION ANALYSIS

Table 4 shows the horizontal and vertical directions at different representative monitoring point earthquake residual deformation size, it can be seen, when the peak acceleration is 0.10g, the deformation in the horizontal direction is 0.21-0.24m, vertical displacement as 0.06-0.08m; when peak acceleration is 0.15g, the deformation in the horizontal direction is 0.23-0.26m, the vertical displacement is 0.06-0.08m; when peak acceleration 0.20g, the deformation in the horizontal direction

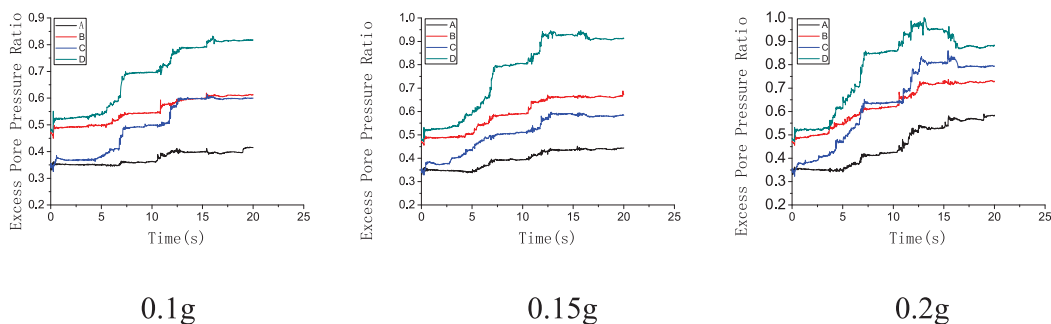


Fig 6 Different acceleration peak under A, B, C, D of excess pore pressure ratio curve



Fig 7: Different acceleration peak liquefaction area

is 0.24m-0.30 m, vertical displacement of 0.07m-0.09m.

Tab 4: Monitoring points horizontal and vertical displacement (unit: m)

Monitoring stations	A		B		C		D	
	Level	Vertical	Level	Vertical	Level	Vertical	Level	Vertical
Peak acceleration								
0.10g	0.21	0.080	0.22	-0.062	0.24	0.082	0.24	-0.065
0.15g	0.23	0.080	0.23	-0.063	0.25	0.083	0.25	-0.066
0.20g	0.24	0.087	0.24	-0.068	0.28	0.080	0.29	-0.069

Three different earthquake, horizontal deformation of 0.2m-0.3m or so, in the same direction with the original model, but the vertical direction appeared deformed in both directions, if the middle part of the junction will appear on the left side a variation of tilt, and the right side of the liquefied area that is larger deformation occurs in the form of sinking, namely the breakwater structure appeared overturning deformation form.

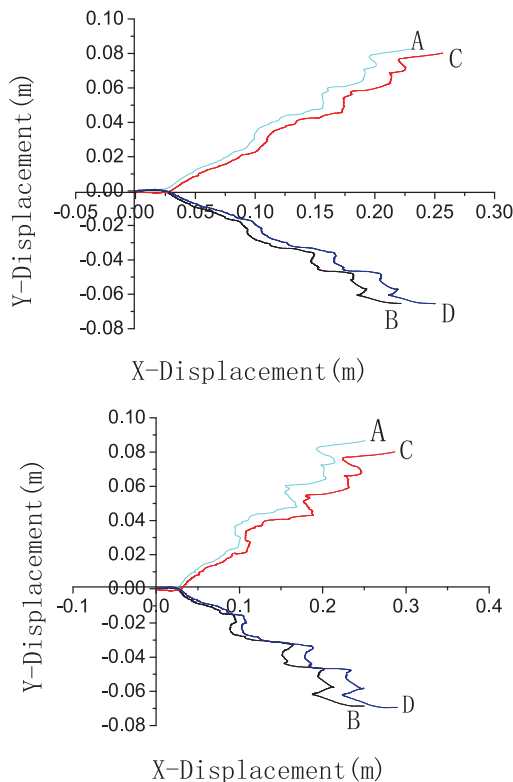


Fig 8: Different acceleration peak under A, B, C, D points of the horizontal and vertical deformation map

Through the analysis of numerical comparative: 0.1g and 0.15g displacement similar, so only indicate the horizontal and vertical deformation maps of 0.1g and 0.2g monitoring points. Figure 8 shows the horizontal and vertical directions at different portions earthquake deformation monitoring

points, and FIG coordinate Z direction indicates the vertical direction of the deformation magnitude, X direction represents the magnitude of displacement in the horizontal direction. Breakwater structure inferred inclination of about 4 percent, according to "Port Engineering Seismic Design Guide" [11] judgment breakwater structural damage can be repaired, the liquefied layer of shallow, you can use vibration dense, compaction, cover weight and other measures.

CONCLUSION

This paper adopts FLAC3D finite difference software for a large reclamation project breakwater structure was simulated from the seismic design, structural foundation for the breakwater was dynamic process analysis, and analysis of the breakwater structure pore pressure ratio and under different earthquake changes in deformation draws the following conclusions:

1. Under the action of earthquake, the peak acceleration is 0.1g, 0.15g and 0.2g. the sand layer foundation breakwater structure will liquefaction occur, along with the increase of earthquake, liquefaction of sand layer area increases, the liquefied area mainly in the upper right side of the structure, liquefied depth by former deep, designed to focus on preventive measures considered;
2. Under the action of earthquake, the peak acceleration is 0.1g, 0.15g and 0.2g. For excess pore pressure and the displacement of part of breakwater structure foundation unit for monitoring, summarized the law of displacement ratio and changes in pore pressure, found in excess pore pressure value close to 1, the structure is relatively large displacement, overturning phenomenon occurs breakwater structure, namely large extent liquefaction.
3. According to the deformation of the foundation structure may determine the extent of damage to this end breakwater is not large, the inclination is about 4%, can be used after repair, take the measures such as vibration compaction, dynamic compaction and heavy weight in the liquefaction area, which is a reference for other similar breakwater structures.

REFERENCE

1. LU Xiaobin, TAN Qingming, WANG Shuyun, et al. Saturated Sand Progress[J]. Advances in Mechanics. 2004,34(1):87-100.(in Chinese)
2. SEEDHB, BOOKERR. Stabilization of potentially liquefied sand deposits using gravel drains [J]. Journal of Geotechnical Engineering Div JCEd, 1976, 102(07):1-15.
3. FANG Yun, TOWHATAI, GHALANDARZADEHA, et al. Mechanism of deformation and failure of gravity-type quay walls under earthquake liquefaction[J]. Earth Science-Journal of China University of

- Geosciences,2001,26(4):415-418.(in Chinese)
4. MA SHUO,LUO QI. Japan's Kobe earthquake damage harbor pier river embankment and Lessons[J]. Disaster, 1998,13(4):47-50(in Chinese)
 5. WANG Liyan, JIANG Pengpeng, LIU Hanlong. Sandy foundation breakwater seismic residual deformation mechanism and liquefaction prediction method[J].Chinese Journal of Rock and Soil Mechanics,2010,31(11).3556-3562. (in Chinese)
 6. JTS146 - 2012,Code of earthquake resistant design for water transport engineering[S].(in Chinese)
 7. HAN SHI,GONG Jinxin, ZHANG Yanqing. Gravity pier foundation under earthquake liquefaction and deformation[J].Hydro-science and Engineering. 2013,8,(4):45-54. (in Chinese)
 8. CHEN Yumin, XU Dingping. FLAC/FLAC3D Foundation and project examples[M].Peking: China Water Power Press,2008.
 9. BYRNEPM, PARKSS. Seismic liquefaction: centrifuge and numerical modeling[J].Third International Symposium on FLAC and FLAC3D Numerical Modeling in Geomechanics, Ontario:2003.
 10. GB50011 - 2010, Seismic Design of Buildings [S].(GB50011-2010, Code for seismic design of buildings[S]. (in Chinese)
 11. International Navigation Association Seismic design guide lines for port structures[M].Netherlands Balkema Publishers,2001.
 12. Zhao jie,wang gui xuan,zheng yang,A nuclear power plant water diversion dam dynamic response and stability analysis[J].Journal of Disaster Prevention and Mitigation Engineering,2013,33(4):412-417.
 13. LIU Hanlong, IAI S, ICHII K. Seismic response analysis of large-size caisson quay wall [J].Chinese Journal of Geotechnical Engineering, 1998, 20(2) : 26-30.(in Chinese)
 14. Xu Zhiying,Shen Zhujing,Two-dimensional dynamic analysis method of seismic liquefaction effective stress[J].Journal of Hohai University(Natural Science Edition),1981,(3):1-14.
 15. Ren Jieming,Su Jingyu,Dou Yuanming, Neural network Sand Liquefaction[J], Hebei University of Technology,2002,31(2):23-25.
 16. Ishihara K.Undrained deformation and liquefaction of sand under cyclic stress[J].Soils and Foundation,1975,15(1):29-44.
 17. McLaren, P. Sediment Trend Analysis (STA (R)): Kinematic vs. Dynamic Modeling[J]. Journal of Coastal Research, 2014,30(3): 429-437.
 18. Han, ZQ; Wang, CY; Zhu, HY. Research on deep joints and lode extension based on digital borehole camera technology[J]. Polish Maritime Research, 2015,22(1): 10-14.

CONTACT WITH THE AUTHOR

Jie Zhao

Civil Engineering Technology Research
and Development Center
Dalian University
Dalian, 116622

CHINA

MARINE INDUSTRIAL CLUSTER STRUCTURE AND ITS COUPLING RELATIONSHIP WITH URBAN DEVELOPMENT: A CASE OF SHANDONG PROVINCE

Xiao Wenwen

Zhao Bingxin

Wang Lili

School of Management, Shandong University, Jinan, Shandong, 250100, China

ABSTRACT

Marine economy is a new economic form, emphasizing new development concept, new operation mechanism and management mode. In recent years, marine economy shows rapid growth, and marine industry presents a clustering development trend. The industrial linkage effect, industrial agglomeration effect and industrial radiation effect of the marine industrial cluster are important motive forces for the development of coastal cities. The marine industrial cluster takes coastal cities as the development platform and space, while the coastal cities achieve rapid and sustainable development based on the marine industrial cluster. The synergetic and coupling development of the marine industrial cluster and coastal cities is an important way for the promotion of industrial competitiveness and urban competitiveness. This paper developed a measure to identify the marine industrial cluster, designed the evaluation index of coupling of marine industrial cluster and coastal cities development from two perspectives of industrial linkage and spatial agglomeration, taking Shandong province, a typical coastal province in China, as an example, it studied the situation of the marine industrial cluster based on input-output data and data of marine enterprises of coastal cities, based on which it explored the coupling relationship between marine industrial cluster and coastal cities of Shandong province.

Keywords: marine industry; industrial cluster; urban development; coupling coordination model

INTRODUCTION

With the increase of human social and economic activity, the supporting capacity of land resource has been overwhelmed, so people need to find new resource supporting point [1]. In this background, economic activity presents an extension from the land to the ocean, which includes both the extension of the land resource to the marine resource and the extension of economic activities from the land space to the ocean space. At the start of this century, the United Nation proposed the assertion of “The 21st century is ocean century”, believing the ocean will become the main area of international competition [2]. Marine economy is a new economic form with synergy of sea and land and sustainable development as the core concepts, emphasizing

new development concept, new operation mechanism and management mode [3, 4]. With the implementation of marine strategy, marine economy shows rapid growth, and marine industry presents a clustering development trend [5]. The industrial linkage effect, industrial agglomeration effect and industrial radiation effect of the marine industrial cluster are important motive forces for the development of coastal cities, and also bases for connection among coastal cities. The marine industrial cluster has become an important factor in explaining competitiveness, innovation and growth of coastal cities [6,7,8]. The marine industrial cluster takes coastal cities as the development platform and space, while coastal cities achieve rapid and sustainable development based on the marine industrial cluster. The synergetic and

coupling development of the marine industrial cluster and coastal cities is an important way for the promotion of industrial competitiveness and urban competitiveness.

The industrial cluster is first proposed by Michael Porter, who defined cluster as a geographically proximate group of interconnected companies and associated institutions in a particular field, linked by commonalities and complementarities [9]. Thus it can be seen that the important external expression of the industrial cluster is geographical agglomeration of relevant enterprises and institutions. Subsequently, scholars pointed out that the formation of industrial cluster is not only because of proximity of geographical position, but also existence of industrial linkage [10,11], besides, some scholars proposed the way to identify industrial cluster from two perspectives of horizontal industrial linkage and vertical industrial linkage to study German industrial cluster [12]. Based on these theories, this paper argued that two conditions needed to be satisfied for the formation of industrial cluster: firstly, there was an existence of linkage among industries; secondly, enterprises and institutions formed a certain agglomeration scale in terms of geographical position. From the point of view of conditions for the formation of industrial cluster, the industrial cluster is a system formed by coupling of inter-industry linkage and inter-enterprise relationship essentially. Coupling is a term in physics originally, which has been extensively applied to the research on the geographic economy, regional economy and relevant management issues in recent years, referring to the dynamic linkage where the mutual influence, interdependence, and inter-coordination of two or more systems are carried out through the interaction [13]. At present, scholars often study the relationship between industrial cluster and urban development as well as industrial cluster and regional economic development using this method [17, 18, 19].

For marine industrial cluster, at present, scholars have conducted empirical analysis of the promotion of marine industrial cluster to regional economic development and the formulation of marine policy [22,23,24],etc., in research methods, analytic processes such as Diamond Model Analytic Process [25, 26], Delphi Analytic Process [27] and Gini coefficient [28] are usually adopted to study industrial cluster. However, these analyses conduct researches from single perspective of either industry agglomeration or enterprise agglomeration. Different from these researches, this paper identified the marine industrial cluster, designed the evaluation index of coupling of development of marine industrial cluster and coastal cities from two perspectives of industrial linkage and spatial agglomeration, taking Shandong province, a typical coastal province in China, as an example, it studied the situation of the marine industrial cluster based on input-output data and data of marine enterprises of coastal cities, based on which it explored the coupling relationship between marine industrial cluster and coastal cities of Shandong province.

RESEARCH METHOD AND INDEX SYSTEM

IDENTIFICATION METHOD OF INDUSTRIAL CLUSTER

Mechanism analysis of industrial cluster

According to existing research, two factors form the industrial cluster: horizontal industrial linkage and vertical industrial linkage. The vertical industrial linkage refers to linkage among industries in industry chain (network), referring to the industry upstream and downstream linkage or linkage formed due to economic and technical reasons; the horizontal industrial linkage refers to cooperation competition linkage between enterprises and institutions in the same area. From the perspective of system theory, the system element of industrial cluster consists of two parts, i.e. industry X_1 and corresponding enterprise and institution X_2 , and the system structure of industrial cluster is a relatively stable linkage set entirely formed by system elements according to some rule. The mathematical description of industrial cluster system is as follows:

$$S = \{X_1, X_2 | X_1 \times X_1, X_2 \times X_2\} \quad (1)$$

The industrial cluster consists of two important subsystems, i.e. industry linkage subsystem $S_1 = X_1 \times X_1$, and enterprise linkage subsystem $S_2 = X_2 \times X_2$. Essentially, the industrial cluster is a compound system coupled by industry linkage subsystem and enterprise linkage subsystem, where, the industry linkage subsystem S_1 connecting industries in technical economy plays the basic and dominant role. It should be noted that both of vertical industrial linkage and horizontal industrial linkage should reach a certain scale and level to form strong linkage. Based on this, this paper proposed an identification method of strong linkage subsystem of industry and strong linkage subsystem of enterprise, based on which it determined the industrial cluster.

Identification method of strong linkage subsystem of industry

The industries in strong linkage subsystem of industry have the characteristics such as high linkage level, strong interaction with other industry, and wide radiation range, which are the basis and the key of the industrial cluster. Industrial linkage is the linkage in industry chain (network), input-output data are those can accurately study the inter-industry relationship currently. It can reflect the relationship between input and output among industries in certain region and can obtain information relating to vertical linkage by processing input-output table. Zhao Bingxin et al. identified these industries as industries of vertical industrial cluster by filtering the weak linkage among industries and finding strong vertical linkage industrial cluster using graph and network method based on input-output data. Specific steps

were as described below:

Step 1: Established industry network model N based on input-output table following the modeling approach of Zhao Bingxin [29, 30].

Step 2: Calculated k -cores of industry network. Supposed industry network $N = (V, E)$, V was point set of network N , E was frontier set of network N , k was natural number, for any given $W \subseteq V$, network subfigure $H_k = (W, E|W)$ of N was called k -cores of N , and met $d_{H_k}(v) \geq k$ only when $\forall v \in W$, moreover, H_k was point pole big subfigure with such kind of characteristics.

Step 3: Defined sub-network H_k with maximum core value as strong linkage subsystem of industry S_1 , and industry set in S_1 was denoted as V_{S1} .

Identification method of strong linkage subsystem of enterprise

The agglomeration situation of enterprise in some region can be identified by calculating concentration ratio of enterprise in some region using agglomeration index. Gini coefficient, Herfindahl index, and location quotient are often adopted in recent literature to calculate the concentration ratio of enterprise in some region [31-32]. This paper adopted the location quotient to calculate the concentration ratio of enterprises in some region to identify the strong linkage subsystem of enterprise. Location quotient (according to P. Haggett,) [33-35]:

$$LQ_{ij} = \frac{x_{ij} / \sum_j x_{ij}}{\sum_j x_{ij} / \sum_i \sum_j x_{ij}} \quad (2)$$

i represented the i th industry, j represented the j th industry, x_{ij} represented the index of the i th industry of the j th region. Location quotient usually can be calculated using industry sales revenue, number of enterprises, number of employee of enterprises, etc. When $LQ_{ij} > 1$, it indicated that the i th industry of the j th region had high concentration ratio of enterprise, supposed $V_{S2} = \{i | LQ_{ij} > 1\}$, and defined the system formed by V_{S2} as strong linkage subsystem of enterprise S_2 .

Supposed V_c was industry set of industrial cluster, industrial cluster was a compound system coupled by industry linkage subsystem and enterprise linkage subsystem, and defined $V_c = V_{S1} \cap V_{S2}$.

COUPLING COORDINATION MODEL

Coupling degree model

The coupling degree describes the degree of influence of multiple systems on each other, the bigger the coupling degree, the closer the linkage among systems, the higher the degree of influence. Before building the coupling degree model of marine industry cluster and urban development, you need to first define the evaluation function of marine industry

cluster and evaluation function of urban development.

Defined the evaluation function of model of marine industry cluster as:

$$U_1 = \sum_{i=1}^m a_i x_i \quad (i = 1, 2, \dots, m) \quad (3)$$

Where a_i represented the weight of each index, and x_i represented the standardized value of each index. Defined the evaluation function of urban development as:

$$U_2 = \sum_{j=1}^n b_j y_j \quad (j = 1, 2, \dots, n) \quad (4)$$

Where b_j represented the weight of each index, and y_j represented the standardized value of each index

This paper mainly studied the two systems of marine industry cluster and urban development, therefore, the coupling degree function was:

$$C = \left\{ \frac{U_1 \times U_2}{\prod(U_1 + U_2)} \right\}^{1/2}, \quad C \in (0, 1) \quad (5)$$

the bigger the coupling degree, the closer the linkage among systems, the higher the synergetic development coordination degree.

Coupling coordination degree model

The coupling degree function is unable to determine the influence of systems under study on each other on lower level or higher level, therefore, the coupling coordination degree function also needs to be calculated for study of synergetic development relationship among systems, i.e.:

$$D = \sqrt{C \times T}, \quad T = \alpha U_1 + \beta U_2 \quad (6)$$

D represented the coupling coordination degree, when $0 < D \leq 0.4$, it indicated that it was low coordination; when $0.4 < D \leq 0.5$, it indicated that it was moderate coordination; when $0.5 < D \leq 0.8$, it indicated that it was high coordination; when $0.8 < D \leq 1.0$, it indicated that it was extreme coordination; T represented the comprehensive evaluation index of marine industry cluster and urban development. α and β represented the undetermined coefficient, these two systems did not show full symmetry in terms of purpose in the process of synergetic development, this paper supposed $\alpha = 0.4, \beta = 0.6$.

INDEX SYSTEM AND DATA SOURCES

Index system

In line with the principle of objectivity, scientificity and operability, this paper selected the index and established the index system of marine industry cluster and urban development. According to expert opinion, combining AHP method, this paper determined the weight of each evaluation index, see Table 1.

Tab. 1 Evaluation Index System of Coupling of Marine Industry Cluster and Urban Development

Target	System	Index	Weight
Coupling of marine industry cluster and urban development	Marine industry cluster	Industrial location quotient	0.47
		Market share	0.29
		Industrial agglomeration degree	0.24
	Urban development	Gross regional domestic product	0.21
		Per capita gross regional domestic product	0.11
		Aggregate income of families	0.14
		Household consumption level	0.18
		Urban population density	0.19

Data sources and processing

The data used in this paper mainly came from Shandong Statistical Yearbook, China Statistical Yearbook, China Marine Statistical Yearbook, Input-Output Data and regional statistical yearbooks such as Qingdao Statistical yearbooks and Yantai Statistical Yearbook, and this paper also consulted economic reference data published periodically by national and local statistical bureau, data from the enterprise yearbook, and data from the industry analysis report and government report.

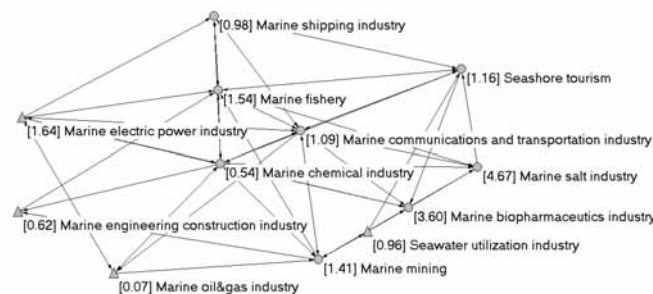
EMPIRICAL ANALYSIS OF MARINE INDUSTRY CLUSTER OF SHANDONG PROVINCE AND ITS COUPLING WITH URBAN DEVELOPMENT

Shandong province is a major marine province, bordering the Bohai Sea in the north and the Yellow Sea in the south. It is a province in China to develop marine industry earlier, in 2009, President Hu proposed “to make great efforts to develop marine economy, develop marine resource scientifically, cultivate marine competitive industries” during his inspection of Shandong province, in 2011, the Development Planning of Shandong Peninsula Blue Economic Zone was approved by the State Council, and developing Shandong’s marine economy became an important part of national marine strategy. After several years of development, Shandong’s marine industries have formed a complete industry system, and some of the industries present a clustering development trend, and these industries boost the local development even the economic development of the whole Shandong province, and are important measures for non-balanced development

of Shandong province. Based on this, this paper selected Shandong province as a research object to first study the situation of marine industry cluster of Shandong province, based on which it further studied the coupling coordination situation of marine industry cluster of the coastal city of Shandong province with its urban development.

ANALYSIS OF MARINE INDUSTRY CLUSTER OF SHANDONG PROVINCE

According to input-output table of Shandong province [1] developed by Zhao Bingxin (2015), this paper determined the strong linkage subsystem of marine industry of Shandong province, and calculated the location quotient of marine industry of Shandong province based on number of enterprises to determine the strong linkage subsystem of enterprise. This paper assigned weight for each industry with location quotient of industry as point weight, and the size of point represented the size of location quotient of industry. The calculation results are as shown in Fig. 1.



Notes: ○ Industry representing strong linkage subsystem of industry

Fig.1 Diagram of Marine Industry Cluster of Shandong Province

According to calculation, the strong linkage subsystem of industry included 7 marine industries, that is, V_{S1} includes industrial cluster, including marine fishery, marine salt industry, marine biopharmaceutics industry, marine communications and transportation industry, marine mining, marine chemical industry, and seashore tourism. The strong linkage subsystem of enterprise includes 7 marine industries, that is, V_{S2} includes industrial cluster, including marine fishery, marine salt industry, marine biopharmaceutics industry, marine communications and transportation industry, marine mining, marine electric power industry and seashore tourism. By definition of industrial cluster made in this paper, $V_c = V_{S1} \cap V_{S2}$, it can thus be seen that 6 marine industries of Shandong province had reached the scale of industrial cluster, including marine fishery, marine salt industry, marine biopharmaceutics industry, marine communications and transportation industry, marine mining, and seashore tourism. According to cities where marine enterprise headquarter of Shandong province and branch office located, this paper determined the regional distribution of marine enterprise of coastal city of Shandong province, so as to determine the

coastal city where 6 marine industries mainly agglomerated, see Table 2.

Tab. 2 Distribution of Marine Industry Cluster of Coastal City of Shandong Province

City	Cluster industry				
Yantai	Marine fishery	Marine biopharmaceutics industry	Seashore tourism	Marine communications and transportation industry	Marine mining
Qingdao	Marine fishery	Marine biopharmaceutics industry	Seashore tourism	Marine communications and Transportation industry	
Weihai	Marine fishery	Marine communications and transportation industry	Seashore tourism		
Rizhao	Marine fishery	Marine communications and transportation industry	Seashore tourism		
Dongying	Marine fishery				
Weifang	Marine fishery				
Binzhou	Marine salt industry				

As seen in Table 2, marine fishery have formed an agglomeration in many coastal cities such as Yantai, Qingdao, Weihai, Rizhao, Dongying and Weifang; marine communications and transportation industry mainly agglomerate in Qingdao, Yantai, Rizhao and Weihai, these cities have China's important coastal harbor and large-scale marine transportation enterprise, too; with the development of tourism in recent years, seashore tourism has formed in coastal cities of Shandong province such as Qingdao, Yantai, Weihai and Rizhao. Different from marine fishery, marine communications and transportation industry and seashore tourism, marine salt industry enterprises, marine biopharmaceutics industry enterprises and marine mining enterprises showed an uneven distribution in coastal cities, marine biopharmaceutics industry enterprises mainly agglomerate in Yantai and Qingdao, forming industrial cluster; marine salt industry enterprises mainly agglomerate in Binzhou with many enterprises dominated by production of crude salt and salt chemical industry, e.g. Shandong Chengkou Salt Chemical Co. Ltd., Shandong Haiming Chemical Co., Ltd, etc.; marine mining enterprises mainly agglomerate in Yantai, forming industrial cluster, which has many marine

mining enterprises, e.g. Shandong Gold Group Co Ltd., Penglai Jutal Offshore Engineering Heavy Industries Co. Ltd., etc., especially Shandong Gold Group Co Ltd. is now the only company engaging in undersea gold mining in China.

EMPIRICAL ANALYSIS OF COUPLING OF MARINE INDUSTRY CLUSTER OF SHANDONG PROVINCE WITH ITS URBAN DEVELOPMENT

This paper calculated the coupling coordination degree of marine industry cluster of 7 coastal cities of Shandong province with its urban development according to coupling coordination degree model, and the calculation results are as shown in Table 3.

Tab. 3 Value and Evaluation of Coupling Coordination Degree of Marine Industry Cluster of Shandong Province with Urban Development

City	U1	U2	C	T	D	Coupling coordination degree
Qingdao	0.69	0.78	0.61	0.75	0.67	High coupling coordination degree
Yantai	0.72	0.59	0.57	0.64	0.61	High coupling coordination degree
Weihai	0.39	0.45	0.46	0.43	0.44	Moderate coupling coordination degree
Weifang	0.21	0.34	0.36	0.29	0.32	Low coupling coordination degree
Dongying	0.37	0.32	0.41	0.34	0.38	Low coupling coordination degree
Rizhao	0.42	0.18	0.36	0.28	0.32	Low coupling coordination degree
Binzhou	0.35	0.31	0.41	0.33	0.37	Low coupling coordination degree

As seen in Table 3, in the process of coupling coordination of marine industry cluster of Shandong province with urban development, only Qingdao and Yantai have high coupling coordination degree, Weihai has moderate coupling coordination degree. Other coastal cities of Shandong province such as Weifang, Dongying, Sunshine and Binzhou still have low coupling coordination degree.

Qingdao and Yantai are important coastal cities in China, important international trade ports and marine transportation junctions, playing an important role in the implementation of marine strategy

by China. In recent years, relying on the abundant marine resources, based on marine fishery, with marine communications and seashore tourism as the developing priority, Qingdao and Yantai have gradually developed the marine biopharmaceutics industry and marine mining and emerging industry. In 2015, the share of GDP of marine economy of Qingdao has exceeded 20%, and the contribution rate of marine cluster industries such as marine fishery, marine communications and transportation industry and seashore tourism to the urban development of Qingdao has been rising. Yantai is rich in marine mineral resources, and its gold reserve ranks first in China, and has the only company engaging in undersea gold mining in China. In addition, Qingdao and Yantai have many marine scientific research institutions, especially Qingdao is home to 30% of marine scientific research institutions, and 50% of high-level marine scientific research personnel of China, all of which promote the marine industry cluster and urban economy.

Weihai is located at the easternmost edge of Jiaodong Peninsular, as an important harbor in the northern China, it is open to navigation all the year round. Meanwhile, Weihai is rich in marine fishery resources, and the largest aquatic products processing base in China. In recent years, seashore tourism has also become a new growth point of Weihai's economy. However, other marine industries develop slowly in Weihai and have not formed an industry agglomeration. Weifang, Dongying, Rizhao and Binzhou still have low coupling coordination degree in coupling coordination of marine industry cluster with urban development, most of the marine industries of these cities have not formed a cluster, and the marine industries also play a limited promoting role in the development of these cities.

CONCLUSION

Based on the analysis of the mutual influence and mutual promotion of marine industry cluster and urban development, this paper constructed the coupling development model of marine industry cluster and urban development, taking Shandong province as an example, analyzed the condition of marine industry cluster, and conducted an empirical research of coupling relationship between marine industry cluster and urban development of each coastal city of Shandong province using the coupling evaluation model calculation method, the results showed that:

(1) After recent years of development, the traditional marine industries had formed an industry cluster, and the emerging marine industries also began to present a clustering development trend, and these industries strongly boosted the urban development, however, most of the emerging marine industries had not formed an industrial cluster, thus playing a limited promoting role in the economic development. The traditional marine industries showed a rapid development, marine fishery, marine communications and transportation industry

and seashore tourism had become important industries in the promotion of development of coastal cities, while the development of coastal cities further promoted the development of these marine industries. The emerging marine industries, such as marine mining, marine power and marine engineering construction industry, had low linkage level, and had not formed an industrial cluster, thus playing a limited promoting role in the urban development.

(2) The marine industry cluster and urban development had obvious coordination coupling development characteristics, presenting mutual promotion and mutual influence. The marine industry cluster promoted the urban development by means of innovation diffusion, employment promotion and increase of production value, while the urban development promoted the marine industry cluster by providing infrastructure and human resources.

(3) The number of marine industry cluster had an important influence on the urban development, and the marine industry cluster had become the new growth point of the urban development, the greater the number of marine industry cluster, the greater the driving force for the urban development. The marine industry cluster realized efficient use of resources and efficient drive of relevant industry by taking cluster advantage, thus achieving the regional economic growth and urban development.

ACKNOWLEDGEMENTS

This work was supported by the National Natural Science Foundation of China (No. 71371108).

REFERENCES

1. Zhao Bingxin, Xiao Wenwen, Tong Ren-Cheng, et al.. Research on the Connotation of Blue Economy and Its Linkage Structure Effect from the Perspective of Industrial Network——A Case of Shandong Province [J]. *China Soft Science*, 2015, 08: 135-147.
2. Wang Lili, Xiao Wenwen. Industry Linkage of Marine Industry and Marine-Land Industry Linkage Development-Based on Input-Output Model [J]. *Economic Geography*, 2016, 01: 113-119.
3. Fernández-Macho J, Murillas A, Ansuategi A, et al. Measuring the maritime economy: Spain in the European Atlantic Arc[J]. *Marine Policy*, 2015, 60: 49-61.
4. Surís-Regueiro J C, Garza-Gil M D, Varela-Lafuente M M. Marine economy: A proposal for its definition in the European Union[J]. *Marine Policy*, 2013, 42: 111-124.
5. Salvador R. Maritime Clusters Evolution. The (not so) Strange Case of the Portuguese Maritime Cluster[J].

- Journal of Maritime Research, 2014, 11(1): 53-59.
6. Morrissey K, O'Donoghue C. The potential for an Irish maritime transportation cluster: An input–output analysis [J]. *Ocean & coastal management*, 2013, 71: 305-313.
 7. Simões A, Soares C G, Salvador R. Multipliers, linkages and influence fields among the sectors of the Portuguese maritime cluster[J]. *Maritime Technology and Engineering*, 2014: 155.
 8. Hammervoll T, Halse L L, Engelseth P. The role of clusters in global maritime value networks[J]. *International Journal of Physical Distribution & Logistics Management*, 2014, 44(1/2): 98-112.
 9. Porter M. *On Competition*[M]. Harvard Business School Press, Boston, MA.,1998.
 10. Roelandt T J A, Den Hertog P. Cluster analysis and cluster-based policy making in OECD countries: an introduction to the theme [J]. *Boosting innovation: The cluster approach*, 1999: 9-23.
 11. Zhao B X, Du P L, Xiao W.W., et al. Industrial cluster core structure and its index system[J].*System Engineering-Theory & Practice*, 2016, 36(1): 55-62
 12. Titze M, Brachert M, Kubis A. The identification of regional industrial clusters using qualitative input–output analysis (QIOA) [J]. *Regional Studies*, 2011, 45(1): 89-102.
 13. Zhou Hong. *The Modern Chinese Dictionary* [K]. Beijing: Guangming Daily Press, 2003.820~821.
 14. Chen Yanyun, Qin Chuan. Interaction of Industrial Agglomeration and Economic Growth: Analysis of 14 City Groups [J]. *Reform*, 2012, 10: 38-43.
 15. Shen Yufang, Liu Shuhua, Zhang Jing, Wang Nengzhou. The Correspondence among Industrial Cluster, City Group and Port Group on the Yangze Delata Area [J]. *Economic Geography*, 2010,05:778-783.
 16. Sheng Yanchao, Zhong Zhiping. Study on the Coupling Coordinative Degree between Tourism Industry and Regional Economy——A Case of Hunan Province [J]. *Tourism Tribune*, 2009,08:23-29.
 17. Gao Nan, Ma Yaofeng, Zhang Chunhui. Space- time Coupling Differentiation of Tourism Industry of Chinese Silk Road Economic Belt and Regional Economy——Based on Panel Data of 9 Provinces in 1993-2012 [J]. *Economic Management*, 2015,09:111-120.
 18. Chang Y C. Maritime clusters: What can be learnt from the South West of England[J]. *Ocean & Coastal Management*, 2011, 54(6): 488-494.
 19. Morrissey K, O'Donoghue C. The Irish marine economy and regional development[J]. *Marine Policy*, 2012, 36(2): 358-364.
 20. Shinohara M. Maritime cluster of Japan: implications for the cluster formation policies[J]. *Marit. Pol. Mgmt.*, 2010, 37(4): 377-399.
 21. Ji Yujun, Liu LinJing. Analysis of the Linkage Relationship Between the Marine Industrial Cluster and the Coastal Regional Economic Development [J]. *Marine Economy*, 2013,03:1-7.
 22. Doloreux D. Understanding regional innovation in the maritime industry: an empirical analysis[J]. *International Journal of Innovation and Technology Management*, 2006, 3(02): 189-207.
 23. da Silva Monteiro J P V, Neto P A, Noronha M T. Understanding the ways and the dynamics of collaborative innovation processes: the case of the maritime cluster of the Algarve region (Portugal)[J]. *Urban, Planning and Transport Research*, 2014, 2(1): 247-264.
 24. Wiese A, Brandt A, Thierstein A, et al. Revealing Relevant Proximities. Knowledge Networks in the Maritime Economy in a Spatial, Functional and Relational Perspective[J]. *Raumforschung und Raumordnung*, 2014, 72(4): 275-291.
 25. Haezendonck E, Pison G, Rousseeuw P, et al. The competitive advantage of seaports[J]. *International Journal of Maritime Economics*, 2000, 2(2): 69-82.
 26. Lee C B, Wan J, Shi W, et al. A cross-country study of competitiveness of the shipping industry[J]. *Transport Policy*, 2014, 35: 366-376.
 27. Benito G R G, Berger E, De la Forest M, et al. A cluster analysis of the maritime sector in Norway[J]. *International Journal of Transport Management*, 2003, 1(4): 203-215.
 28. Duranton G, Overman H G. Testing for localization using micro-geographic data[J]. *The Review of Economic Studies*, 2005, 72(4): 1077-1106.
 29. Zhao Bingxin, Zhang Jianghua. *Introduction to industry network theory* [M]. Beijing: Economic Science Press, 2013
 30. Zhao Bingxin, Yin Chong, Zhang Jianghua. A study on industry complex network and its modeling — On the example of. [J]. *Economic Management*, 2011, 7: 139-148.

31. TORRE A. and RALLET A. Proximity and localization, *Regional Studies* 2005, 39, 47–59.
32. OERLEMANS L. and MEEUS M. Do organizational and spatial proximity impact on firm performance?, *Regional Studies* 2005, 39, 89-104.
33. Haggett P, Cliff A.D., *Locational Models* [M]. London: Edward Arnold Ltd, 1977.

CONTACT WITH THE AUTHOR

Zhao Bingxin

zbx@sdu.edu.cn

School of Management
Shandong University
Jinan, Shandong, 250100
CHINA

SIMULATION AND EXPERIMENTAL STUDY IN THE PROCESS OF WAVE ENERGY CONVERSION

Wei Zhang, Ph. D.,

YanJun Liu, Ph. D.,

Mechanical Engineering Institute, Shandong University,

Jinan, Shandong, China

ABSTRACT

This article introduces the operating principle of the wave energy device and makes AMESim simulated analysis in the influence of the amplitude and period of the wave on the output efficient. By using the result of the simulation to optimize design, the article puts forwards a kind of suitable control technology which based on the disclosed amplitude and period of the wave to control the check valve, invoking the motor in different levels of efficiency. This kind of technology aims to solve the problem which includes low efficiency and high start wave of the wave energy device. The result is verified by the physical experiment, which lays the foundation for the implementation of marine engineering. The established methods of simulation model and analysis results are expected to be useful to designing and manufacturing of wave energy converter

Keywords: Wave energy converter, Suitable control technology, Experimental verification

INTRODUCTION

With the gradual depletion of oil or other fossil fuels and the concern of global climate change caused by greenhouse gas emissions [1], low-carbon and energy saving, development and utilization of renewable energy is becoming the theme of world energy development [2]. The ocean has tremendous energy. The development and utilization of ocean energy is the trend of world energy development. The use of ocean power can replace fossil energy that can cause environmental pollution, which has important economic and social significance [3]. Wave power generation technology which belongs to ocean power generation technology converts wave energy into electrical energy by wave energy absorbing and conversion devices [4].

The point absorbers possess a large power-to-volume ratio

implying a large ratio of absorbed power to the submerged buoy volume compared to other types of absorbers [5]. They are also attractive in terms of easy modelling because the scattered wave field can be neglected and forces on the body are only due to incident waves. A series of studies by Falnes and, Evans (1981) [6] French and Bracewell (1986) [7], Pizer (1993) [8], Vantorre et al. (2004) [9], Babarit et al. (2004) [10] and others have carried out on these devices both in regular and irregular waves.

The difficulties lie in wave energy development process is how to achieve efficient and stable conversion. Due to instability caused by waves, conversion devices' operation condition always out of design condition in a long term, apart from this. Moreover, the instability of energy transfer systems also

limits the efficiency of power generating system. Therefore, the permanent goal of wave energy research is to improve the conversion rate and stability [11].

Wave power generation devices which adopt hydraulic transmission transfer wave energy into hydraulic energy, then transfers hydraulic energy into electrical energy of power generator by using hydraulic motors. The way of hydraulic drive system replacing the traditional mechanical transmission can improve the stability of the systematic output electric power [12].

The wave amplitude and period in wave power generation system directly determine the energy efficiency of the system output [13]. This article centers on the the influence of hydraulic system of single float power generate equipment and the wave amplitude and period on power generation efficiency.

The first section: the introduction of operating principle of hydraulic system; the second section: a theoretical estimation on the movement displacement of the object according to the actual oceanic conditions. The third section is simulation analysis: build simulation model, then design simulation parameters based on theoretical calculations and analyze the output pressure, flow and efficiency of the single float wave power device which influenced by wave height and period. The fourth section: optimize the system design according to the simulation results and propose the adaptive control technology of hydraulic system, solve the low efficiency of power generation and the low utilization rate of wave energy. The fifth section: build the land bench, verify the simulation results; The section sixth: reach a conclusion.

Previous papers were studied from the theoretical to the semi-physical experiments and propose a new technique based on simulation results, which has an important referential value to improve the stability and efficiency of the power generation.

WORK PRINCIPLE AND COMPOSITION OF WAVE ENERGY CONVERTER

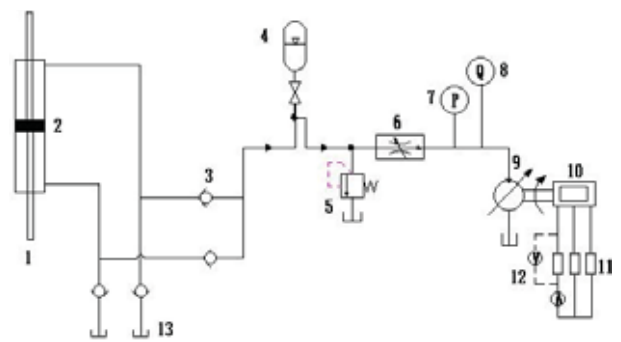
Fig. 1 is a new wave energy device. This device includes wave energy conversion systems, energy transfer system, power consumption system, control and measurement system. Using the hydraulic system as energy transmission can improve the stability of output electric power.



Fig. 1. Wave energy power generation device

HYDRAULIC TRANSMISSION PRINCIPLE

Hydraulic drive system is the key to ensure stability of output power. It can buffer irregular shock wave energy. Wave energy collection system converts wave energy to mechanical energy of the float, the movement of the float converts mechanical energy into hydraulic energy, the hydraulic motor rotated by hydraulic drive system which motivates the power generator, and then output the stable electric power. Fig. 2 is a schematic diagram of the hydraulic drive system. Increasing the output energy efficiency of the hydraulic system by double rod hydraulic cylinders, meanwhile ensure the hydraulic energy discharge when the float downward or upward. Using a check to valve constitute a hydraulic rectifier module, which ensure that the hydraulic output for the same direction and at the same time keep the hydraulic motor rotation direction stay the same . By the reasonable match of the various parts of the hydraulic drive system parameters can make the output power more stable.



1. hydraulic rod 2. hydraulic cylinder 3. one-way valve 4. accumulator 5. relief valve 6. speed regulation valve 7. pressure sensor 8. flow sensor 9. motor 10. generator 11. loads 12. voltage sensor 13. oil tank

Fig. 2. Working principle of hydraulic transmission system

ESTABLISHMENT OF MATHEMATICAL MODEL

In order to study the influence of wave amplitude and period on the operating condition, the first step is to build a math module to estimate the displacement of the float in the actual situation [14].

Under normal conditions, we can describe displacement of the vertical cylindrical float downs System z as the formula below:

$$Z = \frac{\left(\frac{F_0}{\rho g A_{wp}} \right) \cos(\omega t + \gamma - \sigma_z)}{\sqrt{\left(1 - \frac{w^2}{w_z^2} \right)^2 + \left(\frac{2\Delta_z w}{w_z} \right)^2}} \quad (1)$$

$$= Z_0 \cos(\omega t + \gamma - \sigma_z)$$

In the formula:

F_0 - amplitude of the wave force;

m - mass of float;

m_w - additional mass, $m_w = \rho \frac{D^3}{6}$;

D - float diameter;

A_{wp} - water cut area, $A_{wp} = \frac{\pi D^2}{4}$;

w_z - rolling natural frequency, $w_z = \sqrt{\frac{\rho g A_{wp}}{m + m_w}}$.

According to the formula: w_z is related to A_{wp} , after the shape of the float is chosen, w_z is ensured. Therefore, determines the frequency ratio $\frac{w}{w_z}$, then ensure $\frac{Z_0}{\left(\frac{F_0}{\rho g A_{wp}}\right)}$ according Fig. 3. In this case, if the amplitude of the wave force F_0 is determined, the range of motion Z_0 can be determined.

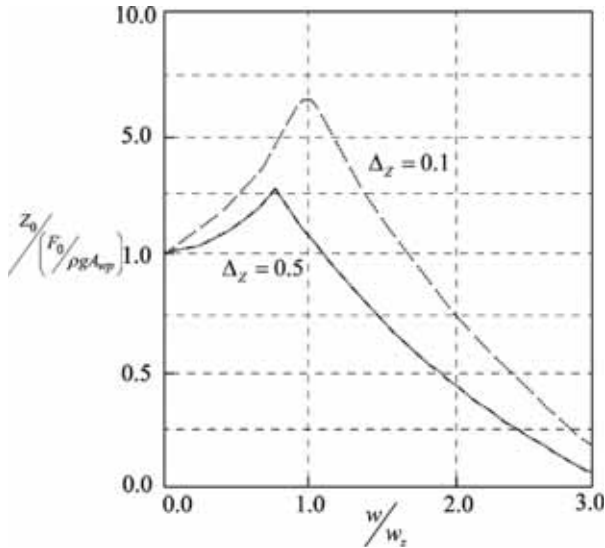


Fig. 3. Amplification coefficient of damping ratio changing with frequency ratio

According to the Froude-Krylov assumption theory that acting on the submerged body of a vertical wave force is:

$$F_v = C_v \iint_S P_z ds \quad (2)$$

When the $\frac{H}{2R}$ value is small, viscous forces are negligible, the vertical wave force is:

$$\begin{aligned} F_v &= C_v \iint_S P_{n_z} ds \\ &= 2C_v \int_0^R \int_0^\pi P \cdot r d\theta dr \\ &= C_v \rho g \pi H \frac{\cosh k(h-d(t))}{\cosh kh} \cos \omega t \int_0^R J_0(kr) r dr \\ &= C_v \rho g \pi H R J_1(kR) \frac{\cosh k(h-d(t))}{k \cdot \cosh kh} \cos \omega t \\ &= F_0 \cdot \cos \omega t \end{aligned} \quad (3)$$

In the formula:

k - number of waves, $k = \frac{2\pi}{\lambda}$;

C_v - diffraction coefficient;

H ---- wave height;

h ---- water depth;

R ----float radius.

According to local meteorological and hydrological data, the wave height of the waves of sea trials focused between 1 m to 2 m, the wave period mainly between 2 s and 8 s. The condition of the trial ocean is shown in the Tab. 1.

Tab. 1. Experimental condition parameters

Physical quantities	Symbol	Value
Depth	h	20 m
Wave height	H	1-2 m
Period	T	2-8 s
Total weight of the moving part of float	m_z	15000 kg
Float radius	R	1.5 m
Density of sea water	ρ	1025 kg/m ³

Substituting the above parameters into the formula can achieve:

$$m_w = \rho \frac{D^3}{6} = \frac{1025 \times 3^3}{6} = 4612.5 \text{ kg} \quad (4)$$

$$m_z = 15000 \text{ kg} \quad (5)$$

$$A_{wp} = \frac{\pi D^2}{4} = \frac{3^2 \times 3.14}{4} = 7.065 \text{ m}^2 \quad (6)$$

$$w_z = \sqrt{\frac{\rho g A_{wp}}{m_z + m_w}} = \sqrt{\frac{1025 \times 9.8 \times 7.065}{15000 + 4612.5}} = 1.902 \text{ kg} \quad (7)$$

$$w = \frac{2\pi}{T} = \frac{2 \times 3.14}{5} = 1.25 \quad (8)$$

$$\frac{w}{w_z} = \frac{1.04}{3.92} = 0.55 \quad (9)$$

Take $\Delta_z = 0.5$, from fig 3 can achieve:

$$\frac{Z_0}{\left(\frac{F_0}{\rho g A_{wp}}\right)} = 1.5 \quad (10)$$

Thus:

$$Z_0 = \frac{1.5 F_0}{\rho g A_{wp}} = \frac{1.5 \times F_0}{1025 \times 9.8 \times 7.065} \quad (11)$$

According wave condition ranges from 1 to 2 m, the wave height is taken respectively 1 m, 1.5 m, 2 m, corresponding to the movement of the float displacement Z_0 is calculated, the calculation results is as below in Tab. 2.

Tab. 2. The calculation results

Calculation Case	λ	k	C_v	F_0/N	Z_0
H=1 m	15.23	0.41	1.33	16218	0.34
H=1.5 m	18.40	0.34	1.12	34646	0.732
H=2 m	20.94	0.30	1.12	65880	1.39

According to the theoretical calculations and actual oceanic conditions, this article selects float displacement Z_0 as 0.5 m, 0.7 m, 1.0 m and period as 2.5 s, 5 s, and 7.5 s.

SIMULATION AND ANALYSIS

THE ESTABLISHMENT OF MODEL

Fig. 4 is a principle diagram based on hydraulic drive system to build a simulation model by AMESim. We can simulate condition of float in the designed term by inputting the amplitude and period of the signal.

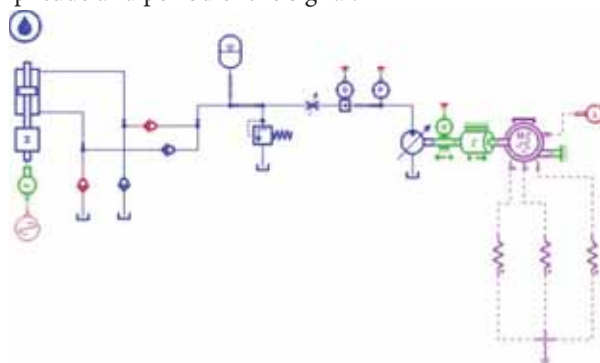


Fig. 4. Simulation model

The main parameters of model are shown in Tab. 3:

Tab. 3. Main parameters of the model

Main model	Settings parameters
Piston diameter	180 mm
Diameter of piston pole	140 mm
Hydraulic cylinder stroke	5 m
Hydraulic motor	speed: 1000 rev/min; displacement: 160 mL/r
Electrical generators	three-phase permanent synchronous generators
Coefficient of viscous friction	0.1 Nm / (rev/min)

SIMULATION ANALYSIS ON DIFFERENT WAVE PERIOD

In order to study the affect of wave period on the power output of a wave power generation system, using the simulation model of AMESim to make detailed analysis [15-17]. Setting the amplitude of float motion as 1 m and the working period as 2.5 s, 5 s, 7.5 s to run the model, at this point the motor output pressure flow curve shown in Fig. 5-7:

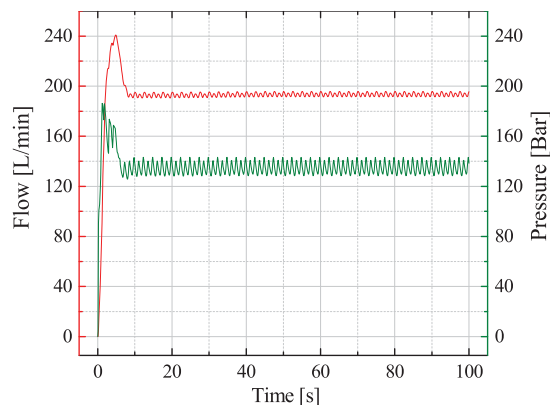


Fig. 5. Motor pressure and flow curves when the cycle is 2.5 s

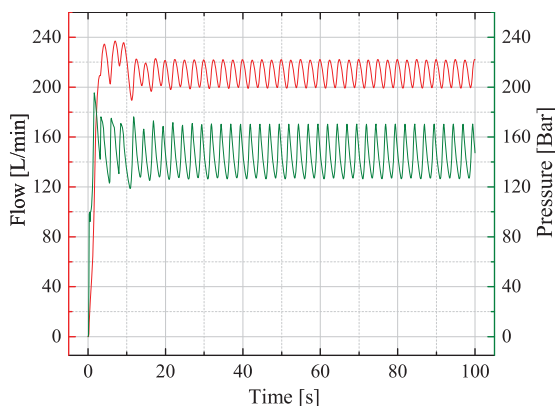


Fig. 6. Motor pressure and flow curves when the cycle is 5 s

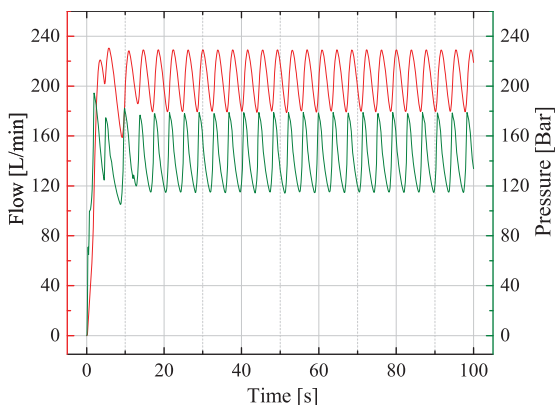


Fig. 7. Motor pressure and flow curves when the cycle is 7.5 s

It can be drawn from the above graph that when the period is 2.5 s, the input fluent of the motor is stable as 190 L/min, and when the pressure is 130 Bar, as the period of the wave increased, the fluctuation scale of the fluent pressure and the efficiency of the system increased, the output stability comes

down, which makes the followed electric process become difficult.

SIMULATION ANALYSIS ON DIFFERENT AMPLITUDE

Set analog wave period as 5 s, amplitude of movement of the float as 0.5 m, 0.7 m, 1 m to run the simulation model and analyze the output port pressure, flow and efficient curve of the motor, as is shown in Fig. 8-10:

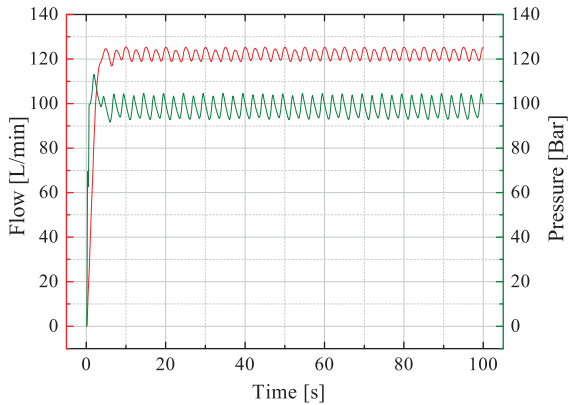


Fig. 8. Motor pressure and flow curves when amplitude is 0.5 m

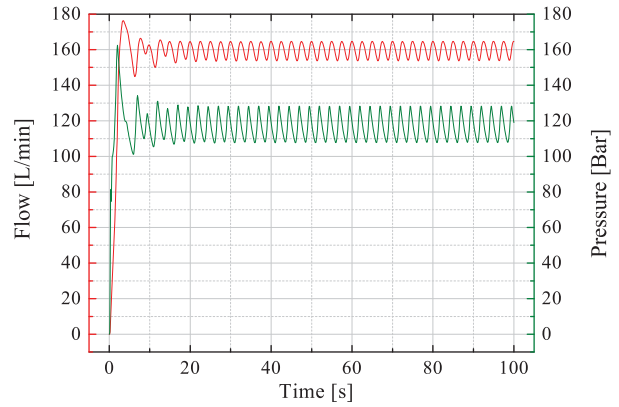


Fig. 9. Motor pressure and flow curves when amplitude is 0.7 m

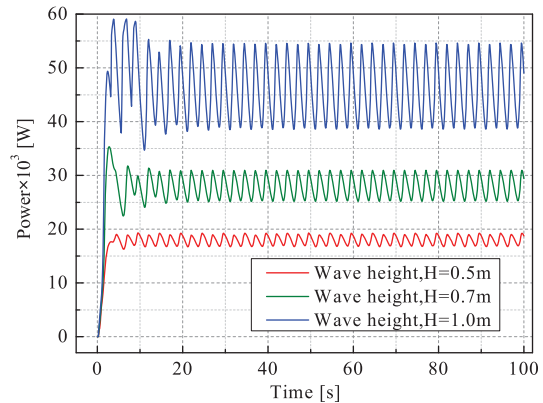
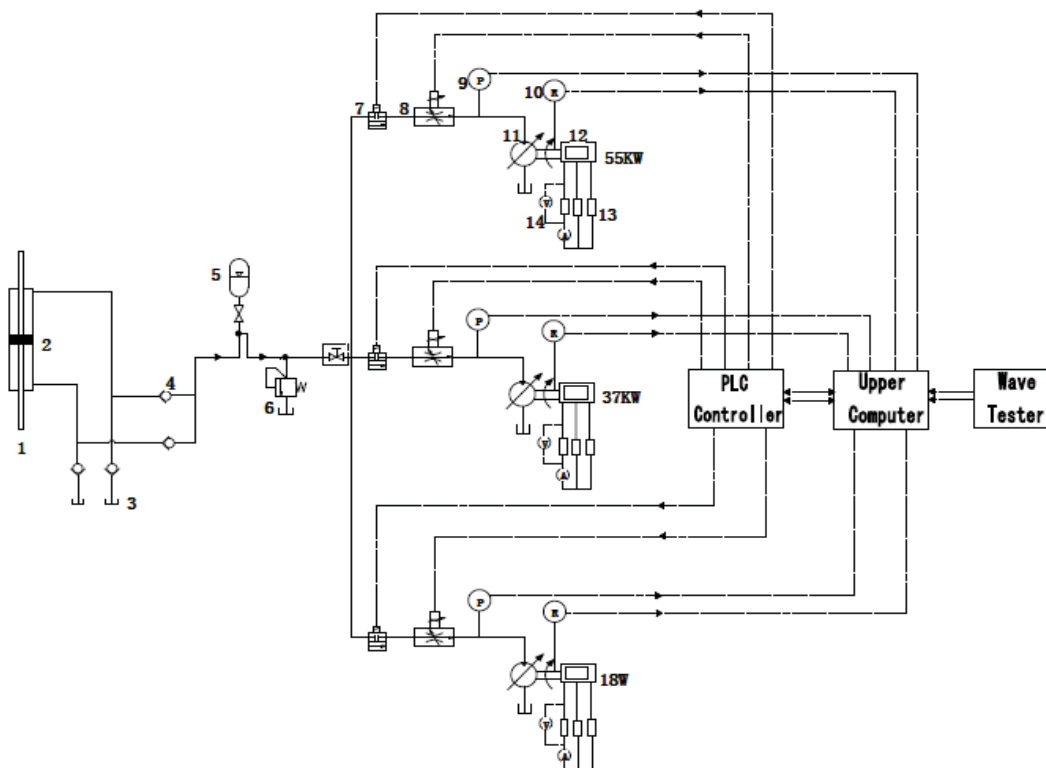


Fig. 10. Power contrast curves with different amplitudes



1. hydraulic rod 2. hydraulic cylinder 3. oil tank 4. one-way valve 5. accumulator 6. relief valve 7. Electromagnetic valve 8. speed regulation valve 9. pressure sensor 10. speed sensor 11. motor 12. generator 13. loads 14. voltage sensor

Fig. 11. Self-adaptive control theory

According to the curve above, when the amplitude is 0.5 m, the system begins to operate, output has concussion, 3 s later the input flow of motor stable at 120 L/min, the pressure is 100 Bar, the output efficiency of hydraulic system is 18 kW :when the amplitude is 0.7 m, the input flow of motor stable at 160 L/min, the pressure is 120 Bar the output sharp efficiency of hydraulic system is 36 kW :when the amplitude is 1.0 m, the input flow of motor stable at 210 L/min, the pressure is 150 Bar the output sharp efficiency of hydraulic system is 55 kW.

With the increase of float movement amplitude, the fluent pressure and efficient are increased, the stability declined and we can see obvious concussion.

OPTIMIZATION DESIGN OF WORK PRINCIPLE

Conclude from the simulation, the output electric efficiency has great changes in different conditions. In order to solve the problem of the low wave energy conversion efficiency of power generation equipment and the high wave of the start, we propose suitable control technology of wave energy device.

According to the amplitude and period of the wave, we control the electric check valve, using different power rating of the generator at 18 kW, 37 kW, 55 kW to realize the suitable control. Thereby expand the wave energy device operating range, so it can automatically adjust the working conditions in the marine changing load, in order to improve the efficiency of the wave energy. The suitable control technology schematic diagram is Fig. 11.

EXPERIMENTAL AND RESULT ANALYSIS

CONSTRUCTION OF EXPERIMENTAL APPARATUS

In order to study the impact of wave amplitude and period to stability and efficiency of the output power further, and to verify the simulation results. The land experiment stand is shown in Fig. 12. Shown in the Figure, the hoist pulls the float moves up and down along the buoy to simulate movement of the float in a vertical wave forces, and then to get the hydraulic energy transmission, and finally output electric power.

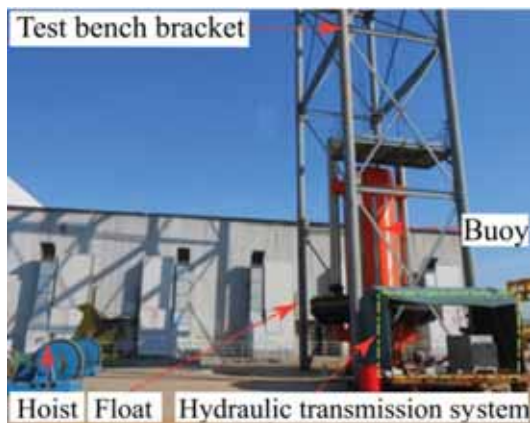


Fig. 12. Experimental apparatus

The following Fig. 13 is an energy delivery system. Through monitoring real-time oceanic state information to control electromagnetic valve. Owing to the low efficiency and poor ability of single generator to adapt the sea state, selection of different rated power generators can solve the problem. Software can collect real-time movement of the float, outlet pressure and flow of the motor, output voltage and current parameters of the generator, which in order to facilitate further analysis.

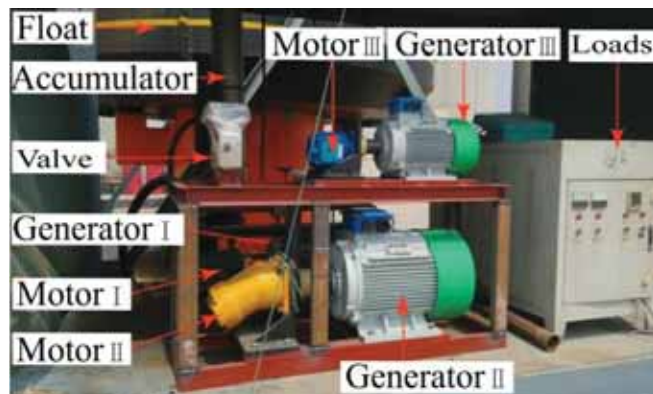


Fig. 13. Energy delivery system

EXPERIMENTAL DATE ANALYSIS

Effects of different wave periods

Fig. 14-16 is the input pressure-flow curve of motor, analog movement amplitude of the float is 1 m, periods were taken 2.5 s, 5 s, 7.5 s.

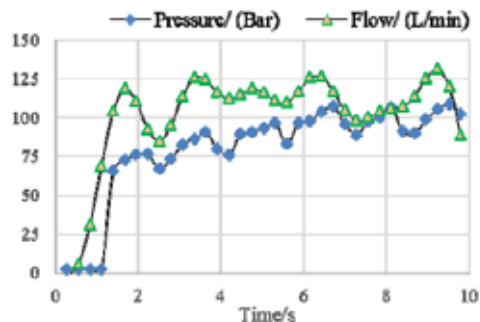


Fig. 14. Motor pressure and flow curve when the cycle is 2.5 s

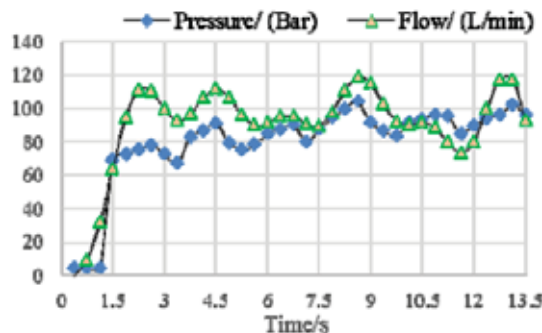


Fig. 15. Motor pressure and flow curve when the cycle is 5 s

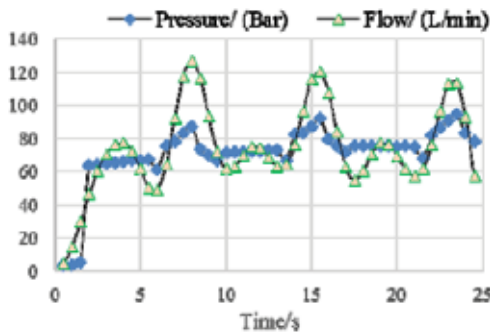


Fig. 16. Motor pressure and flow curve when the cycle is 7.5 s

Analyzing Fig. 14-16 curve we can achieve that: When the period is 2.5 s and the system starts to work, output is shocked, steady mean flow of imports of the motor is 117 L / min, pressure is 98.2 Bar, When the cycle is 5 s, Steady flow of imports of the motor is 97 L / min, pressure is 93 Bar, When the cycle is 7.5 s, Steady flow of imports of the motor is 68 L / min, pressure is 78 Bar, With increasing wave period, the output flow and pressure of the system is decreasing. When the period is 5 s, the stability is better.

Effects of different wave amplitude

Fig. 17-20 is the input pressure-flow-power curve of motor, analog movement amplitude of the float is 0.25 m, 0.5 m, 0.75 m, the periods were taken 5 s.

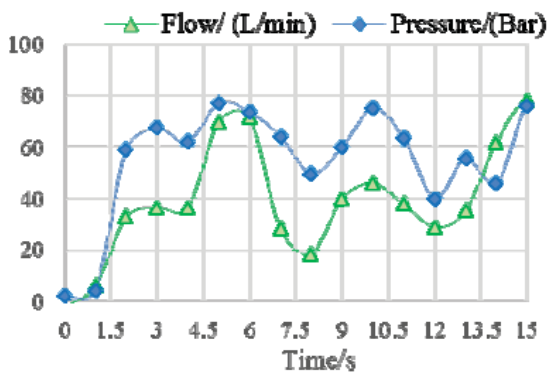


Fig. 17. Motor pressure and flow curves when amplitude is 0.25 m

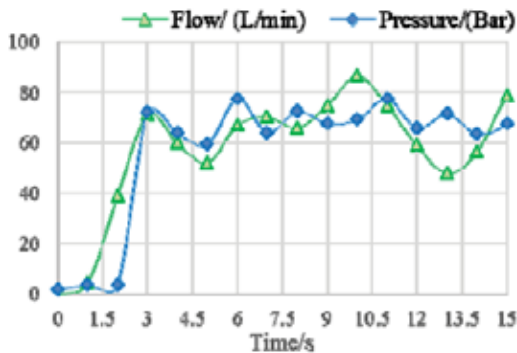


Fig. 18. Motor pressure and flow curves when amplitude is 0.5 m

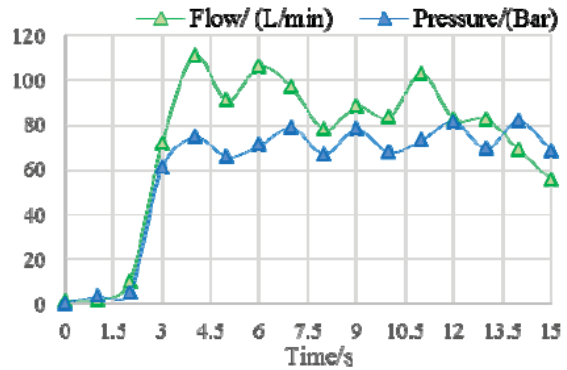


Fig. 19. Motor pressure and flow curves when amplitude is 0.75 m

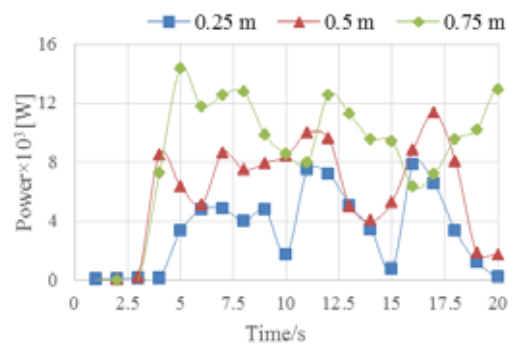


Fig. 20. Power contrast curves with different amplitudes

Analyzing Fig. 17-20 curves we can achieve: When the amplitude is 2.5 m, the system starts to work, output is shocked, steady mean flow of imports of the motor is 40 L / min, pressure is 60 Bar, and the average power is 4.6 kW. When the amplitude is 0.5 s, steady flow of imports of the motor is 60 L / min, pressure is 65 Bar, the average power is 7.5 kW. When the amplitude is 0.75 s, Steady flow of imports of the motor is 95 L / min, pressure is 71.5 Bar, the average power is 10.2 kW. With the wave amplitude increase, the output flow, pressure and power of the system is decreasing, which is consistent with the simulation results.

CONCLUSIONS

- 1) The experimental data are coinciding with the simulation curve trend, this manifests the hydraulic system design is feasible and the build of simulation is right.
- 2) The amplitude of wave has an obvious effect on output efficiency, as the amplitude increase, the output efficiency increased. And the period of wave determines the stability of output efficiency, as the period increased the stability of output efficient decline, and the concussion becomes obviously.
- 3) Further optimize the designation and guarantee the location and working condition for the waters of the device by simulation and land experiments. Put forward the suitable technology to meet the need of the device in different oceanic conditions to continuous output power and improve the utilization of wave.

ACKNOWLEDGEMENTS

This project is partially supported by Renewable Energy Special Foundation of China Oceanic Administration (GHME2010ZC01), Renewable Energy Special Foundation of China Oceanic Administration (SDME2010GC02) and Shandong University Oriented Project “Research on Key Scientific Problems of Marine Resources and the Use (2014QY006)”.

BIBLIOGRAPHY

1. Shi, H.D., Cao, F.F., Ma, Z., Liu, Z., 2014. *Physical Model Experimental Study on the Floating Buoy Wave Power Generator*. Journal of Ocean Technology. 33 (4):98–104.
2. Gao, H.T., Li, B., 2015. *Establishment of motion model for wave capture buoy and research on hydrodynamic performance of floating-type wave energy converter*. Polish Maritime Research. 22 (S1):106–111.
3. Birgersson, K.E., Balaya, P., Yan, J., 2011. *Energy Solutions for a Sustainable World*. Applied Energy. 90 (1), 1-2.
4. Esteban, M., Leary, D., 2012. *Current developments and future prospects of offshore wind and ocean energy*. Applied Energy, 90(1):128-136.
5. Yang, L., Hals, J., Moan, T., 2010. *Analysis of dynamic effects relevant for the wear damage in hydraulic machines for wave energy conversion*. Ocean Engineering. 37(13):1089-1102.
6. Evans, D.V., 1981. *Maximum wave-power absorption under motion constraints*. Applied Ocean Research 3 (4):200–203.
7. Choi, K.S., Yang, D.S., Park, S.Y., Cho, B.H., 2012. *Design and performance test of hydraulic PTO for wave energy converter*. International Journal of Precision Engineering & Manufacturing. 13(5), 795-801.
8. Pizer, D.J., 1993. *Maximum wave-power absorption of point absorbers under motion constraints*. Applied Ocean Research. 15 (4), 227–234.
9. Vantorre, M., Banasiak, M., Verhoeven, R., 2004. *Modelling of hydraulic performance and wave energy extraction by a point absorber in heave*. Applied Ocean Research 26, 61–72.
10. Babarit, A., Duclos, G., Clement, A.H., 2004. *Comparison of latching control strategies for a heaving wave energy device in random sea*. Applied Ocean Research 26, 227–238.
11. Ma, Z., 2013. *The Study on Hydrodynamic Performance of Oscillating Floater Buoy Wave Energy Converter [D]*. Ocean University of China.
12. Zhang, D.H., Li, W., Lin, Y.G., 2009. *Wave energy in China: Current status and perspectives*. Renewable energy. 34(10), 2089–2092.
13. Bailey, H., Bryden, I.G., 2011. *Influence of a quadratic power take-off on the behavior of a self-contained inertial referenced wave energy converter*. Proc. Inst. Mech. Eng. Part M J. Eng. Marit. Environ., 226 (1), 15–22.
14. Zhang, D.X., 2001, *Analyzing primary parameters of twin-floater ocean wave generate electricity device and designing it with most optimal geometric shape*. Yan shan University. 46-50.
15. Antonelli, M., Baccioli, A., Francesconi, M., Psaroudakis, P., Martorano, L., 2015. *Small Scale ORC Plant Modeling with the AMESim Simulation Tool: Analysis of Working Fluid and Thermodynamic Cycle Parameters Influence*. Energy Procedia. 81:440-449.
16. Lisowski, J., 2014. *Comparison of dynamic games in application to safe ship control*. Polish Maritime Research. 21(3), 3-12.
17. Phan, L.K., Stive, M.J.F., 2015. *Coastal Mangrove Squeeze in the Mekong Delta*. Journal of Coastal Research. 31(2), 233-243.

CONTACT WITH THE AUTHOR

Yanjun Liu, Ph.D.

lyj111ky@163.com

Mechanical Engineering Institute
Shandong University
Jinan Shandong
250061 China
CHINA

NUMERICAL SIMULATION AND EXPERIMENTAL STUDY ON FORMATION OF HIGH CONCENTRATION OF H₂ GENERATED BY GAS EXPLOSION

Baiwei Lei ¹

Bing Wu ¹

Yatong Zhao ¹

Muhammad Aqeel Ashraf ²

¹ Faculty of Resources and Safety Engineering, China University of Mining & Technology (Beijing),
Beijing 10083, PR China

² Faculty of Science and Natural Resources, University Malaysia Sabah 88400 Kota Kinabalu Sabah,
Malaysia

ABSTRACT

In coal mine fire rescues, if the abnormal increase of gas concentration occurs, it is the primary thing to analyze the reasons and identify sources of the abnormal forming, which is also the basis of judge the combustion state of fire area and formulate proper fire reliefs. Nowadays, related researches have recognized the methane explosion as the source of high concentration of H₂ formation, but there are few studies about the conditions and reaction mechanism of gas explosion generating high concentration of H₂. Therefore, this paper uses the chemical kinetic calculation software, ChemKin, and the 20L spherical explosion experimental device to simulate the generating process and formation conditions of H₂ in gas explosion. The experimental results show that: the decomposition of water vapor is the main base element reaction (R84) which leads to the generation of H₂. The free radical H is the key factor to influence the formation of H₂ generated from gas explosion. With the gradual increase of gas explosion concentration, the explosive reaction becomes more incomplete, and then the generating quantity of H₂ increases gradually. Experimental results of 20L spherical explosion are consistent with the change trend about simulation results, which verifies the accuracy of simulation analysis. The results of explosion experiments show that when gas concentration is higher than 9%, the incomplete reaction of methane explosion increases which leads to the gradual increase of H₂ formation

Keywords: gas explosion, high concentration of H₂, numerical simulation, explosion experiment

INTRODUCTION

Since the ignition sources are very difficult to approach in fire zone, it is the most important method to judge the combustion status of coal mine fire by gas analysis method. Once the exceptions of gas composition or gas concentration occurs, the basic action for developing rational fire disaster relief plan and preventing secondary disasters is to analyze causes for the exceptions with gas analysis method (Xinquan, 2013). Nowadays, studies about the change law and abnormal variations of indicator gas (CO, CO₂, C₂H₄, C₂H₂, C₂H₆ etc.) in coal mine fire have gained abundant achievements (Singh et al., 2007; Kim et al., 2004; Deng et al., 2015; Lingqi et al., 2008), but there are relatively less studies of the change patterns of H₂, especially lacks in researches on formation mechanism of

high concentration of H₂ in in fire area.

H₂ is a kind of flammable gas with its explosion limits from 4% to 74.2%. There are many sources of H₂ in coal mine, during normal operation, the pyrolysis of coal (Handong, 2001; Arenillas et al., 1999), the leakage of battery, bacterial decomposition of wood (Xinquan et al., 2013) in coal mines, etc, will all produce H₂. But when the mine fire happens, the H₂ in the fire area mainly comes from the oxidized spontaneous combustion with coal, so it is practical to analyze combustion state (Peng et al., 2010; Nehemia et al., 1999; Grossman et al., 1996) and verify whether the re-ignition exists according to the change of H₂ concentration in fire area (Fubao et al., 2010; Shao et al., 2014; Yang et al., 2015). In common mine fire, the concentrations of

H₂ are usually no higher than 2% due to the coal pyrolysis and incomplete combustion (AMSA, 2008). However, sometimes the concentration of H₂ could be monitored to be higher than 2%, reaching to 7% or even higher. Due to the lower explosion limit, high concentration of H₂ have high risks of explosion. Therefore, it is crucial to analyze the formation mechanism of high concentration of H₂ for perfecting gas analysis theory and implementing fire relief measures.

Through literature reviews (AMSA, 2008; Yingmei et al., 2009; Lianhua Dong, 1999), it could be found that gas explosion is an important source of high concentration of H₂. Researchers had detected high concentrations of H₂ (about 4%) after gas explosion in Dashan coal mine of Fushun early in 1917. High concentration of H₂ (higher than 3%) was also detected by the American Mining Bureau and French Institute of Metrology in the process of gas explosion experiment. AMSA (2008) proposed that high concentration of H₂ was generated when gas explosion reactions were not complete. However, the formation conditions and mechanism of high concentration H₂ after gas explosion are still absent of sufficient studies.

Chemical reaction kinetics simulation is an effective method to analyze gas explosion process, it can analyze the influences that the intermediate component or activation center have on gas explosion processes, and the kinetics factors of explosive gas products generation could also be analyzed. Xiangcun (2016) had studied the influences of different concentrations of gas on the gas explosive products and TKERS (The key elementary reaction steps). The chemical kinetic characteristics of gas explosion were simulated and analyzed by Na (2014). Baoshan (2013) had compared the inhibition effect of N₂ and CO₂ on gas explosion in the view of TKERS, while Yuntao (2009) had analyzed the explosion suppression characteristics with chemical kinetics model. The above studies are related to the change analysis of gas products after explosion, but the gas products are limited to carbon oxides and nitrogen oxides.

This paper takes research on the formation mechanism of high concentration of H₂ in gas explosion by numerical simulation and experiment. Firstly, it analyzed the change trend of mole fraction, TKERS and free radical of some catastrophic gases (CO, CO₂ and H₂) during the gas explosion process by using constant volume reactor model which be in Chemkin. Then, the 20L spherical explosion experimental device is applied to verify the H₂ quantity generated by gas explosion.

GAS EXPLOSION REACTION DYNAMICS ANALYSIS

REACTION MECHANISM

Gas explosion reaction process is not a single step chemical reaction, but a kind of complex "hot chain" reaction, and it is directly influenced by the generation and disappearance of free radicals. In order to analyze the kinetics characteristics of gas explosion, the article used the detailed chemical kinetics mechanism of methane combustion from Livermore

Lawrence National Laboratory of the United States, which includes 53 components, 325 reactions (Gregory et al., 2016). The calculation has been verified by a large number of researchers at home and abroad. Table one shows parts of the reaction steps of chain reaction of gas explosion. Table one shows parts of the reaction steps of chain reaction of gas explosion.

Table 1 partial reaction basis in the chain reaction of gas explosion

No.	elementary reaction
R3	$O + H_2 \rightleftharpoons H + OH$
R53	$H + CH_4 \rightleftharpoons CH_3 + H_2$
R58	$H + CH_2O \rightleftharpoons HCO + H_2$
R75	$H + C_2H_4 \rightleftharpoons C_2H_3 + H_2$
R84	$OH + H_2 \rightleftharpoons H + H_2O$
R126	$CH + H_2 \rightleftharpoons H + CH_2$
R284	$O + CH_3 \rightleftharpoons H + H_2 + CO$

INITIAL CALCULATION CONDITION

In order to analyze the reaction kinetics of H₂ in gas explosion in confined space, it used the constant volume reactor model in Chemkin software to solve the energy equation of gas explosion process. The solving procedure assumes that the enclosed space is an ideal adiabatic environment, the reaction rate keeps the same for every position in the computation space with no gradient difference of temperature and concentration. In the calculation condition, the volume fraction of O₂ and N₂ is 79/21. In this paper, 6 kinds of gases with different gas concentration are calculated in the gas explosion experiment processes. Its initial conditions are set as shown in table 2.

Table 2 Initial parameters of gas explosion

No.	Initial temperature (K)	Initial pressure (Mpa)	CH ₄ (%)	O ₂ (%)	N ₂ (%)	Computing time (s)
1	1300	0.1	6	19.74	74.26	0.02
2	1300	0.1	7	19.53	73.47	0.02
3	1300	0.1	9	19.11	71.89	0.02
4	1300	0.1	11	18.69	70.31	0.02
5	1300	0.1	13	18.27	68.73	0.02
6	1300	0.1	15	17.85	67.15	0.02

RATE OF PRODUCTION ANALYSIS

When analyzing the gas explosion process, distinguish the most influential elementary reactions for H₂ generation is

very important to understand of the formation process of H₂. In this paper, the ROP analysis in Chemkin software is used to analyze the elementary reaction affecting the H₂ generation.

Rate of production analysis (ROP for short) could be used to quickly extract and analyze which element reactions are most important to the generation or consumption of a component, it could also be used to analyze the direction of the chemical reaction at the same time. The calculation formulas of ROP are as follows:

$$P_K = \omega_K = \sum_{i=1}^I v_{ki} q_i \quad (1)$$

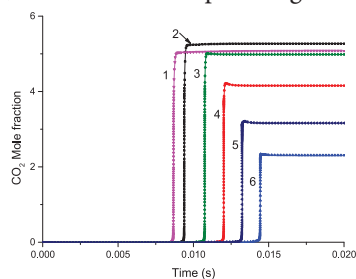
$$\frac{P_K}{C_{Ki}} = \frac{\max(v_{ki}, 0) q_i}{\sum_{i=1}^I \max(v_{ki}, 0) q_i} \quad (2)$$

Where P_K is the molar production of a species per unit volume, v_{ki} is the stoichiometric for the gas reactions, q_i is the rate of progress of the I gas-phase reactions. The calculation results of $\frac{P_K}{C_{Ki}}$ are indicators to judge the importance degree of different element reactions.

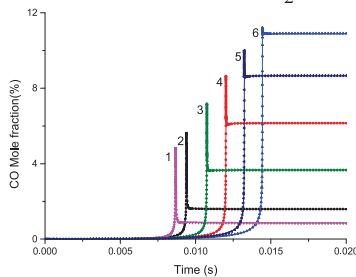
CALCULATION RESULTS AND ANALYSIS

The influences of gas concentration on gas compositions

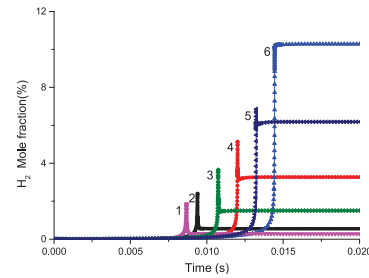
Figure 1 is the change regulation of main gas products CO, CO₂ and H₂ with different gas concentrations in dry and moist air environment. According to Figure 2, the explosion reaction processes within 5 to 10 milliseconds, the products concentration increased rapidly in the moment of explosion, and then stabilized quickly as well. With the increase of gas concentration, the time of the explosion gradually delayed.



(a) CO₂



(b) CO



(c) H₂

Fig. 1 The change trend of CO₂, CO and H₂ mole fraction in gas explosion process

From Figure 1 (a), with the increase of gas concentration, the mole fraction of CO₂ increased firstly and then decreased gradually. From Figure 1 (b) (c) it shows that CO and H₂ firstly increased rapidly and then rapidly decayed in the explosion with low concentration of methane during explosion reaction process. With the increase of explosion concentration, the increment of CO and H₂ becomes more significant, and the decline range gradually decreases. Eventually the final production of CO and H₂ would increase gradually. It indicates that the CO and H₂ formation is inevitably produced in the process of gas explosion, but parts of the CO and H₂ will quickly participate in the explosion reaction and then be consumed

CO/(CO+CO₂) is known as the combustion balance ratio. The ratio change indicates the severity of reaction. It shows that the greater the value is the more incomplete the reaction is, and vice versa. In order to analyze the relationship between H₂ generation and the degree of explosive reaction, the change of H₂ mole fraction under different test conditions is shown in Figure 3, and the ratio of CO/(CO+CO₂) is plotted in Figure 4.

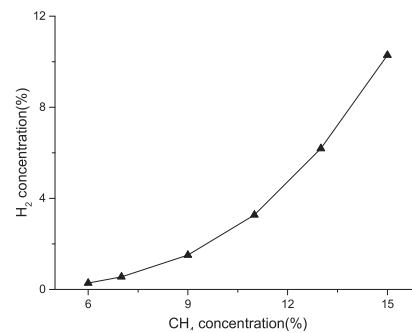


Fig. 3 H₂ mole fraction contrast curve

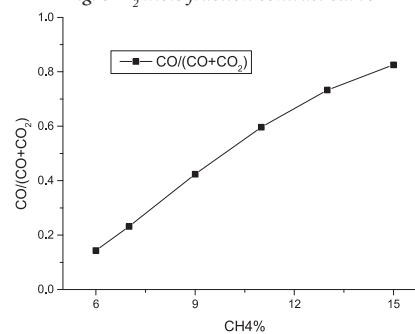


Fig. 4 The change trend of CO/(CO+CO₂)

The contrast analysis between Figure 3 and Figure 4 shows that with the increase of concentration of gas explosion, the amount of H_2 is gradually increased, and $CO/(CO+CO_2)$ also gradually increases. Therefore, it is implied that H_2 is mainly produced by incomplete gas explosion. And the greater the incomplete reaction degree of gas explosion is, the greater amount of H_2 is generated. In order to demonstrate this point, this paper makes further analyses of changes of TKERS and free radicals which affect the H_2 formation.

Analysis of TKERS and free radicals affecting H_2 generation

After the gas explosion, the gas composition balance is quickly completed, therefore, in order to effectively extract TKERS which affect the H_2 generation, ROP analysis was carried out to analyze the moment of explosive reaction. Use the ROP analysis tool in Chemkin software to search out 5 basic elements that have most important effects on the rate of H_2 generation, which are shown in Figure 5.

If the value of ROP is positive, it means the undergoing reaction is to promote the generation of H_2 . If the value of ROP is negative, the reaction is to suppress H_2 generation. The greater the absolute value of ROP is, indicates the larger promotion (or suppression) effects on H_2 generation. Through observation of Figure 5, with different gas concentrations, the TKERS are not the same all the time. However, in all test conditions, the reaction step of greatest impacts to H_2 formation responses are R84($OH + H_2 \rightleftharpoons H + H_2O$). In the early stage of explosion, R84 reaction mainly consumes free radicals OH and H_2 to generate water, thereby inhibiting the generation of H_2 . And in the later stage of the explosion, R84 is mainly to promote formation of H_2 , that is, the decomposition of H_2O under the influence of free radical H to generate H_2 . With the increase of the gas concentration, the promotion effects of R53 and R58 on H_2 formation becomes more and more obvious, while the effects of R3 consuming H_2 is getting smaller and smaller, resulting in the increments of H_2 generation quantity after gas explosion. The analysis result also reveals that the existence of water vapor in the explosion

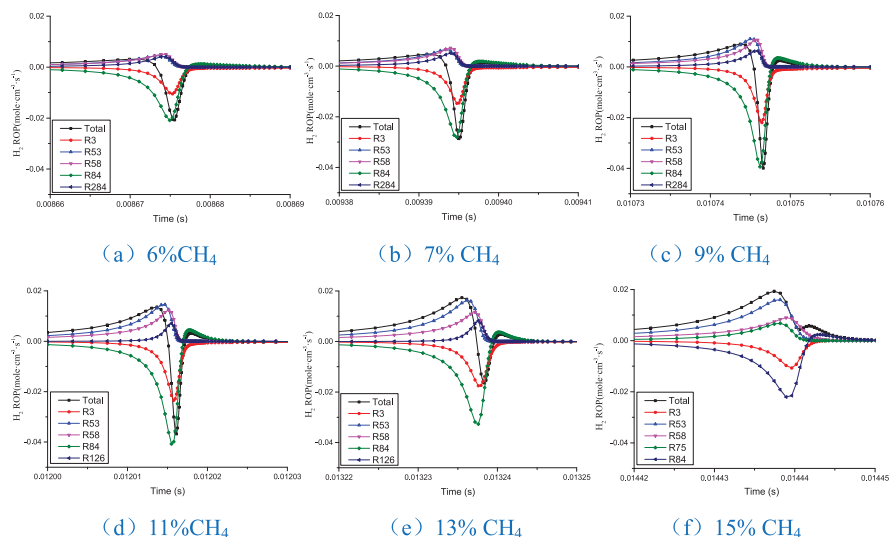


Fig. 5 Key basic element reaction step of gas explosion H_2

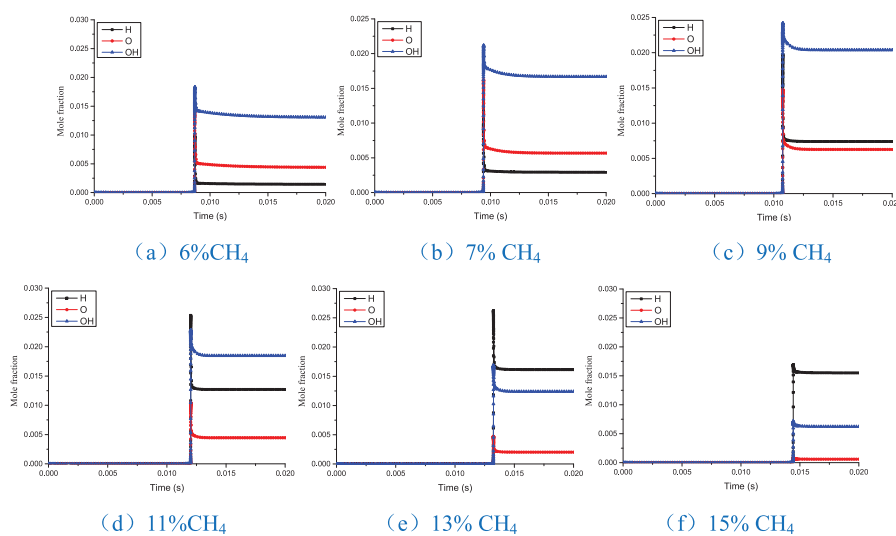


Fig. 6 Trend of free radical change in gas explosion process

environment would accelerate H_2 generation.

Through the analysis of R3, R53, R58, R84, R126, it could be known that the higher proportion of free radical H there is, the smaller proportion of free radical O and OH is, therefore, the more amount of H_2 generation is from the explosion reaction. The changes of free radical H, O and OH in different gas concentrations during methane explosion process are drawn in Figure 6.

According to Figure 6, with the increase of the concentration of gas explosion, the mole fraction of free radical O and OH increased firstly in the enclosed space, it reaches the maximum at the 9% gas concentration, and then gradually decreased. The mole fraction of free radical H gradually increased, and then decreased slightly at the 15% gas concentration, and the free radical H is gradually increasing in the overall ratio of free radical H, OH and O. It shows that the proportion of free radical H is proportional to the amount of H_2 generated during the gas explosion.

EXPERIMENTAL STUDY ON GAS EXPLOSION

The numerical simulation of gas explosion shows that the higher the concentration of gas explosion is, the more incomplete the reaction is. And the amount of H_2 generated is greater. In order to analyze the reliability of simulation, this paper makes a comparative study on the numerical simulation results by measuring the variation of the gas concentration about H_2 , CO and CO_2 in different gas concentrations.

EXPERIMENTAL DEVICE

The experimental devices are shown in Figure 7, which is mainly composed of explosion cavity, gas distribution device, ignition device, explosion control device and data acquisition device. The main body cavity is a 20L steel ball, which is composed of 3 parts, the cylinder, the top cover and the bottom cover. An observation hole is arranged on the

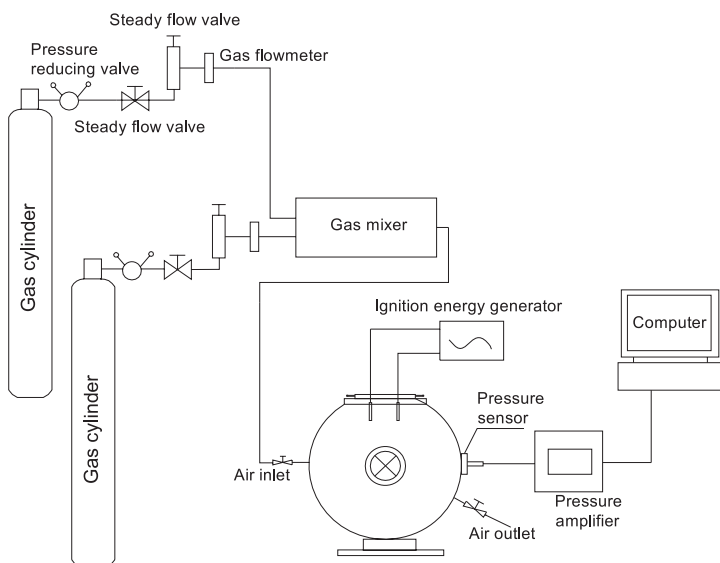


Fig. 7 The device of explosion experiment

cylinder body, and the internal gas explosion phenomenon can be observed through the observation hole. The air distribution device is mainly composed of a gas cylinder, a pressure reducing valve, a pressure stabilizing valve, a flow meter and a connecting gas path. The gas distribution are controlled the flow rate of different gases. The experiment used electric spark ignition, the ignition device can produce two kinds of strength of electric spark with energy 12J and 2J respectively. And a strong electric spark was used to carry out ignition during the experiment. Explosion control device is mainly to control the ignition energy and time, the sampling system, the system security.

EXPERIMENTAL PROCESS

Methane and air flows from the cylinder through pressure reducing valve, pressure stabilizing valve, flow valve successively into the mixing chamber in fixed air ratio. The mixed gas fills with explosive cavity, which is detonated by electric spark. The pressure generated by explosion acts on the pressure sensor inside the explosion tube and is converts to electronical pressure signal. When the pressure exceeds the original pressure by 7%, it indicates that the explosion experiment was successful. Then make analysis of gas collected through the air exhaust vent with gas chromatograph.

In order to analyze the variation of H_2 , CO_2 and CO after gas explosion at different gas volume fractions, 6 groups of gas explosion experiments were carried on with gas concentrations of 6%, 7%, 9%, 11%, 13%, 15% respectively.

EXPERIMENTAL RESULTS AND ANALYSIS

According to the results of different volume fraction in the gas explosion experiment, the change regulations of H_2 , CO and CO_2 with the variations of gas volume fraction are shown in Figure 7, and the ratio of $CO/(CO+CO_2)$ is plotted in Figure 8.

By observing Figure 7 and Figure 8, it could be seen that when the concentration of CH_4 is lower than 9%, only small amounts of CO and H_2 production is produced. The main gas products are CO_2 , so the calculation results of $CO/(CO+CO_2)$ is nearly 0, which means the gas explosion is completely reaction. When the gas concentration is higher than 9%, the volume fraction of CO_2 decreases gradually, while the amount of H_2 and CO increased rapidly, and $CO/(CO+CO_2)$ increased gradually, which shows that the degree of incomplete reaction of gas explosion is increasing gradually. The results are consistent with the trends of numerical simulation data, which shows that the formation of H_2 during gas explosion is mainly due to the incomplete reaction of gas explosion.

Through the comparison of experimental data of methane explosion generating H_2 and numerical simulation calculation data, it could be found that the results of simulation value is relatively higher. The deviation is mainly because the difference between experimental conditions and simulation conditions. In the

numerical simulation it assumed confined space as an ideal diabatic environment, and the reaction rates are the same in every location in the calculation area with no temperature gradients and concentration gradients. Therefore, the calculation of explosion process is complete reaction, resulting in the simulation data is higher compared with practical experimental

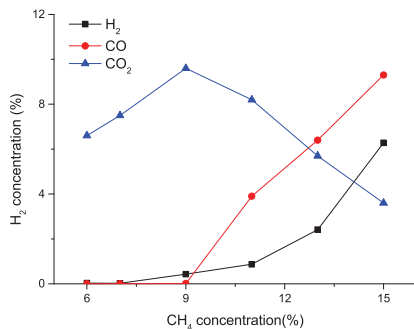


Fig. 8 Trend of gas product after gas explosion

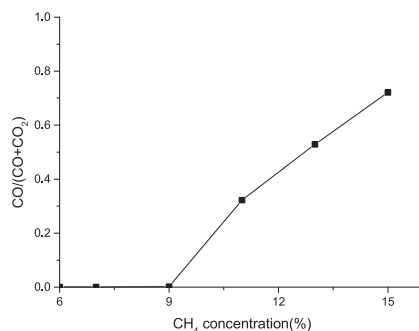


Fig. 9 change trend of CO/(CO+CO₂)

CONCLUSIONS

In this paper, the H₂ change rules and mechanism of gas explosion are firstly simulated with Chemkin, then the calculation results are verified by gas explosion experiment. The following conclusions are obtained:

- (1) R84 is the greatest impact on H₂ generation in the process of gas explosion reaction, that is, the decomposition of water vapor is the main reason for the formation of H₂. The free radical H is the key factor to accelerate the H₂ formation and free radicals OH and O are the inhibiting factors for H₂ formation. With the increase of concentration of gas explosion, the explosion reaction is more incomplete, and the proportion of free radical H increases gradually. At the same time, free radical O and OH gradually decreases, resulting in a gradual decrease in the amount of H₂ consumption and gradual increase in the amount of H₂ formation.
- (2) The experimental results of gas explosion are consistent with the changing trends of H₂, CO and CO₂ in simulation calculation. The experimental results show that the reaction of gas explosion is more sufficient when the concentration of gas explosion is lower than 9%, and the amount of H₂ generation is relatively small. When the gas concentration

is higher than 9%, the degree of incomplete reaction of gas explosion process will increase gradually, leading to the gradual increase in the amount of H₂ generation. Therefore, high concentration of H₂ is mainly caused by the incomplete reaction of high concentration of gas explosion.

REFERENCES

1. Arenillas, A., Rubiera, F., Pis, J.J. (1999). Simultaneous thermogravimetric–mass spectrometric study on the pyrolysis behavior of different rank coals. *Journal of Analytical and Applied Pyrolysis*, 50(1), 31-46.
2. Alberta Mine Safety Association. (2008). *British Columbia Mine Rescue Manual*. British Columbia: British Columbia Mining and minerals Division.
3. Yang, X.M.; Zhao, N.; Bian, Z.C.; Chai, J.Q.; Mi, C. (2015). An Intelligent Storage Determining Method for Inbound Containers in Container Terminals. *Journal of Coastal Research*, 73, 197-204.
4. Baoshan Jia, Haiyan Wen, Yuntao Liang, et al. (2013). Mechanism characteristics of CO₂ and N₂ inhibiting methane explosions in coal mine roadways. *Journal of China Coal Society*, 38(03), 361-366.
5. Deng, J., Xiao, Y., Li, Q., Lu, J., & Wen, H. (2015). Experimental studies of spontaneous combustion and anaerobic cooling of coal. *Fuel*, 157, 261-269.
6. Fubao Z, Jinhai L I, Yusheng L I U, et al. (2010). Rules of variation in hydrogen during reignition of underground fire zones of spontaneous coal combustion. *Mining Science and Technology (China)*, 20(4), 499-503.
7. Gregory P. Smith, David M. Golden, Michael Frenklach, Nigel W. Moriarty, Boris Eiteneer, Mikhail Goldenberg, C. Thomas Bowman, Ronald K. Hanson, Soonho Song, William C. Gardiner, Jr., Vitali V. Lissianski, and Zhiwei Qin http://www.me.berkeley.edu/gri_mech/, accessed April 20, 2016.
8. Grossman, S. L., Davidi, S., Wegener, I., et al. (1996). Explosion risks of bituminous coals in contact with air: Due to molecular hydrogen accumulation in confined spaces (underground mines and ships holds): A hypothesis study. *Erdöl, Erdgas, Kohle*, 112(7-8), 322-324.
9. Handong Liang. (2001). Correlation of outburst events of coal and gas with natural hydrogen gas from coal. *Journal of China Coal Society*, 26(6), 637-642.
10. Jia Yingmei, Liu Zhentang, Wang Congyin, et al. (2009). Experimental Study on Gas Composition After Gas Explosion. *Coal Technology*, 28(12), 78-81.

11. Kim, A. G. (2004). Locating fires in abandoned underground coal mines. *International Journal of Coal Geology*, 59(1), 49-62.
12. Lianhua Dong. (1991). *The character of harmful gas and monitoring technology*. Shenyang: Northeast institute of technology press
13. Lingqi, Z., Xinquan, Z., & Jianguo, X. (2008). Analysis of indicator gas of spontaneous combustion and its optimal selection. *Journal of Mining & Safety Engineering*, 25(4), 440-443.
14. Na Gao, Yansong Zhang, Yiting Hu, et al. (2014). Dynamics analysis of gas explosion chain reaction in restricted space. *China Safety Science Journal*, 24(1), 60. 69-75.
15. Nehemia, V., Davidi, S., Cohen, H. (1999). Emission of hydrogen gas from weathered steam coal piles via formaldehyde as a precursor: I. Oxidative decomposition of formaldehyde catalyzed by coal-batch reactor studies. *Fuel*, 78(7), 775-780.
16. Peng Wei, He Qilin, Ge Xinyu. (2010). Experimental studies on the index gases of spontaneous of coal. *Journal of Safety Science and Technology*, 6(6), 140-144.
17. Shao H, Fubao Z, Kaiyan C, et al. (2014). Study on the Hydrogen Generation Rules of Coal Oxidation at Low Temperature. *Journal of Engineering Science & Technology Review*, 7(3), 499-503.
18. Singh, A. K., Singh, R. V. K., Singh, M. P., Chandra, H., & Shukla, N. K. (2007). Mine fire gas indices and their application to Indian underground coal mine fires. *International Journal of coal geology*, 69(3), 192-204.
19. Xiangchun Li, Baisheng Nie, Chunli Yang, et al. (2016). Effect of gas concentration on disastrous gases produced by gas explosion in confined space. *China Safety Science Journal*, 26(1), 69-75.
20. Xinquan Zhou. (2013). Proposals on Improvement of Spontaneous Combustion Prevention and Control in Mining Goaf and Emergency Handling Capacity. *Coal Science and Technology*. 41(9), 151-153.
21. Xinquan Zhou., Bing Wu. (1996). *Theory of mine fire rescues and applications*. Beijing: Coal Mining Industry Press.
22. Yuntao Liang, Wen Zeng. (2009). Kinetic simulation of gas explosion and inhibition mechanism in enclosed space. *CIESC Journal*. 60(7), 1700-1706.

CONTACT WITH THE AUTHOR

Baiwei Lei

leibws@163.com

Faculty of Resources and Safety Engineering
China University of Mining & Technology (Beijing)
Beijing 10083
CHINA

SIMULATION ON VESSEL INTELLIGENT COLLISION AVOIDANCE BASED ON ARTIFICIAL FISH SWARM ALGORITHM

Weifeng LI

Wenyao MA

Navigation College, Dalian Maritime University, Dalian 116026, China

ABSTRACT

As the rapid development of the ship equipments and navigation technology, vessel intelligent collision avoidance theory was researched world widely. Meantime, more and more ship intelligent collision avoidance products are put into use. It not only makes the ship much safer, but also lighten the officers work intensity and improve the ship's economy. The paper based on the International Regulation for Preventing Collision at sea and ship domain theories, with the ship proceeding distance when collision avoidance as the objective function, through the artificial fish swarm algorithm to optimize the collision avoidance path, and finally simulates overtaking situation, crossing situation and head-on situation three classic meeting situation of ships on the sea by VC++ computer language. Calculation and simulation results are basically consistent with the actual situation which certifies that its validity.

Keywords: simulation; collision avoidance; artificial fish swarm algorithm

INTRODUCTION

According to the survey, more than 80% of ship's collision accidents are related to human factors. There are two ways to solve the human factor. First, strengthen the skills of training and management abilities of ship's crew which will improve their quality. Second, implementing the automatic navigation and improving the automatic level of decision-making which can avoid errors caused by the judgment of human. As the development of technology, bridge resources provide more and more navigational information. If crews are not fully trained, a lot of navigational information may cause them to make incorrect judgments and decisions. And if crews make the wrong decision, it may lead to huge losses. Therefore, an effective method to reduce the human factor is to use high

technology to improve the automatic level of navigation, which will reduce the crew's subjective judgment as well as the burden of the officer on the watch (OOW). Thus, the research on automatic collision avoidance decision system has practical significance for the safety of the ship.

Although automatic radar plotting aids (ARPA) can solve parts of problem about information processing of ship collision avoidance. It is not a fully automatic collision avoidance system. The OOW use it based on their subjective judgment of the experience and professional skills. Electronic Chart Display and Information System (ECDIS) can obtain navigational information and exchange the data and information by connecting other nautical navigation devices such as GPS (Global Position System), AIS (Automatic Identification

System), radar, compass, log, VDR (Voyage Data Recorder), which is becoming a new type of ship navigation system and decision support system, namely ship navigation information system, and it gradually becomes the information core of the ship bridge. Ship collision avoidance strategy is a complex decision-making process, which includes sailing data collection, data preprocessing, division of vessel meeting situation, calculation of collision risk degree, selection method of collision avoidance, and the optimization of collision avoidance (Bai Yiming, 2012). Therefore, it is very difficult to describe ship collision avoidance with the precise mathematical model. Even with a very precise mathematical model, it is impossible to require real-time collision avoidance decision environment. Therefore, in recent years, scholars have begun to bring artificial intelligence methods such as artificial neural networks, fuzzy logic, genetic algorithms, ant colony algorithm in the field of ship collision avoidance (Lee S.M, 2004).

As the ship collision avoidance decision is a nonlinear problem with multiple indexes. It pursues not only the safety but also economic consumption. This study uses artificial fish swarm mixture optimization algorithm which different from the mathematical model. The algorithm imitates fish's forage, clusters rear-ends behavior and searches for the optimal solution. The algorithm can be used to solve highly complex engineering problems. Therefore it is suitable to ship collision avoidance route planning. Combining the international regulations for prevention collisions at sea (COLREGs 1972) and the safety domain of a ship, the algorithm can be used to get the most recommended ship collision avoidance path. This study combines ECDIS platform and forms the ship automatic collision avoidance decision support system which provides automatic route monitoring, collision warning and collision avoidance decision support prompts.

SHIP DOMAIN AND MEETING SITUATION DIVISION

Ship domain is an effective regional areas surrounding the ships which other ships and stationary targets should keep outside, and it is required waters to maintain safe navigation of any ship. Ship domain is an important concept of maritime traffic engineering, which widely used in ship collision avoidance and risk assessment. Fujii, Goodwin and Wu Zhaolin studies on the ship domain details (Fujii Y, 1971). In this paper, the collision avoidance decision supporting system requires that the target ship need to pass out of the ship domain.

According to the COLREGS, meeting situations can be divided into three types:

- (i) Head-on situation: Target vessel approaches from Figure 1 F area. Own ship and target ship are meeting on reciprocal or nearly reciprocal courses so as to involve risk of collision and each shall alter her course to starboard so that each shall pass on the port side of the other.
- (ii) Crossing situation: Target ship approaches from Figure 1 A, B, E area. Own ship and target ship are crossing so as to involve risk of collision, the vessel

which has the other on her starboard side shall keep out of the way.

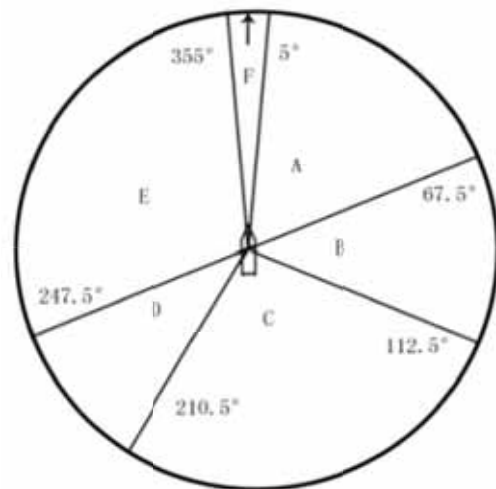


Fig 1. Division for ship meeting situation

- (iii) Overtaking situation: Target ship approaches from Figure 1 C, D area. The ship shall be deemed to be overtaking when coming up with another ship from a direction more than 22.5 degrees abaft her beam. Overtaking vessel shall keep out of the way of the vessel being overtaken.

MODELING OF COLLISION AVOIDANCE ROUTE PLANNING SYSTEM

When two vessels are meeting, and the own vessel and the target vessel keep their original course and speed. When the target ship goes into the observation distance (observation information of the target vessel comes from own ship's AIS equipment), the direction of relative movement, distance to closet point of approach (DCPA) and time to closet point of approach (TCPA) will be got. The COLREGS established a knowledge guidance, which can be used to determine which meeting situation is forming between own ship and the target ship, and which ship is the give way vessel. If risk of collision exists and own ship is the give-way vessel, the study of decision supporting system will provide a collision avoidance route planning and recommend a safe and economical route. In fact, the route may not be the most feasible route, but the system theoretically can guarantee a safe and economical recommended route at least, which will contribute to early warning and decision supporting. Therefore, the OOW can use this route as a reference for the use of collision avoidance scheme.

According to the different mission phases, avoidance route is divided into three phases:

- (i) Warning stage.

When the target ship goes into the observation and tracking phase, it needs to determine the meeting situation of the own ship and the target ship. It needs to determine whether risk of collision exists according to the target vessel's DCPA, if it

less than the safety domain of own vessel, risk of collision exists. If the risk of collision exists and the own ship is give-way vessel, collision avoidance route planning algorithm will work. This stage, the algorithm will give the latest turning point of collision avoidance and maintain the original course and speed sailing sustainable time. The OOW can serve as a reference for the drawing up collision avoidance decisions.

(ii) Collision avoidance stage.

After steering for some time, the vessel sails into the stage of collision avoidance stage. The vessel altering course action should not be too small, otherwise, it's intention would be not easy to be found. If the altering course action is too large, it will result in the own vessel deviates too far from the original route. However, this angle must ensure that the target ship passes out of the security area of the own ship.

(iii) Course recovery stage.

The time to recovery her original course and the altering course angle should guarantee that two vessels will not form a new hazardous situation in the course recovery stage.

COLLISION AVOIDANCE ROUTE PLANNING BASED ON ARTIFICIAL FISH SWARM ALGORITHM

THE PRINCIPLE OF ARTIFICIAL FISH SWARM ALGORITHM

The principle of artificial fish swarm algorithm is to simulate natural fish's forage, clusters, rear-ends behavior and mutual assistance between fish to achieve global optimization (Ming-Cheng Tsou, 2010). Artificial fish foraging behavior is the random walk based on the current value of their adaptation, it is an individual extreme optimization process and self-learning process. The fish's clusters and rear-end behavior is the interaction with the surrounding environment. The conduct of algorithm is self-adaption process for artificial fish, the process includes fish's forage, clusters and rear-ends behavior, and the optimal projection emerges in the process. Thus, artificial fish swarm algorithm is a kind of optimization method based on swarm intelligence. The optimization process of artificial fish makes full use of their information and environmental information to adjust its search direction, and ultimately searches to the highest places of food concentration, namely the global extreme value.

Therefore, artificial fish swarm algorithm is an effective global optimization intelligent algorithm, which has a unique and superior performance compared with other traditional optimization methods for some complex optimization problems.

ARTIFICIAL FISH INDIVIDUAL CODING SCHEME

There are four parameters of collision avoidance system should be encoded.

(i) The time from current position to the position of turning point to avoid collision, T_s : altering course must be carried out within the T_s . The altering course action must be executed

at least when the ship is at turning point, otherwise the risk of collision exists.

(ii) The minimum altering course angle ΔC_o , which indicates that the ship can pass with a safe distance with the target ship when altering this angle. The actual altering angle should be not less than ΔC_o ; otherwise the risk of collision exists.

(iii) The time from taking altering course action to her original course recovered, T_a . This parameter indicates that the ship must navigate with T_a minutes before her original course recovered.

(iv) Course changing amount when the ship taking action to her original course, ΔC_b . It is the maximum angle the ship needs to change when taking action to come back to her original course.

Four variables of collision avoidance route optimization decision corresponds to the artificial fish individual $\theta_i = [T_s, \Delta C_o, T_a, \Delta C_b]$.

THE OBJECTIVE FUNCTIONS

The distance from the point the ship is taking action to avoid collision to the point the ship's course recovered, which can be used to assess the route planning. Therefore, it can be used as the objective function. The paper tries to get the shortest path to avoid collision with artificial fish optimization algorithm and makes the following constrains.

(i) Collision avoidance distance should be minimal;

(ii) Risk of collision should be minimal and, own ship and target ship should pass at a safe distance;

(iii) The altering course angle should be minimal;

(iv) The track should be minimal during the circuitous voyage when the ship is taking collision avoidance action;

(v) The course changing amount should be minimal if there is no other new meeting situation or urgent situation.

Assuming that the target vessel course C_t , speed V_t , relative to the own vessel's position Q, distance d , the own vessel course C_o , speed V_o , and after avoiding collision action the new course C'_o , then the objective function is:

$$J = \min \{d_s + d_r\} \quad (1)$$

d_s is the own vessel steering distance during the collision avoidance, d_r is the own vessel steering distance during the the process of ship's course recovered.

$$d_s = T_a \cdot V_o \quad (2)$$

$$d_r = T_a \cdot V_o \cdot \frac{\sin C'_o}{|\sin C'_b|} \quad (3)$$

C_o is course changing amount when collision avoidance. C_b is course changing amount when the ship is coming back to her original course. T_a is the time from taking altering course action to her original course recovered. The constraint condition is shown as function(4).

$$\begin{cases} 30 \leq C'_o \leq 90 \\ -60 \leq C_b \leq -30 \\ T_{CPA1} \leq T_a \leq 60 \\ (d_{CPA1} \leq d_G) \text{ and } (d_{CPA2} \geq d_G) \end{cases} \quad (4)$$

C'_o is course changing amount when collision avoidance, positive values indicate right turn; C_b is course changing amount when the ship is coming back to her original course, negative values indicate the left turn; T_a should not exceed 60 minutes and must be at least more than the time of encountering T_{CPA1} (the new recent time after collision avoidance action); d_{CPA1} and d_{CPA2} are distance to closet point of approach after collision avoidance and recovery of her original course.

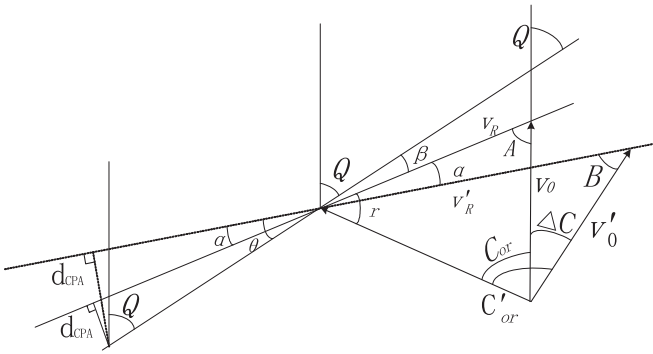


Fig.3 Collision avoidance decision modal after the home ship is turned

d_{CPA} is distance to the closest point of approach and T_{CPA} is time to closest point of approach are key factors meeting the objective function limiting conditions, which can be calculated according to the literature mentioned methods. Figure 3, $new d_{CPA1}$ and T_{CPA1} can be calculated in the following method after the preventing collision and steering:

$$\begin{cases} d_{CPA1} = d * \sin \theta \\ T_{CPA1} = d * \cos \theta / V'_R \end{cases} \quad (5)$$

θ is the angle between the relative motion line of the own vessel and the bearing line of the target vessel; d is the distance between the own vessel and the target vessel; B is the angle between the relative motion line of own vessel and the route of the own vessel after taking collision avoidance action; C_{OT} is the angle between the own vessel and the target vessel after steering; V'_R is the relative velocity of the own vessel after steering.

$$C'_{OT} = C'_o - C_T \quad (6)$$

$$V'_R = \sqrt{V_T^2 + V_o^2 - 2 * V_T V_o \cos C'_{OT}} \quad (7)$$

if $C'_{OT} \geq 0^\circ$, $\theta = B + C'_o - Q$;

$$B = \cos \left(\left(V_o^2 + V_R^2 - V_T^2 \right) / 2 V_o V'_R \right) \quad (8)$$

if $C'_{OT} \leq 0^\circ$ $\theta = -(B + C'_o - Q)$;

$$B = -\cos \left(\left(V_o^2 + V_R^2 - V_T^2 \right) / 2 V_o V'_R \right) \quad (9)$$

d_G is radius of safe passing circle; and the new d_{CPA} should be more than the radius at least. The value depends on the maritime traffic environment and ship type.

SIMULATION STEPS

Step 1. Initialization of groups. Randomly generated N artificial fish individuals in the variable feasible region, and got the initial fishes. Setting artificial fish visual field $Visual$, the maximum moving step length $step$, crowding factor δ , the biggest temptation for each mobile number $trynumber$. Setting the iteration number of initial bulletin board optimal state of not changing or little changing of optimal artificial fish state $Beststep=0$, the initial iteration $Num=0$.

Step 2. Initialization of bulletin board. Calculate the initial fish each artificial fish the objective function value and compare the size of it, whichever is the optimal state and its value is assigned to the artificial fish bulletin board.

Step 3. Behavior selection. Simulate rear-end behavior and swarming behavior for each artificial fish, choose the best behavior and perform by comparing the value of the objective function, the default behavior is foraging behavior.

Step 4. Update Bulletin Board. Each artificial fish compares their own function value and bulletin board value, if their own function value is better bulletin board value, bulletin board value is replaced, otherwise the value of the bulletin board is unchanged.

Step 5. Introduce genetic algorithm to conditional judgement. If $Beststep$ has reached the preset consecutive not changing the maximum threshold $Maxbest$, genetic algorithm crossover and mutation algorithm of Step 6 is executed, otherwise, go to Step 7.

Step 6. The operation of genetic algorithm crossover and mutation. all other artificial fish do these operation except the best individual bulletin board: ① crossover: Randomly select a number of individual fish from artificial fish based crossover probability P_c , divide into group and execute the operation of crossover for two individual fish. Compare function calculated of new individual fish formed to the optimal value of the bulletin board, if it is better than the bulletin board's value, the bulletin board's value is replaced, and the new instance replace the old individuals. ② mutation: Randomly select a number of individual fish based on the mutation probability P_m , execute the operation of the mutation of these individuals. Calculate function value of newly formed artificial fish, and in comparison with the optimal value of bulletin board, if it is better than the value of the bulletin board, then it replaces the value of the bulletin board. ③ set $Beststep=0$.

Step 7. Terminate conditional judgment. Repeat steps Step 3-6 until the optimal solution to achieve the bulletin board's satisfactory error bounds.

Step 8. Terminate the algorithm. Output the optimal solution (artificial fish bulletin board's status and its function values).

SIMULATION RESULT

The algorithm decision supporting system settings and results are shown in Figure 4. Ship's dynamic information is from the AIS, and the vessel speed is 14kn, initial course is 000° , and course changing can be performed only when to avoid collision. Target vessel speed is 15kn. Vessel's collision avoidance can be divided into head-on situation, overtaking situation and crossing situation according to the COLREGs. Simulating the algorithm by following three typical cases:

- (I) The own vessel is crossing encountering with right frontage of the target vessel.
- (II) The own vessel is crossing encountering with right rear of the target vessel.
- (III) Head-on situation.

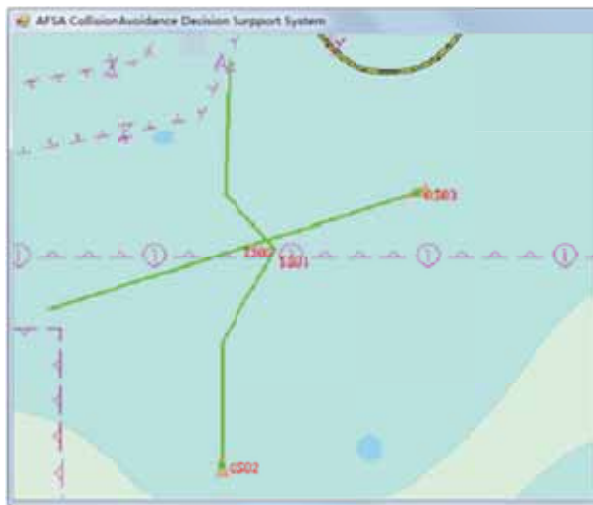


Fig 4. Decision supporting system for collision avoidance route planning

Table 1 shows the simulation results and route planning data above three cases by artificial fish swarm algorithm. d_{CPA} is the distance to closet point of approach and t_{CPA} is time to closet point of approach in initial state. In this table, $d_{CPA} > 0$, the target vessel passes by the bow of the own vessel; $d_{CPA} < 0$, the target vessel passes by the stern of the own vessel. T_1 is time to turning point, which means that the moment of reaching T_1 begins to steer from the observed moment calculated, C_1 is steering angle to the right avoiding collision, it is limited $[30,60]$ within the range, if the angle is less than C_1 , then the risk of collision exists. T_2 represents that the vessel should sail T_2 minutes with new course after avoiding collision and steering. In order to ensure the safe passage of the target vessel; C_2 represents the altering course angle to recovery her original course, if the altering course angle is too large, it may cause a

Tab.1. Parameters of collision avoidance of AFSA

$C_T(^{\circ})$	d_{CPA} (nm)	t_{CPA} (min)	T1	C1	T2	C2	Q($^{\circ}$)	d(nm)	d_s (nm)
246	0.74	73	67	47	13	-46	41	28	5.85
286	-0.22	80	61	53	15	-55	80	23	6.78
190	0.42	66	52	45	13	-37	2	33	6.32

new risk of danger with the other vessels in the vicinity.

The simulation suggests that the improved artificial fish swarm algorithm can give the optimal collision avoidance route, which is both safe and economy. When connecting with ECDIS, collision avoidance parameters can be dynamically displayed in the ECDIS platform, which can provide decision supporting to avoid collision and can effectively reduce the burden of the OOW and improve the safety of traffic on the sea.

CONCLUSION

The study combines safety domain of ship and the COLREGs, adopts artificial fish optimization model to optimize the key parameters of collision avoidance decision model and forms a collision avoidance decision supporting system, which can quickly provide the OOW a safe and economical collision avoidance route. Although the study uses the instance of the single target vessel avoidance as a demonstration, the decision optimization algorithm is suitable for multi-target vessel avoidance situations. Once the system connects with the bridge navigational equipment and ECDIS, it will provide some security and support for collision avoidance at sea and VTS monitoring waters.

ACKNOWLEDGEMENTS

This work was financially supported by the Fundamental Research Funds for the Central Universities with number of 3132015009.

REFERENCE

1. Lee, S.M., Kwon, K. Y. and Joh, J. A fuzzy logic for autonomous navigation of marine vehicles satisfying COLREG guidelines[J]. International Journal of Control Automation And Systems, (2004).2, 171-181.
2. Egil Pedersen and Kinzo Inoue. Simulator Studies on a Collision Avoidance Display that Facilitates Efficient and Precise Assessment of Evasive Manoeuvres in Congested Waterways[J]. Journal of Navigation.2003(56):411-427.
3. Ming-Cheng Tsou, Sheng-Long Kao, Chien-Min Su. Decision Support from Genetic Algorithms for Ship Collision Avoidance Route Planning and Alerts[J]. Journal of Navigation, 2010, 63(1), 1-16.
4. Ming-Cheng Tsou, Chao-Kuang Hsueh. The Study of Ship Collision Avoidance Route Planning by Ant Colony Algorithm. Journal of Marine Science and Technology,

2010,18(5):746-756.

5. Rafal Szlapczynski. A Unified Measure Of Collision Risk Derived From The Concept Of A Ship Domain[J]. Journal of Navigation.2006(59):477-490.
6. Jang San, Je Yefei, Dasgupta S. Artificial Fish Swarm Algorithm for Solving Road Network Equilibrium Traffic Assignment Problem [J]. Journal of computer emulation,2011,28(6): 326-329.
7. Pedersen.E, Inoue .K, Masanori. T. Simulator Studies on a Collision Avoidance Display that Facilitates Efficient and Precise Assessment of Evasive Manoeuvres in Congested Waterways [J]. The Royal Institute of Navigation (2003). 411-427.
8. Bi Xiuying, Jia Chuanying, Wu ZhaoLin. Opportunity and Actions Taken of Ship's changing speed collision avoidance. Journal of Dalian Maritime University, 2003, 29(1):9-12.
9. Liu Dexin, Wu ZhaoLin and Jia ChuanYing. Decision Making Model of DCPA, TCPA and Object's Movement Parameter . Journal of Dalian Maritime University, 2004, 30(1), 22-25.
10. Zhao Yuelin. Ships collision avoidance and watch keeping[M].Dalian Maritime University,2012.
11. Gemeinder M, Gerke M. GA-Based Path Planning for Mobile Robot System Employing an Active Search Algorithm [J]. Applied Soft Computing, 2003,(3):149-158.

CONTACT WITH THE AUTHOR

Weifeng LI

sddmlwf@163.com

Navigation College
Dalian Maritime University
Dalian 116026
CHINA

AN ANTI-COLLISION METHOD OF SLIP BARREL FOR AUTOMATIC SHIP LOADING IN BULK TERMINAL

SHEN Yang

Higher Technical College, Shanghai Maritime University, Shanghai, China

ABSTRACT

During the loading operation of a ship loader in bulk terminal, in order to bring bulk cargo, such as coal and ore, precisely into every corner of the cabin and not to raise dust at the same time, the slip barrel mechanism usually is placed fully inside the ship cabin near the cargo as close as possible. However, if too close, it will increase the risk of collision between slip barrel and cargo, which poses a security risk to loading operation.

This article proposes an anti-collision method for slip barrel in the process of automatic ship loading in bulk terminal. This method can accurately position the cargo of cabin which is blocked by slip barrel and shovel, and provide a reliable guarantee for the automatic loading operation. Firstly, this method use an array of laser radar mounted on the maintenance platforms to perceive the collision objects around the slip barrel, including the cargo and cabin. Meanwhile, it provides a compensation algorithm to reduce the effect of anti-collision recognition brought by dust and various obstacles during the operation. According to the calculated effective distance between the cargo and slip barrel, the automatic control system of ship loading can adjust the loading operation on a real-time basis. In the end, this article analyze and illustrate the reliability and validity of this method by the case of the application in automatic ship loading system in Tianjin coal terminal.

Keywords: Automatic Ship Loading, Bulk Terminal, Anti-Collision, Slip Barrel

INTRODUCTION

In recent years, with the development of information technology and automation equipment or technology, they are widely used in the field of ports. A number of automated and intelligent terminals have been built in succession in the world [1][2]. In the next few decades, it is foreseeable that in order to improve their competitiveness in the related business, automation will not only be preferred at the planning stage for new terminals, but for the existing terminals [3]. These terminal will complete the automatic transformation of the machinery equipment to meet today's increasingly high labor costs and increasingly complex loading and unloading requirements [4].

Among the existing automated terminals, container

terminals account for a large majority while the number of automated bulk terminals are relatively small [5][6][7]. This is mainly due to the continuity of the cargo transport, the randomness of the form of cargo and the poor operating environment. These factors have brought serious challenges to the automatic operation of bulk terminals. Regardless of the shape of cargo perception, the precise control of real-time decision-making and the equipment, automated bulk terminals are made to extremely high requirements [8].

As the main working machine of the bulk terminal, the automation degree of the ship loader directly represents the automatic level of the whole terminal. When operating, the factors, such as the structure of the ship loader, the shape of bulk ship, the orientation of the hatch cover, the size of the

cabin, the type and form of the cargo, dust and pitch angle, will affect the safety and efficiency of the automatic loading operation [9][10][11]. But among all these factors, the real direct one is slip barrel mechanism. So How to reduce the possibility of collision with ship or cargo is the point of research. In some previous studies, some anti-collision protection methods during the period of the port machinery operation have been proposed. Mi Chao et al. has devised an algorithm for ship identification in the automated process of loading operation which not only can be used to detect the edge of the cabin in order to achieve partly anti-collision effects, but also can automatically generate slip barrel position of the ship loading process based on the size of the cabin [12]. Gang Zhou introduced a method of Distance and velocity measurements in automobile anti-collision application [13]. This method use millimeter-wave radar to realize automobile anti-collision in highway. Frederic Maire proposed an anti-collision system based on vision [14]. The system can solve the specific problems of the reflectance of rails and allow the creation of a completely self-calibrating system

In the above studies, how to position the cargo of the cabin is not directly involved. And some research methods are not suitable for the identification of the cargo in the bulk terminals, especially those in the harbor bulk terminals. As for the large ship loader, the shovel connecting with the slip barrel and the thrown cargo occlude various detection sensors installed around the slip barrel. And then the sensors will fail to identify the heap area just below slip barrel, so that the scanning shape of the cargo is not complete, because the top of it is missing.

Consequently, this article proposes an anti-collision method for slip barrel in the process of automatic loading in bulk terminal. This method gets the point cloud data of the cargo in the cabin with laser radar arrays and reconstructs the missing surface contour because of the shielding caused by the throwing shovel and the thrown material. Then it restores the complete cargo contour by means of the compensation algorithm, so that it can position and identify the height of the cargo. The automatic control system of the ship loader can adjust the safe distance between cargo and slip barrel in order to operate safely[15].

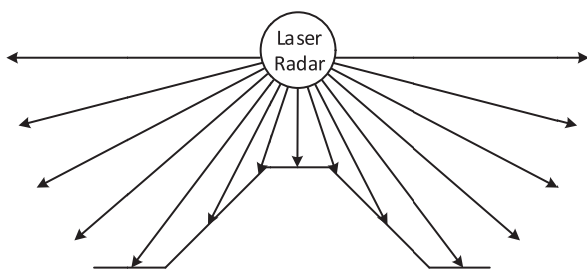


Fig.1 Diagram of LMS scanning

PROBLEM DESCRIPTION

LASER MEASUREMENT SYSTEM

LMS is a laser-based multi-angle distance scanner. As shown in Figure 1, the LMS can send and receive the laser in each 0.25 degree. An optical monitor section is made by those lasers. In the optical monitoring section, any target that the laser cannot pass through will be detected. The distance and the sectional plane shape of the target can also be computed by LMS .

As shown in Figure 2, LMSs are installed on the maintenance platform connected the barrel of the ship loader. Those LMSs are grouped a scanning array which can scan the cargo below them at any direction. Because of the shovel and the tossing bulk cargo, the LMS array can only detect the cargo that is not shaded. Figure 3 is the sectional schematic diagram of LMS scanning cargo. In this figure, the center vertical line is center line of slip barrel and the horizontal line above bulk cargo is shovel.



Fig.2 LMSs installed on the ship loader in Tianjin Port

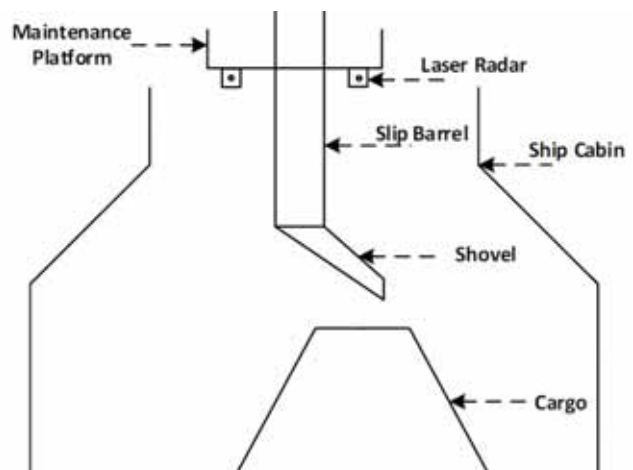


Fig.3 Schematic diagram of LMS scanning cargo

PROBLEM DESCRIPTION

As shown in Figure 4, the edges of the hold, the cargo inside hold and the shovel are all scanned by the LMS. It is

obvious that the bulk cargo surface curve is broken for the shovel blocks the laser beam from the LMS. If there is no anything that blocks the laser beam, the curve of the cargo surface should be unbroken. The bulk cargo is tossed from the shovel into the hold, so the point of falling bulk cargo is shaded by the shovel. The point of the falling bulk cargo is also the highest point of the cargo inside the hold which is the key point for the automatic ship loader. This paper mainly discusses how to rebuild the broken cargo surface curve and compute the highest point of the cargo.

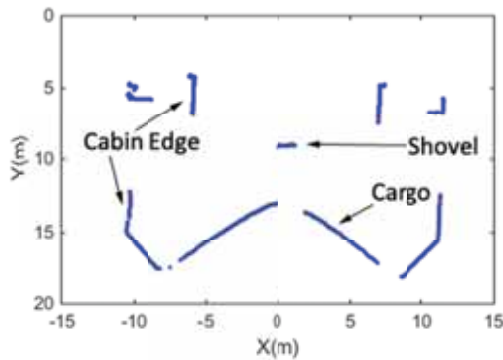


Fig. 4 Scanning result of the LMS

APPROACH FOR BULK CARGO HEIGHT DETECTION

IMAGE PREPROCESSING

In the sectional plane generated by LMSs shown in Figure 4, an image preprocess should be used to remove the edges of the cargo hold. Reference 16 shows a method to inspect the edges of the cargo hold. Then, as shown in Figure 5, the edges in the original image are removed. Only the cargo and shovel information is kept.

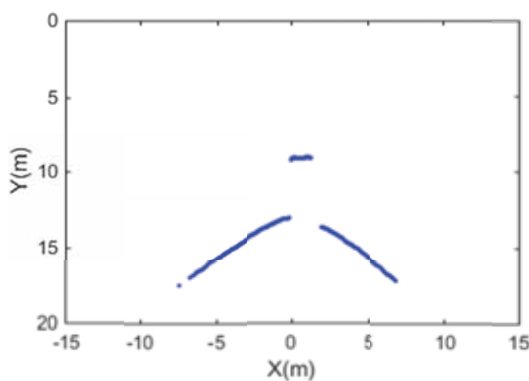


Fig.5 Scanning result after preprocessing

After removing the point cloud of edges of the cargo hold, the point cloud of image should be rasterized for increasing the efficiency of project algorithm and ensuring fast calculation in the automation controller of the ship loader [17, 18]. Therefore, the set of point cloud would be Rasterized.

$$P_{grid}(X, Y) = \begin{cases} 1 & (\exists P_{cloud}(x, y), st. x/D \in [X, X + 1), y/D \in [Y, Y + 1)) \\ 0 & (\nexists P_{cloud}(x, y), st. x/D \in [X, X + 1), y/D \in [Y, Y + 1)) \end{cases} \quad (1)$$

Rasterizing process is shown in Equation 1. Assumed that set $P_{cloud}(x, y)$ represents the original point cloud edge after removing the hold, where x, y denote the horizontal coordinate and vertical coordinate in Cartesian coordinate. The set $P_{grid}(X, Y)$ is the results after set $P_{cloud}(x, y)$ is rasterized, where X, Y represents horizontal coordinate and vertical coordinate in the binary image. D represent the length and width of each grid, the smaller grid size is, the more accurate the project algorithm is, but the greater calculate complex is. When a grid exist one or more points $P_{cloud}(x, y)$, the horizontal and vertical coordinates of $P_{cloud}(x, y)$ is in the interval $[X, X + 1)$ and $[Y, Y + 1)$, the grid can be assigned to the value '1'. According to the analysis of LMS parameters and ship hold size, 0.1m is a suitable value of D . Image rasterization is shown in Figure 6 .

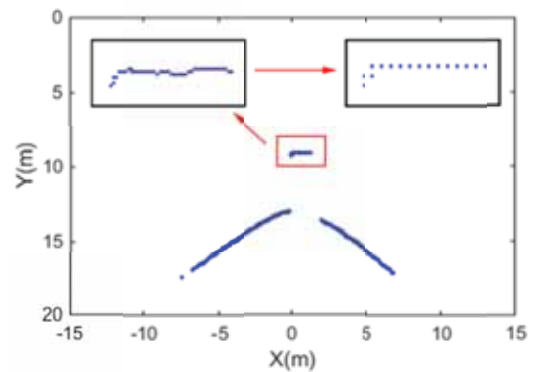


Fig.6 Image rasterization

SHOVEL RECOGNITION

According to the mechanical relationship between the LMS array and the shovel, the shovel sectional curve in the scanning result should be a short horizontal line. And the shovel curve is always higher than the cargo inside the hold, so there should be a chasm between the shovel curve and the cargo sectional curve. Based on the two distinguishing features, the shovel curve can be separated from the preprocessing image.

The shovel sectional curve is a short horizontal line while the cargo sectional curve is a short oblique line. Therefore, a project algorithm is used to locate the shovel position in the image.

$$\begin{cases} C(Y_1) = Count(\{P_{grid}(X, Y_1) | P_{grid}(X, Y_1) = 1\}) \\ \vdots \\ C(Y_{n-1}) = Count(\{P_{grid}(X, Y_{n-1}) | P_{grid}(X, Y_{n-1}) = 1\}) \\ C(Y_n) = Count(\{P_{grid}(X, Y_n) | P_{grid}(X, Y_n) = 1\}) \\ Y_n - Y_{n-1} = 1 \end{cases} \quad (2)$$

Each grid whose value is 1 in image $P_{grid}(X, Y)$ is projected onto the y-axis, and counts the number of grid of each line. As shown in Equation 2, Y_n represents the vertical coordinate where grid is n while symbol $C(Y_n)$ represents the statistical value of grid's count in vertical coordinate Y_n .

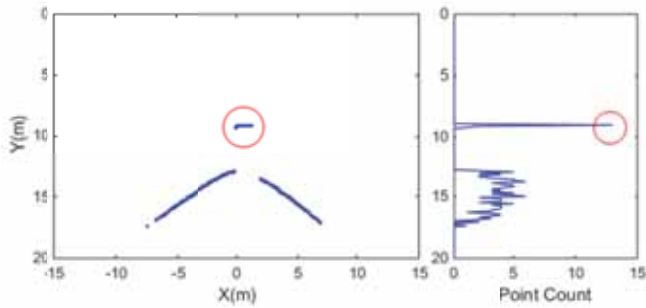


Fig.7 Y-axis projection

As shown in Figure 7, the left image is original binary image coordinate system, the right one is projected coordinate system. In the projected coordinate system, the shovel y-axis interval is different from the cargo y-axis interval and they are discontinuous (if they are continuous, that means the shovel location and cargo location is very close. This situation is not allowed in the process of normal operations because of safety). Therefore, it can be concluded that shovel location in a projected coordinate system is in the first continuous interval R_1 .

Assumed that an interval $R = [Y_{begin}, Y_{end}]$ exists in y-axis of a projected coordinate system, it must satisfy Equation 3, all statistical value within the interval is greater than or equal to the threshold T, and the statistical value of the y-axis coordinates $Y_{begin} - 1$ or $Y_{end} + 1$ is less than the threshold T. If the interval R satisfies Equation 3, it can be defined as a continuous interval in y-axis of a projected coordinate system. Through analyzing a large number of experimental data, the value of threshold T is set to 1.

$$\begin{cases} C(Y \in [Y_{begin}, Y_{end}]) \geq T \\ C(Y = Y_{begin} - 1 \text{ or } Y_{end} + 1) < T \end{cases} \quad (3)$$

After finding out the first continuous interval R_1 , we need to find vertical coordinate of the most obvious shovel characteristics where there is the maximum statistical value. As shown in Figure 7, the place of the most obvious shovel characteristics is marked by a red circle. Therefore, by Equation 4, vertical coordinate Y_{shovel} of shovel can easily be got in a projected coordinate system.

$$C(Y_{shovel}) = \max_{Y \in R_1} C(Y) \quad (4)$$

After obtaining vertical coordinate of shovel in a projected coordinate system, we need to remove all feature points which belong to shovel in the binary image for preventing bad impact on cargo height detection. Searching connected domain from binary image is a good way to achieve the effect of removing shovel [19, 20]. It uses the connectivity of pixel to quickly find all connected domains from an image and make different markers to different connected domains. There are a larger distance between the shovel curve and cargo curve, so they belong to different connected domains.

In this paper, 8-Connected Neighborhoods is used to define neighborhood range $N_{P(X,Y)}$ of pixel $P(X, Y)$, the surrounding eight pixels are adjacent to the $P(X, Y)$, so the neighborhood of $P(X, Y)$ need to satisfy Equation 5. By Equation 5, a connected domain set D_S can be obtained from binary image. And then a point $P(X, Y_{shovel})$ whose y-axis coordinate is equal to Y_{shovel} can be chosen randomly. The connected domain where the point stay is the one of shovel D_{shovel} . The connected domain can be expressed by Equation 6.

$$N_{P(X,Y)} = \{P(X + i, Y + j) | -1 \leq i \leq 1, -1 \leq j \leq 1, i, j \text{ As integer and Not all zero}\} \quad (5)$$

$$D_{shovel} = \{D_S | P(X, Y_{shovel}) \in D_S\} \quad (6)$$

As shown in Figure 8, several connected domain can be got by searching binary image. And by using a point $P(X, Y_{shovel})$, shovel connected domain can be reversed to find out and easily be removed. Since the dust and spray in loading operation process and the impact of some foggy weather, cargo sectional curves are not necessarily only two connected domain (the left half and the right half). In figure 8, the different colors mark is defined as different connected domain, the left half cargo sectional curve is divided into three connected domain, but this does not affect the shovel identification.

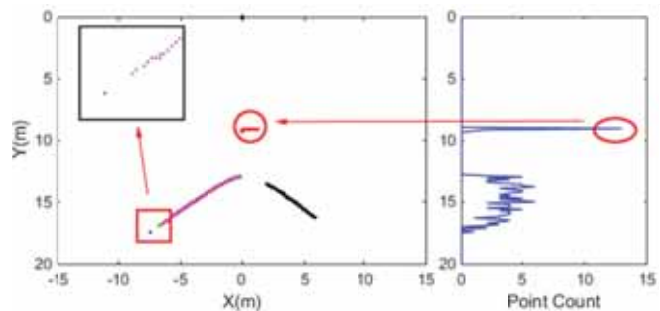


Fig.8 the process of finding connected domain of shovel

After detecting the connected domain of shovel from image, connected domain of cargo can be remained by Equation 7 and the result is shown in figure 9.

$$D_{cargo} = D_S - D_{shovel} \quad (7)$$

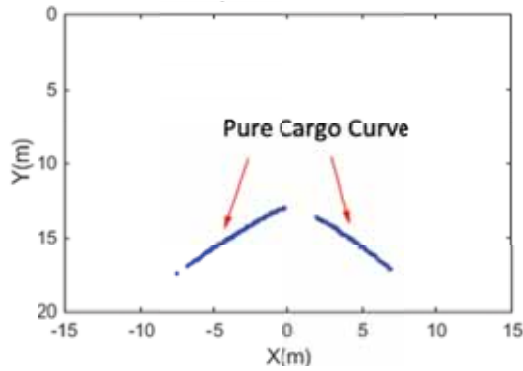


Fig.9 The process of removing connected domain of shovel

CARGO HEIGHT DETECTION

After removing the section curve of shovel, a pure section curve of cargo is remained. Normally, the location of maximum height of the cargo is the location which is nearest from LMS in vertical direction. However, due to the point cloud of this location is substantially obscured by shovel, so we need to fit the cargo sectional curve which is not obscured, and finally calculate the position of cargo vertex, which is the maximum height of the cargo.

There is many kinds of curve fitting algorithm, such as least square procedure, polynomial fitting, Gaussian function fitting and so on [21, 22]. The project algorithm in this paper fits the cargo curve by Hough transform. The reason is that Hough transform can meet automatic ship loader's real-time requirements in process of automatic loading operations and increase the efficiency of its implementation in the computer, using the Hough transform to fit the windrow curve, this algorithm is not susceptible to interference noise in the image. At the same time, considering the surface tension and internal friction interaction of the bulk cargo, incline shape of cargo generally approximates a straight line, so the straight line fitting of Hough transform is used.

In the theory of line fitting of Hough transform, each pixel of binary image can be represented by in with polar coordinates of the Equation 8 [23-25]. θ is the angle between point and the x-axis and r is the distance between point with coordinate origin. As shown in Figure 10, assuming that there is point cloud set $\{P(x_1, y_1), \dots, P(x_{n-1}, y_{n-1}), P(x_n, y_n)\}$ in the binary image space and θ and r is defined as the Hough space variables, every point are able to be expressed as a sine curve in the Hough space. These points cloud can be represented by Equations 9. The Hough space is divided to many small grid. By taking the quantification value of θ into each expression in Equations 9, r can be obtained and mapped into corresponding grid to make counter of the grid plus 1. According to do statistics of each grid counter value, θ and r of larger value could be as polar parameter of fitted straight line.

In order to ensure project algorithm accuracy and real-time performance, the resolution of r is set to 1 while the resolution of θ is set to 1 in this algorithm.

$$r = \cos \theta \times x + \sin \theta \times y \quad (8)$$

$$\begin{cases} r = \cos \theta \times x_1 + \sin \theta \times y_1 \\ \vdots \\ r = \cos \theta \times x_{n-1} + \sin \theta \times y_{n-1} \\ r = \cos \theta \times x_n + \sin \theta \times y_n \end{cases} \quad (9)$$

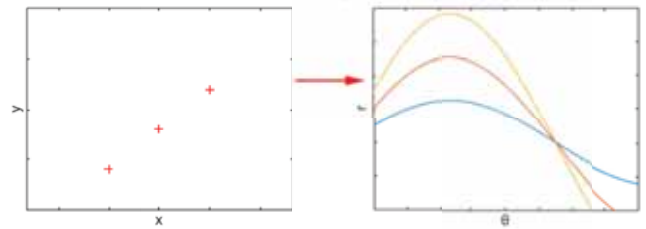


Fig.10 Transition from binary image space to Hough space

As shown in Figure 11, two red straight line $L1$ and $L2$ can be obtained by using Hough transform algorithm to fit the cargo incline curve. The four points $P(X1, Y1), P(X2, Y2), P(X3, Y3), P(X4, Y4)$ are defined as four endpoints of the two red straight line. The two red straight line can be represented by Equation 10..

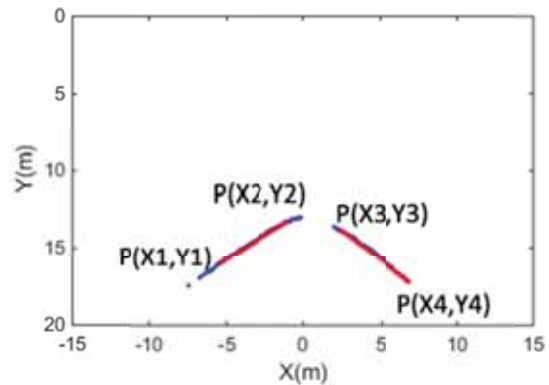


Fig.11 Match cargo incline curve by using Hough transform

$$\begin{cases} (Y1 - Y2) \times X + (X2 - X1) \times Y + (X1 \times Y2 - X2 \times Y1) = 0 \\ (Y3 - Y4) \times X + (X4 - X3) \times Y + (X3 \times Y4 - X4 \times Y3) = 0 \end{cases} \quad (10)$$

After fitting straight line of the cargo incline, an intersection $P(X_{peak}, Y_{peak})$ can be obtained by extending the two lines, the coordinate of the intersection is the coordinate of cargo vertex. The $P(X_{peak}, Y_{peak})$ can be obtained by Equation 11.

$$P(X_{peak}, Y_{peak}) = L1 \cap L2 \quad (11)$$

As shown in Figure 12, Y_{peak} in the point $P(X_{peak}, Y_{peak})$ is defined as the vertical distance between LMS and bulk cargo vertex position. It does not directly represent the height of the cargo H_{peak} from the hold bottom surface. As shown in Figure 13, the bottom surface of the hold is substantially perpendicular to the mid perpendicular of LMS, and is farthest in the y-axis direction from each other. Therefore, the vertical distance Y_{bottom} between LMS and hold bottom surface can be quickly determined by Equation 12, which is equal to the largest point cloud y-axis coordinate Y_{max} . Finally, cargo height H_{peak} can be obtained by Equation 13, which is equal to the difference between the hold bottom vertical coordinate Y_{bottom} and cargo vertex vertical coordinate Y_{peak} .

$$Y_{bottom} = Y_{max} \quad (12)$$

$$H_{peak} = Y_{bottom} - Y_{peak} \quad (13)$$

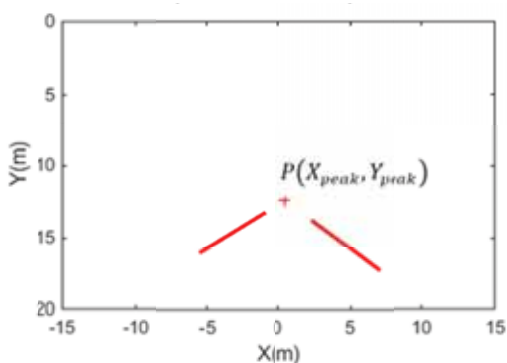


Fig.12 The calculation of cargo height in y-axis direction

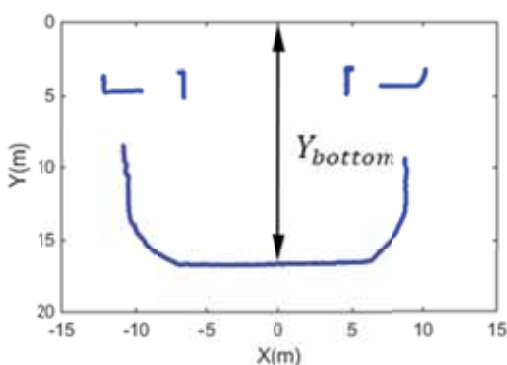


Fig.13 The calculation of ship hold bottom in y-axis direction

EXPERIMENTAL RESULTS

The method as part of the ship loader automation control system has been applied automatic loading machine in Tianjin Coal Terminal. The automated control system includes a two-dimensional laser radar sensor installed in the maintenance platform of slip barrel, rotary motor and servo system, master control existing system in computer of the electrical room

and the real-time loading status monitoring system and other subsystems, these sub system communicates with each other by fiber-optic network for data interaction, data acquisition, data processing, active control and status monitoring and a series of tasks of ship loader. With a large number of dock loading business, making slip barrel anti-collision method can be verified by many continuous uninterrupted testing on the basis of the bulk cargo ships of different size and structure.

Two sets of experimental data are selected in all experiments to analyze and explain the anti-collision method of this paper. As shown in Table 1, there is a bulk cargo ship A with five cabins and bulk cargo ship B with four cabins. In this Table, four laser radar are used to scan cargo ship cabin, point cloud data acquisition and calculate error rate of cargo height detection simultaneously in each experiment. The point cloud data acquisition time for each laser radar are selected when a loading operation is nearly completion from starting loading in the cabin. It is about 40 minutes after starting loading. This is because that the distance between cargo and slip barrel is closed at the moment, it is easy to generate collisions between them. In Table 1, the actual value of each radar measurements is taken from the measurements result when the direction of shovel is rotated to other angle where there is no block between the laser radar and cargo directly measured, and the measurement value can be obtained by compensation algorithm when laser radar is blocked. It can be seen by cargo curve compensation and identification algorithm, the error rate of cargo height detection is maintained at about 3% to 6%, the range is mainly affected by the different laser radar installation location and installation angle of deviation. But the average error rate remained at around 4.5%. The value is considered accurate for a harsh operating environment in bulk cargo terminal. By reasonable threshold adjustments of automatic ship loader control system, the anti-collision subsystem policy can be maintained at a relatively safe level.

Tab.1 two sets of measurement result of LMSs

		LMS No.1	LMS No.2	LMS No.3	LMS No.4
Ship A					
Cabin No.1	Actual Value	12.3	12.6	12.1	12.3
	Measurement	12.7	12.0	11.4	12.8
	Error Rate	3.3%	4.8%	5.8%	4.1%
Cabin No.2	Actual Value	11.3	11.5	11.1	10.9
	Measurement	11.8	12.1	10.5	11.3
	Error Rate	4.4%	5.2%	5.4%	3.7%
Cabin No.3	Actual Value	10.4	10.2	10.8	10.2
	Measurement	10.0	9.7	11.3	9.8
	Error Rate	3.8%	4.9%	4.6%	3.9%
Cabin No.4	Actual Value	11.2	12.0	11.8	11.5
	Measurement	10.8	12.6	12.4	11.9
	Error Rate	3.6%	5.0%	5.1%	3.5%
Cabin No.5	Actual Value	12.1	12.4	12.3	12.9
	Measurement	12.6	13.0	11.7	12.3

	Error Rate	4.1%	4.8%	4.9%	4.7%
Ship B					
Cabin No.1	Actual Value	10.8	10.5	10.8	10.3
	Measurement	11.2	11.0	10.2	10.7
	Error Rate	3.7%	4.8%	5.6%	3.9%
Cabin No.2	Actual Value	11.6	11.7	12.2	11.9
	Measurement	11.2	12.2	12.8	12.3
	Error Rate	3.4%	4.3%	4.9%	3.4%
Cabin No.3	Actual Value	11.1	11.5	10.5	11.4
	Measurement	10.7	11.0	10.0	11.0
	Error Rate	3.6%	4.3%	4.8%	3.5%
Cabin No.4	Actual Value	11.7	12.3	12.1	11.6
	Measurement	12.1	11.8	11.4	11.1
	Error Rate	3.4%	4.1%	5.8%	4.3%

The error rate of cargo height detection against Ship A and Ship B were recorded in four time node of operation. When around 10 minutes at the start of the operation, the error rate is higher, about 6%, since the cargo capacity in the cabin is small, the distance between cargo and laser radar is greater, more dust could be generated by the material falling. However, with the extension of loading time, cabin cargo increased gradually and the distance between cargo and laser radar is reduced, the recognition accuracy is increasing and the error rate is stabilized at 4%. At the same time, it can be found that the error rate of the Ship B when 10 minutes after loading is smaller than Ship A. The comparison indicate that recognition accuracy of small ship is better than the big one due to the influence of size and depth of the cabin.

Tab.2 Error rate of cargo height in four time node of operation

	10min	20min	30min	40min
Ship A				
Cabin No.1	6.5%	5.7%	5.5%	4.5%
Cabin No.2	5.1%	5.6%	4.9%	4.7%
Cabin No.3	6.3%	6.0%	5.2%	4.3%
Cabin No.4	6.5%	5.4%	5.1%	4.3%
Cabin No.5	5.7%	5.3%	5.0%	4.6%
Ship B				
Cabin No.1	5.1%	5.2%	4.8%	4.5%
Cabin No.2	5.6%	6.1%	4.5%	4.0%
Cabin No.3	6.2%	5.4%	4.6%	4.1%
Cabin No.4	5.8%	5.1%	5.3%	4.4%

CONCLUSION

A large number of continuous experiment against automatic ship loader of bulk terminal proved that the anti-collision method described in this paper can detect the original outline shape of the cabin and cargo precisely by laser radar array, exclude the block of shovel and cargo being thrown with compensation algorithm for helping to identify the position and height of the cargo more accurately. The method can serve in most automated ship loader or manual one and maintain a

safe distance between cargo and slip barrel. It can reduce the impact accidents and fatigues for a long time of operations monitor personnel and realize safe, efficient operation in ship loading.

REFERENCES

- Nadilo Branko, "BULK CARGO TERMINAL IN PLOCE PORT International cooperation on the project," GRADEVINAR, Vol. 66, No. 10, pp. 953-964 (2014)
- Bugaric, U.; Petrovic, D., "Increasing the capacity of terminal for bulk cargo unloading," SIMULATION MODELLING PRACTICE AND THEORY, Vol. 15 No. 10 pp. 1366-1381 (2007)
- Mi Chao, Zhang Zhiwei, He Xin, Huang Youfang, Mi Weijian. "Two-Stage Classification Approach for Human Detection in Camera Video Bulk Ports," Polish Maritime Research, Vol. 22, No. 86, pp. 163-170 (2015).
- Song, Gyeuei, "A Study on Improvement of Handling Dirty Bulk Cargo in Busan Port," JOURNAL OF KOREA PORT ECONOMIC ASSOCIATION, Vol. 26, No. 3, pp.114-129 (2010)
- Froyland, Gary; Koch, Thorsten; Megow, Nicole; "Optimizing the landside operation of a container terminal," OR SPECTRUM, Vol. 30, No. 1 pp. 53-75 (2008)
- Mi Chao, Zhang Zhiwei, Huang Youfang, Shen Yang, "A FAST AUTOMATED VISION SYSTEM FOR CONTAINER CORNER CASTING RECOGNITION," Journal of Marine Science and Technology-Taiwan, Vol. 24, No. 1, pp. 54-60 (2016)
- Choe, Ri; Kim, Jeongmin; Ryu, Kwang Rye, "Online preference learning for adaptive dispatching of AGVs in an automated container terminal," APPLIED SOFT COMPUTING, Vol. 38, pp. 647-660 (2016)
- Mi Chao, Huang Youfang, Liu Haiwei, Shen Yang, Mi Weijian. "Study on Target Detection & Recognition Using Laser 3D Vision System for Automatic Ship Loader," Sensor & Transducers, Vol. 158, No.11, pp. 436-442 (2013).
- Zupancic, Nina; Horvat, Aleksander; Skobe, Simona, "Environmental impact of dusting from the Koper port bulk cargo terminal on the agricultural soils," ACTA GEOGRAPHICA SLOVENICA-GEOGRAFSKI ZBORNIK, Vol. 55, No.1, pp. 140-158 (2015)
- Mi Chao, He Xin, Liu Haiwei, Huang Youfang, Mi Weijian. "Research on a Fast Human-Detection Algorithm for Unmanned Surveillance Area in Bulk Ports," Mathematical Problems in Engineering, (2014).

11. Liu Pengfei, Lin Bin, Zhang Xiaofeng, "Safety and Stability Analysis of the Ship loader during Shipping," *ADVANCES IN MATERIALS MANUFACTURING SCIENCE AND TECHNOLOGY XV*, Vol. 777, pp. 189-193 (2014)
12. Mi Chao, Shen Yang, Mi Weijian, Huang Youfang. "Ship Identification Algorithm Based on 3D Point Cloud for Automated Ship Loaders," *Journal of Coastal Research*, Vol. 73, pp. 28-34 (2015).
13. Gang Zhou. "Automobile Anti-collision Millimeter-Wave Radar Signal Processing," *Intelligent Human-Machine Systems and Cybernetics (IHMSC)*, Vol. 2, pp. 484-486 (2015)
14. Frederic Maire. "Vision based anti-collision system for rail track maintenance vehicles," *Advanced Video and Signal Based Surveillance*, pp. 170-175 (2007)
15. Mi Chao, Liu Haiwei, Huang Youfang, Mi Weijian, Shen Yang, Fatigue alarm systems for port machine operators, *ASIA LIFE SCIENCES*, Vol. 25, No.1, pp. 31-41 (2016)
16. Mi Chao, Liu Haiwei, Zhao Ning, Shen Yang. "A ship cargo hold inspection approach using laser vision systems," *Telkomnika*, pp. 330-337 (2013).
17. Rodriguez-Cuenca Borja, Garcia-Cortes Silverio, Ordonez Celestino, "An approach to detect and delineate street curbs from MLS 3D point cloud data," *AUTOMATION IN CONSTRUCTION*, Vol. 51, pp. 103-112 (2015)
18. Diaz-Vilarino Lucia, Conde Borja, Lagueela Susana, "Automatic Detection and Segmentation of Columns in As-Built Buildings from Point Clouds," *REMOTE SENSING*, Vol.7, No. 11, pp. 15651-15667 (2015)
19. Tsz Ching Ng, Gu Xianfeng, Lui Lok Ming, "Computing Extremal Teichmuller Map of Multiply-Connected Domains Via Beltrami Holomorphic Flow," *JOURNAL OF SCIENTIFIC COMPUTING*, Vol. 60, No. 2, pp. 249-275 (2014)
20. Wei Xiangzhi, Joneja Ajay, "On computing the shortest path in a multiply-connected domain having curved boundaries," *COMPUTER-AIDED DESIGN*, Vol. 48, pp. 39-41 (2014)
21. Paille Gilles-Philippe, Poulin Pierre, Levy Bruno, "Fitting Polynomial Volumes to Surface Meshes with Voronoi Squared Distance Minimization," *COMPUTER GRAPHICS FORUM*, Vol. 32, No. 5, pp. 103-112 (2013)
22. Luo Ding, Kuang Cuifang, Liu Xu, "Fiber-based chromatic confocal microscope with Gaussian fitting method," *OPTICS AND LASER TECHNOLOGY*, Vol. 44, No. 4, pp. 788-793 (2012)
23. Chan-Hon-Tong Adrien, Achard Catherine, Lucat Laurent, "Simultaneous segmentation and classification of human actions in video streams using deeply optimized Hough transform," *PATTERN RECOGNITION*, Vol. 47, No. 12, pp. 3807-3818 (2014)
24. Jiang, Haibo; Tang, Kai; He, Xinlin, "Experimental Studies on Reduction of Evaporation from Plain Reservoirs in Drought Areas by Benzene Board Covering Technology," *JOURNAL OF COASTAL RESEARCH*, Vol. 73, pp. 177-182 (2015)
25. Lazarowska, Agnieszka, "Swarm Intelligence Approach to Safe Ship Control", *POLISH MARITIME RESEARCH*. Vol. 22, No. 4, pp. 34-40 (2015)

CONTACT WITH THE AUTHOR

SHEN Yang

yangshen@shmtu.edu.cn

Higher Technical College
Shanghai Maritime University
Shanghai
CHINA

GROUP-BAY STOWAGE PLANNING PROBLEM FOR CONTAINER SHIP

Shen Yifan ^a

Zhao Ning ^b

Mi Weijian ^b

^a Scientific Research Academy, Shanghai Maritime University, 201306, Shanghai, CHINA

^b Logistics Engineering College, Shanghai Maritime University, 201306, Shanghai, CHINA

ABSTRACT

Stowage planning is the core of ship planning. It directly influences the seaworthiness of container ship and the handling efficiency of container terminal. As the latter step of container ship stowage plan, terminal stowage planning optimizes terminal cost according to pre-plan. Group-Bay stowage planning is the smallest sub problem of terminal stowage planning problem. A group-bay stowage planning model is formulated to minimize relocation, crane movement and target weight gap satisfying both ship owner and container terminal. A GA-A hybrid algorithm is designed to solve this problem. Numerical experiment shown the validity and the efficiency.*

Keywords: Container Terminal, Group-Bay Stowage Plan, Terminal Stowage Plan, Hybrid GA

INTRODUCTION

Despite the economic contraction of recent years, the container trade volume has been sustaining expanding. To meet the expanding demand of maritime transportation, container terminals has been focusing on management and decision evolution to enlarge their operation capability. Now, the research on the container terminal mainly focuses on two aspects, equipment automation and intelligent decision-making. There are quite a few scholars who have carried out some research work on these two points[3-4, 9-11]. In intelligent decision, container stowage plan has always been a major problem in terminal decision problems. As a core phase of ship planning, stowage planning affects equipment efficiency and energy consumption to a large extent. Since 1970s, stowage planning has been modeled and analyzed by experts and scholars from many scopes, such as decision making systems,

mathematical modeling, simulation, intelligent algorithms.

H. P Wang[5] designed an automated stowage expert system with knowledge inference techniques, and implementation principles are provided. Kang et al and Kim et al[6-7] solved stowage planning problem with greedy algorithm and tree search algorithm. Ambrosino and Sciomachen[8] proposed a decision support system to solve Master Bay Plan Problem(MBPP), feasible solution was found by constraint satisfaction method, but objective function and optimal solution was not provided. Winter et al[12] introduced a stowage planning problem combining loading plan, and a decision support system was proposed to optimize the balance of quae cranes. Cho et al[13] and Botter[14] proposed a LP model for container ship stowage planning problem, some assumptions was made to simplify the problem. The planning result shows a weak compatibility to actual operation process.

Avriel et al[15-16] proposed a 0-1 integer programming model, a heuristic method was designed to solve this problem. Numerical experiment with actual data shows an acceptable solution quality and computing efficiency. But this heuristic method is not without flaws, it can only solve simplified stowage planning problem and lacks flexibility. Ambrosino et al[17] proposed a model minimizing total loading time, with some operational constraints such as container type and load limit. The solution allocates containers with same port of discharge into same bay to avoid unnecessary restow. Sciomachen and Tanfani[18] solved stowage planning problem with 3D-BPP, optimizing total loading time and quae crane utilization. Pacino et al[19] and Delgado et al[20] solved stowage planning problem with two steps. The first step separates containers into different categories based on Master Bay Plan, and the second step decides the specific stowage location for each container.

These researches focuses mainly on optimizing ship stability, equipment utilization and total loading time. Other impact factors such as reshuffling operation and yard crane shifting are ignored. In practical application, stowage planning is a two-step process. In the first step, ship stability constraint is claimed and solved by ship line, and the result of the first step so called preplan is the input and constraint of the second step. This research focuses on the second step, which optimizes costs of container terminal, on condition that the constraint of the first step's results are satisfied. Formal researches about the second step often scales down the whole problem into ship bay stowage plan, for the independence of different bays of ship in stowage planning process. In practice, containers of the same bay and with the same key feature(container type, container size, port of discharge) are called a container group. In bay-wise stowage planning, decisions of different container groups are relative independent, thus a bay-wise stowage planning can be separated into several sub-bay-wise or so called group-bay planning problem. Therefore, a group-bay stowage planning model optimizing key cost factors of container terminal considering preplan constraints and operation constraints is proposed to solve stowage plan problem. A hybrid A*-genetic algorithm is introduced to solve this problem. The stowage location is solved by the genetic phase and the loading sequence is updated by A*. Numerical experiments verifies the validity of the algorithm. This model and algorithm can be implemented to make stowage plans automatically.

GROUP-BAY STOWAGE PLANNING PROBLEM ANALYSIS

INTRODUCTION OF STOWAGE PLANNING PROBLEM

Planning a ship's stowage is a two-step process[1-2]. The first step is executed by the shipping line, so called pre-plan. This pre-planning phase optimizes general loading positions for each container group (containers with same POD, container type, size, status and height) from the shipping line's point of view to minimize the ship's utilization. Constraints contains mainly the stability of the ship. The second step is executed by container terminals, so called terminal-plan. This planning

phase optimizes specific slots and loading sequences for dedicated containers from the container terminal's point of view. Constraints are the result of the first step, and some operation constraints. Group-bay stowage planning is a part of the second step.

DEFINITION OF GROUP-BAY STOWAGE PLANNING

A container group is a set of containers with same POD, container type, size, status and height.

As is shown in Fig.1, the pre-plan loading positions of container group A are distributed in to ship bays, thus this container group A can be subdivided into two sets 02H-A and 06H-A. These subsets called group-bays are the smallest decision unit in the terminal planning problem. In group-bay stowage planning problem, constraints are stability of the ship reflected in pre-plan(mainly the weight distribution constraints) and operation constraints.

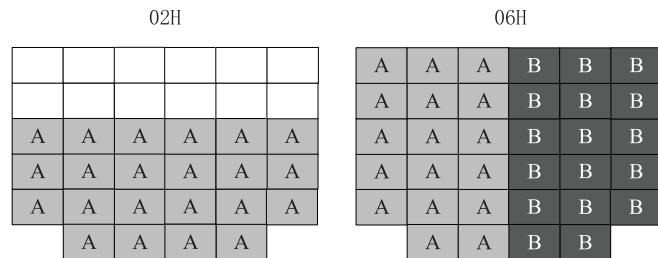


Fig.1 Group-bays of a pre-plan

OPTIMIZATION OBJECTIVES IN GROUP-BAY STOWAGE PLANNING

(1) Reshuffles: In the loading process, if the previous loading container locates right under the subsequent loading container, the subsequent loading container must be removed from its row first to operate the previous loading container, this is called reshuffle.

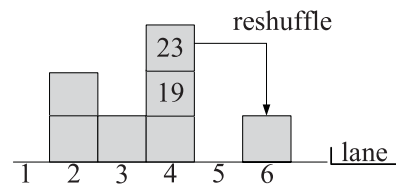


Fig.2 Reshuffles in yard

In Fig.2, two containers are located in the same row of a yard bay. The container with sequence 19 is located right under the container with sequence 23. When the yard crane carries containers in sequence, the 19th container should be transferred before the 23th container, and at that time, the 23th container must be reshuffled to another available location for the yard crane to get 19th container. Reshuffles cost time

and resources.

(2) Yard crane shifts: refers to yard crane movements between yard bays. A yard crane move from bay A to bay B is a shift.

Containers of same ship bay often locate in different yard bays, the loading sequence must be optimized to reduce yard crane shifts. Fig.3 shows that an inferior loading sequence can cause frequent shifts, which costs time and resources.

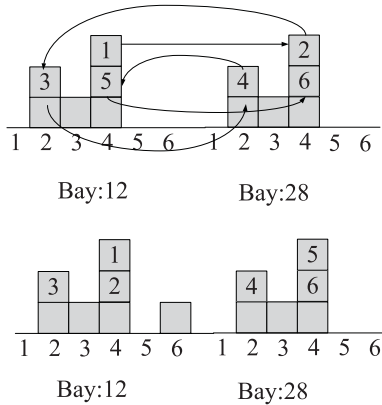


Fig.3 Yard crane shifts between different loading sequence

(3) Ship stability: In pre-plan optimization, container weight is a key decision factor. In terminal stowage planning, the final weight distribution must be as close as possible as the optimal weight distribution to ensure a feasible ship stability and seaworthiness.

GROUP-BAY STOWAGE PLANNING MODEL

Group-Bay stowage planning problem is a core and difficult planning problem of all planning in container terminals. This problem is a multi-objective combinatorial optimization problem with complex constraints. The major decision context is the specific loading location of each container and loading sequences of these containers. The constraints mainly embodies operation restrictions and ship stability control.

MODEL ASSUMPTIONS

1. The export containers to be stowed are no less than ship slots to be allocated;
2. The specific location of each container to be stowed is known;
3. The type of each container to be stowed is the same as the ship slots to be allocated;
4. Equipment failure is ignored;
5. Enough horizontal transportation trucks available;
6. The quae crane handles only one container per move.

SYMBOL DEFINITION

(1) Dimensions

I : set of all containers to be stowed, $i, i' \in I$;

J : set of all ship slots to be allocated, $j, j' \in J$;

S : set of all loading sequences, $s \in S$;

R : set of rows of ship slots to be allocated, $r, r' \in R$;

T : set of tiers of ship slots to be allocated, $t \in T$;

(2) Parameters

A_{jr} : Whether ship slot j is in ship row r , equals 1 if ship slot j is in ship row r , otherwise 0;

GP_i : Whether container i is a GP container, equals 1 if container i is a GP container, otherwise 0;

HC_i : Whether container i is a HC container, equals 1 if container i is a HC container, otherwise 0;

GP_r : Number of GP containers allowed in ship row r ;

HC_r : Number of HC containers allowed in ship row r ;

W_j : Minimum container weight of tier of ship slot j according to pre-allocation according to pre-plan;

M_j : Maximum container weight of tier of ship slot j according to pre-allocation according to pre-plan;

w_i : Weight of container i ;

δ : Maximum weight difference of heavier containers above lighter containers allowed in each ship row;

Q_s : Matrix of serial numbers of loading sequences;

$YP_{ii'}$: 0-1 Matrix, relative location of container i and i' , equals 1 if i locates right above i' in yard, otherwise 0;

$VP_{jj'}$: 0-1 Matrix, relative location of ship slots j and j' , equals 1 if j locates right above j' in yard, otherwise 0;

YB_i : Yard bay of container i ;

F_j : Pre-allocation weight of ship slot j according to pre-plan;

(3) Decision variables

s_{ij} : 0-1 variable, whether container i is allocated to ship slot j with loading sequence s , 1 for true, 0 for false;

$\beta_{ii'}$: 0-1 variable, relative loading sequence relation of container i and i' , equals 0 if container i is to be loaded earlier than i' , otherwise 1;

ϕ_s : 0-1 variable, whether containers with consecutive loading sequence locates at the same yard bay, 1 for true, 0 for false;

OBJECTIVE FUNCTION

(1) Minimize reshuffles

Expression 3-1 is the relative loading sequence of container i and i' , if i is to be loaded earlier than i' then $\beta_{ii'}$ equals 0, otherwise 1.

$$\beta_{ii'} = \begin{cases} 0, & \sum_{s \in S} \sum_{j \in J} X_{sij} Q_s - \sum_{s \in S} \sum_{j \in J} X_{si'j} Q_s < 0 \\ 1, & \sum_{s \in S} \sum_{j \in J} X_{sij} Q_s - \sum_{s \in S} \sum_{j \in J} X_{si'j} Q_s > 0 \end{cases} \quad 3-1$$

Thus the number of reshuffles is shown in expression 3-2:

$$\min Z_1 = \sum_{i, i' \in I} YP_{ii'} \beta_{ii'} \quad 3-2$$

(2) Minimize yard crane shifts

Expression 3-3 is whether the yard crane needs to shift from container $s-1$ to s , 1 for true, 0 for false.

$$\phi_s = \begin{cases} 0, & \sum_{i \in I} \sum_{j \in J} X_{sij} \cdot YB_i - \sum_{i \in I} \sum_{j \in J} X_{(s-1)ij} \cdot YB_i = 0 \\ 1, & \sum_{i \in I} \sum_{j \in J} X_{sij} \cdot YB_i - \sum_{i \in I} \sum_{j \in J} X_{(s-1)ij} \cdot YB_i \neq 0 \end{cases} \quad 3-3$$

Thus, minimizing total yard crane shifts can be expressed as:

$$\min Z_2 = \sum_{s \in S} \phi_s \quad 3-4$$

(3) Minimizing total weight gap between planned containers and optimal weight distribution

$$\min Z_3 = \sum_{j \in J} \left| \sum_{s \in S} \sum_{i \in I} X_{sij} \cdot w_i - F_j \right| \quad 3-5$$

(4) Overall objective

These three sub objects are all cost objects, the overall objective should cover the interaction of sub objects. According to practical handling cost measures, these sub objects can be treated as costs without normalizing. After consulted stowage planning stuff of Ningbo Daxie Container Terminal, a weighted overall function is given as follow:

$$Z_{total} = 0.5Z_1 + 0.2Z_2 + 0.3Z_3 \quad 3-6$$

CONSTRAINTS

(1) Uniqueness constraint

A container can only be allocated to a ship slot with only one loading sequence:

$$\sum_{s \in S} \sum_{j \in J} X_{sij} = 1 \quad 3-7$$

$$\sum_{s \in S} \sum_{i \in I} X_{sij} = 1 \quad 3-8$$

$$\sum_{i \in I} \sum_{j \in J} X_{sij} = 1 \quad 3-9$$

(2) GP and HC constraint

In ship handling process, GP and HC containers are mixed in a ship row, which means in stowage planning, GP and HC containers are only restricted in numbers in quantity in a ship row, not in specific ship slots. HC quantity restriction of a ship row can be expressed as:

$$\sum_{s \in S} \sum_{i \in I} \sum_{j \in J} X_{sij} A_{jr} HC_i = HC_r \quad 3-10$$

HC quantity restriction of a ship row can be expressed as:

$$\sum_{s \in S} \sum_{i \in I} \sum_{j \in J} X_{sij} A_{jr} GP_i = GP_r \quad 3-11$$

(3) Slot Weight limit

According to optimal weight distribution based on pre-plan, slot weight limit is applied with a certain extent of relaxation. Container allocated to a slot must weights in this rang:

$$W_j \leq \sum_{s \in S} \sum_{i \in I} X_{sij} w_i \leq M_j \quad 3-12$$

(4) Maximum weight difference of heavier containers above lighter containers limit

To ensure the stability of the ship, the containers located above others should be lighter or a little bit heavier than the beneath container. This limitation can be expressed as:

$$\left(\sum_{s \in S} \sum_{i \in I} X_{sij} w_i - \sum_{s \in S} \sum_{i \in I} X_{sij} w_i \right) VP_{jj'} \leq \delta \quad 3-13$$

(5) Handling sequence constraint

The lower ship slots should be loaded before the upper ship slots, which means a container cannot be loaded to a ship slot above a not yet loaded ship slot.

$$\sum_{s \in S} \sum_{i \in I} X_{sij} Q_s \leq \sum_{j' \in J} \left[\sum_{s \in S} \sum_{i \in I} (X_{sij} Q_s) VP_{jj'} \right] \quad 3-14$$

ALGORITHM FOR GROUP-BAY STOWAGE PLANNING

INTRODUCTION OF HYBRID ALGORITHM

A hybrid algorithm combining GA and A* is proposed to solve this planning problem. In this algorithm, the genetic part is dedicated to solve the allocation of containers to ship slots, and the A* part solves the most feasible loading sequence of these containers to this allocation. The work flow of this algorithm is shown in Fig.4.

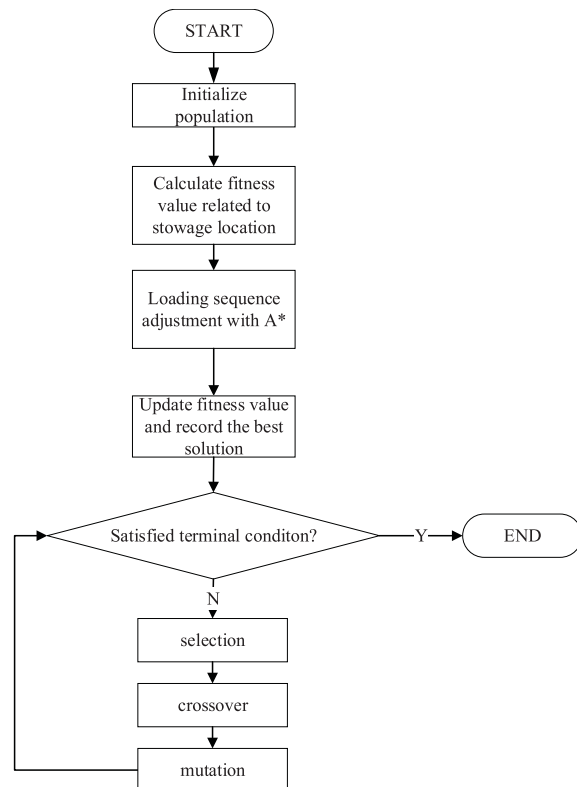


Fig.4 Work flow of hybrid algorithm

CHROMOSOME DESIGN

Fig.5 shows a Chromosome of the genetic part, a gene is a ship slot for a container.

A	B	C	D	E	F	G	H
2	1	8	4	7	5	3	6

Fig.5 Example of a chromosome

SELECTION

GA part selects individuals to breed new generation with Roulette, the probability of individuals to be chosen to the new generation is calculated by fitness-based function:

$$p_i = f_i / \sum_{i=1}^n f_i \quad (15)$$

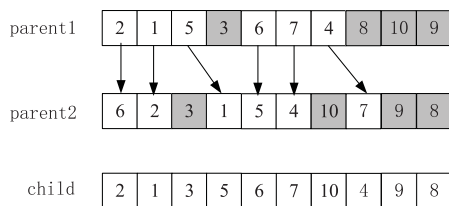
p_i is the probability that i is chosen to the new generation, f_i is the fitness of i , n is the population quantity.

GENETIC OPERATORS

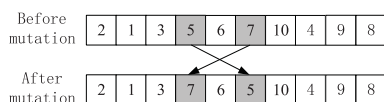
Fig.6(a) shows that an order crossover(OX) operator is applied to make sure the generated chromosome has no ship slot repeat conflicts, but the GP and HC quantity may be infeasible. Therefore the GP and HC quantity constraint is converted into a penalty function to eliminate infeasible chromosomes during selection process.

Fig.6(b) is the mutation operator. This operator selects two different genes of one chromosome and switch them.

These genetic operators adjusts only the chromosome of slot allocation, not the loading sequence. The loading sequence is optimized through the A* part.



(a) Order crossover



(b) Mutation

Fig.6 Genetic operators

A* FOR LOADING SEQUENCE ADJUSTMENT.

This A* part adjusts loading sequence to minimize yard crane shifts after the genetic operators allocates the slots.

$$Z_2(i) = g_2(i) + h_2(i) \quad 4-16$$

Expression 4-16 shows that the cost function consists of two parts: $g_2(i)$ is the actual cost from start node to loading container i , which is total yard crane shifts until loading container i ; $h_2(i)$ is the estimated minimum yard crane shifts after container i is loaded till the end of the loading, which is the total number of yard bays who have containers to be loaded after container i .

Fig.7 shows the expansion of child node of A*, a constraint branch pruning is introduced to eliminate infeasible solution. In the searching process, these gray slots are slots that can be loaded according to handling sequence constraint, which means only these gray slots are feasible child nodes. This A* part expands feasible nodes from start node and calculates the cost function, and selects the node with the least cost function as the current node to expand, and the final loading sequence is get through iterations. After loading sequence searching for each chromosome, the fitness function is calculated according to the slot allocation and the loading sequence to get the selection probability of each chromosome.

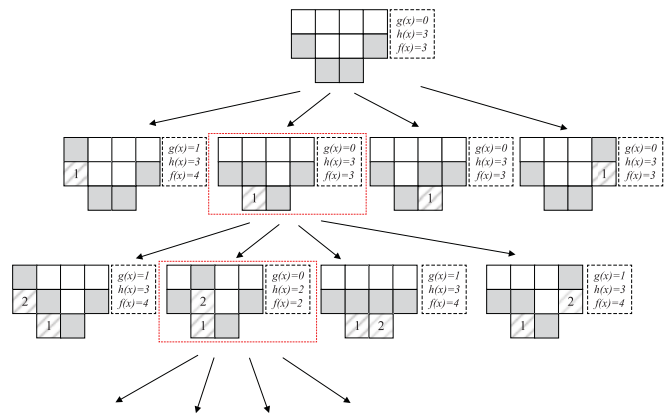


Fig.7 A* expansion and searching process

NUMERICAL EXPERIMENT

In this part, a numerical example from Ningbo Daxie Container Terminal is chosen to validate the feasibility of the proposed model and algorithm.

NUMERICAL EXAMPLE

This numerical is 30H bay of a container ship. The 42 containers to be stowed distributes in 6 yard bays. Fig.8 shows the pre-plan of this group-bay, blue slots are to be allocated to. Fig.9 shows the containers and their yard locations and weight, yellow containers are to be allocated. The experiment platform is a computer with a dual core 2.50GHz Intel Core

i7 CPU, 4.00GB RAM and a Win7 64bit OS.

RESULTS AND ANALYSIS

(1) Preset of Parameters

The parameter set is in Table.1:

Tab.1 Parameter set of GA

Population	Iterations	Crossover Prob.	Mutation Prob.
50	1000	0.85	0.05

(2) Validation of proposed algorithm

The stowage plan of proposed algorithm is in Fig.10. Yard crane shifts in yard block 2A according to loading sequence is 56→10→48→06→62→32→62. Total reshuffle is 0, total shifts are 6, with only one shift back from yard bay 32 to yard bay 62. And all allocated containers satisfies the weight constraint and maximum weight difference of heavier containers above lighter containers constraint.

(3) Convergence of proposed algorithm

The convergence curve is Fig.11:

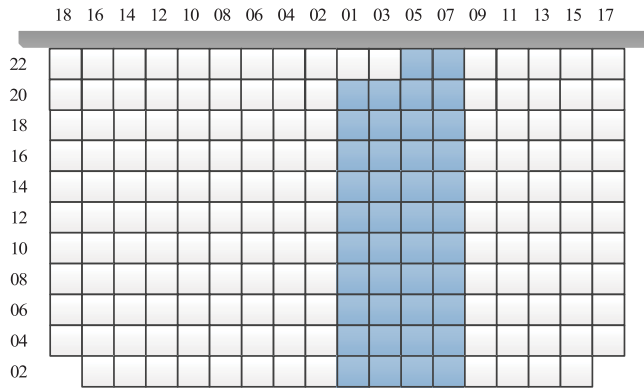


Fig.8 Pre-plan of bay 30H

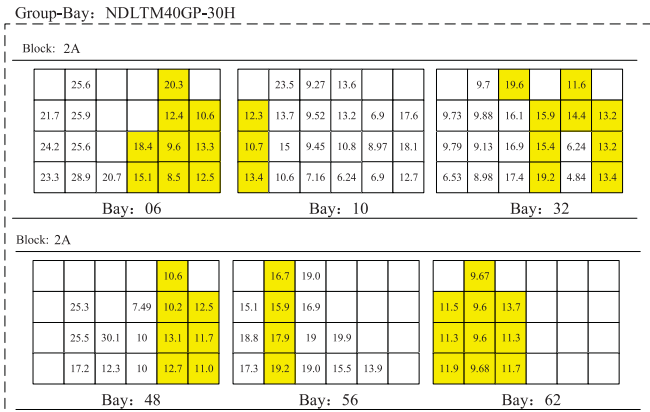


Fig.9 Yard distribution of containers



Fig.11 Convergence curve of proposed algorithm

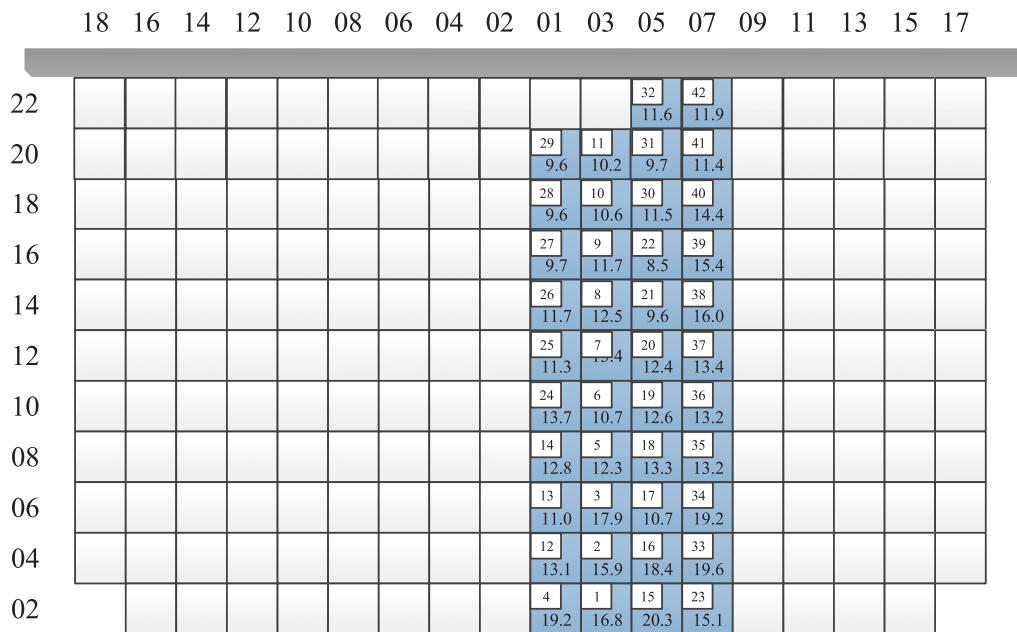


Fig.10 Stowage planning result by proposed algorithm

As is shown in Fig.11, proposed algorithm converged to a near-optimal solution, the curve went flat afterwards, which shows an acceptable convergence.

To go a step further, the algorithm is run 30 times. Table.2 is the result. *Iterations to get near-optimal solution* is the convergence speed.

Tab.2 30 run time result of proposed algorithm

NO.	Iterations to get near-optimal solution	NO.	Iterations to get near-optimal solution	NO.	Iterations to get near-optimal solution
1	322	11	504	21	485
2	356	12	492	22	317
3	467	13	412	23	587
4	451	14	563	24	425
5	332	15	395	25	536
6	353	16	536	26	328
7	289	17	529	27	489
8	567	18	462	28	439
9	351	19	551	29	595
10	326	20	595	30	400

For 30 independent experiments, the max iteration to get near-optimal solution is 595, the min iteration is 289, and the average is 448. This result shows a relatively high convergence efficiency, and an acceptable stability. For all numerical examples tested, the proposed algorithm converges in 600 iterations, the parameter of 1000 total iterations is feasible, and the convergence of proposed algorithm is validated.

(4) Effectiveness of proposed algorithm

To verify effectiveness of proposed algorithm, a standard GA is used as control. The two algorithms use both 1000 iterations. Average iterations to get near-optimal solution, average fitness value, standard deviation of fitness and average solution time are listed in Table.3.

Tab.3 Comparison of proposed algorithm and GA

	Average iterations to get near-optimal solution	Average fitness value	Standard deviation of fitness	Average solution time(s)
Proposed hybrid algorithm	448	322.5	6.45	37.51
Standard GA	729	584.2	22.39	59.28

Table.3 shows that proposed algorithm has advantage over standard GA in all four measures, although both algorithms

can get near-optimal solution in given iterations, and this shows the performance of the proposed algorithm. Standard GA gets near-optimal solution in average 729 iterations against hybrid algorithm's 448. This verifies the convergence speed superiority of proposed hybrid algorithm. The average value shows that proposed algorithm gets a much more global optimized result. The standard deviation of fitness advantage of proposed algorithm shows the stability advantage of hybrid algorithm over GA. And the hybrid algorithm has a 21.37s advantage over GA in average solution time, which counts as has a better solution efficiency.

With better result and less time consumption, the propose algorithm can be considered to be a feasible algorithm for solving Group-bay stowage planning problem.

CONCLUSIONS

This study developed stowage planning problem in three major aspects:

(1) Defines group-bay stowage planning problem which is the smallest planning sub problem in the terminal planning problem.

(2) A MIP model of group-bay stowage planning problem optimizing yard reshuffles, yard crane shifts and weight distribution is introduced with operational principles.

(3) A GA-A* hybrid algorithm is proposed to solve both the stowage location allocation and loading sequencing of the group-bay stowage planning problem.

(4) Numerical experiment shows the convergence and effectiveness of the proposed algorithm in solving group-bay stowage planning problem.

In the synthesis, group-bay stowage planning problem can be solved through proposed algorithm, which provides a feasible solution and an aspect of view to the terminal stowage planning problem.

REFERENCES

1. Steenken, D., Voß, S., & Stahlbock, R. Container terminal operation and operations research A classification and literature review. *OR Spectrum*, 26(1), 2004, 3–49.
2. Alvarez, J. Ambrosino, D., Anghinolfi, D., Paolucci, M A heuristic for vessel planning in a reach stacker terminal[J]. *Journal of Maritime Research*, III(1), 2006, 3–16.
3. Mi Chao, Zhang Zhiwei, Huang Youfang, Shen Yang, A FAST AUTOMATED VISION SYSTEM FOR CONTAINER CORNER CASTING RECOGNITION, *Journal of Marine Science and Technology-Taiwan*, 2016, 24(1): 54-60. DOI: 10.6119/JMST-016-0125-8
4. Mi Chao, Shen Yang, Mi Weijian, Huang Youfang, Ship Identification Algorithm Based on 3D Point Cloud for Automated Ship Loaders, *Journal of Coastal Research*, 2015, 2015(SI.73):28-34. DOI: 10.2112/SI73-006.1

5. Wang Hongpeng. Knowledge-based Container Ship Automatic Stowage Expert System [J]. Journal of Shanghai Maritime University, 2002, 23(1): 46-49.
6. Kang, J.-G., & Kim, Y.-D. Stowage planning in maritime container transportation[J]. Journal of the Operational Research Society, 53(4), 2002, 415-426.
7. Kim, K. H., Kang, J. S., & Ryu, K. R. A beam search algorithm for the load sequencing of outbound containers in port container terminals[J]. OR Spectrum, 26(1), 2004, 93-116.
8. Ambrosino D., Sciomachen A.. A constraints satisfaction approach for master bay plans[J]. In: Sciotto, G., Brebbia, C. (Eds.), Maritime Engineering and Ports. WIT Press, Boston, 1998, pp: 155-164.
9. Mi Chao, Zhang Zhiwei, He Xin, Huang Youfang, Mi Weijian, Two-stage classification approach for human detection in camera video in bulk ports, Polish Maritime Research, 2015, 22(SI.1):163-170. DOI: 10.1515/pomr-2015-0049
10. Mi Chao, He Xin, Liu Haiwei, Huang Youfang, Mi Weijian, Research on a Fast Human-Detection Algorithm for Unmanned Surveillance Area in Bulk Ports, Mathematical Problems in Engineering, 2014, Article No.386764. DOI: 10.1155/2014/386764
11. Mi Chao, Liu Haiwei, Huang Youfang, Mi Weijian, Shen Yang, Fatigue alarm systems for port machine operators, ASIA LIFE SCIENCES, 2016, 25(1): 31-41.
12. Winter T.. Online and Real-Time Dispatching Problems[D], PhD thesis, Technical University of Braunschweig, Germany, 1999.
13. Cho D.W.. Development of a methodology for containership load planning[D], PhD thesis, Oregon State University, 1984.
14. Botter R.C., Brinati M.A.. Stowage container planning: a model for getting an optimal solution[J], IFIP Trans. B (App. in Tech.), 1992, B-5: 217-229.
15. Avriel M., Penn M.. Exact and approximate solutions of the container ship stowage problem[J]. Computers & Industrial Engineering, 1993, 25: 271-274.
16. Avriel M., Penn M., Shpirer N., Witteboon S.. Stowage planning for container ships to reduce the number of shifts[J]. Annals of Operations Research, 1998, 76: 55-71.
17. Ambrosino D., Sciomachen A., Tanfani E.. Stowing a containership: the master bay plan problem[J]. Transportation Research A, 2004, 38(2): 81-99.
18. Sciomachen A., Tanfani E.. A 3D-BPP approach for optimising stowage plans and terminal productivity[J]. European Journal of Operational Research, 2007, 183: 1433-1446.
19. Pacino, D., Delgado, A., Jensen, R. M., & Bebbington, T. Fast generation of near-optimal plans for eco-efficient stowage of large container vessels. In Proceedings of the second international conference on computational logistics, 2011, ICCL'11 (pp. 286-301), Berlin, Heidelberg: Springer-Verlag.
20. Delgado, A., Jensen, R. M., Janstrup, K., Rose, T. H., & Andersen, K. H. A constraint programming model for fast optimal stowage of container vessel bays. European Journal of Operational Research, 2012, 220, 251-261.

CONTACT WITH THE AUTHOR

Mi Weijian

Logistics Engineering College
Shanghai Maritime University
201306, Shanghai
CHINA

STORAGE ALLOCATION IN AUTOMATED CONTAINER TERMINALS: THE UPPER LEVEL

Xia Mengjue¹

Zhao Ning²

Mi Weijian²

¹ Scientific Research Academy

² Logistics Engineering College

Shanghai Maritime University, 1550 Haigang Avenue, Shanghai, China. 201306

ABSTRACT

Nowadays automation is a trend of container terminals all over the world. Although not applied in current automated container terminals, storage allocation is indispensable in conventional container terminals, and promising for automated container terminals in future. This paper seeks into the storage allocation problem in automated container terminals and proposed a two level structure for the problem. A mixed integer programming model is built for the upper level, and a modified Particle Swarm Optimization (PSO) algorithm is applied to solve the model. The applicable conditions of the model is investigated by numerical experiments, so as the performance of the algorithm in different problem scales. It is left to future research the lower level of the problem and the potential benefit of storage allocation to automated container terminals.

Keywords: storage allocation, automated container terminal, upper level model, PSO algorithm

INTRODUCTION

Container terminals are important interfaces of global container transportation, which connect trucks on land and container vessels over sea. Different in arrival and departure directions, containers passing through a container terminal could be divided into three classes. One is inbound containers from vessels to trucks; the second is outbound containers from trucks to vessels; the third is transshipment containers from vessels to vessels. No matter the class it belongs to, one container is unloaded to the storage yard on its arrival, and stored there for some time till it is loaded to some other vessel or truck and leave the terminal.

Storage space allocation is a decision problem in determining the stacking location of containers in the storage yard,

especially in Asian container terminals. Before the arrival of one container vessel, some of the storage space in the yard are designated for the outbound and transshipment containers to the vessel, and some other are designated for the inbound and transshipment containers from the vessel. Although the specific stacking locations are not determined in this allocation, it is confined the storage spaces available for the containers from and to the vessel. It is widely agreed by terminal operators that, proper allocation of storage spaces has a far-reaching impact on the loading and unloading efficiencies of the vessels, and at the same time contributes a lot to a high utilization of the storage space.

Following the trend of large vessels, automation is nowadays a trend for container terminals in major ports all over the

world. In recent years, the capacity of the largest container vessels have reached up to 18000 TEUs, with their lengths kept at not much more than 400 meters. To serve these huge vessels collecting and discharging probably thousands of containers at a time, terminals built in the past few years are much larger than before, with yard areas extending, and stacking cranes equipped in the yard increasing at the same time. In case that the yard cranes are operated at site following the traditional way, in which one worker is needed for every yard crane in work, a large number of operators are needed for the terminal and the manual cost will be very high. As a result, yard cranes in large terminals are usually automated reformed, hence multiple cranes could be remote controlled simultaneously by a single operator, and the manual cost of the terminal could be kept in a reasonable range.

Storage allocation is an important decision in conventional container terminals, while things are a bit different in the current automated ones. In these automated terminals located mainly in Europe, the storage spaces of containers to be loaded onto or unloaded from some vessel are decided by rule, i.e. to the nearest crane or to the crane with the shortest queue, while no space allocation is applied. Rule-based allocation is a practical strategy in European automated container terminals, where the information of some containers is missing or incorrect now and again. However, in other automated container terminals where the container information is always complete and correct, pre-determined storage allocation plans may lead to better performance.

This paper deals with the storage allocation problem in automated container terminals where container information is complete and correct, especially for those terminals under construction in Asian countries which will be put into use in the near future. This problem is divided into two levels, and only the upper level is discussed in this paper. The rest of the paper is organized as follows. Section 2 gives a literature review on storage allocation problems in conventional terminals and storage allocation strategies in automated ones. A detailed description to the automated container terminal and storage space allocation is given in section 3. Section 4 presents a mixed integer programming model with multiple objectives for the storage space allocation problem in automated container terminals. In section 5, a modified Particle Swarm Optimization (PSO) Algorithm is proposed to solve the model. In section 6 numerical experiments are conducted to show the performance of this algorithm in various problem scales. A conclusion is driven in the last section.

LITERATURE REVIEW

Storage space allocation is a fully studied problem in conventional container terminals. Some researchers focus on allocations within a given time length, while others are interested in the designation of yard templates which could be used repeatedly every week.

Mi Chao et al. [1-5] have done a bunch of researches about information acquisition of inbound and out bound containers, which supports an information-complete storage space

allocation decision.

Kap Hwan Kim and Kang Tae Park [6] discussed the storage space allocation problem for outbound containers only. With no grouping strategy applied, containers are distinguished only by vessels. Blocks were treated as simple container holders, without consideration on structure. The objective of their problem is to minimize the total travelling distance.

Chuqian Zhang et al. [7] studied the container storage allocation problem in Hong Kong. Inbound and outbound containers are both considered in their problem, and a rolling horizontal approach is applied, following which storage plan is made daily for the coming three days. Balance of workloads was set the objective of their problem, while special attention is paid to workloads related to vessel loading and unloading. Still, no grouping strategy or block structure is mentioned in their work.

Thanks to the team led by Loo Hay Lee and Ek Peng Chew, many researches has been done to the storage allocation problem in transshipment hubs, as for terminals in Singapore. Loo Hay Lee et al. [9] studied the storage yard allocation problem on a known yard template, considering only the outbound and transshipment containers that are to be loaded. Blocks were divided into sub-blocks with fixed capacity, and the set of sub-blocks which could be reserved for vessels was known. They considered both 20ft and 40ft containers, while grouped only to their destination vessel respectively. A work balancing protocol was proposed to reduce traffic congestion, and a model was built for a weekly template in which the number of yard cranes deployed to the allocated storage locations were minimized. Yongbin Han et al. [11] presented an extension to the former study. In their problem, a sub-blocks could be reserved for any vessel in the planning horizon. The considered the workloads from both loading and unloading. Liang Ping Ku et al. [17] proposed a generic yard plan template problem specification, which was believed to contribute to the design of an IT-based search engine for an optimum planning strategy. In a later research [19], they proposed a robust approach in finding a nimble yard template for a storage spaces allocation problem under uncertainty, in which the arrival schedule of vessels might change. Xinjia Jiang [23, 30] researched further into dynamic yard planning problems. In a former study [18], a space sharing strategy was proposed for the yard template planning problem. Some bays in a block are treated as sharing spaces, which could be shared by the sub-blocks on both sides. In a latter study [30], a flexible space sharing strategy was further proposed, in which storage locations could be reserved alternately for containers of different vessels. Both strategies led to higher utilization of the storage spaces.

Weijian Mi et al. [12] sought into storage allocation problem for outbound containers only. The objective function of their model was a combination of travel distance, work balance among blocks and work balance among vessels.

Mohammad Bazzazi [13] proposed an extended storage space allocation problem for inbound containers. Different types of containers were considered in the problem, and the objective of their model was the balance of workloads among blocks in every time period.

Der-Horng Lee et al. [14] proposed an approach which integrates the truck scheduling problem and the storage allocation problem. Containers were allocated to storage locations which led to a minimized total travel distance of trucks.

Etsuko Nishimura [15] addressed the storage allocation problem of transshipment containers. Transshipment containers were grouped to different feeder vessels, and each group was allocated a block hence the container handling time of the feeder ships could be minimized.

Yanwei Zhang et al. [16] studied the storage planning problem for outbound containers in container terminals. Only 20 ft containers were considered in the problem, and a three level model was built for this problem. In the first level, containers of the same vessel were allocated to blocks which lead to a minimized total transfer distance.

Mingkun Li and Shiyang Li [20] studied the yard template designing problem for outbound containers in terminals with limited storage space and heavy workload. Spaces are allocated in bays, which could be reserved for various vessels in different periods.

Youn Ju Woo and Kap Hwan Kim [21] proposed a method for allocating storage spaces to outbound containers grouped to destination ports. Spaces were reserved on arrivals of containers, and a rule-based method was addressed for determining the sizes of spaces to be reserved.

Yeon-Ho Jeong et al. [24] proposed a block assignment method based on QC schedule. Aiming at the balance of workloads, a block was selected for a coming container group according to YC workload and space availability.

Der-Horng Lee et al. [25] studied the management of transshipment flows in a transshipment container terminal. Containers to different feeder vessels are located to different blocks hence both the total travel distance and the workload imbalance could be minimized. In a later study [28], he extended the problem to a large container transshipment hub with multiple terminals. Containers were grouped to inbound and outbound vessels. An integral programming model was developed, for the berthing terminal of every vessel, and the storage block for every container group, aiming at the minimization of total inter-terminal and intra-terminal handling costs.

Pei-yu Li and Xiao-ming Sun [26] addressed the storage space allocation problem in a novel container terminal layout, in which containers are carried between the quayside and the storage yard by vehicles running on crossing rails. Some rails were laid parallel to the quay line below the QCs, while others were perpendicular to the quay line, connecting the rails laid at the quayside, and YCs in the blocks. Given that the number of transport channels limited, a non-linear model was proposed, aiming at the balance of YC workloads in every planning horizon.

Lu Chen and Zhiqiang Lu [28] addressed the storage location assignment problem for outbound containers, which was a two stage problem consisting of a storage space allocation problem in the upper level and a storage location determination problem in the lower level. In the upper level, containers were

assumed to be the same size, and grouped by the destination ports. Container groups are allocated to bays, aiming at the minimization of total travel distances, and balance of workloads among blocks.

Seung Hwan Won et al. [29] proposed an integrated decision-making framework for yard-planning problem in container terminals, in which various resources were considered, including spaces, YCs, yard trucks and driving lanes. A minimum-cost network-flow model was built, with an objective to minimize the total costs of container flows.

Deniz Türsel Eliiyi et al. [31] considered an outbound container storage problem at some container terminal in Turkey. They proposed a two-stage approach, similar to Lu Chen and Zhiqiang Lu [23], in which containers of the same vessel are assigned to several bays in the storage yard in the first step, while their objective was that containers of the same vessel should be located as concentrated as possible.

Omor Sharif and Nathan Huynh [32] modeled a container terminal as a network of berths, gates and blocks. The storage space allocation problem of containers among blocks was solved in real-time, with the objectives of workload balance and travel distance minimization.

L Zhen [34,36] made an exploratory study in yard template designing problem of transshipment hubs under uncertainty. This research was a further research of Liang Ping Ku et al. [20], for reason that the berthing location was treated uncertain, aside from the arrival time of vessels.

Dissimilar to the conventional container terminals, in automated ones the storage allocation of containers are decided in real-time (online) by rules. To the extent of our knowledge, no research could be found on the storage allocation problem in automated container terminals. In this regard, simulation is a usual approach to study different allocation strategies.

Rommert Dekker et al. [10] investigated into online container stacking policies at an automated container terminal. Two stacking strategies, namely random stacking and category stacking, are compared by simulation. The results showed that, the former strategy stacking containers of the same category in the same stack outperformed the latter one stacking containers in random stacks for fewer reshuffles.

Bram Borgman et al. [18] evaluated the performance of random strategy and leveling strategy on stacking a container by simulation. The difference of the two online strategies was, whether the stacking position of a container was decided in random, or an unfilled stack got the priority in case that the top container was to be retrieved later. Trade-off could be observed in simulation experiments, between travel time of the cranes and the probability of reshuffles.

Taejin Park et al. [22] proposed an online search algorithm for inbound containers which dynamically adjusts and optimizes a stacking policy. For every incoming container to the storage yard, the stacking block was determined depending on the short-term workload of cranes in each block, while the stacking position was determined in comprehensive considerations.

Mingzhu Yu and Xiangtong Qi [33] focused on the retrieval efficiency of inbound containers in automated

container terminals. The stacking positions of containers were determined following a segregation strategy, in which containers were always stacked upon another one that is to be retrieved later. It is verified in this paper that, the approach allocating multiple container batches together outperformed the approach allocating one batch at a time.

The ultimate goal of our research is, to discuss the potential benefit of storage allocation in automated container terminals, in case that it could be applied instead of online strategies in future automated container terminals. However, only part of the storage allocation problem is studied in this paper; the remaining part is left to further research, so as the benefit evaluation of storage allocation plans when applied instead of online strategy. The works in this paper could be characterized as follows.

- » It is put forward in this paper the storage allocation problem in automated container terminals, a novel problem to the existing ones in conventional terminals. Moreover, it is proposed that this problem could be decomposed into two levels.
- » A mixed integral programming model with rolling horizontal approach is proposed for the upper level of the problem.
- » A modified particle swarm optimization (PSO) algorithm is proposed to solve the simplified model. The modified algorithm makes a multi-stage search process with multiple swarms, hence better solution could be found than using the original PSO algorithm. Moreover, for large scale problems in particular, a simplified coding method is proposed, which leads to shorter particle length and faster convergence.

PROBLEM DESCRIPTION

Storage allocations in conventional and automated container terminals are similar problems while not the same. The priorities of the two allocations varies, according to differences in block layouts and operation modes between the two terminals. Therefore, storage allocation in automated container terminals could be treated a novel problem from that in conventional ones.

STORAGE ALLOCATION IN CONTAINER TERMINALS

To launch the container handling works of vessels, a series of decisions must be made before the handling process whether in a conventional terminal or an automated one. According to Steenken D et al. [8], these decisions include but are not limited to:

Berth allocation: to allocate a berth for every vessel before its arrival, and to predict the departure time of the vessel.

Storage allocation: to reserve spaces in the yard for the temporal storage of outbound, inbound and transshipment containers.

Stowage planning: to assign the containers stacked in the yard and to be loaded one by one to the respective cells of their

destination vessel.

Quay crane scheduling: to allocate quay cranes to vessels or sections of vessels, and to determine the handling sequence of each quay crane.

For every vessel to visit the terminal, the four decisions above are executed in sequence, as shown in Fig. 1 below. Berth allocation is the first decision to be made, after which the storage allocation, in which the space for containers to be loaded onto and unloaded from the vessel is reserved on the basis of berth allocation. Generally, the spaces reserved for containers will not be quite far from the berth allocated to the vessel, and the storage allocation must be done before the terminal starts to collect outbound containers for this voyage. Stowage planning is carried out after the cut-off time of a vessel, when the container collection of this voyage expires. The quay crane scheduling is made later before the vessel handling.

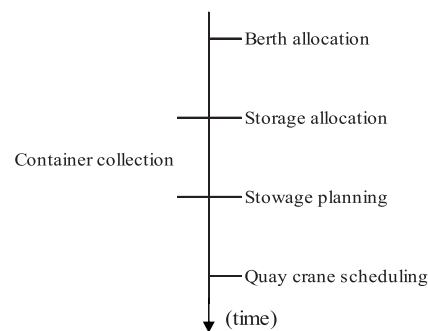


Fig. 1 Sequence of main decisions before vessel handling

The storage spaces in the storage yard of a container terminal is separated into blocks, which are continuous storage spaces separated by roads or some other spaces not for storage. Blocks in a container terminal are lined up, while the layouts of blocks differs in conventional terminals from automated ones. The storage space in a block is a three-dimension bay-row-tier space, as is shown in Fig. 2 below. Generally, a 20ft container is stored in a single cell, and a 40ft container is stored in two neighboring cells in a same row and a same tier. Two neighboring bays in the same block is often called a double bay, which is designated for containers larger than 20ft. Containers even larger than 40ft are put in double bays in the two double

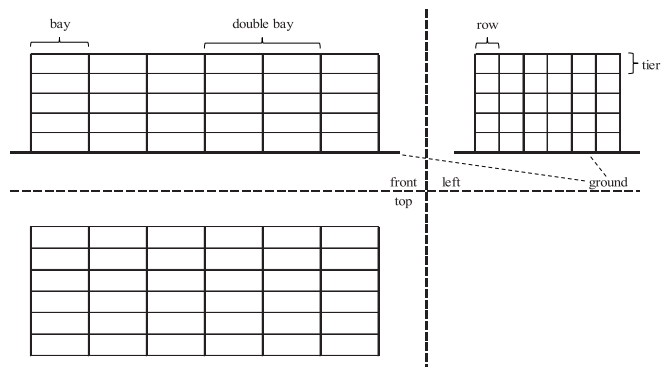


Fig. 2 Orthographic view of a block

bays at the ends of a block. There are no brackets between neighboring cells in a block, hence containers located in the same bay (or double bay) and the same row are piled up as a stack. It is the practice of container terminals that, containers located in the same stack should be of the same size.

To the convenience of the following stowage planning, spaces in a container terminal are allocated to containers in units of container groups when making a storage plan. Generally, containers from or to a vessel is divided into container groups, and some blocks or some bays in some blocks are allocated to such groups but not to single containers. Within a container group, specific stowage space is not a major concern when making the plan. Outbound containers are usually grouped according to sizes, types, destination ports, weight levels, and etc., hence containers collected in a same stack could be interchangeable when making a stowage plan, which is an effective method to reduce reshuffles when loading them onto the vessel. Similarly, inbound containers are also grouped according to sizes, types and owners. Because inbound container has less groups, it is a common scene in container terminals that, the scale of inbound container groups are often much larger than the scale of outbound groups.

The fundamental objective of storage allocation is, to optimize vessel handling efficiency while ensuring that storage capacity of the terminal is not exceeded. Handling of every container from or to a vessel is a multi-stage process using Quay Cranes (QC), Yard Cranes (YC) and horizontal movers (HM), which is the handling system of containers. To load a container from some block to a vessel, an YC picks it up and puts it onto a HM, which sends this container to a QC according to some work plan, after which the container is loaded by that QC onto the destination vessel. A reversed process is carried out when unloading a container from a vessel to some block. As the scarcest and most efficient equipment in the handling system, QCs should be taken full advantage of to maximize the handling efficiency of the whole system. In other words, QCs should be kept handling as long as possible. For this purpose, attentions must be paid to following two key features.

- Numerical relationship between QC and YCs.

Since the technical handling efficiency of QCs are much higher than that of YCs, it is a major key point in ensuring the handling efficiency of QCs to keep a “one-to-many” relationship between QCs and YCs. Thus, for each QC, it is preferred that multiple YCs could be designated to a QC handling thread, otherwise the operation of the QC would be interrupted because of lack of YC handling capacity. However, it is hard to determine the exact best number of YCs that is needed to serve a QC, for reason that YCs could handle some extraneous containers when serving the QC, i.e. containers handled by some other QC, or containers collected from / delivered to somewhere out of the terminal.

- Turnaround times of HMs.

Turnaround times of HMs is another key point in keeping a high QC handling efficiency. In the visit interval of a QC,

a HM spends time at some YC and on the road, Hence the turnaround time of a HM could be lengthened by far travel distance, blocks on the road, and long waiting time at some YC. Repeated long turnaround times may interrupt the handling of QC, no matter how many HMs are designated to it.

A major difficulty in making a storage plan is that, the handling launch time and duration of the container groups could not be estimated accurately when making a storage plan. Since the stowage plan and QC schedules are made afterwards, handling sequences of the container groups and containers within each group are unknown for storage space allocation. If two groups are located in spaces where only one YC is allowed to work at a time, an YC will have to take account of them simultaneously when they are handled at the same time, which causes inefficiency.

Due to differences in layouts and operations, as are listed below, storage allocation problems in conventional container terminals and in automated ones are a bit different. Except for the priorities on travel distance, work balance and space utilization, the two problems pay attentions to different targets, which are explained in the rest of this section.

- Direction of blocks and locations of Input / Output (I/O) points
- Numerical relationship between YCs and blocks
- Operation modes of YCs

COMPARISON OF STORAGE ALLOCATIONS IN TWO KINDS OF TERMINALS

Storage layouts in conventional container terminals and automated ones are different [30]. Fig. 3 is a typical storage layout of a conventional container terminal. Blocks are positioned in parallel to the quay line, and the I/O points are scattered on a path lane for HMs alongside the block. At every block, storage and retrieval of containers to or from one bay are executed at a same I/O point. The YCs could be either Rail Mounted Gantry Cranes (RMG) that are confined to blocks on the same rail track, or Rubber Tired Gantry Cranes (RTG) that could move freely between all the blocks. As a result, the number of YCs that work at the same block is variable at different times. The presence of an YC and a HM at the I/O point is required when storing or retrieving a container, and no gantry move is needed in the handling process.

Travel distance between allocated spaces and the berth position of vessels is a major objective to be optimized in storage allocation problems in conventional container terminals. This distance should be minimized to reduce turnaround time. Work balance among blocks is also paid much attention to, since it contributes a lot to the “one-to-many” relationship between QCs and YCs. However, due to the fact that multiple YCs are allowed to work simultaneously at one block, workload balance is often carried out among sections of some adjacent bays within the blocks, called “sub-block” as in [4, 12, 18, 20], in which only one YC is permitted at most. Space utilization is the least important priority to be considered. In most cases,

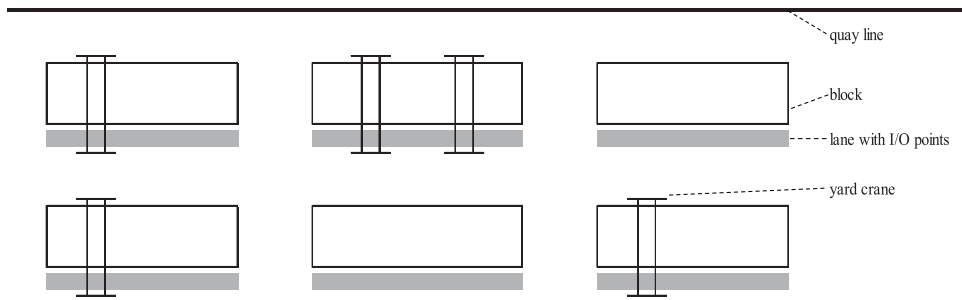


Fig. 3 Storage layout of a conventional container terminal

it is only treated as a constraint of the allocation problem.

Besides the three priorities above, there are other optimization factors, and some principles should be followed when making a storage plan, which are listed below.

- Interference of HMs between sub-blocks in a same block should be considered. Since the I/O points of a same block are located on the same path, hence a HM may be blocked by some other HM ahead, either at its destination I/O point or still on the way, which adds to the HM's turnaround time. It is recommended that inbound containers and outbound containers are allocated with spaces in different blocks, hence interferences between HMs for loading and unloading in the same block could be prevented.
- Distance of the nearby bays allocated for the same container group should also be minimized, which is related to gantry movements of YCs when handling these containers in sequence. Spaces allocated in a same sub-block to the same container group should attract neighboring bays to store similar containers, hence the gantry movement of YC will not be very long, which leads to shorter waiting time of HMs at the YC, and shorter turnaround time of HMs as a result. Likewise, containers allocated to the same bay should be of same size.
- Large container groups should be located in multiple blocks, or multiple sub-blocks distant to each other in some same block. Owing to the fact that containers in a same group are always handled in succession by one QC, locating them in such a scattered way enables simultaneous handling of multiple YCs, as to keep the "one-to-many" relationship between QC and YCs.

Fig. 4 is a storage layout of an automated container terminal. Distinct from the conventional ones, terminal blocks are positioned perpendicular to the quay line, and I/O points are located at both ends of the blocks. Seaside I/O points are designated for vessel loading and unloading, while landside points are for container collection and delivery. YCs in this layout are almost all RMGs characterized by high gantry moving speed, known as Automated Stacking Cranes (ASC). The Number of YCs in every block is fixed, usually 2 YCs in one block, in which the seaside YC focuses on vessel loading and unloading, while the landside one is for container collection and delivery in the daylight, and storage reshuffling at night. Differ from those in the conventional terminals, YCs in this layout following a double-cycling operation mode. An YC could pick up a container from some bay in the block, carry it to the I/O point and put it down, then pick up another container from the I/O point, carry it to some bay in the block and put it down. In this way, an YC could handle stacking and retrieving containers alternatively, known as the double-cycling operation mode. And YC gantry movement is inevitable in stacking or retrieving containers, and the operation time of different bays varies. The further one bay is to the I/O point, the longer the YC operation time will be.

In an automated container terminal, travel distance between allocated spaces and the berth position of vessels is no longer a major optimization objective of the storage allocation problem. HMs for vessel handling are confined between the quay line and the blocks, hence the travel distances are much shorter than those in the conventional terminals. Owing to the fact that there is only one YC in each block for vessel handling, work balance among blocks should be seriously considered. Still, space utilization is the least important objective to be considered. Consequently, there are some differences between

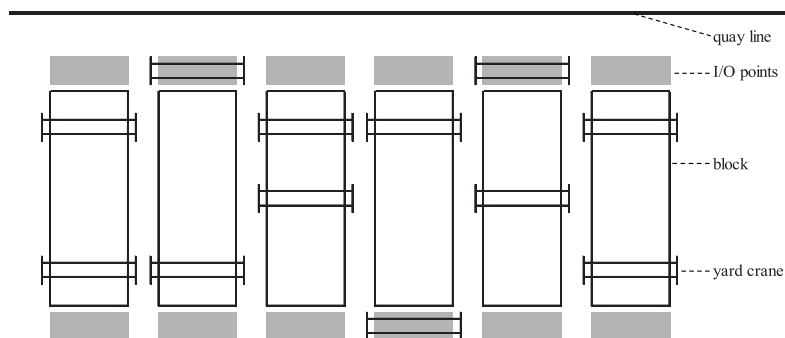


Fig. 4 Storage Layout of an automated container terminal

storage allocations in conventional terminals and in automated ones, which are listed below.

- Influences between I/O points in automated container terminals are much less than those in the conventional ones, to the extent that it could even be omitted when making a storage plan. Consequently, there is no need to distinguish inbound and outbound containers, and they could be located in the same block.
- It is no longer recommended that containers of the same group should be located in neighboring bays, and containers of different sizes could be allocated in the same bay. However, it will be appreciated that container groups which is likely to be handled simultaneously are allocated with bays closer to the I/O point.
- Storage allocation in automated container terminals could be treated as a two level problem. The upper level is to determine only the number of available stacks allocated to each container group; the lower level decides the specific locations of these stacks in each block. Solutions of the upper level are responsible to the “one-to-many” relationship between QCs and YCs, the travel distance and the space utilization. Solutions of the lower level are only related to YC handling times of the containers, which have nothing to do with the upper level model. As a result, the storage allocation problem in automated container terminals could be treated in a two-level manner, in which the upper level and lower level problems are solved separately to improve computing efficiency.

MATHEMATICAL MODEL

Storage planning in automated container terminals could be abstracted into planning models executed following a rolling-horizon approach, a common way in making storage plans in the conventional container terminals. As mentioned before, only the upper level model is proposed in this section.

PLANNING HORIZON AND ASSUMPTIONS

Automated container terminals runs in two modes by day and at night. Although vessel handling is carried out 24 hours a day in the workdays, container collections and deliveries are handled only in the daylight. During the night hours when no HM is allowed into the terminal, containers stored in the blocks are reshuffled if necessary. As described in [30], mainly two kinds of reshuffles are executed overnight. One is called re-marshalling, in which some containers to be loaded in the coming day are moved to a new location near the seaside end. The other is called pre-marshaling, in which some containers unloaded from vessels are carried in the opposite direction. Thanks to the reshuffles during the night, outer HM and vessel handlings in the next day could be fastened for shorter YC gantry movements.

Due to the operation mode alternations every day, in automated container terminals, a daily storage plan is needed. As shown in Fig. 5 below, the horizon of a storage plan covers a

whole day, while the deadline of a storage plan for the coming day is laid to the beginning of the current night, before the reshuffles are executed. A reshuffle plan should be made just before the storage plan, hence the storage spaces available for the inbound containers in the next day could be determined. This pattern goes on continuously, howbeit the reshuffle plans are not content of this paper.

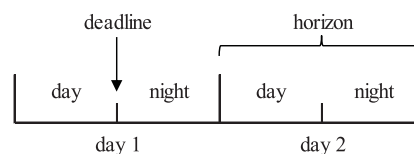


Fig. 5 Deadline and horizon of a storage plan

A mixed integral programming model is proposed here for every storage plan, based on several assumptions as are listed below:

- (1) The total volume capacity of the blocks are always enough for storage allocation.
- (2) Container information is all known when making a new storage plan, so as the available storage spaces in each block.
- (3) The berth plan is known, including the berthing positions of the corresponding vessels, so as the berthing start times and berthing end times. On this basis, travel distances between container groups and blocks could be calculated, and the handling time windows of container groups are determined as the berthing start time and berthing end time of the corresponding vessel.
- (4) Only 20ft and 40ft general containers are considered in this model. Containers of other sizes or types are excluded, for instance 45ft containers, refrigerated containers, and etc.
- (5) Only inbound and outbound containers are considered in this model. Transshipment containers are not concerned in this paper.
- (6) Reshuffles at night could be always well executed, hence outbound containers to be loaded in the coming day could be all positioned in the storage spaces as defined in the storage plan, and inbound containers unloaded in the current day could be relocated to some positions near the landside I/O points.
- (7) Containers are divided into groups before storage planning, according to rules as described in section 3.1. Storage spaces are allocated to container groups, but not to individual containers.
- (8) Spaces are allocated in stacks. One stack could be allocated to one container group at most. Moreover, number of stacks needed for every container group is pre-determined.
- (9) Container groups are preferred to be divided and scattered in a recommended number of blocks. The value of these recommended numbers are related to the scale and direction of the container groups, and could be determined when making a storage plan. Based on this division, a new concept, namely allocation unit, is used in the model instead of container group. The number of allocation units for every container group equals to its recommended division

number, and the total number of stacks required for the allocation units equals to that of the container group.

For better understanding of the assumptions, some explanations of assumption (3), (8) and (9) are given here as a further step. In assumption (3), it is believed that the handling time of container groups cannot be accurately predicted since the handling sequence among them are not decided when making a storage plan. As a result, the handling time windows of container groups are determined according to the berth start time and end time of the corresponding vessels in this paper. Shorter time window for container groups will be better in case that the handling sequences of container groups could be pre-determined. In assumption (8), the number of free stacks needed for a container group depends on the number of containers in the group, and the volume of a free stack. In this paper, this number is set as the minimum of free stacks that could hold all the containers in the group. Larger numbers will also be feasible, while leading to less space utilization. In assumption (9), division numbers of the container groups are fixed to recommended values. This assumption causes a smaller solution space excluding storage plans in which container groups could be scattered in a number of blocks that differs to the recommended value. Adoption of this assumption leads to a great reduction of decision variables needed in this model. However, in case that the spaces needed for allocation is close to the total available spaces in the terminal, the solution of this model may be probably not a satisfactory storage plan, or even no feasible solution could be found at all.

THE MODEL FORMULATION

Notations used in the upper level model are listed as follows.

- I total number of allocation units, indexed by integer i and j . $1 \leq i, j \leq I$.
- G total number of groups, indexed by integer g . $1 \leq g \leq G$.
- B total number of blocks, indexed by integer b . $1 \leq b \leq B$.
- S_i size of allocation unit i . If unit i consists of 20ft containers, $S_i = 1$; else $S_i = 2$.
- L_i direction of allocation units. If unit i consists of outbound containers, $L_i = 1$; else $L_i = 2$.
- WS_i start of time window of allocation unit i .
- WE_i end of time window of allocation unit i .
- D_{ib} travel distance between block b and the handling point of allocation unit i .
- DU_i maximal travel distance between unit i and the blocks.
- DL_i minimal travel distance between unit i and the blocks.
- N_g number of stacks needed for group g .
- R_{ig} relationship between unit i and group g . If unit i belongs to group g , $R_{ig} = 1$; else $R_{ig} = 0$.
- P_g division number of group g .
- F_b maximal number of 40ft free stacks in block b .
- T_b maximal number of 20ft free stacks in block b .

- δ_{ij} time window overlap of allocation units i and j .
- μ_{ij} total time length of time windows of allocation units i and j .
- η_{ij} the time span of time windows of allocation units i and j .

Decision variable are shown as follows.

- x_{ib} 0-1 variable. If allocation unit i is allocated to block b then $x_{ib} = 1$, else $x_{ib} = 0$.
- n_i nonnegative integer variable, for the stacks needed for allocation unit i .

The constraints in this stage are listed as follows.

$$\sum_i x_{ib} n_i (S_i - 1) \leq F_b, \forall b \quad (1)$$

$$\sum_i x_{ib} n_i S_i \leq T_b, \forall b \quad (2)$$

Equation (1) and (2) are for the volume capacities of blocks. Besides the volume capacity constraint on TEU as in Equation (2), special volume capacity constraint for 40ft stacks should also fulfilled as well, hence the containers allocated to the block could be indeed placed in the block. An example is shown in Fig. 6, which is a top view of a block section. In this block section of 4 bays and 3 rows, 6 stacks are occupied by some other containers and could not be used in the current storage plan, as the gray cells in the figure. There seems to be enough spaces for 3 40ft stacks by checking the TEU capacity, however only 1 40ft stack could be actually placed in this block section.

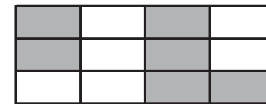


Fig. 6 Illustration for constraints on block capacity

$$\sum_i n_i R_{ig} = N_g, \forall g \quad (3)$$

Equation (3) is a constraint on the total stack number of allocation units in a same group.

$$\sum_b x_{ib} = 1, \forall i \quad (4)$$

Equation (4) means that every allocation unit should be allocated to one block only.

Some objectives are listed as following.

$$\text{Min } f_1 = \text{Min} \frac{\sum_{i,b} x_{ib} n_i (D_{ib} - DL_i)}{\sum_{i,b} x_{ib} n_i (DU_i - DL_i)} \quad (5)$$

Objective (5) is for the minimization of travel distance. Since travel distance is not a major priority in making a

storage plan, this objective is presented in a normalized form.

$$\text{Min } f_2 = \text{Min } \sum_i \left| n_i - \sum_g (B_{ig} N_g / P_g) \right|^2 \quad (6)$$

Objective (6) means that it is preferred that the number of stacks in need for every container groups are divided evenly.

$$\text{Min } f_3 = \text{Min } \sum_{b,i,j} x_{ib} x_{jb} \delta_{ij} \text{Min}(n_i, n_j) \quad (7)$$

$$\delta_{ij} = \begin{cases} 0, i = j \text{ or } L_i \neq L_j \\ \frac{\mu_{ij} - \eta_{ij} + |\mu_{ij} - \eta_{ij}|}{2(WE_i - WS_i)} + \sum_{b,g} x_{ib} x_{jb} B_{ig} B_{jg}, \text{ otherwise} \end{cases} \quad (8)$$

$$\mu_{ij} = WE_i - WS_i + WE_j - WS_j \quad (9)$$

$$\eta_{ij} = \text{Max}(WE_i, WE_j) - \text{Min}(WS_i, WS_j) \quad (10)$$

Objective (7) means that allocation units of the same direction with overlapping handling time windows are better not allocated in the same block. Equation (8-10) are definitions of parameters δ_{ij} , μ_{ij} and η_{ij} respectively. These equations are concluded from all the possible overlap schemes of two units' time windows, as is shown in Fig. 7 below. It is supposed in the figure that, the time window length of unit i is longer than that of unit j . The time window of unit i starts earlier than that of unit j in scheme (a), (b) and (c), while it is opposed in scheme (d) and (e). In scheme (a) handling of unit j starts later than the end of unit i 's time window; in scheme (b) handling of unit j starts before the end of unit i 's time window; in scheme (c) handling of unit j ends before the end of unit i 's time window. In scheme (d), handling of unit j ends before unit i 's time window, while in scheme (e) handling of unit j ends after the beginning of unit i 's time window. It could be concluded from all the schemes that, overlap occurs when and only when sum of time window duration of the two units is longer than their time span, which is the time range between the earlier start time and the later end time of the two windows. For reason that allocation units of the same container group are preferred to be allocated in different

blocks, equation (8) is designed that δ_{ij} will be larger than 1 when and only when unit i and j belongs to a same group and allocated to a same block.

The global objective is shown as equation (11) below, in which α_1 , α_2 and α_3 are coefficients for objectives (5), (6) and (7) respectively.

$$\text{Min } f = \text{Min } \alpha_1 f_1 + \alpha_2 f_2 + \alpha_3 f_3 \quad (11)$$

SOLUTION METHOD

Owing to the fact that the objectives formulas f_2 and f_3 in the model are not linear, the model cannot be solved using those well-developed linear solvers, including CPLEX as an instance. Intelligence algorithms are feasible methods in solving these none liner optimization model. Considering that the scale of storage allocation problems in practical terminals may be quite large, Particle Swarm Optimization (PSO) seems a promising optimizing mechanism for fast convergence. Since single PSO searching process will probably end in a local optimum, a PSO-based progressive (PSOP for short) algorithm is proposed in this paper as the solution method of the model raised in section 3. In this progressive algorithm, the best solution found in the current searching process is treated as knowledge in a next searching process, which attempts to get a better solution than the current stage.

ENCODING REPRESENTATION AND GROUP INITIALIZATION

In this algorithm, a particle is encoded in an array, which has a length of twice the number of allocation units. The former half of this array are real numbers, the minimal integer larger than which indicates the number of block that the units are allocated to. The latter half of the array are integer numbers, indicating the number of free stacks needed for the allocation units. Fig. 8 gives an example of a particle for a solution including two allocation units. In this particle, allocation unit 1 needs 7 free stacks and is allocated to block 1, while allocation unit 2 needs 6 free stacks and is allocated to block 6. As a distinction of the two halves of a particle, notation pf is used for the former half of the array, while pl is

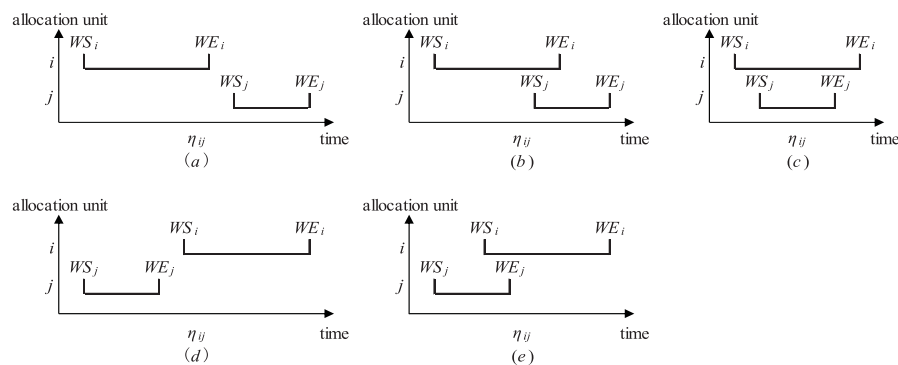


Fig. 7 Possible time window overlap schemes of two allocation units

for the latter half. The speed of a particle is coded as an array of real numbers. The length of the speed array equals to the number of allocation units.

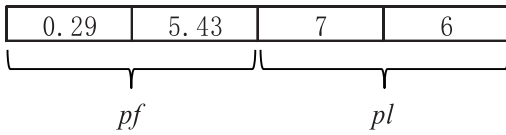


Fig. 8 An example of particle encoding

The particles, speeds, the swarm's best array and the particles' best arrays, are initialized in the following manners when a searching stage starts. Elements in the former half of a particles are randomly valued in range $(0, B)$, and those in the latter half are given an integer number, valued according to the container group which the allocation units belong to. In order to minimize the value of f_2 in the initialization, number of free stacks for the allocation units in a same group g are valued as integers near N_g/P_g , and the sum of these numbers are kept as N_g at the same time. The speeds are valued randomly in range $(-B, B)$. The particles' best arrays are set the particles themselves, and the swarm's best array is set the current best particle in the swarm.

FITNESS FUNCTION AND PARTICLE REPAIR TECHNIQUE

With the encoding representation and group initialization method described above, constraint (3) and (4) are already fulfilled. However constraints (1) and (2) are not satisfied yet: the capacity of some block may be exceeded so that too many allocation units are allocated to it at the same time, which leads to an infeasible solution. Due to the random initialization and iteration, dissatisfactions of particles with constraint (1) and (2) are inevitable in the searching process. Hence, a punishment is added to the fitness function for the volume exceeding of blocks, and a repair technique is proposed for infeasible particles.

The fitness function F of particles is defined as equation (12) below. In this equation, f is defined as in equation (11), E^F is the total number of 40ft stacks exceeding the block capacities, E^T is the total number of stacks in TEU that exceed the block capacities. Notation α_p is the punishment coefficient, valued much larger than α_1 , α_2 and α_3 as in equation (11).

$$F = f + \alpha_p (E^F + E^T) \quad (12)$$

The particle repair technique is designed with greedy strategy. The repair procedure starts with the array of current particle. The technique changes the array step by step. A new array is generated from the current array by moving one container from an exceeded block to another, in which an allocation unit of the same container group is allocated. Every possible move makes a new array, and the fitness value is calculated. Only the best array is kept as the new particle array, and other arrays are deleted. In case that the current array is

feasible or no better than the last one, it is used to replace the array of the particle and the repairing ends. Otherwise, the repairing goes on to a next step.

Although the repairing technique is effective in changing an infeasible array into a feasible one, the burden of repairing process on time consumption is quite heavy. Usage of repairing technique in the searching processes should be limited, otherwise the computation time of the algorithm will be unacceptably long. Consequently, this technique is applied only to some infeasible particles, the fitness value of which are no larger than a pre-defined value. Moreover, repairing is not executed in every iteration of the searching process.

ITERATION AND PROGRESSIVE SEARCHING STRATEGY

The total number of iterations is fixed in a searching process. In the first searching process, the former halves of particles are iterated following the standard iteration mechanism, as is presented in equation (13) and (14), and the latter halves are set as the initial arrays in every iteration. In the equations below, pf is for the former half of a particle array and v is for the speed array. pbf is for the former half of the particle's best array and sbf is that of the swarm's. w_v , w_p and w_s are coefficients, which decrease linearly as the iterations go on. Fitness value of particles are calculated in each iteration, and the best arrays of particles and the swarm are updated once better arrays are found in the searching process.

$$v = w_v \cdot v + w_p (pbf - pf) + w_s (sbf - pf) \quad (13)$$

$$pf = pf + v \quad (14)$$

The best solution found in the first searching process is probably not the best solution of the model. In search of a better solution, progressive searching are executed repeatedly, till the fitness value of the best solution found in the current searching process is not much better, i.e. to a predefined extent, than that of the last one. Mechanisms of a progressive searching and the first searching are almost the same. The only difference of progressive searching to the first one is the determination of the swarm's best particle. In the first searching process, this particle is a result of the current searching, while in a progressive searching process, the swarm's best particle is inherited from a last searching process.

Similar to the repair technique, progressive searching is as well a potential burden to the time consumption of the searching process, if not properly treated. The computation time of the algorithm may be quite long when progressive searching are executed repeatedly, while the decreases of best fitness values between two successive searching processes are very small. To avoid this, requirements are attached to the decreasing margin of best fitness values between successive searching processes. At the beginning of a searching process, a required best value F^* is calculated according to the best

fitness value of a last searching process F_{last} and an attenuation coefficient d , as is shown in Equation (15) below. In case that the best fitness value of this searching process is no more than F' , F_{last} is updated and another progressive searching starts. Otherwise, the algorithm terminates, returning the best particle array found in the last two searching processes as the solution.

$$F' = (1 - d)F_{last} \quad (15)$$

The outline of the PSOP algorithm is shown by flowchart as in Figure 9.

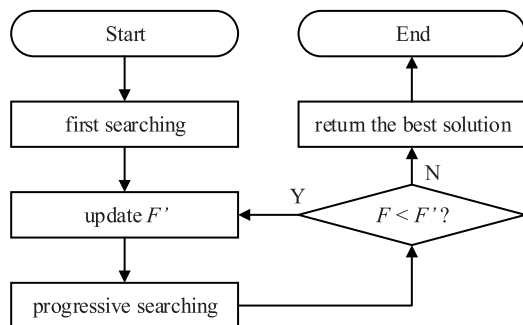


Fig. 9 Outline of the PSOP algorithm

NUMERICAL EXPERIMENTS

In order to verify the effectiveness of the PSOP algorithm, and to test the performance of the PSOP algorithm for storage allocation problems in different scales, experiments are carried out in solving examples generated in three terminals, different in berth lengths and total number of blocks, as shown in Table 1. In each terminal, a berth plan of vessels is first generated, so as the free spaces available for storage allocation in every block. On this basis, examples are generated in random according to various capacity rates (noted as r_s), which equals to the value of spaces needed for allocation divided by the total available spaces in the terminal. 10 examples are generated for every r_s , ranging from 0.05 to 0.8 with an interval of 0.05, and each example is solved 20 times with PSOP algorithm. All the experiments are executed in a desktop work station with 28 GB memory and 2 Inter Xeon E5520 @ 2.26 GHz processors.

The main purpose of the experiments in this section is to simulate applicable conditions of the model and algorithm proposed in this paper. As described in assumption (9), this model is a simplification of the practical storage allocation problem, hence it is not assured that a feasible solution could always be found, especially when value of r_s is rather large. Since the fitness value of the solution found is with little practical significance, a secondary attention is paid to the solving times only. Moreover, the benefit and burden of the progressive searching processes in solving the examples is investigated, so as the burden of repair processes. The parameters of the algorithm are set as follows. There are 30

particles in a swarm, and the iteration time of every searching process is fixed to 100. The values of α_1 , α_2 , α_3 and α_p are set 1, 1, 2 and 10 respectively. The value of w_v is fixed to 0.7, while values of w_p and w_s decrease from 1 down to 0 in every searching process. Repairs are executed every 10 iterations, while applied only to particle arrays of which the value $E^F + E^T$ is no more than 15. The value of d is set to 0.05.

Table 1 Scales of terminals

terminal scale	berth length (m)	total number of blocks
small	400	9
medium	700	18
large	1000	27

EXPERIMENTS OF SMALL TERMINAL

A berth plan of 4 vessels for a small terminal is shown in Fig. 10 below.

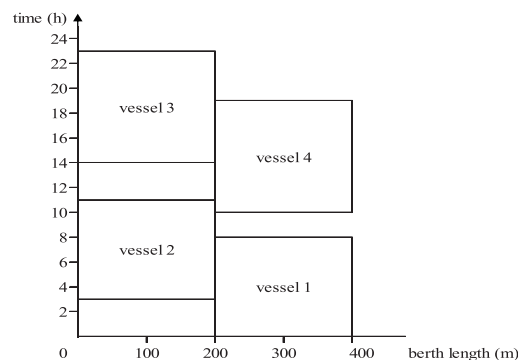


Fig. 10 Berth plan of the small terminal

The performance of the PSOP algorithm in the small terminal is shown in Fig. 11.

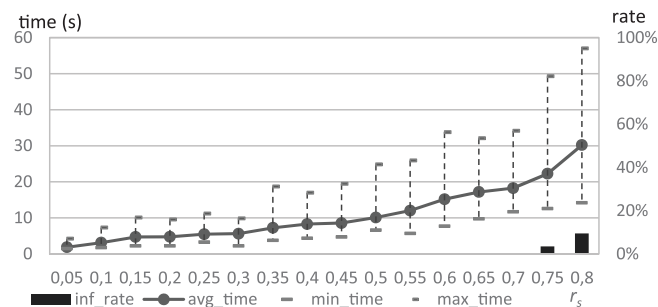


Fig. 11 Performance of PSOP in the small terminal

Attentions are paid to the solving times of the algorithm, and the chances of infeasible solutions in different capacity rates. Notations avg_time, min_time and max_time are the average, maximal and minimal solving times respectively, of which the values are presented by the left vertical axis.

Notation inf_rate is the chance of infeasible solutions among the examples, of which the value is presented by the right vertical axis. It could be observed from the figure that, the solving times increase with the capacity rate, and a solution could always be obtained in one minute. For examples with a capacity rate no more than 0.7, a feasible solution could be assured.

The effect and burden of progressive searchings are shown in Fig. 12. Notations avg_t_first and avg_t_prog are the average time of first searching process and progressive searching processes of the examples respectively. They are prepared in percentage by histograms. Notation avg_fit_dec is the percentage of fitness decrease after first searching processes. It could be observed from the figure that, progressive searching processes lead to a 8% decrease of fitness value on average, while taking roughly 1.4 times as long as the time consumed by first searching processes.

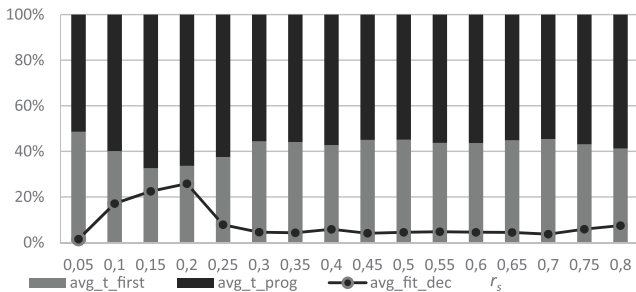


Fig. 12 Effect and burden of progressive searching in the small terminal

The burden of repair process is shown in Fig. 13 below. Notation avg_t_repair and avg_t_comp are the average time spent by repair processes and other computation processes, which are presented in percentage by histograms, and valued by the left axis. Notation avg_n_repair is the average times that repairing processes is executed in solving an example. Except for an inflection point near capacity rate 0.6, the average number of repairs executed in solving an example increase as the capacity rate raises. The percentage of time spent in repairing goes up with the capacity rate, up to roughly 20% when the capacity rate is 0.8.

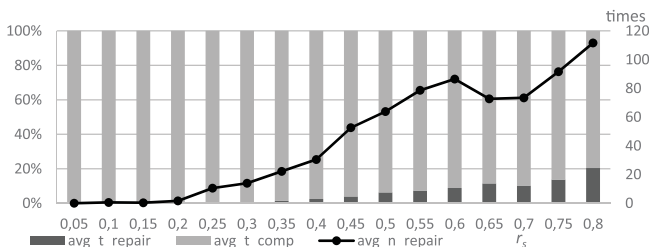


Fig. 13 Burden of repair technique in the small terminal

EXPERIMENTS OF MEDIUM SIZED TERMINAL

A berth plan of 6 vessels for a small terminal is shown in Fig. 14 below.

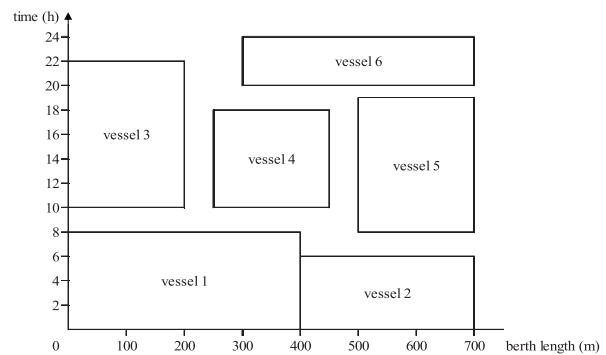


Fig. 14 Berth plan of the medium sized terminal

The performance of the PSOP algorithm in the medium sized terminal is shown in Fig. 15. According to this figure, the solving times increase with the capacity rate, and a solution could always be obtained in 100 seconds. Examples with a capacity rate no more than 0.65 will be assured with a feasible solution.

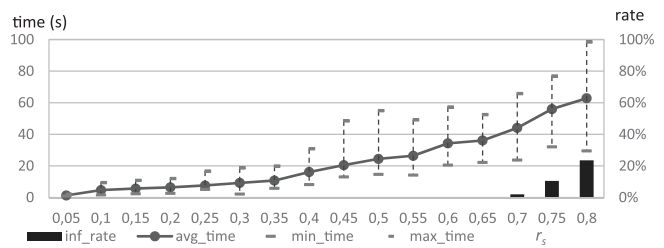


Fig. 15 Performance of PSOP in the medium sized terminal

The effect and burden of progressive searching are shown in Fig. 16 below. Here progressive searching processes lead to a 16% decrease of fitness value on average, while taking roughly 1.7 times as long as the time consumed by first searching processes.

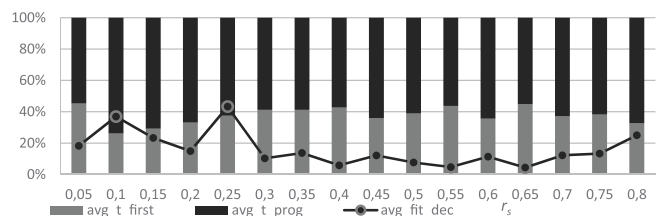


Fig. 16 Effect and burden of progressive searching in the medium sized terminal

The burden of repair process is shown in Fig. 17 below. Similarly, Except for an inflection point near capacity rate

0.45, the average number of repairs executed in solving an example increase as the capacity rate raises. The percentage of time spent in repairing goes up with the capacity rate, up to roughly 25% when the capacity rate reaches 0.8.

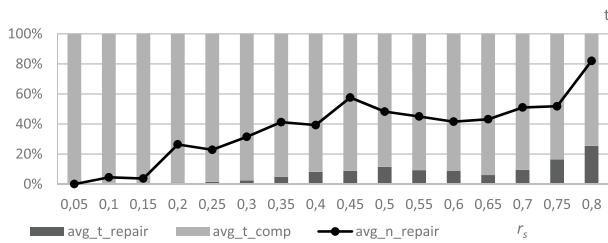


Fig. 17 Burden of repair technique in the medium sized terminal

EXPERIMENTS OF LARGE TERMINAL

A berth plan of 8 vessels for a large terminal is shown in Fig. 18 below.

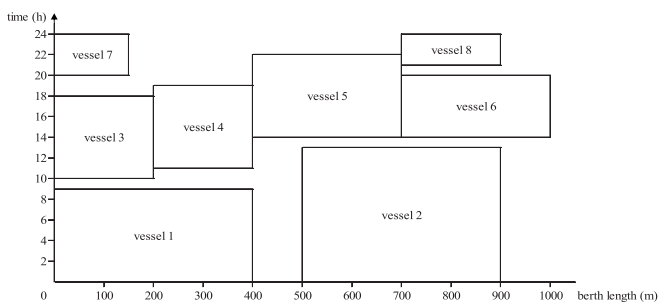


Fig. 18 Berth plan of the large terminal

The performance of the PSOP algorithm in the large terminal is shown in Fig. 19. In this figure, the solving times increase with the capacity rate, and a solution could always be obtained in 200 seconds. For examples with a capacity rate no more than 0.6, a feasible solution could be ensured.

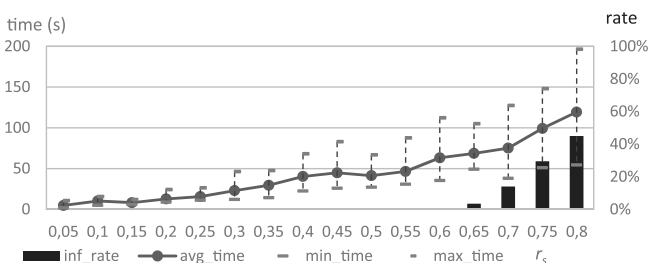


Fig. 19 Performance of PSOP in the large terminal

The effect and burden of progressive searching are shown in Fig. 20 below. Here progressive searching processes lead

to a 23.5% decrease of fitness value on average, while taking roughly 2.1 times as long as the time consumed by first searching processes.

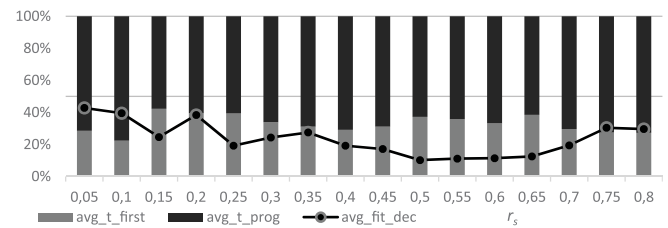


Fig. 20 Effect and burden of progressive searching in the large terminal

The burden of repair process is shown in Fig. 21. Obvious inflection sections could be seen near capacity rates 0.4 and 0.6. Generally, the average number of repairs executed in solving an example increase with the capacity rate. The percentage of time spent in repairing goes up with the capacity rate, up to roughly 28% when the capacity rate reaches 0.8.

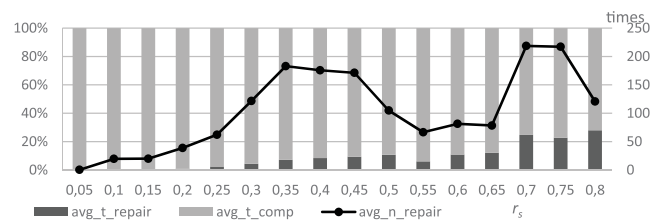


Fig. 21 Burden of repair technique in the large terminal

SUMMARY

According to the experiments above, some conclusions could be drawn as listed below.

- The model and algorithm raised in this paper is effective in solving storage allocation problems in container terminals in case that the capacity rate is not very large, and the solving time could be limited within several minutes. However, for large capacity rates, roughly more than 0.7, the solution will not be feasible every time.
- Progressive searching is an effective approach in further optimizing the result of a single PSO searching process, while the searching time of the whole algorithm will be lengthened, possibly doubled or tripled in terminal of different scales.
- Computation burden caused by repairing processes is roughly in proportion. The percentage of time taken by repairing processes could be limited to 30%, in all terminal scales and capacity rates.

CONCLUSION

This paper focus on the storage allocation problem in

automated container terminals. The problem is divided into two levels, and only the upper level problem is discussed in this paper. With some simplifications of the actual problem, a mixed integer programming model is proposed, and a progressive PSO algorithm is applied for solution. It is verified by numerical experiments that, the algorithm could converge to a feasible best solution in several minutes, in case that the ratio of space needed for allocation to the available space in the terminal is not extremely high.

This paper is a research to the storage allocation problem in automated container terminals, which is expected of great value to the automated container terminals to be built in near future. Given that almost all container information could be pre-determined by state of the art techniques as in some conventional terminals in China, pre-determined storage plans may lead to higher handling efficiency than real-time allocation strategies by rules. As a future work, the lower level of the problem and the potential efficiency increase will be discussed.

ACKNOWLEDGEMENT

This research is supported by the Young Scholar of Distinction Project for Postgraduate Students at Shanghai Maritime University (YXR2015109).

REFERENCE

1. Mi Chao, Zhang Zhiwei, Huang Youfang, Shen Yang, A FAST AUTOMATED VISION SYSTEM FOR CONTAINER CORNER CASTING RECOGNITION, *Journal of Marine Science and Technology-Taiwan*, 2016, 24(1): 54-60.
2. Mi Chao, Shen Yang, Mi Weijian, Huang Youfang, Ship Identification Algorithm Based on 3D Point Cloud for Automated Ship Loaders, *Journal of Coastal Research*, 2015, 2015(SI.73):28-34.
3. Mi Chao, Zhang Zhiwei, He Xin, Huang Youfang, Mi Weijian, Two-stage classification approach for human detection in camera video in bulk ports, *Polish Maritime Research*, 2015, 22(SI.1):163-170.
4. Mi Chao, He Xin, Liu Haiwei, Huang Youfang, Mi Weijian, Research on a Fast Human-Detection Algorithm for Unmanned Surveillance Area in Bulk Ports, *Mathematical Problems in Engineering*, 2014, Article No.386764.
5. Mi Chao, Liu Haiwei, Huang Youfang, Mi Weijian, Shen Yang, Fatigue alarm systems for port machine operators, *ASIA LIFE SCIENCES*, 2016, 25(1):31-41.
6. Kim K H, Park K T. A note on a dynamic space-allocation method for outbound containers [J]. *European Journal of Operational Research*, 2003, 148(1): 92-101.
7. Zhang C, Liu J, Wan Y, et al. Storage space allocation in container terminals [J]. *Transportation Research Part B: Methodological*, 2003, 37(10): 883-903.
8. steenken D, Voß S, Stahlbock R. Container terminal operation and operations research-a classification and literature review [J]. *OR spectrum*, 2004, 26(1): 3-49.
9. [9] Lee L H, Chew E P, Tan K C, et al. An optimization model for storage yard management in transshipment hubs [J]. *Or Spectrum*, 2006, 28(4): 539-561.
10. Dekker R, Voogd P, van Asperen E. Advanced methods for container stacking [M] // *Container terminals and cargo systems*. Springer Berlin Heidelberg, 2007: 131-154.
11. Han Y, Lee L H, Chew E P, et al. A yard storage strategy for minimizing traffic congestion in a marine container transshipment hub [J]. *OR Spectrum*, 2008, 30(4): 697-720.
12. Weijian Mi, Wei Yan, Junliang He and Daofang Chang. An investigation into yard allocation for outbound containers [J]. *COMPEL: The International Journal for Computation and Mathematics in Electrical and Electronic Engineering*, 2009, 28(6): 1442-1457.
13. Bazzazi M, Safaei N, Javadian N. A genetic algorithm to solve the storage space allocation problem in a container terminal [J]. *Computers & Industrial Engineering*, 2009, 56(1): 44-52.
14. Lee D H, Cao J X, Shi Q, et al. A heuristic algorithm for yard truck scheduling and storage allocation problems [J]. *Transportation Research Part E: Logistics and Transportation Review*, 2009, 45(5): 810-820.
15. Nishimura E, Imai A, Janssens G K, et al. Container storage and transshipment marine terminals [J]. *Transportation Research Part E: Logistics and Transportation Review*, 2009, 45(5): 771-786.
16. Zhang Y, Zhou Q, Zhu Z, et al. Storage planning for outbound container on maritime container terminals [C] // *Automation and Logistics, 2009. ICAL'09. IEEE International Conference on. IEEE*, 2009: 320-325.
17. Ku L P, Lee L H, Chew E P, et al. An optimisation framework for yard planning in a container terminal: case with automated rail-mounted gantry cranes [J]. *OR spectrum*, 2010, 32(3): 519-541.
18. Borgman B, van Asperen E, Dekker R. Online rules for container stacking [J]. *OR spectrum*, 2010, 32(3): 687-716.
19. Ku L P, Chew E P, Lee L H, et al. A novel approach to yard planning under vessel arrival uncertainty [J]. *Flexible Services and Manufacturing Journal*, 2012, 24(3): 274-293.
20. Li M, Li S. An effective heuristic for yard template design

- in land-scarce container terminals [C] // Industrial Engineering and Engineering Management (IEEM), 2011 IEEE International Conference on. IEEE, 2011: 908-912.
21. Woo Y J, Kim K H. Estimating the space requirement for outbound container inventories in port container terminals [J]. *International Journal of Production Economics*, 2011, 133(1): 293-301.
 22. Park T, Choe R, Hun Kim Y, et al. Dynamic adjustment of container stacking policy in an automated container terminal [J]. *International Journal of Production Economics*, 2011, 133(1): 385-392.
 23. Jiang X, Lee L H, Chew E P, et al. A container yard storage strategy for improving land utilization and operation efficiency in a transshipment hub port [J]. *European Journal of Operational Research*, 2012, 221(1): 64-73.
 24. Jeong Y H, Kim K H, Woo Y J, et al. A Simulation Study on a Workload-based Operation Planning Method in Container Terminals [J]. *Industrial Engineering & Management Systems*, 2012, 11(1): 103-113.
 25. Lee D H, Jin J G, Chen J H. Schedule Template Design and Storage Allocation for Cyclically Visiting Feeders in Container Transshipment Hubs [J]. *Transportation Research Record: Journal of the Transportation Research Board*, 2012, 2273(1): 87-95.
 26. Li P, Sun X. Storage Space Allocation Planning in the New Container Terminal [C] // *Proceedings of 2012 3rd International Asia Conference on Industrial Engineering and Management Innovation (IEMI2012)*. Springer Berlin Heidelberg, 2013: 429-437.
 27. Lee D H, Jin J G, Chen J H. Terminal and yard allocation problem for a container transshipment hub with multiple terminals [J]. *Transportation Research Part E: Logistics and Transportation Review*, 2012, 48(2): 516-528.
 28. Chen L, Lu Z. The storage location assignment problem for outbound containers in a maritime terminal [J]. *International Journal of Production Economics*, 2012, 135(1): 73-80.
 29. Won S H, Zhang X, Kim K H. Workload-based yard-planning system in container terminals [J]. *Journal of intelligent manufacturing*, 2012, 23(6): 2193-2206.
 30. Jiang X, Chew E P, Lee L H, et al. Flexible space-sharing strategy for storage yard management in a transshipment hub port [J]. *OR spectrum*, 2013, 35(2): 417-439.
 31. Türsel Eliyi D, Mat G, Ozmen B. Storage Optimization for Export Containers in the Port of Izmir [J]. *PROMET-Traffic&Transportation*, 2013, 25(4): 359-367.
 32. Sharif O, Huynh N. Storage space allocation at marine container terminals using ant-based control [J]. *Expert Systems with Applications*, 2013, 40(6): 2323-2330.
 33. Yu M, Qi X. Storage space allocation models for inbound containers in an automatic container terminal [J]. *European Journal of Operational Research*, 2013, 226(1): 32-45.
 34. Zhen L. Yard template planning in transshipment hubs under uncertain berthing time and position [J]. *Journal of the Operational Research Society*, 2012, 64(9): 1418-1428.
 35. Carlo H J, Vis I F A, Roodbergen K J. Storage yard operations in container terminals: Literature overview, trends, and research directions [J]. *European Journal of Operational Research*, 2014, 235(2): 412-430.

CONTACT WITH THE AUTHOR

Mi Weijian

mwj@shmtu.edu.cn

Logistics Engineering College
Shanghai Maritime University
1550 Haigang Avenue
Shanghai
China. 201306
CHINA

MUCK PROBLEMS IN SUBWAY SHIELD TUNNELING IN SANDY COBBLE STRATUM

Kai CUI

Weikang LIN

Key Laboratory of Transportation Tunnel Engineering of the Ministry of Education , Southwest

Jiaotong University, Chengdu, 610031, China

School of Civil Engineering, Southwest Jiaotong University, Chengdu, 610031, China

ABSTRACT

Experiments aiming at the muck improvement for Chengdu's subway shield tunneling in water-rich sandy cobble ground initially finds out the kinds and ratio of muck improver suitable for the this strata, and through the field application determines the reasonable ratio of muck improver for shield tunneling in sandy cobble ground, providing a reference to other muck improvement for shield tunneling in similar ground. And the earth pressure balanced shield is widely used in tunnel engineering, with its characteristics as wide adaptability, safe operation, fast driving speed, low environmental noise and low cost. Taking Chengdu Metro Line as the background, aiming at the difficulty faced by EPB shield tunneling in water-rich sandy cobble ground, and based on the explorations and researches of the predecessors and scholars, engineering and technical personnel, the present paper combines with engineering examples to make a systematic summary and research on key construction technology of EPB shield tunneling through sandy cobble ground from the aspects of EPB shield adaptability, structure and transformation of cutter and helical unearthed wares, settlement control method, and muck improvement measures. It has certain reference value and guiding significance to the selection of shield machine and the reconstruction of shield machine in complex geological condition.

Keywords: shield, sandy cobble ground, muck improvement

INTRODUCTION

The key of earth pressure balanced shield is to adjust the soil mass in the pressure chamber to a "plastic flow state" [1]. In order to get ideal muck which is beneficial for EPB shield tunneling, scholars all over the world have made a large number of experimental studies [2]. These studies mainly use foaming agent, bentonite, polymers and their combination for muck improvement [3], and rarely involve muck improvement for EPB shield tunneling in water-rich sandy cobble stratum; In addition, there are no examples to take reference in the past of EPB shield tunneling. Therefore Chengdu muck improvement for EPB shield tunneling in water-rich sandy cobble stratum water is crucial EPB shield tunneling. The muck improvement effect will directly affect the speed of shield machine driving,

driving cost, and even the success of the construction project.

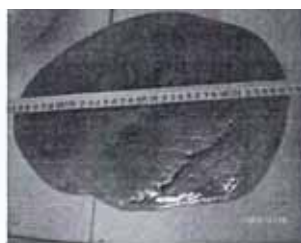
GENERAL SITUATION OF THE PROJECT

Chengdu sandy cobble stratum is rich in groundwater with large particles porosity and strong water permeability, the pebbles are working as skeleton in the soil, making the structure loose; The pebble content is high, and pebbles are mainly sub-circular with a small amount of circular ones. It has poor sorting, and filled mainly with fine sand and medium sand; Boulders are randomly distributed in stratum; according to the scene digging situation, maximum size of boulder is above 200mm; less amount of mud is contained in sandy cobble stratum, belonging to the category of non-cohesive granular

soil. Figure1 is sandy cobble soil dug out in shield tunneling of Chengdu Metro Line.



(a) Sandy cobble soil after digging and mixing



(b) Single sandy cobble

Fig.1 The Dug out Sandy cobble Soil

ANAYSIS OF CHENGDU WATER-RICHED SANDY COBBLE STRATUM

Test materials are selected from sandy cobble stratum buried in different depths of Chengdu metro line and 3 sample groups are selected. The first group is slightly dense sandy cobble layer; the second is middle dense sandy cobble layer; the third group is a highly dense sandy cobble layer. The grades of typical particle obtained from construction field are shown in Table1. The uneven coefficient and the curvature coefficient indicate that the stratum is a poorly graded. The mud content is relative low, belonging to the non-cohesive granular soil. Based on the relative density test, the density of sandy cobble in natural state is relatively large, which means that sandy cobble in natural state is relatively dense. And the measured gradation of sandy cobble is shown in Table1.

There are plain filled soil and sandy cobble along with Chengdu Metro line. The mechanical properties of sandy cobble stratum are distributed very uneven. And based on

Tab.1 Gradation of Sandy cobble in Chengdu Subway

particle size	>200	200-100	100-60	60-40	40-20	20-10	10-5	5-2	<2
/mm	mass percent /%								
slightly dense sandy cobble	0	9.6	17.3	15.7	16.8	3.3	0.7	0.9	35.7
middle dense sandy cobble	0.4	10.5	20.4	19.2	17.6	2.9	0.6	0.8	27.6
highly dense sandy cobble	0.5	11.6	23.6	24.2	20.2	2.7	0.5	0.5	16.2

this experiment, and survey report of Chengdu Metro Line, the physic-mechanical parameters of plain filled soil, slightly dense sandy cobble soil, middle dense sandy cobble soil and highly dense sandy cobble soil is shown in Table2..

Tab.2 Physic-mechanical Parameters of soils

Soil Name	Dense/(kg/m ³)	Cohesion/(kPa)	Internal Friction Angle /(°)	Deformation Modulus/(MPa)	Lateral Pressure Coefficient
plain filled soil	1800	15	20	6	0.43
slightly dense sandy cobble soil	2000	0	38	20	0.30
middle dense sandy cobble soil	2100	0	44	28	0.25
highly dense sandy cobble soil	2200	0	48	38	0.20

SHIELD DIGGING PROBLEMS

Because of poor cementation and different particle size of sandy cobble soil, sandy cobble soil with high big-size cobble will have great volume of stone of (see Figure 2). The cobble in sandy cobble stratum has big particle size, high strength and low cohesion. The force of the soil mass is transferred among individual particles and the stratum is characterized by a non continuous structure, so sandy cobble stratum has a very strong dispersion quality. And the combination with relatively abundant groundwater will result poor plastic flow of musk in soil tank which can not meet the need of EPB shield. In the actual construction process, the poor muck plastic flow often leads to the various situations such as failure of establishing EPB cutting face, surface over-break and settlement controlling difficult, spiral machine spewing, mechanical failure, tool consumption seriously, the shield machine cutter disc stuck caused by tool large thrust and torque.



Fig.2 Sandy Cobble Stratum with High Content of Big-sized Cobble

COUNTERMEASURES AND SOLUTIONS

First of all, the muck in soil warehouse and screw conveyor should have good plastic fluidity. This is mainly to enable Jack's force on clapboard being averagely and regularly put in digging surface, and ensure the dug out muck can be continuously sent to screw conveyor. Therefore, it can avoid the muck stacked at low-voltage part of soil warehouse, the adhesion to cutter disc and the blockage to soil warehouse, avoiding the rise of rotation torque and driving torque of the cutter disc and screw conveyor. Muck cut down by the disk is conveyed by screw conveyor from the pressure chamber to tunnel under barometric pressure. If brake gear is used in the transportation from screw conveyor to belt conveyor, muck should also have low permeability. Low permeability can avoid water in muck going through t screw conveyor. In addition, front center of cutter disc should be arranged with foam injection hole which can reduce the permeability of the excavation, avoiding the water infiltration on the excavation face, and maintaining stability of the excavation face. In addition, there is a very important requirement for the construction muck, namely: the internal friction angle of the muck should be relatively small. If the internal friction angle of the muck is large, frictional resistance of the soil will increase. This will lead to the poor fluidity of the muck; on the other hand it will increase the thrust of cutter disc torque, screw conveyor and shield Jack, failing the excavation of soil. In order to successfully carry out EPB shield tunneling, the mechanical properties of soil should be met: 1) soil mass should not be easy to drainage and consolidation (not easy to "incrust"); 2) soil mass should be in plastic flow state (easy to transfer under pressure and stir); 3) soil mass should have water-tightness (does not occur "spewing situation").

MUCK IMPROVEMENT METHODS

The usual way is to inject some materials into pressure ware to improve soil state and makes it meet the construction requirements. Generally used materials can be divided into four categories. These materials are sometimes used alone, and sometimes used in combination. Their characteristics are summarized as follows:

1) Minerals

In order to make the excavated soil become mud with fluidity and permeability, some fine particles need to add in. According to shield tunneling experience, the content of fine particles in excavated soil must reach about 30%-35%. If the fine particles in excavated soil are insufficient, the most commonly way is to produce mud with bentonite, montmorillonite and other materials to make up the insufficiency.

2) High water- absorbent resin

Because high water-absorbent resin can absorb groundwater with weight of several hundred times of itself into gel state, it has good effect on preventing the spewing of the foundation with high water pressure. But in high concentrations of salt water or the foundation containing a large number of irons, copper and other metals, and foundations with strong acid, strong alkaline and chemical reinforcement range, its water absorption capacity will be greatly reduced.

3) Water soluble polymer

It is a polymer material same as resin, which has the effect of increasing the viscosity of the soil with good pumping performance. In past shield tunneling, CMC is used in many cases. But sometimes muck will become mushy state and it will be treated as industrial waste.

4) Interfacial active material

It is current advanced method to improve the properties of the soil, which is injecting foams that are made by special foaming agent and compressed air. At present, domestic shield tunneling mainly uses bentonite and foam as muck improvement admixture. But, water-absorbent resin and water soluble polymer materials are used relatively rare. TAC polymer is creatively introduced into Kuizu shield tunneling in water-rich sandy stratum. TAC polymer has excellent hydrophilicity and significant effect of increasing viscosity. It can improve fluidity and water-tightness of water-rich sandy stratum and prevent the incrusting of cutter disc. This admixture is well applied in Kuizu shield tunneling in water-rich sandy cobble stratum. The appearance and experimental results of TAC polymer are shown in Figure 3.



Fig.3 The appearance and experimental results of TAC polymer

According to the analysis of particle composition and physical-mechanical parameters of sandy cobble stratum, muck improvement for shield tunneling in this stratum needs to solve the following problems:

1. Improve the anti-permeability of muck in soil ware to avoid large surface subsidence or collapse caused by drainage consolidation on face;
2. Increase the fluidity of muck in soil ware to avoid occlusion accident by poor dumping poor;
3. Reduce internal friction angle of muck in soil ware and soil in tunnel face to reduce the friction to cutter disc and a cutter wear as well as cutter disc torque;
4. Improve the plasticity of muck in soil ware to avoid incrustated accidents caused by adhesion of muck on cutter disc.

Through the above analysis, interfacial active material compared with other modified agents is more suitable for muck improvement in Chengdu shield tunneling in water-rich sandy cobble stratum. So in the construction of Chengdu subway, foaming agent is used to improve muck.

APPLICATION OF FOAMING SYSTEM IN MUCK IMPROVEMENT

Foaming system [4] in shield tunneling of this project consists of six roads (single pump and single supply). It is mainly composed of foam liquid pump, high pressure (40bar 1bar = 0.1MPa) three cylinder plunger pump, electromagnetic flow meter (gas, liquid), electric ball valve, foam generator, pressure sensors, pipeline components and other components. Figure 4 shows working principle of foam and bentonite system, as well as the position of cutter disc nozzle.

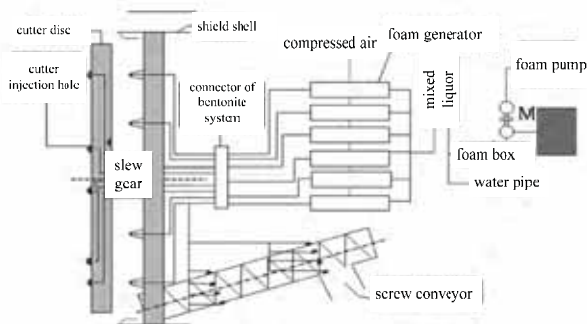


Fig.4 Working Principle of Foaming System

Under the condition of maintaining certain pressure in soil ware during tunneling, shield tunneling parameters are significantly improved through injecting foam into tunnel face. Add foam with the ratio of 30% to make tunneling average speed of 33-37 ring reach 44mm/min, the total thrust of the jack be reduced by about 22.4%, and the torque of the cutter be reduced by about 18.30%; After adding foams in tunneling process, muck discharged from the soil ware is at plastic flow state, and shield tunneling is normal. And surface settlement has been effectively controlled. Specific tunneling parameters

are shown in Table3 and Table4 [5-7].

Tab.3 Tunneling Parameters of Sandy Cobble Stratum without Foams

Assembling ring number	Thrusting progress/(mm/min)	Pressure in soil ware/MPa	Total thrust /kN	Cutter torque /MINm	Muck state	Maximum ground settlement/mm
15	6—20	0.221	14.192	4.32	spewing	+4/-27
16	12—25	0.217	15.256	4.43	water and soil separation	+6/-24
17	9—19	0.218	14.681	4.35	difficulty in sending soil	+6/-28
18	7—15	0.224	14.697	4.26	Spewing	+5/-25
19	0—10	0.210	16.273	4.59	difficulty in sending soil	+3/-29

Tab.4 Tunneling Parameters of Sandy Cobble Stratum with Foams

Assembling ring number	Thrusting progress/(mm/min)	Pressure in soil ware /MPa	Total thrust /kN	Cutter torque /MINm	Muck state	Maximum ground settlement/mm /mm
33	35—52	0.213	11.356	3.67	plastic flow	+3/-17
34	26—43	0.221	11.487	3.71	plastic flow	+3/-20
35	41—65	0.215	11.689	3.56	plastic flow	+4/-16
36	37—56	0.219	11.947	3.52	plastic flow	+3/-18
37	38—54	0.216	11.773	3.48	plastic flow	+2/-14

According to the geological and environmental conditions of Chengdu subway, the main role of the foam in EPB shield tunneling is to reduce the mechanical wear of shield machine. When tunneling in soil mass with large friction, cutting tools of EPB shield machine are easy to be worn out. Bt injecting

foam on the cutter disc, friction of soil mass and wear of cutter can be reduced. Adjust plastic fluidity in soil ware smooth. In EPB shield tunneling, soil nature will directly influence the shield tunneling process. Muck after cutting has good plasticity and fluidity, which can not only can make tunneling surface maintain good support pressure, and ensure the smooth implementation of soil conveying. In shield tunneling, due to the change of the stratum, soil in ware is difficult to possess the expected plastic fluidity which will lead to “incrusting” and “jamming” problems, seriously affecting tunneling efficiency. This problem can be solved effectively by injecting foam. Reduce water permeability of muck, because when EPB shield machine works in the gravel layer with strong water permeability, high water pressure on tunneled face will lead to a large number of groundwater loss at or even spewing at the export of screw conveyor which seriously effects the shield tunneling. Injection of foam can effectively reduce the permeability of muck, and effectively prevent tunneling spewing. Reduce internal friction of cutting muck which will reduce wear of cutter disc, screw conveyor, as well as cutting wheel torque. It will prevent mechanical malfunction caused by heating of high energy consumption.

CONCLUSION

Due to the fact that there are few researches both at home and abroad about muck improvement in EPB shield tunneling in water-rich sandy cobble stratum, this paper carries out analysis and experiment based on the characteristics of Chengdu water-rich sandy cobble stratum and makes successful application in the project which achieves positive effect of muck improvement. It provides an effective method and the reference for muck improvement in similar shield tunneling, having important guiding significance.

ACKNOWLEDGEMENT

The research is supported by the National Natural Science Foundation of China (Grant No. 41572245).

REFERENCES

1. ZHU Wei, CHEN Renjun. Technical Problems and Construction Management of Shield Tunneling [J]. Geotechnical Engineering World, 2001(12): 18-20.
2. LIN Jian, ZHU Wei, ZHONG Xiaochun. 358. Study on the Effect of Foam Stability on Muck Improvement in Shield Tunneling [J]. Geotechnical Engineering World, 2005, 8(12): 38-41.
3. QIN Jianshe, ZHE Wei, LIN Jinye. Assessment of the Foam Application in EPB Shield Tunneling [J]. Underground Space, 2004, 24(3): 350-358.
4. ZHAO Guangzi, JIA Lu, WEN Faqing, CHEN Runshui, XU Xiuting. Study on Muck Improvement Technology for

EPB Shield in Water-rich and Pebbly Sand Stratum in Nan Chang [J]. 1002-8498 (2015) S0-0160-05.

5. MA Liancong. Study on Ground Conditioning for EPB Shield in Water-rich Sandy cobble Ground [J]. 1672-741 X (2010) 04- 0411 –OS.
6. Watson, PJ. Development of a Unique Synthetic Data Set to Improve Sea-Level Research and Understanding [J]. Journal of Coastal Research. 2015, 3(3): 758-770.
7. Elbisy, MS. Sea Wave Parameters Prediction by Support Vector Machine Using a Genetic Algorithm [J]. Journal of Coastal Research. 2015, 31(4): 892-899.

CONTACT WITH THE AUTHOR

Kai CUI

Key Laboratory of Transportation Tunnel Engineering of
the Ministry of Education
Southwest Jiaotong University
Chengdu, 610031
CHINA

NONLINEAR DRIFT OF THE SPRING GRAVIMETER CAUSED BY AIR PRESSURE FROM THE KUNMING GS15 GRAVIMETERS

WEI Jin ^{1,2}

SHEN Wenbin ¹

LI Hui ²

Liu Ziwei ²

¹ School of Geodesy and Geomatics, Wuhan University, Wuhan 430079, China

² Key Laboratory of Earthquake Geodesy, Institute of Seismology, CEA, Wuhan 430071, China

ABSTRACT

In order to monitor and correct the meteorological factors of the spring gravity meter, the characteristics of the time varying gravity changes caused by meteorological factors were analyzed. Kunming GS15 gravity meter from 2007 continuous gravity observation has been carried out with the sampling rate of the pressure observation. In this study, we first compare the effects of 4 types of gravity meter and 3 different types of stations on the gravity observed seasonal gravity signals. It is indicated that the observed seasonal gravity signal of the cave is only 1/10, and there is a constant temperature and constant pressure device. Compared with the same time, the gravity signal of the gravity signal is about 100 times smaller. The influence of the pressure load of the gravity meter is tested by using the theory of pressure. The results show that only the actual value of 2cpd - 3cpd pressure load varies from -0.395 to $-0.280 \times 10^{-8} \text{ms}^{-2}$, and the 1cpd to 1cpm periodic partial type gravity meter is also in accordance with the law of gravity and air pressure. And with the characteristics of time lag. In this paper, the nonlinear zero drift parameters of the linear regression model with time lag and the time series of the GS15 gravity meter are used to simulate the nonlinear zero drift parameters of the gravity meter. The results show that the gravity signal contains time lag 35 hours, and the air pressure admittance is $0.8 \times 10^{-8} \text{ms}^{-2}/\text{mbar}$. The correlation can reach 79%. The gravity changes signal and satellite gravity as well as the gravity water load signal of the land water model are the same as the gravity water load signal in the autumn as the minimum value, and the seasonal variation of the maximum value of gravity in summer.

Keywords: GS15 gravimeter meter, air pressure admittance, nonlinear air pressure correction, superconducting gravimeter

INTRODUCTION

Kunming GS15 gravity meter has had a digital transformation from the GS metal spring gravimeter[1] which is originally produced by German Askania factory, it has been connected into the digital earthquake observation network to do the continuous gravity observation. When the research on influence of meteorological factors to gravity has been done, pressure has received great attention from both theoretical research and actual observation. Chinese Academy of Sciences had a summary on the relationship between pressure and gravity from the perspectives of theory and actual observation in 1997[2], and in 2008, it has found that gravity and frequency domain between pressure has dependencies in the superconducting gravity observation[3]. In analysis of

the LCR-ET20 spring tidal gravimeter, it has found when it is good condition, the pressure and the oceanic gravity signals within the tidal frequency can be effectively recorded, while the proposal of the long-period correction of zero drift caused by creep characteristics of spring need to be paid attention [4, 13]. China Seismological Bureau concluded the Padang M5.1 earthquake occurred in 2013 and found that the observation data from Yichang DZW gravimeter has broken the year rule before the earthquake. It also had analysis on the influencing factors to year cycle change and on the possible factors caused the rule breaking. When having the data analysis, it simply used theory of pressure load to correct the pressure load, having no further consideration on the influence of nonlinear factor caused by pressure load[5]. Therefore, this paper studies

to use Kunming GS15 gravity meter from 2007 continuous gravity observation has been carried out with the sampling rate of the pressure observation, after comparing the constant temperature and constant pressure system(see Table 1) of 4 types and 5 sets of gravity meter[6-9], the station type and the seasonal factor which can have influence on gravity, on this basis, using the theoretical air pressure admittance in the air pressure load theory to study the nonlinear characteristics of different period observation data responded to air pressure. With the consideration of time lag, using Kunming GS15 gravimeter observation data as example, constructing the nonlinear correction model of air pressure load to have nonlinear-factor correction, providing a new research and analysis method for using spring gravimeter to analyze the time-varying gravity change characteristics in local area caused by non-meteorological factors.

COMPARATIVE ANALYSIS OF CONTINUOUS GRAVITY OBSERVATION AND INFLUENCE OF AIR PRESSURE LOAD

The relationship between gravity observation data and air pressure change should conform to the theoretical correlation referred in reference [2-3]. Therefore this paper firstly have processed at least 4-year observation data from Jiufeng seismostation (DZW) gravimeter,academy of sciences Jiufeng station SG superconducting gravimeter, Zhangjiakou gphone gravimeter, Nnshan GS15 gravimeter and Kunming GS15 gravimeter, using the gravity residual time series corrected by using theoretical gravity earth tide to study the same-address observation data of air pressure and its load influence rule.

DATA PRE-PROCESSING MODEL

When the continuous gravity observation data has been processed, adopting the elimination - recovery data pre-processing method to eliminate all factors which will interfere the earth tide observation include jump error, drift, error data, seismic vibration caused by the earthquake. Meanwhile, using model (1) in the elimination process of the above pre-processing to simulate gravity residual time series which includes: formation process of the spring relaxation, change of the linear shift before and after the machine failure and the nonlinear drift of the spring gravimeter caused by drift or other causes before and after the failure, and correct them[10,11]. Figure 1 is the pre-processing with Kunming GS15 gravimeter as an example.

$$g_{res}(t_i) = g_{unlinear}(t_i) + v_i = d_0 + d_1 t_i + \sum_{j=1}^{N_{a1}} (a_j \cos(\frac{2\pi}{T_j} t_i) + b_j \sin(\frac{2\pi}{T_j} t_i)) + \sum_{j=1}^{N_{a2}} g_j H(t_i - T_{gj}) + \sum_{j=1}^{N_k} h_j H(t_i - T_{hj}) + \sum_{j=1}^{N_k} k_j \exp(-(t_i - T_{kj}) / \tau_j) H(t_i - T_{kj}) + v_i \tag{1}$$

Among them: t_i is the sample epoch. Here the unit is minute; $g_{res}(t_i)$ is the gravity residual time sequence after

the tidal correction; H is the step function; d_0 is the constant term of the residual time sequence; d_1 is the linear term of the gravity observation data; parameter a_j , b_j are simulated annual or seasonal load factors in the residual by using sine-cosine function. g_j is the jump error caused at time T_{gj} . When T_{gj} is the seismic moment, g_j is the coseismic gravity change. h_j is the gravity change rate after the earthquake. k_j is the amplitude of spring's relaxation process simulated by using exponential function after the earthquake; τ_j is the relaxation time of spring gravimeter after the earthquake.

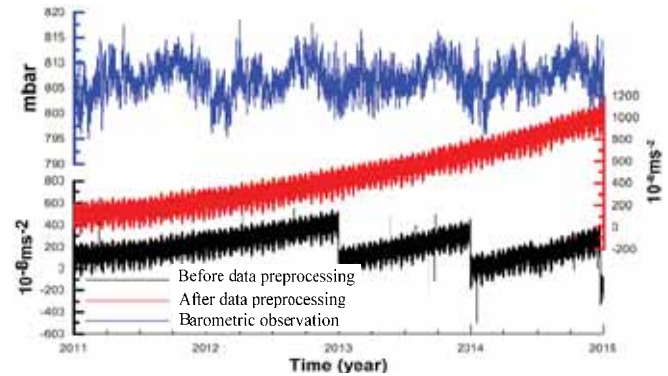


Fig.1 Comparison of Kunming GS15 gravimeter before and after the data pre-processing

Note: The comparison of observation time sequence before and after the data pre-processing shows no significant jump or drift observation data. The color of the longitudinal axis is same with the corresponding color of the observation sequence. The air pressure load influence of Kunming station shows seasonal characteristics. While the gravity earth tide observation appears about $100-200 \times 10^{-8} m \cdot s^{-2}$ / a change rate and the increasing zero drift.

COMPARATIVE ANALYSIS OF DIFFERENT TYPE GRAVIMETER OBSERVATION AND INFLUENCE OF AIR PRESSURE CHANGE

According to the continuous gravity observation data from the above 4 types and 5 sets gravimeters, having elimination-recovery method to pre-process the data. And all adopting gravity earth tide theoretical value to have tidal correction and have zero drift correction to polynomial which is not more than 3 steps. Comparing the residual time series with the air pressure (see as Figure 2). Meanwhile, combining the analysis result in Table 2 with the gravimeter station and the devices information to have a comparative analysis (see Table1).

The results showed that among the 5 gravimeters: the seasonal changing amplitude of gravity residual of the gravimeter which used constant temperature device almost only $\pm 10 \times 10^{-8} m \cdot s^{-2}$. Which the two types of gravimeter (GS15 and DZW) which didn't use the constant temperature device will change according to the change of the observation station type. Among them, the smallest seasonal change of gravity residual is the cave ($\pm 10 \times 10^{-8} m \cdot s^{-2}$), the biggest one is the earth surface ($\pm 1200 \times 10^{-8} m \cdot s^{-2}$). If the constant temperature device is the reduced pendulum causes the nonlinear drift

of the spring because of the change of temperature or air pressure, cave observation plays a role of the above constant temperature effect at some degree. Thus, if using gravity residual seasonal change as the measurement of judge the gravimeter observation quality, its size is not only related with the constant-temperature device, but also related with the observation types. The comparison of 4 sets of different type of continuous gravity observation gravity residual time series and the air pressure change is shown as Figure 2.

Tab.1 Comparison of observations and air pressure of gravity meter

Station name	Observation station type	Constant temperature and constant pressure device	Device type	Seasonal change of gravity residual	
				Amplitude ($\pm 10^{-9}\text{ms}^{-2}$)	Correlation with the air pressure
Kunming	Cave	-	GS15	10	+
Academy of sciences Jiu Feng station	Basement	Dewar	GWRC032	10	-
Panzhihua	Semi-basement	-	GS15	50	+
Jiu Feng earthquake station	earth surface	-	DZW	1200	-
Zhangjiakou earthquake station	Cave	Constant temperature air bag	gPh70	10	+

Note: gPhone uses constant temperature and constant pressure air bag to work, in order to insure that the observation of metal spring of the device maintains in the smallest change of environment [08]; the superconducting ball

of the GWR gravimeter works in the Dewar bottle (constant temperature, almost vacuum)[09]; gPh70 indicates the No.70 device of the gPhone gravimeter. The correlation with the air pressure “+” indicates positive correlation, “-” indicates negative correlation.

The academy of sciences Jiu Feng station and the Jiu Feng earthquake station which are all not belong to the cave observation and located less than 5 km away from each other, their gravity residual time series shows that: the observation quality with the constant temperature device (dewar) is 100 times than which without the constant temperature device. While the same type, both with no constant temperature device 2 sets of GS15 gravimeters, since the different observation station type, their annual changing amplitude of the different observation data only different between 5 to 10 times (cave type is better than that of half basement type). According to the comparison of the data quality different times, the effect of controlling the constant temperature device is much more greater than the effect of the observation station type (almost 20 times).

From the rule of the annual cycle changing rule of the gravity residual time series and the air pressure: Wuhan Jiu Feng area 2 sets of gravimeters are all presented the negative correlation characteristics which is the same changing direction with pressure load influence. While the other 3 sets of gravimeters showed the positive correlation characteristics. Based on the disagree of the above two kinds of observation results and the air pressure load theory results[2-3], this paper will analyze the relation of different time scale between gravity observation and the air pressure load influence.

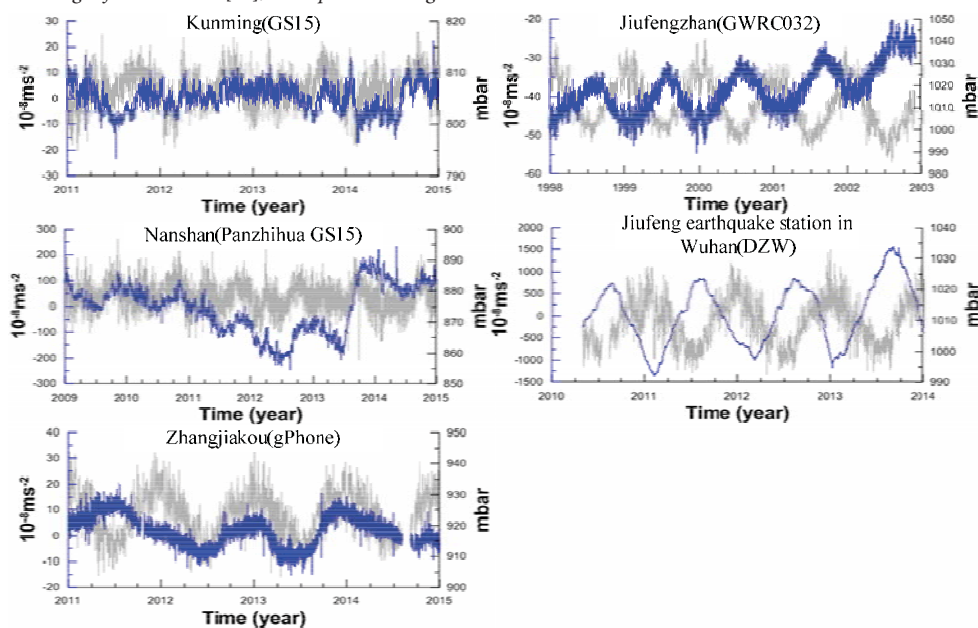


Fig.2 Comparison of 4 sets of different type of continuous gravity observation gravity residual time series and the air pressure change

Note: In the figure the gray time series is the air observation of the continuous gravimeter same-addressed observation; blue time series is the gravity residual time series of the continuous gravity observation;

ANALYSIS OF RELATIONSHIP BETWEEN GRAVITY OBSERVATION AT DIFFERENT TIME AND PRESSURE LOAD

The pressure load theory shows that [2], the changing of air pressure and gravity should be negative correlation. The magnitude of the air pressure admittance is changing from -0.395 to $-0.280 \times 10^{-8} \text{m} \cdot \text{s}^{-2}$. The above 4 types and 5 sets of devices' annual periodic change is not completely consistent with the air pressure load theory. Therefore, this paper uses VAV harmonic analysis method [6] to analyze the air pressure load influence within 1-7cpd frequency range, while the air pressure admittance of 3 days, 1 week, 2 weeks, 1 month, 1 season, 0.5 year, 1 year uses gravity residual and air pressure sequence of linear regression to obtain. The analysis results as shown in Figure 3.

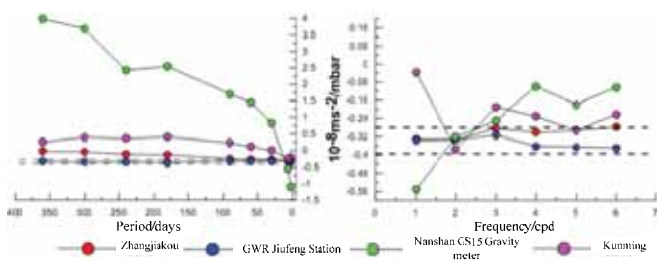


Fig.3 Relationship between gravity observation at different time and pressure load

From the above analysis results of 4 sets of devices show that, the superconducting gravimeter, no matter its 1 year scale change or its admittance relationship between air pressure and gravity within 1/6 daily wave frequency range is all changing within the theoretical value scope. While in the analysis of spring gravimeter less than 1 day periodic cycle, change of air pressure and gravity mainly be negative correlation, the observation sequence within 2cpd and 3cpd frequency scope basically conforms to the pressure load theory. Other frequency scope almost pass the scope of the theoretical simulation. The observation data which more than the 1 day periodic cycle only within 1-2 weeks (gPhone gravimeter about 100 days) the observation sequence still conform to the air pressure load theory. A longer time-span observation data show that the changing characteristics of air pressure admittance increasing. Among them, gPhone gravimeter changes slowly, the Nanshan GS15 which located in semi-basement and without constant temperature device changes in fastest way. Furthermore, the air pressure load influence of long term gravity observation data is far greater than the theoretical observation value, and with the phenomenon of time delay.

THE NONLINEAR PRESSURE CORRECTION AND CHARACTERISTIC STUDY OF KUNMING GS15 GRAVIMETER

From the above different observation environment,

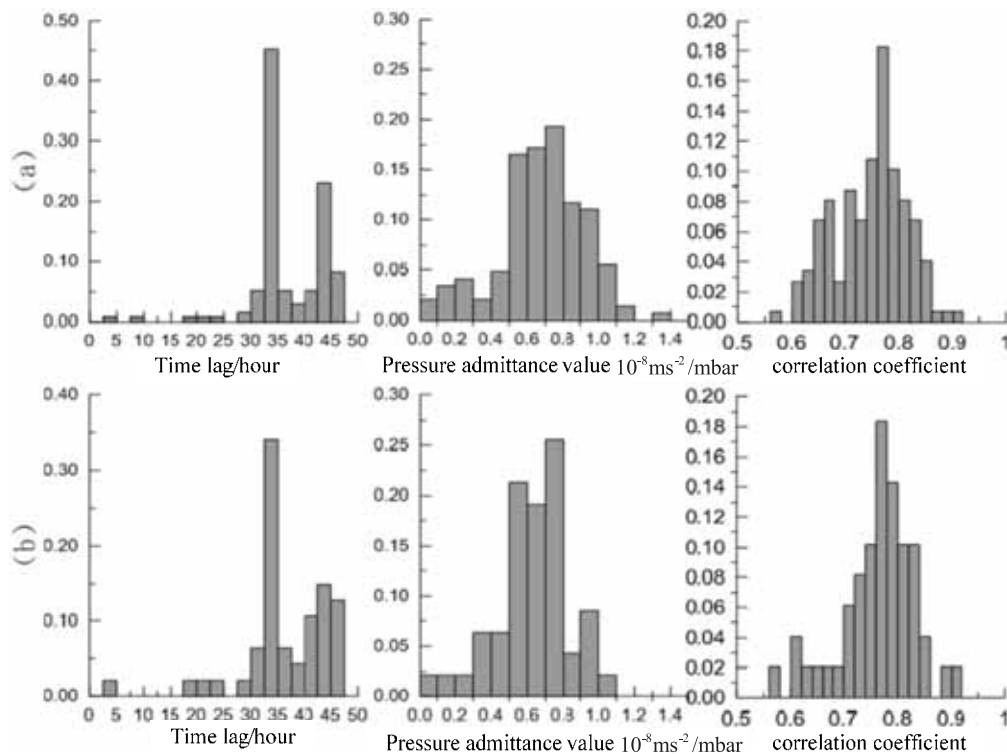


Fig.4 Study on the statistical characteristics of the influence parameters of different time scale air pressure

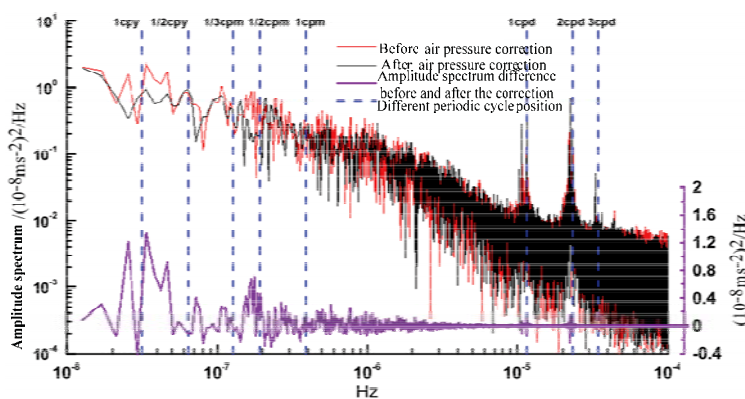
Note: (a) is the statistics of calculation results of observation data between 1 month to 1 year time span; (b) is the statistics of calculation of time delay, air pressure admittance and related coefficient of 1 month observation data; vertical coordinates are all ratio which is the corresponding statistical samples account for the total calculation samples.

observation device, time scale to study the rule of influence of pressure to the gravity, indicating that the pressure load scale produced by the air pressure to the spring gravimeter will gradually increase, and with some nonlinear changing characteristics such as time delay and so on. In order to obtain the gravity change of the spring gravimeter caused by non-pressure elements, choosing the station observation environment, data observation quality, with same-value meteorological observation Kunming GS15 gravimeter's observation data, with the consideration of phase lag characteristics to have correction of nonlinear air pressure load influence and characteristics study.

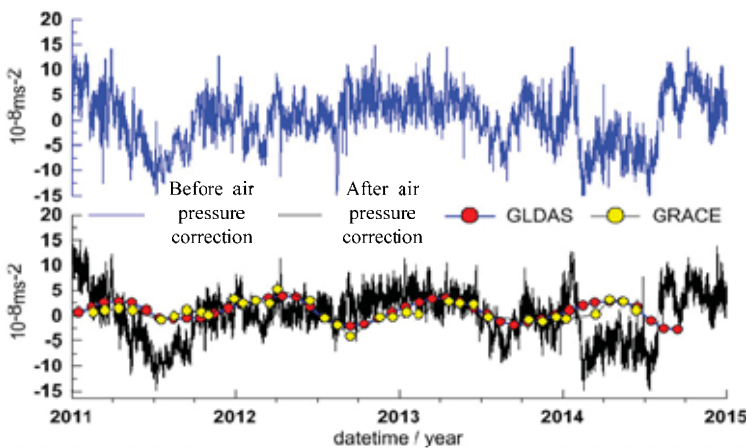
NONLINEAR AIR PRESSURE CORRECTION MODEL AND ANALYSIS

Due to the air pressure has different influence situation to the different gravity observation time sequence, and accompanied by the characteristics of the phase lag. This study chooses different time scale, different time lag characteristics and adopts the following model to have the statistical analysis, the results show:

$$\Delta g_i = a\Delta P_{i+\Delta t} + b + ct_{i+\Delta t} \quad (2)$$



(a) Comparison of gravity residual before and after the correction within the frequency scope



(b) Comparison of gravity residual before and after the correction within the time scope

Fig.5 Comparison of time series and spectral analysis results of nonlinear pressure corrections for gravity residuals

Note: cpy, cpm, cpd are respectively short for cycle percent year, cycle percent month, cycle percent day. The blue dotted line indications in the figure are positions of frequency respectively is 1cpd, 2cpd, 3cpd, 1/3cpm, 1/2cpm, 1cpm, 1/2cpy, 1cpy

Among which: Δg_i is the gravity residual time sequence, a is the air pressure admittance, b is the pressure time-varying change constant, c is the pressure time-varying change first-degree item. Δt is the time delay. ΔP is the pressure changing value.

The statistical results show that, about 45% statistical results show there exists 35 hours phase lag between gravity and air pressure; the range scope of air pressure admittance is $0.6-1.0 \times 10^{-8} \text{m}\cdot\text{s}^{-2}$; Above 45% statistical records show that the correlation between gravity and air pressure is above 80%. Therefore, this paper adopts 35 hours phase lag, air pressure nonlinear load influence $0.8 \times 10^{-8} \text{m}\cdot\text{s}^{-2}$ to correct Kunming GS15 gravimeter received air pressure nonlinear load influence.

COMPARISON AND ANALYSIS OF NONLINEAR AIR PRESSURE CORRECTION

By using the above model to have pressure correction to Kunming station gravity residual time series. Using amplitude spectrum analysis method to compare the amplitude spectrum difference before and after the correction (as shown in Figure 5-a). The result shows: the tide of gravity residual (1cpd ~ 3cpd) signal's amplitude is less than long period (1cpm ~ 1cpy). The difference value of gravity residual signal amplitude spectrum before and after the correction shows: annual period signal (1cpy ~ 1/2cpy) and seasonal period signal (1/3cpm~1/2cpm) decrease. Annual period decreases $1.4 \times (10^{-8} \text{m}\cdot\text{s}^{-2})^2/\text{Hz}$, seasonal period signal decreases $0.6 \times (10^{-8} \text{m}\cdot\text{s}^{-2})^2/\text{Hz}$, signal which less than 1cpm period shows no decreasing characteristic. Only the period at 1cpd, 2cpd, 3cpd signals only decrease. Thus it can be seen, the nonlinear influence of pressure's long period mainly effects the annual and seasonal period signal of the gravity observation. For the period less than 1cpm has no significant influence.

The residual time series used pressure to have nonlinear zero drift correction (as shown in Figure 5-c), the comparison with that before the correction (Figure 5-b), the observed gravity changing details are more obvious. Comparing the above pressure-corrected gravity residual time series with the gravity change caused by this area water-loaded seasonal factor which is simulated by satellite gravity (Grace) and global land water model (Gldas) [11, 12], the result shows that the above two all reach the smallest gravity in fall in 2012, 2013, while reaching the biggest in summer, this is the seasonal changing characteristics. The inconsistency of magnitude of the seasonal load influence may be the result of simulation model which simulated the largest space scale, it is not completely consistent with the gravity change of Kunming station Local area.

CONCLUSION AND DISCUSSION

This paper firstly uses non-tidal analysis method to deal with and compare 4 types and 5 sets of continuous gravimeters' over 4-year pre-processing gravity earth tide observation data, using gravity residual annual and seasonal change as the indicator to measure the observation quality of gravimeter, it found that the size of seasonal change is not only related to the observation station type, but also related with the constant temperature device. The data quality with the precised constant temperature device is about 100 times than the device without the constant temperature device. The comparison of observation station type shows: cave station observation is 5-10 times than the earth surface observation.

For the pressure signal which is the most significant one in the above gravity seasonal change, the study found that 4 types spring gravimeters' observed gravity signal within 2cpd to 3cpd frequency scope the observation sequence conform to the pressure load theory. The gravity signal within 1 month also presents negative correlation characteristic with the meteorology, a longer periodic cycle pressure load influence is far greater than the theoretical observation value, and accompanied with the phenomenon of time delay. In order to eliminate the influence of the above factors, taking Kunming GS15 gravimeter whose observation environment is better and assistant observation is complete as example, using the linear regression formula with time delay to analyze the gravity residual time series and the pressure sequence of the same-addressed observation, it has found that gravity signal of Kunming GS15 contains time lag 35 hours, and the air pressure admittance is $0.8 \times 10^{-8} \text{ms}^{-2}/\text{mbar}$ nonlinear zero drift.

Through the above model to correct the gravity residual time series, comparing the frequency scope characteristics and the time span characteristics of the gravity residual time series signal before and after the correction, within the frequency scope, Kunming station's nonlinear pressure corrected the annual period signal and seasonal period signal in the gravity signals (decreased $1.4-0.6 \times (10^{-8} \text{m} \cdot \text{s}^{-2})/2/\text{Hz}$), the earth tide frequency has no significant correction. Within the time span: the details of the gravity changing are more obvious. The gravity changes signal and satellite gravity as well as the gravity water load signal of the land water model are the same as the gravity water load signal in the autumn as the minimum value, and the seasonal variation of the maximum value of gravity in summer. Due to the regional gravity field change and the difference of the local gravity field, the different scale between the two has been resulted.

REFERENCE

1. Wei Jin, Shen Chongyang, Liu Shaoming, Dai Miao. Analytic study on abnormal change in time - variable gravity at Yichang seismostation before the M5.1 Badong earthquake. *Geodesy and Geodynamics*, 2014, 5 (1) : 55-63

2. Xu jianqiao. The theory and analysis of gravity tidal – superconducting gravimeter data analysis and processing in Wuhan station[D]. Institute of Geodesy and Geophysics Chinese Academy of Sciences, 1997
3. Mahmoud Abd El –Gelil, et al. Frequency – dependent atmospheric pressure admittance of superconducting gravimeter records using least squares response method [J]. *Physics of the Earth and Planetary Interiors*, 2008, (170): 24-33
4. Sun Heping, Chen Xiaodong, Liu Ming, etc. Analysis and Comparison of the Tidal Gravity Observations Obtained with LCR-ET20 Spring Gravimeter [J]. *ACTA SEISMOLOGICA SINICA*, 2002, 24 (5) : 510-515
5. Wei J, Li H, Liu Z W, et al. Observation of superconducting gravimeter at Jiufeng seismic station. *Chinese J. Geophys.* (in Chinese), 2012, 55(6): 1894- 1902, doi: 10. 6038/j. issn. 0001- 5733. 2012. 06. 010.
6. Kang Kaixuan, Li Hui, Peng Peng, Hao Hongtao, Wei Jin. Seasonal variations in hydrological influences on gravity measurements using gPhones[J]. *Terr. Atmos. Ocean. Sci.*, 2011, 22(2): 157-168, doi: 10.3319/Tao. 2010. 08. 02. 01(TibXS)
7. gPhone/PET gravimeter Manual (V1). gMonitor User's Manual, 2008: gMonitor Gravity Data Acquisition and Processing Software
8. GWR Superconducting Gravimeter Manual GWR (superconducting gravimeter) User 's Manual 2008
9. Wei Jin, Zhao Bin, Tan Hongbo, Yu Dan, Shen Chongyang, Li Hui. Detection of a half-microgal coseismic gravity change after the Ms7.0 Lushan earthquake. *Geodesy and Geodynamics*, 2013, 4(3):7-11.
10. Wei jin, Li hui, Liu Ziwei, Hao Hongtao, Kang Kaixuan. Study on influence of pressure on gravimeter SGC053 by use of product spectra[J]. 2011, 31(4):47- 51.
11. David Crossley, Jacques Hinderer, Umberto Ricciardi. The measurement of surface gravity[J]. *Reports on Progress in physics*, 2013, 76(046101)47pp, doi: 10. 1088/0034-4885/76/4/046101
12. Zhou Xin, Sun Wenke, Zhao Bin, et al. Geodetic observations detecting coseismic displacements and gravity changes caused by the Mw=9.0 Tohoku-Oki earthquake[J]. *J Geophys Res*, 2012, 117: B05408. Doi: 10. 1029/2011JB008849
13. Wang L S, Chen C, Zou R, et al. Using GPS and GRACE to detect seasonal horizontal deformation caused by loading of terrestrial water: A case study in the Himalayas. *Chinese*

J. Geophys. (in Chinese), 2014, 57(6): 1792-1804, dio: 10.6038/cjg20140611

14. Cai, C (Cai, Chuang); Cai, XY (Cai, Xinyong); Li, Y (Li, Yi). MODEL TESTS FOR SHALLOW-WATER SHIP MANEUVERABILITY IN THREE GORGES RESERVOIR [J]. POLISH MARITIME RESEARCH. 2015, 22(2): 136-140.

Fund Project: Natural Science Foundation of China (NSFC) (41204058), China Seismological Bureau Earthquake Research Institute Director Fund (IS201326123)

CONTACT WITH THE AUTHOR

Wei Jin

Key Laboratory of Earthquake Geodesy
Institute of Seismology
CEA, Hongshan side road No 40
Wuhan 430071
CHINA

ANALYSIS AND APPLICATION OF MECHANICAL SYSTEM RELIABILITY MODEL BASED ON COPULA FUNCTION

Hai AN

Hang YIN

Fukai HE

School of Aerospace and Civil Engineering, Harbin Engineering University, Harbin 150001,
Heilongjiang, China

ABSTRACT

There is complicated correlations in mechanical system. By using the advantages of copula function to solve the related issues, this paper proposes the mechanical system reliability model based on copula function. And makes a detailed research for the serial and parallel mechanical system model and gets their reliability function respectively. Finally, the application research is carried out for serial mechanical system reliability model to prove its validity by example. Using Copula theory to make mechanical system reliability modeling and its expectation, studying the distribution of the random variables (marginal distribution) of the mechanical product' life and associated structure of variables separately, can reduce the difficulty of multivariate probabilistic modeling and analysis to make the modeling and analysis process more clearly.

Keywords: copula function, mechanical system reliability, model

INTRODUCTION

There is complex correlations between each unit of the mechanical system and its failure models. There are a lot of analysis about the mechanical system reliability, but the studies to analyze the reliability from the correlation of mechanical system are few. In recent years, some scholars apply the connection function copula to discuss the correlation in financial, insurance and engineering, and achieve satisfactory results [1-3]. Literature [4-5] discussed some studies that the copula function is used in mechanical system reliability, but there were no deep study. Anyway, they contributed the reference value for the Copula function' deep study in terms of the mechanical system reliability. Based on the existing theories, this paper constructs the mechanical

system reliability model based on copula function, and apply it to practice.

THEORETICAL BASIS

DEFINITION AND NATURE OF COPULA FUNCTION

In 1959, Sklar decomposed a joint distribution into k edge distributions and a Copula function, and this Copula function can describe the correlation among variables[6]. So, actually, Copula function is a function that connects the joint distribution of a multivariate random variables with their respective marginal distribution[7]. Use R^n to note the expand n -dimensional space (n is

any positive integer), $a = (a_1, a_2, \dots, a_n)$ represents the point in R^n , for all the k , if $a_k \leq b_k$, then $a \leq b$. If $a \leq b$ use $[a, b] = [a_1, b_1] \times [a_2, b_2] \times \dots \times [a_n, b_n]$ represents n -dimensional cube, and its volume is noted $V_c([a, b])$. n -Copula function has the following basic properties:

(1) $C(u_1, u_2, \dots, u_n)$ is the n -distribution function which is defined in $[0, 1]^n$, that is $C: [0, 1]^n \rightarrow [0, 1]$;

(2) For any variable $u_i, i = 1, 2, \dots, n$, $C(u_1, u_2, \dots, u_n)$ is monotonically increasing all the time;

(3) C_i , the marginal distribution of $C(u_1, u_2, \dots, u_n)$ meets $C_i(u_i) = C(1, \dots, 1, u_i, 1, \dots, 1) = u_i$, in which, $u_i \in [0, 1], i \in [1, n]$;

(4) For $u_i \in [0, 1], i \in [1, n]$, $C(u_1, \dots, u_{i-1}, 0, u_{i+1}, \dots, u_n) = 0$ all the time;

(5) If the variables $u_i \in [0, 1], i = 1, 2, \dots, n$ are independent

from each other, then $C(u_1, u_2, \dots, u_n) = \prod_{i=1}^n u_i$, noted as C^\perp ;

(6) For any $u_i, v_i \in [0, 1], i = 1, 2, \dots, n$,

$$|C(u_1, u_2, \dots, u_n) - C_2(u_1, u_2, \dots, u_n)| \leq \sum_{i=1}^n |u_i - v_i| \text{ all the time.}$$

SKLAR THEOREM

Theorem[8] assumes H is n -dimensional distribution function, the edge distribution is $F_1, F_2 \dots, F_n$, then there is an n -dimensional Copula function C , for any $x \in R^n$.

$$H(x_1, x_2, \dots, x_n) = C(F_1(x_1), F_2(x_2), \dots, F_n(x_n)) \quad (1)$$

If $F_1, F_2 \dots, F_n$ is continuous, then C is unique, conversely, if C is n -dimensional Copula function, $F_1, F_2 \dots, F_n$ is distribution function, then the above formula defines an n -dimensional distribution function, its edge distribution is $F_1, F_2 \dots, F_n$.

From Sklar Theorem, it can be seen that Copula function can independent from marginal distribution of random variables and reflects the correlation structure of random variables, which can divide joint distribution into two separated parts to deal with respectively: the correlations structure among variables and the marginal distribution of variables, in which the correlation structures is described with Copula function.

Inference [9] assumes $X_1, X_2 \dots, X_n$ are random variables whose distribution function is $F_{x_1}(x_1), F_{x_2}(x_2), \dots, F_{x_n}(x_n)$, the joint distribution function is $H(x_1, x_2, \dots, x_n)$, then there is an n -dimensional Copula function that makes (1) set up. If

$F_{x_1}(x_1), F_{x_2}(x_2), \dots, F_{x_n}(x_n)$ is continuous, then C is unique. Otherwise, the uniqueness of C should be determined by

$$\text{Ran}F_1 \times \text{Ran}F_2 \times \dots \times \text{Ran}F_n.$$

According to Sklar theorem, using Copula function can study the marginal distributions and the correlation structure among variables separately, and it can reduce the difficulty of multivariate probabilistic modeling and analysis.

MECHANICAL SYSTEM RELIABILITY MODEL BASED ON COPULA FUNCTION

RELIABILITY ANALYSIS OF SERIAL MECHANICAL SYSTEM BASED ON COPULA

As long as one unit fails, the system will fail, the system is called serial system, which is shown in Figure 1. In mechanical system, the random variables of reliability function often have real physical meaning, such as time, number of cycles, mileage and so on. For ease of presentation, herein it is called life in the analysis.



Fig.1 The reliability of serial system

Assume the mechanical system is consists of n units in series, and the life of each unit is $T = (T_1, T_2 \dots, T_n)$, the joint distribution function $H(t_1, t_2, \dots, t_n) = P\{T_1 \leq t_1, T_2 \leq t_2, \dots, T_n \leq t_n\}$, $F_i(t)$ is the distribution function of T_i , the reliability function of each component is $R_i(t) = 1 - F_i(t)$, the reliability function of system is $R(t)$.

From the Sklar theorem, there is an n -dimensional Copula function C that makes $H(t_1, t_2, \dots, t_n) = C^n(F_1(t_1), F_2(t_2), \dots, F_n(t_n))$, in which the $C^n(\bullet)$ represents n -dimensional Copula function C , because $F_i(t)$ is continuous, so $C^n(F_1(t_1), F_2(t_2), \dots, F_n(t_n))$ is unique.

When each unit of system is in series, the life of the system is the smallest in all the units, that is $T = \min(T_1, T_2 \dots, T_n)$, then the reliability of system can be expressed as:

$$\begin{aligned} R(t) &= P\{\min(T_1, T_2, \dots, T_n) > t\} = P\{T_1 > t, T_2 > t, \dots, T_n > t\} \\ &= 1 - \sum_{i=1}^n P(T_i - t) + \sum_{1 \leq i < j \leq n} P(T_i \leq t, T_j \leq t) + \dots + \\ &(-1)^k \times \sum_{1 \leq i_1 < i_2 < \dots < i_k \leq n} P(T_{i_1} \leq t, T_{i_2} \leq t, \dots, T_{i_k} \leq t) + \dots + \\ &(-1)^n P(T_1 \leq t, T_2 \leq t, \dots, T_n \leq t) = 1 - \sum_{i=1}^n F_i(t) + (-1)^k \times \\ &\sum_{1 \leq i_1 < i_2 < \dots < i_k \leq n} C^n(F_{i_1}(t), F_{i_2}(t), \dots, F_{i_k}(t), 1, 1, \dots, 1), \quad 2 \leq k \leq n \end{aligned} \quad (2)$$

RELIABILITY ANALYSIS OF PARALLEL MECHANICAL SYSTEM BASED ON COPULA

Assume the mechanical system is formed by n units in parallel, then the life of each unit is $T = (T_1, T_2, \dots, T_n)$, $F_i(t)$ is the distribution function of T_i , the joint distribution function is $H(t_1, t_2, \dots, t_n) = P\{T_1 \leq t_1, T_2 \leq t_2, \dots, T_n \leq t_n\}$, the reliability function of each component is $C, i = 1, 2, \dots, n$.

From the Sklar theorem, there is an n -dimensional Copula function C that makes

$$H(t_1, t_2, \dots, t_n) = C^n(F_1(t_1), F_2(t_2), \dots, F_n(t_n)),$$

When each unit of system is in parallel, the life of the system is the largest in all the units, that is $T = \max(T_1, T_2, \dots, T_n)$, then the reliability of parallel system can be expressed as:

$$\begin{aligned} R(t) &= P\{\max(T_1, T_2, \dots, T_n) > t\} = \\ &= 1 - P(\max(T_1, T_2, \dots, T_n) \leq t) = \\ &= 1 - C^n(F_1(t), F_2(t), \dots, F_n(t)) = \\ &= 1 - C^n(1 - R_1(t), 1 - R_2(t), \dots, 1 - R_n(t)) \end{aligned} \quad (3)$$

When each unit is independent, from

$$\begin{aligned} C^n(1 - R_1(t), 1 - R_2(t), \dots, 1 - R_n(t)) &= \\ = C^\perp(1 - R_1(t), 1 - R_2(t), \dots, 1 - R_n(t)) &= \\ = (1 - R_1(t))(1 - R_2(t)) \cdots (1 - R_n(t)) &= \prod_{i=1}^n (1 - R_i(t)) \end{aligned} \quad (4)$$

the $R(t) = \prod_{i=1}^n (1 - R_i(t))$, can be obtained. This is consistent with the parallel system reliability model which is traditional and no considering in the correlation.

So far, this paper has established the mechanical system reliability model based on Copula. So under the premise of not studying the multidimensional random variable joint distribution function, by constructing appropriate Copula function to calculate the reliability value of the mechanical system in the condition of considering the relevance, which can effectively solve the difficult problem of mechanical system reliability modeling.

PARAMETER ESTIMATION

Copula function parameter estimation methods can be divided into three types: (1) the relevance index method which mainly uses the relationship between parameter θ of Copula function and Kendall's rank correlation coefficient (as shown

in Table 1) to calculate parameter indirect. (2) fitting line method, that is under certain fitting line guideline to calculate the statistical parameter of frequency curve which is optimal to fit with the experience point. (3) maximum likelihood method, for three-dimensional and above Copula function, correlation index method is not applicable clearly, then most of them use the maximum likelihood method to estimate parameter. On the basis of analyzing the first two methods, Xiao Yi^[10] thinks that comparing with the single-variable distribution, the parameter estimation of Copula function has higher requirement for the length of the information. For the middle and small samples, it may result in the bigger estimated value sampling error, and the estimated value is unstable. He uses bootstrap and coupling method to estimate parameter. Statistical test shows that the confidence interval of correlation index method parameter estimated value is narrow, the result is more stable. The bootstrap can improve the estimation ability of the correlation index method, but the effect is poor for fitting line method. It will result in the severe larger estimated value.

Tab.1 The relationship between parameter θ of Copula function and Kendall's rank correlation coefficient T

Name of function	Relationship between θ and T
C-H Copula function	$T = 1 - 1/\theta$
Clayton Copula function	$T = \theta/(2 + \theta)$
AMH Copula function	$T = (1 - 2/3\theta) - 2/3(1 - 1/\theta)^2 \ln(1 - \theta)$
Frank Copula function	$T = 1 + \frac{4}{\theta} \left[\frac{1}{\theta} \int_0^\theta \frac{r}{e^r - 1} dt - 1 \right]$

APPLICATION EXAMPLE

Using mechanical system reliability model based on Copula, by constructing the Copula function which can reflect the relevant structural features of the mechanical system's various componential units, regarding the unit life as a basic input (assuming the life distribution rule of each unit is known), it can estimate the parameter of Copula, thus to expect the reliability of mechanical system. In the following part, take a certain type armored vehicle suspension system for instant to illustrate the application of the mechanical system reliability model based on Copula in the reliability forecast.

DESCRIPTION OF PROBLEM

The serial mechanical system consists of n units, the life of i -th unit is T_i , which distribution function (the

probability of failure) is recorded as $F_i(t_i)$, the reliability is $R_i(t_i) = 1 - F_i(t_i)$, a set of observation value of each unit is known $(t_{1j}, t_{2j}, \dots, t_{nj})$, $j = 1, 2, \dots, w$, try to estimate the system reliability.

By the formula (2), it can be obtained that:

$$R(t) = 1 - \sum_{i=1}^n F_i(t) + (-1)^k \times \sum_{1 \leq i_1 \leq i_2 \leq \dots \leq i_k \leq n} C^n(F_{i_1}(t), F_{i_2}(t), \dots, F_{i_k}(t)) = 1 - \sum_{i=1}^n F_i(t) + (-1)^k \times \sum_{1 \leq i_1 \leq i_2 \leq \dots \leq i_k \leq n} C^n(F_{i_1}(t), F_{i_2}(t), \dots, F_{i_k}(t), 1, 1, \dots, 1), 2 \leq k \leq n \quad (5)$$

In the above formula, $F_i(t)$ can be obtained by determining the distribution type and its distribution parameter. First, select the appropriate Copula model, by the nature of Copula function, estimate the parameter of $\sum C^n(F_1(t), F_2(t), \dots, F_n(t))$ to make $F_j(t) = 1$, $j = i_k + 1, i_k + 2, \dots, n$, so you can get $1 \leq i_1 \leq i_2 \leq \dots \leq i_n$, $2 \leq k \leq n$.

Thus, the basic steps of using the mechanical system model based on Copula to expect the system reliability:

1. Determine the marginal distribution, that is the distribution type $F_i(t)$ of unit life, and estimate the distribution parameter;
2. Choose an appropriate Copula function, to make it can describe the relevant characteristics of each unit life well;
3. Estimate the parameter of Copula model;
4. Calculate system reliability.

CONSTRUCTING COPULA MODEL

In view of the correlation among the mechanical parts life usually shows the positive correlation, and at the same time, taking into account of the simple requirement to the model parameter estimation and calculation, this paper chooses the multi Gumbel Copula function in Archimedean Copula function family. Gumbel Copula function can accurately portray the correlation of mechanical system. The distribution function and density function of multi Gumbel Copula function respectively is:

$$C(u_1, u_2, \dots, u_n; \theta) = \exp\left(-\left[\sum_{i=1}^n (-\ln u_i)^{1/\theta}\right]^\theta\right), \quad (6)$$

$$c(u, v; \theta) = \frac{\partial C(u_1, u_2, \dots, u_n; \theta)}{\partial u_1 \partial u_2 \dots \partial u_n} \quad (7)$$

In the formula, $\theta \in (0, 1]$ is the correlation coefficient, $\theta = 1$ represents the random variables u_1, u_2, \dots, u_n , is independent,

$\theta \rightarrow 0$ represents the random variables u_1, u_2, \dots, u_n tend to full correlation.

If $u_i = F_i(t_i) = 1 - e^{-(t_i - \gamma_i)^{m_i}/\eta_i^{m_i}}$, from formula (6), it can get

$$C^n(F_1(t_1), F_2(t_2), \dots, F_n(t_n); \theta) = \exp\left(-\left[\sum_{i=1}^n (-\ln F_i(t_i))^{1/\theta}\right]^\theta\right) \quad (8)$$

Then, according to formula (5), the system reliability is

$$R(t) = 1 - \sum_{i=1}^n F_i(t) + (-1)^k \times \sum \exp\left(-\left[(-\ln F_{i_1}(t))^{1/\theta} + (-\ln F_{i_2}(t))^{1/\theta} + \dots + (-\ln F_{i_n}(t))^{1/\theta}\right]^\theta\right) \quad (9)$$

It needs to estimate the value $\hat{\theta}$ of Copula function's parameter θ , then make $F_j(t) = 1$, $j = i_k + 1, i_k + 2, \dots, n$ Put $\hat{\theta}$ and the Weibull distribution parameter estimated value $\hat{\gamma}_i, \hat{m}_i, \hat{\eta}_i$ of each unit into (9), the system reliability can be obtained.

ESTIMATE SYSTEM RELIABILITY

From 3.2 to calculate the system reliability function, if estimating the reliability of the suspension system when the vehicle is traveling to 6000km, put the $t = 6000$ km into reliability function equation, the $R(6000) = 0.532$ can be obtain.

Without considering the correlation among the units, the reliability of suspension system when the vehicle is traveling to 6000km is $R(t) = 0.425$. Hydraulic shock absorber is the reliability lowest unit in the suspension system. When the vehicle is traveling to 6000km, the reliability is $R_3(6000) = 0.535$.

If the system reliability based on Copula function is $R_c(t)$, assuming the system reliability when the units are independent from each other is $R_I(t)$, the corresponding system reliability of the weak link theory is $R_W(t)$. From the calculation results of the above examples, $R_c(t) = 0.532$, $R_I(t) = 0.425$, $R_W(t) = 0.535$, Then clearly there is $R_I(t) \leq R_c(t) \leq R_W(t)$.

This is consistent with the conclusion of reliability margin model, which also verifies the reasonableness of mechanical system reliability model based on Copula function.

The many years' actual use data of the armed forces show that this equipped suspension system' travelling damage rate of 6000km is 48%, which is equivalent to the suspension system' reliability is 0.520 when using it to 6000km, slightly

lower than the expected value 0.532. Excluding the damage caused by human operation error and improper repairs, it can be considered that the model is basically consistent with the actual situation. This confirms the correctness and rationality of the model from the theory and practice aspects.

CONCLUSIONS

Using Copula theory to carry out mechanical system reliability modeling and its expectation to study the distribution of random variables (marginal distribution) of the mechanical product life and the associated structure of variables separately, which reduces the difficulties of multivariate probabilistic modeling and analysis, and make the modeling and analysis process more clearly. Based on the theory make a detailed analysis to the serial and parallel system, proposes a method to calculate the system reliability of the components related serial system. The method takes into account the correlation of the various components in the system to make the results of system reliability more reasonable, which provides a new method for evaluating the reliability of the suspension system. The correlation problem of mechanical system reliability is widespread and unavoidable. The proposal of the mechanical system reliability model based on Copula function provides a scientific and practical approach for solving the problems of mechanical system reliability modeling and expectation.

BIBLIOGRAPHY

1. WEI Yanhua, ZHANG Shiyong. Copula Theory and Its Applications in Financial Analysis [M]. Beijing: Tsinghua University Press, 2008: 1-33.
2. ZHANG Yaoting. Copula Technology and Financial Risk Analysis [J]. Statistical Research, 2002, (4):48-51.
3. LUO Junpeng. Copula Theory and Its Application Study on Financial Analysis [J]. Tianjin: Tianjin University, 2005.
4. Zieja M.; Wazny, M. A model for service life control of selected device systems [J]. Polish Maritime Research, 2014, 21(2) 45-49.
5. TANG Jiayin, ZHAO Yongxiang, HE Pingdeng. Copulas New Theory for Reliability Calculation Involving Correlation in Mechanical Systems [J]. Mechanical Science and Technology, 2009, 28(4): 532-535.
6. HOU Bin. Application of Copulas in reliability theory [J]. Journal of Southwest University for Nationalities: Natural Science Edition, 2008, 34(4):660-668.
7. H Joe. Multivariate Models and Dependence Concepts [M]. Chapman & Hall, 1 977.
8. Sklar A. Fonctions de repartition an dimensions et leura marges [J]. Publication de l'insitutit de Statistique de l'

Universite de Paris, 1959, 8:229-231.

9. Nelson R.B. An introduction to Copulas[M]. Springer, New York, 1999.
10. Atkins, R J; Tidd, M; Ruffo, G.[J]. Sturgeon Bank, Fraser River Delta, BC, Canada: 150 Years of Human Influences on Salt Marsh Sedimentation [J]. Journal of Coastal Research, 2016, SI 75, 790-794.
11. YI Wende. Reliability of the dependent components in simple system [J]. Journal of Western Chongqing University (Nature Sciences Edition), 2005, 4(2): 5-8.
12. XIAO Yi. Study on Multivariate Hydrological Analysis Calculation Based on Copula Function. [D]. Wuhan: Wuhan University, 2007.

CONTACT WITH THE AUTHOR

Hai AN

School of Aerospace and Civil Engineering
Harbin Engineering University
Harbin 150001
Heilongjiang
CHINA